

FINAL REPORT

Atmospheric Plasma Depainting

SERDP Project WP-1762

FEBRUARY 2015

Stephen Hudak
Jerry Cuomo
North Carolina State University

Distribution Statement A

This document has been cleared for public release



REPORT DOCUMENTATION PAGE			<i>Form Approved</i> OMB No. 0704-0188	
Public reporting burden for this collection of information is estimated to average 1 hour per response, including the time for reviewing instructions, searching existing data sources, gathering and maintaining the data needed, and completing and reviewing this collection of information. Send comments regarding this burden estimate or any other aspect of this collection of information, including suggestions for reducing this burden to Department of Defense, Washington Headquarters Services, Directorate for Information Operations and Reports (0704-0188), 1215 Jefferson Davis Highway, Suite 1204, Arlington, VA 22202-4302. Respondents should be aware that notwithstanding any other provision of law, no person shall be subject to any penalty for failing to comply with a collection of information if it does not display a currently valid OMB control number. PLEASE DO NOT RETURN YOUR FORM TO THE ABOVE ADDRESS.				
1. REPORT DATE (DD-MM-YYYY) 02-08-2015		2. REPORT TYPE Final Report		3. DATES COVERED (From - To) 14-Apr-2010 to 30-Dec-2014
4. TITLE AND SUBTITLE Atmospheric Plasma De-Painting			5a. CONTRACT NUMBER W912HQ-10-C-0026	
			5b. GRANT NUMBER N/A	
			5c. PROGRAM ELEMENT NUMBER N/A	
6. AUTHOR(S) Hudak, Stephen J.			5d. PROJECT NUMBER WP-1762	
			5e. TASK NUMBER N/A	
			5f. WORK UNIT NUMBER N/A	
7. PERFORMING ORGANIZATION NAME(S) AND ADDRESS(ES) NORTH CAROLINA STATE UNIVERSITY 2701 SULLIVAN DR STE 240 CAMPUS BX 7514 RALEIGH NC 27695-7003			8. PERFORMING ORGANIZATION REPORT NUMBER	
9. SPONSORING / MONITORING AGENCY NAME(S) AND ADDRESS(ES) Strategic Environmental Research USACE, Humphreys ENGR CTR And Development Program SPT ACTIVITY Robin Nissan, Program Manager ATTN: CECT-HC 4800 Mark Center Drive, Suite 7701 Telegraph Road Alexandria, VA 22350-3605 Alexandria VA, 22315-3860			10. SPONSOR/MONITOR'S ACRONYM(S) SERDP HECSA	
			11. SPONSOR/MONITOR'S REPORT NUMBER(S)	
12. DISTRIBUTION / AVAILABILITY STATEMENT Approved for public release; distribution is unlimited.				
13. SUPPLEMENTARY NOTES In collaboration with AP Solutions, Inc., NAVSEA, NAVAIR, and AFRL				
14. ABSTRACT The overall objective of this project was to develop an innovative media-free atmospheric plasma coating removal system for use on Department of Defense (DoD) ship and vehicle platforms. This system is capable of removing all coating layers or partial layers and leaves the surface in condition suitable for new paint. Atmospheric plasma uses electrical energy to convert air into a reactive chemical state capable of breaking down paint into small molecular weight components such as carbon dioxide and water, thereby eliminating the associated costs and equipment necessary to handle media. The technology is portable, can be operated by manual or automatic means, can be scaled to a desired size, presents no undue occupational hazards to the tool operators, and creates no waste beyond the breakdown products of the original coating material. In addition to improving system design, development, and operation, scientific research was performed in order to obtain fundamental information regarding plasma properties, characterize depainted steel surfaces, test stripped then newly painted coupons, identify solid and gaseous ejecta waste material, and identify environmental and operational attributes.				
15. SUBJECT TERMS atmospheric plasma, plasma, depainting, paint, removal, stripping, grit blasting, coating, Navy, steel, cleaning, waste, disposal, hazard, mitigation, Clean Air Act, Clean Water Act				
16. SECURITY CLASSIFICATION OF:			17. LIMITATION OF ABSTRACT UU	18. NUMBER OF PAGES 201
a. REPORT UU	b. ABSTRACT UU	c. THIS PAGE UU		
			19b. TELEPHONE NUMBER (include area code) 919-515-7218	

Table of Contents

Table of Contents	i
List of Tables	iii
List of Figures	iv
List of Equations	ix
List of Acronyms	x
Keywords	xii
Acknowledgements	xiii
Abstract	1
Objective	3
Background	4
Technical Approach	9
Materials and Methods	11
Results and Discussion	12
Task 1 Determine capabilities of atmospheric plasma to remove Navy paint.....	12
1.1 Prepare Experimental Design	12
1.2 Perform Experimental Design.....	20
1.3 Adequate Removal Rates	25
Task 2 Substrate Condition after Paint Removal	29
2.1 Obtain Background Information & Prepare Samples	29
2.2 Analyze Treated Samples	31
2.3 Satisfactory Substrate Condition.....	57
Task 3 Characterize Atmospheric Plasma Plume	57
3.1 Spectroscopic Studies	57
3.2 CFD Modeling	75
3.3 Photographic and Electrical Studies	85
Task 4 Large Area Plasma Removal System.....	92
4.1 Design Large Area Plasma System.....	92
4.2 Fabricate and Test Large Area Plasma Device	110
Task 5 Hybrid Module Construction and Evaluation (cancelled)	139
5.1 Design Hybrid Module (cancelled).....	139
Task 6 Technologies for Waste Stream Management	139

6.1 Lab-Scale Manual System	139
6.2 Automated Large Area System	140
6.3 Hybrid Modules (cancelled)	144
Task 7 Quantify Risks for Environmental Hazards and Operator Safety	144
7.1 Milestone - Qualitative Gas Analysis	146
7.2 Lab-Scale Manual System	147
7.3 Large Area Automated System	157
7.4 Hybrid Modules (cancelled)	163
Task 8 Systems Integration and Transition.....	163
8.1 Lab-Scale Manual System and.....	163
8.2 Automated Systems	163
Task 9 Conferences and Meetings	173
9.1 NAVSEA Coordination meeting	173
9.2 External Conferences	176
9.3 SERDP/ESTCP Washington Annual Symposium.....	176
9.4 In Progress Review Meetings	176
Task 10 Reports	176
Conclusions and Implications for Future Research/Implementation.....	177
Literature Cited	180
Appendices.....	184
A. Glossary of Terms for Multiple Nozzles.....	184
B. List of Scientific/Technical Publications	185

List of Tables

Table 1: Itemized list of PlasmaFlux™ benefits compared to the statement of need.....	6
Table 2: Project team for Atmospheric Plasma Depainting under SERDP WP1762.....	9
Table 3: Factors and limits for CCD DoE.	21
Table 4: JMP data table obtained from the CCD DoE.....	22
Table 5: A few factors to be considered for paint removal.....	25
Table 6: Paint mass on different Navy ships by mass and estimates of time to remove using grit blasting or plasma.	26
Table 7: Summary of samples submitted for glancing angle x-ray diffraction.	44
Table 8: Optical profilometry results from grit blasted depainted surfaces and plasma surfaces.	52
Table 9: Summary of environmental performance testing of repainted, depainted test coupons.....	53
Table 10: Adhesion Test first and second run comparison ASTM D4541.....	55
Table 11: Actual and spliced wavelength ranges for the S2000 Spectrometer.....	64
Table 12: Wavelengths of the various N ₂ second positive system and N ₂ first negative system bands adapted from Reference [40].	67
Table 13: Average total and per-nozzle mass removed for various array angles.	115
Table 14: Conditions used for two-nozzle DoE.....	118
Table 15: Listing of design improvements for atmospheric plasma high power supply.	120
Table 16: Total and average Antifouling paint mass removed using one, two, three, or four active nozzles with the new power supply and four-pen array.	122
Table 17: Comparison of current and previous single- and multi-pass removal results.....	124
Table 18: Conditions tested in this DoE.....	128
Table 19: Calculation of CO ₂ which would be generated using atmospheric plasma to remove paint from Navy ships assuming all paint is converted to CO ₂ and H ₂ O.	145
Table 20: Quantitative measurements of gas and solid components which the operator would be exposed to during the operation of atmospheric plasma depainting.....	147
Table 21: Quantitative results from Area EDS scan of FB particulate residue.	151
Table 22: Quantitative results from Area EDS scan of AF particulate residue.	152
Table 23: Total Mass Recovered and Unrecovered from FB and AF samples.	153
Table 24: Mass spectra fragment patterns and relative peak intensity of gases from SRS UGA300 reference library.	155
Table 25: Comparison of performance of different vacuum sources.	168
Table 26: Shipyard visit highlights.....	173

List of Figures

Figure 1: Flow diagram illustrating the technical approach used for atmospheric plasma depainting..... 10

Figure 2: Automated setup for atmospheric plasma depainting at NC State University..... 12

Figure 3: Automated setup for atmospheric plasma depainting at AP Solutions..... 13

Figure 4: Test coupon with an experimental silicone ablative white paint subject to marine immersion testing in which the right half was removed with atmospheric plasma..... 14

Figure 5: Freeboard (FB) paint schematic typically used above the waterline..... 15

Figure 6: Examples of single plasma pass experiments to depaint coupons prepared using different manufacturers paints..... 15

Figure 7: Mass loss versus plasma distance to the substrate from three different paint suppliers..... 16

Figure 8: Illustration of coordinates for orientation of plasma to surface direction..... 16

Figure 9: An example FB coupon exposed to various single pass exposures in which the plasma to substrate angle was varied according to Figure 8..... 18

Figure 10: Statistical analysis of mass removed versus angle using JMP software..... 19

Figure 11: Antifouling (AF) paint schematic typically used below the waterline..... 19

Figure 12: 4"x 6"x 1/4" steel painted with Freeboard (FB) ready for testing..... 20

Figure 13: 4"x 6"x 1/4" steel painted with Antifouling (AF) ready for testing..... 20

Figure 14: Prediction profiler calculated from the CCD DoE..... 23

Figure 15: Removal rate response surfaces for the factors a) speed and flow, b) height and angle, c) angle and speed, d) flow and height, e) height and speed, and f) angle and flow..... 24

Figure 16: Removal rate calculation based on mass per unit time removal..... 26

Figure 17: Removal rate calculation based on area removed per unit time..... 27

Figure 18: IR photo of surface temperature during removal..... 27

Figure 19: Atmospheric Plasma Depainted FB panel, 2' x 3' x 3/8" (610 mm x 914 mm)..... 28

Figure 20: Enlarged area photo from Atmospheric Plasma Depainted FB panel..... 29

Figure 21: 4 x 6 inch painted steel panels in which the lower half was depainted using atmospheric plasma..... 30

Figure 22: The center photograph is from a control, unpainted, and near white metal blasted steel. Photos on the left and right are enlarged areas showing each layer uncovered by atmospheric plasma..... 30

Figure 23: DH36 steel surfaces after three different surface treatments..... 31

Figure 24: Plasma plume temperature measured using a thermocouple..... 33

Figure 25: Photograph of steel after plasma exposure at position (75, 50)..... 34

Figure 26: Thermal image model by Arnold using a proprietary algorithm to predict thermal input from plasma in motion..... 35

Figure 27: Dynamic steel temperature measured during plasma depainting in which the plasma was rastered in +/- Y stepped in the X direction..... 36

Figure 28: Gaussian distribution function used as heat source geometry for input to heat transfer model..... 37

Figure 29: Snapshot of modeled thermogram A) during static plasma treatment at the center position and calculated thermocouple traces at positions X = 5, 50, 75, 100, 145 mm B)..... 38

Figure 30: Results of using Neira dynamic heat transfer model to simulate plasma rastering over a surface..... 39

Figure 31: Atmospheric plasma long scan model with induced cooling correction..... 40

Figure 32: XPS spectra obtained from steel after AF paint was removed by grit blasting..... 41

Figure 33: XPS spectra obtained from steel after AF paint was removed by plasma. 42

Figure 34: XPS spectra obtained from steel after AF paint was removed by grit blasting, then by plasma. 43

Figure 35: Analysis of grit blasted A4 indicated the presence of iron on the surface. 45

Figure 36: Analysis of grit blasted A5-br indicated the presence of iron on the surface. 45

Figure 37: Analysis of plasma depainted A3 indicated the presence of iron oxides on the surface
..... 46

Figure 38: Analysis of plasma depainted A5 indicated the presence of iron oxides on the surface
..... 46

Figure 39: Various forms of oxides on iron obtained from sources [13] and [14]. 47

Figure 40: Oxide growth on Fe versus time at four temperatures [15]. 48

Figure 41: Progression of flash rusting on iron surface after water jet paint removal [17] [13]. 49

Figure 42: Steel panels subject to ultra-high pressure water jet (UHPWJ) [16]. 49

Figure 43: Optical micrographs from steel surfaces painted with AF then depainted using grit
blasting (left) and plasma (right). 50

Figure 44: Optical profilometry plots obtained from the surfaces of steel samples painted with
AF paint. 51

Figure 45: Scanning Electron micrographs of as received and grit blasted steel surfaces, which
were treated with atmospheric plasma. 52

Figure 46: Cross section optical micrographs obtained from depainted then repainted steel
coupons. 54

Figure 47: Examples of ASTM 4541 pull-off adhesion from dry samples. 54

Figure 48: Example test coupons subject to B117 salt after 3,000 hours. 55

Figure 49: Photographs from test specimens during ASTM G95 cathodic delamination testing.
..... 56

Figure 50: Examples of coupons after cathodic disbondment testing for 60 days according to
ASTM G95. 56

Figure 51: Example test coupons from alternate immersion testing at Key West, FL after four
months. 57

Figure 52: Optical emission spectrum of the plasma pen ranging from 200 to 800 nm. 61

Figure 53: Detail of the optical emission spectrum of the free jet plasma pen from 300 to 400 nm
showing the second positive N₂ bands. 61

Figure 54: The triplet neutral atomic oxygen lines cannot be resolved by the current Ocean
Optics spectrometer. 62

Figure 55: The triplet neutral atomic nitrogen lines are easily resolved by the current Ocean
Optics Spectrometer. 62

Figure 56: Detail of neutral copper emission lines captured by fast acquisition capability of
Ocean Optics spectrometer. 62

Figure 57: Diagram of the OES characterization setup indicating the various aspects of the
plasma torch, the radial and axial directions with the intersection denoting the 0,0 point, and
arrangement of the computer controlled 4-channel Ocean Optics S2000 spectrometer connected
via fiber optic cable to a pinhole aperture. 65

Figure 58: A broadband OES spectrum of the plasma torch with several peaks identified. 65

Figure 59: OES N₂ second positive system and N₂ first negative system bands and two Cu I
lines. 66

Figure 60: OES spectrum of Cu I lines.....	66
Figure 61: OES spectrum of atomic N I lines.....	67
Figure 62: OES spectrum of O I line.....	68
Figure 63: Atomic N I lines with the exception of the intense atomic O I line at 844.54 nm.	68
Figure 64: Radial OES spectra acquired at an axial position of 0 mm.....	69
Figure 65: Radial OES spectra at an axial position of 1 mm.....	69
Figure 66: Radial OES spectra at an axial position of 2 mm.....	70
Figure 67: Radial OES spectra at an axial position of 3 mm.....	70
Figure 68: Radial OES spectra at an axial position of 4 mm.....	70
Figure 69: Radial OES spectra at an axial position of 5 mm.....	71
Figure 70: The radial distribution of the intensity of the 777 nm atomic oxygen line normalized to the N ₂ Second Positive System band head.....	71
Figure 71: Radial distribution of the intensity of the N ₂ Second Positive System band head.....	72
Figure 72: Axial OES spectra at a radial position of 0 mm.....	72
Figure 73: The axial distribution of the intensity of the 777 nm atomic oxygen line normalized to the N ₂ Second Positive System band head.....	73
Figure 74: The axial distribution of the N ₂ Second Positive System band head.....	73
Figure 75: The log intensity of spectra over a wider axial range showing a decrease in the atomic and molecular nitrogen intensities and an increase in a broadband continuum.....	74
Figure 76: The ratio of intensity/area as a function of axial position.....	75
Figure 77: A simple converging/diverging nozzle is used to generate a supersonic flow.....	83
Figure 78: Volume filling tetrahedral mesh used to discretize the Navier-Stokes equations.....	83
Figure 79: Velocity contours for incompressible fluid in converging/diverging nozzle.....	84
Figure 80: Velocity vector plot for incompressible flow in converging/diverging nozzle.....	84
Figure 81: Velocity contour for compressible flow.....	85
Figure 82: Density contours for compressible flow, flow from right to left showing reduced density as fluid accelerates.....	85
Figure 83: A schematic drawing of the Plasma Vortex torch with components of a) nozzle, b) nozzle retaining nut, c) barrel length extender, d) primary barrel, e) dielectric spacer, f) electrode, g) spring, h) dielectric electrode holder and gas delivery, and i) end cap.....	86
Figure 84: The Plasma Vortex shown in a) side view, b) front isometric, and c) the rear isometric view.....	87
Figure 85: Major components of the disassembled Plasma Vortex.....	87
Figure 86: Plumes created by various flow, power, frequency, nozzle geometry and materials.....	88
Figure 87: I/V characteristics of the Plasma Vortex operating at 50 kHz and 50 slm with a RMS power of 598 W and resistance of 2 k Ω	89
Figure 88: Fluid flow modeling from the SOLIDWORKS model using FloExpress software... ..	89
Figure 89: Operation of the Plasma Vortex with free exhaust expansion.....	90
Figure 90: Example of use of high speed photography coupled with a pulse generator to trigger the shutter on a high speed infrared camera.....	91
Figure 91: A series of photographs showing the presence of mach discs in plasma plumes.....	92
Figure 92: A multi-nozzle configuration utilizing the existing internal pen geometry.....	93
Figure 93: Nozzle arrangement for a twelve-nozzle (3x4) configuration. Three individual 1x4 modules are visible, as well as the vacuum shroud.....	94
Figure 94: Coaxial source schematic; (a) photograph of the assembly (b) and image down the barrel of the assembly during a 500 W, 5 L/s ambient air discharge (c).....	98

Figure 95: Electrical and Optical Diagnostics Used to Characterize the Coaxial VHF Source. .	99
Figure 96: Equivalent circuit used to obtain plasma density n_e and sheath reactance X_s	101
Figure 97: Plasma resistance R_p (◆) and reactance X_p (■) measured as a function of delivered power for ambient air flow of 5 L/s.	102
Figure 98: Electron density (◆) and sheath thickness (■) estimations made from electrical measurement of source impedance as a function of delivered power to the source.	102
Figure 99: Representative B-loop measurement of current waveforms produced in the coaxial plasma source. 1 Volt is approximately equal to 0.1A induced current on the loop diagnostic.	103
Figure 100: Response of bulk plasma resistance R_p at the RF drive frequency as a function of electron density for various frequencies.	105
Figure 101: Integrated spectra as a function of delivered power from 350 W to 595 W.	106
Figure 102: Normalized spectra as a function of delivered power. Species of interest, including NO, OH, and O are highlighted.	106
Figure 103: Removal rates as a function of air flow at two power levels. Applicator was positioned 0.76 cm from the painted surface. The VHF electrode was recessed 1.5 cm from the end of the applicator.....	107
Figure 104: Removal rates as a function of power for two applicator-to-surface gaps. Note the significant increase in removal rate as the gap is decreased.	108
Figure 105: Schematic diagram of a shower head design plasma concept and an actual individual cell.....	109
Figure 106: Depainting brush head concept using atmospheric plasma.....	110
Figure 107: Four-nozzle plasma in operation.	112
Figure 108: Four-pen array and coupons. A) Array is at a 90° angle to the coupon, removal swaths are separated by 1.25". B) Array is at a 23.6° angle to the coupon, removal swaths are separated by 0.5".....	113
Figure 109: Removal swaths from the first four-pen removal test. The white areas are chipped paint; this paint was missing prior to plasma treatment. Scale is in 1/8" increments.....	113
Figure 110: Widths of removal features from a two-nozzle removal conducted with an array angle of 90°.....	114
Figure 111: Per-nozzle removal masses for various array angles.....	115
Figure 112: Interaction of two plasma nozzles on an Antifouling coating surface.	116
Figure 113: Multi-nozzle multi-pass removal on an Antifouling coupon.	117
Figure 114: Sample SER-AF-187, which was treated at a speed of 7 in/s with an array angle of 1.8 degrees. (Treatment rate 7 ft ² /hr).	119
Figure 115: Sample SER-AF-195, which was treated at a speed of 7 in/s with an array angle of 2.3 degrees. (Treatment rate 8.75 ft ² /hr).	119
Figure 116: Sample SER-AF-199, which was treated at a speed of 5 in/s with an array angle of 1.4 degrees. (Treatment rate 3.75 ft ² /hr).	119
Figure 117: Four active nozzles driven by the new power supply during a single pass experiment to remove Antifouling paint.....	121
Figure 118: Mass removed per nozzle for different number of active nozzles in a single-pass experiment.....	122
Figure 119: Photograph of Antifouling sample after a single-pass experiment with four active nozzles and the new power supply. (Mass removed was 2.649 g, or 0.6623 g per nozzle).	123
Figure 120: Four active plasma nozzles over the Antifouling coating surface during a multi-pass experiment.....	125

Figure 121: A sample treated by a single pass with an 80 degree array angle.	127
Figure 122: Antifouling sample treated with conditions: angle of 2.42°, speed 2.953 in/s (75 mm/s), treatment rate 15.557 ft ² /hr (1.445 m ² /hr)	129
Figure 123: Antifouling sample treated with conditions: angle of 3.00°, speed 2.953 in/s (75 mm/s), treatment rate 19.342 ft ² /hr (1.797 m ² /hr).....	130
Figure 124: Antifouling sample treated with conditions: angle of 2.42°, speed 3.937 in/s 100 mm/s), treatment rate 20.768 ft ² /hr (1.929 m ² /hr).....	130
Figure 125: 2' x 3' x (3/8inch) Panels Prepared for Scale-up Work.	132
Figure 126: Illustration of the path of travel for the eight-nozzle array conducting a removal with a normal pass and an additional subpass: angle array is 5.82°.	132
Figure 127: The 20 kW plasma power supply manufactured for task 4.2.4.	134
Figure 128: Photograph of eight-nozzle plasma applicator operating at full power.....	135
Figure 129: A treatment at $\alpha=90^\circ$, with a treatment rate of 19.7 ft ² /hr. Note the high degree of both over treatment and under treatment in different areas.	136
Figure 130: A treatment at $\alpha=3.0^\circ$, with a treatment rate of 25.8 ft ² /hr.	137
Figure 131: A treatment at $\alpha=\sim 0^\circ$, with a treatment rate of 37.8 ft ² /hr.	138
Figure 132: Large area waste collection system.	141
Figure 133: Schematic diagram of a single operator grit blasting operation.	143
Figure 134: Schematic illustration of set up for ejecta collection during depainting.	148
Figure 135: Example of SEM of smaller FB particles on Carbon tape.	149
Figure 136: Example of SEM of larger FB particles on Carbon tape.....	150
Figure 137: Example of SEM of AF particles on Carbon tape.....	150
Figure 138: Area EDS scan showing elemental species present in the collected FB residue. ..	151
Figure 139: Area EDS scan showing atomic species present in the collected AF residue.....	152
Figure 140: Reaction chamber for gas analysis connected to a UGA300 mass spectrometer via a capillary.....	154
Figure 141: Mass spectrum obtained from plasma depainting of a test coupon.....	154
Figure 142: Graph in Pressure vs time mode of mass spectra obtained from plasma depainting of a test coupon.	156
Figure 143: UV intensity of a bare 15 Watt Fluorescent Bulb.	158
Figure 144: UV intensity of a 15 Watt Fluorescent Bulb through plastic Safety Glasses.....	159
Figure 145: UV intensity of an unshielded plasma pen array (twelve inches from source).....	160
Figure 146: UV intensity of a plasma pen array through plastic safety glasses (twelve inches from source).....	160
Figure 147: Common sound source intensities compared to an operating plasma applicator...	161
Figure 148: Electromagnetic Field Strength of Common Sources compared to plasma pen. ...	162
Figure 149: Static vacuum shroud test setup.	165
Figure 150: Removal pattern for static vacuum shroud testing (Antifouling sample). The vacuum shroud shown in Figure 149 was located at the bottom of the sample as oriented in this photograph (at $x=\sim 0$).	167
Figure 151: Prototype integrated vacuum shroud installed on a four-pen applicator.....	170
Figure 152: Prototype vacuum shroud as installed for testing.....	171
Figure 153: Photographic example from the web of a ship's hull supported in dry dock for renovation (from www).	174
Figure 154: Example collection setup for general area vacuum containment (From www).	175

List of Equations

Equation 1. Estimate of mean free path of electrons. 33

Equation 2. Three-dimensional transient heat transfer solution using Fourier’s law 36

Equation 3. Heat source mathematical model used for input to heat transfer model 37

Equation 4. Heat loss due to surface to ambient radiation..... 38

Equation 5. Heat loss factor as a function of natural external convection..... 38

Equation 6. Oxidation of iron. 43

Equation 7. Hydration of iron. 44

Equation 8. Iron hydroxides and reactions evolving water..... 44

Equation 9. Oxidation of nitric oxide to nitrous oxide. 73

Equation 10. Description of Reynolds number..... 81

Equation 11. Plasma impedance along a transmission line. 99

Equation 12. Real portion of plasma impedance. 100

Equation 13. DC resistance of plasma. 100

Equation 14. Cross section for charged species..... 100

Equation 15. Inductor model of bulk plasma reactance..... 101

Equation 16. Imaginary part of the plasma discharge impedance. 101

Equation 17. Plasma spacing of four nozzle plasma as a function of angle. 112

Equation 18. Desired spacing calculated based on array angle..... 112

List of Acronyms

Symbol	Identity	Description
AF	Antifouling	Paint below waterline on ships
AFRL	Air Force Research Labs	Dayton, OH
AP	Atmospheric Plasma	Plasma at atmospheric pressure
APS	Atmospheric Plasma Solutions	Cary, NC
ASTM	American Society for Testing Materials	
CARC	Chemical Agent Resistant Coatings	
CCD	Charge Coupled Device	Digital imaging sensor
CCD	Central Composite Design	Statistical method in DoE
CFD	Computational Fluid Dynamics	Computer based physics/math approach to problem solving
COTS	Commercial Off The Shelf	definition
C _p	Heat Capacity	Units of J/K
DoE	Design of Experiments	Statistical method of testing
DOD	Department of Defense	
ϵ	Emissivity	energy radiation from a surface
ejecta	Waste generate during plasma depainting	definition
EPA	Environmental Protection Agency	
FB	Freeboard	Haze grey paint above waterline on ships
FEA	Finite Element Analysis	Use many small defined sections to analyze a problem
g	Accelerating gap	Plasma term
GAXRD	Glancing Angle X-Ray Diffraction	Technique for analyzing surfaces
IR	Infrared	
JMP	JMP	Statistics software from SAS
κ	Thermal Conductivity	(W/(m·K)) or W·m ⁻¹ ·K ⁻¹
n _e	electron density	free electrons per unit volume in the plasma
NAVAIR	Naval Air Systems Command	
NAVSEA	Naval Sea Systems Command	
NSWCCD	Naval Surface Warfare Center Carderock Division	West Bethesda, MD
NCSU	North Carolina State University	Raleigh, NC
OAS	Optical Absorption Spectroscopy	Visible light analysis
OES	Optical Emission Spectroscopy	Visible light analysis
P _e , P _a	Pressure at exhaust and ambient	Arbitrary units
PID	Photo Ionization Detector	Measures volatiles, particles
Q-factor		ratio of the dissipated energy over the stored energy
R _a	Surface roughness	Arithmetic mean
R _p	Plasma resistance	used to estimate electron density in bulk plasma

Rq	RMS roughness average	Root mean square
<i>Re</i>	Reynolds number	Fluid flow numeric
σ	Heat distribution parameter	Volume description of heat
SAS	Statistical Analysis Software	Cary, NC
SRS	Stanford Research Systems	Manufactures scientific equipment
SERDP	Strategic Environmental Research and Development Program	
UV	Ultraviolet	
<i>v</i>	Streamer head velocity	Plasma term
VHF	Very High Frequency	30 MHz to 300 MHz
XPS	X-ray photoelectron spectroscopy	Surface analysis technique
XRD	X-ray diffraction	Crystal structure identification

Keywords

Atmospheric plasma, plasma, depainting, paint, removal, stripping, grit blasting, coating, Navy, steel, cleaning, waste, disposal, hazard, mitigation, NCSU, AP Solutions, NAVSEA, NAVAIR, AFRL, Clean Air Act, Clean Water Act

Acknowledgements

Special thanks to;

SERDP program management and supporting staff for sponsoring this work; Bruce Sartwell, Robin Nissan, Jonathan Bunger, Jeff Houff, Caitlin Rohan.

Alisa Hunt-Lowery Extension Specialist at NCSU for all the help with JMP design and analysis. Harold Morton and Mahdi Fahim NCSU Environmental Health & Safety for exhaust gas analysis.

Mark Walters Duke University for help in the lab with XPS, XRD, FTIR; Roberto Garcia NCSU Analytical Instrumentation Facility for metallurgy and XRD.

Members who contributed, but have not been credited elsewhere or have been re-assigned, promoted, moved on or otherwise deserve recognition; Michelle Barga (AFRL), Elizabeth Haslbeck, Jacob Vestal (NSWCCD), Roger Sanwald, Sarah Daniell, Anthony McWilliams, Brian Owen, Stephen White, Dick Guarnieri, Bob Roth, James Mulling, Darin Thomas, David Rowson, Brandon Byrnes, Greg Sabin, Alderson Neira (NCSU), Bruce Roach, Alex Panhorst, Jess Beasley, Chris Morano, Daniel Jonsen, Olga Asanov (APS).

Views, Opinions, and/or finding contained in this report are those of the author(s) and should not be construed as an official Department of Defense position or decision unless so designated by other official documentation.

This research was supported wholly (or in part) by the U.S. Department of Defense, through the Strategic Environmental Research and Development Program (SERDP).

This material is based upon work supported by the US Army Corps of Engineers, Humphreys Engineer Center Support Activity under Contract No. W912HQ-10-C-0026.

Abstract

The objective of this project was to develop an innovative media-free atmospheric plasma coating removal system for use on Department of Defense ship and vehicle platforms. Coating removal processes currently used produce massive quantities of hazardous wastes such as spent blast media, wastewater, or toxic chemicals. Disposing of these waste products is a burden with high costs and intense scrutiny under environmental regulations. Additional costs are also incurred to inventory, store, and handle media prior to use, and to contain and collect the waste media before disposal. Current technologies including wet or dry media blasting, mechanical sanding, laser ablation, induction heating, FlashJet™ technology, and chemical stripping, have limited flexibility as a complete coatings removal solution. The Laboratory for Integrated Manufacturing Science and Technology at NC State University and industrial partner, Atmospheric Plasma Solutions Inc. have conducted fundamental and applied research in order to investigate the use of atmospheric plasma as a total coating removal system. Contributing to the current research were additional partners from NAVSEA, NAVAIR, and AFRL. The PlasmaFlux™ system, a broadly applicable plasma coating removal system, was used to remove two major coating systems commonly found on Navy ships; 1) Freeboard paint typically used above the waterline, and 2) Antifouling paint typically used below the waterline. The research was conducted in three overlapping phases; 1) determining the capability of atmospheric plasma to remove paint, 2) development and investigation of large area plasma devices, and 3) investigation of environmental and process hazards, waste mitigation, operational safety, integration and transition. In the course of this research effort, it was determined that an appropriate plasma source could remove topcoat and primer from metal test panels. Due to the oxidizing nature of the plasma, the iron surfaces were cleaned to atomic levels leaving a stable form of iron oxide. Substrate temperature was monitored and did not exceed 200 °C (392 °F) during depainting with plasma. It was also demonstrated that residual paint left by incomplete grit blasting was subsequently removed to bare metal and its oxide using plasma. The plasma treatment did not alter the surface profile created by grit blasting. Test panels depainted using plasma along with grit blasting panels for comparison, were subsequently coated with new paint, then subject to performance tests including adhesion pull-off, B117 salt fog, cathodic disbondment, and alternate immersion in sea water. Some panels were repainted immediately, but one set was aged two weeks after plasma depainting, before they were recoated for performance testing. There were no statistically significant differences in any of the sample sets which indicated that using plasma to remove paint provided similar paint adhesion performance when compared to grit blasting for paint removal.

The PlasmaFlux™ system uses a low pressure compressed air source and electricity to produce a special form of atmospheric pressure, air plasma, which is highly chemically activated and attacks (oxidizes) the organic components of paints and other coatings. Optical emission spectroscopy was used to identify the presence and distribution of chemically active atomic and molecular species of oxygen and nitrogen in the complex makeup of the plasma. Organic components of paint were broken down into small molecular weight components, primarily carbon dioxide and water, as determined by mass spectroscopy. Inorganic fillers used in the paint were the primary components of solid waste as determined using optical and electron microscopy and energy dispersive x-ray analysis. Depending on the operational conditions,

especially when using aggressive removal conditions upon scale-up of the plasma system, some smaller not completely broken down fragments of the coating system were also part of the waste stream. Theoretical calculations were performed to determine the mass of gaseous and solid products which would be expected if all initial paint was converted to mineral constituents including carbon dioxide and water. Removing paint from one aircraft carrier as an example, carbon dioxide would be produced in the amount similar to that produced by five average automobiles per year. In terms of solid waste, using plasma to remove paint, approximately 40 to 60% of the original coating mass is collected, primarily due to the inorganic fillers, the remainder of which is converted to gas. These numbers were confirmed experimentally by measuring mass before and after a confined depainting experiment. When operated with free exhaust to the air, NO, a nuisance gas was detected. Through design and ensuring that plasma is in contact with paint for removal, generation of nuisance gas should be minimized. Early results of removal rates measured using a single applicator indicated that approximately eight to fourteen nozzles would be needed to achieve reasonable commercial removal rates. Scale-up in design, manufacture, and testing was performed in increments up to an eight-nozzle plasma system including the power supply. Removal rates were calculated in many experiments and found suitable for scale-up potential. A waste management system was integrated with the plasma system and preliminary operation and experimentation completed. No occupational or undue environmental hazards were identified. Measurements did not identify any undue hazards including sound, EMF, UV/visible and other potential operational hazards. The technology was portable, could be operated by manual or automatic means, was scaled to a desired size, presented no undue occupational hazards to the tool operators, created no significant waste beyond the breakdown products of the original coating materials, did not negatively alter the steel surface, and produced acceptable repaint adhesion performance.

Objective

The overall objective of this project is to develop an innovative media-free atmospheric plasma-based coating removal system for use on Department of Defense (DOD) ship and vehicle platforms. This was in response to BAA-09-0001 “Environmentally Benign, High-performance non-media paint strippers” WPSO-10-05, in which a number of improved features were desired which included; preparation of the substrate for recoating without negatively impacting condition or profile of the substrate, production rates similar to existing technologies, deployable in a DoD environment, allow other work nearby, not generate or be susceptible to interference, remove multiple or select coating layer removal in air and/or underwater, be amenable to current capture technology integration to manage removed coatings, allow manual or automated means, generate no inherent waste streams other than removed coating, and to present no environmental or occupational safety and health concerns which limit broader application and use. The atmospheric plasma system is anticipated to be capable of selectively removing individual coating layers, partial layers, or complete layers and not damaging the underlying substrate. Atmospheric plasma uses electrical energy to convert air into a reactive chemical state capable of breaking down paint into small molecular weight components such as carbon dioxide and water, thereby eliminating the associated costs and equipment necessary to handle media. The technology requires no media, is portable, can be operated by manual or automatic means, results in a clean surface ready for re-coating, presents no undue occupational hazards to the tool operators, and creates no waste beyond the breakdown products of the original coating material which can be collected using existing technologies.

Background

The US Navy and other DOD Components have a critical need for media-free, high performance, environmentally friendly coatings removal processes for ship hulls and numerous other weapons platforms. A versatile and environmentally friendly coating removal process is also desired in many commercial sectors including the aviation and automotive industries. Current technologies including wet or dry media blasting, mechanical sanding, laser ablation, induction heating, FlashJet™ technology, and chemical stripping have limited flexibility as a complete coatings removal solution to address multiple substrates, coating types, and applied thicknesses. This project presents a novel technology to remove coatings from virtually any substrate material. Atmospheric plasma (AP) technology requires no media, is portable, can be operated by manual or automatic means, often results in a clean surface ready for immediate re-coating, presents no undue occupational hazards to the tool operators, and creates no waste beyond the original coating material. AP is a dry, media-free coating removal technology which uses only compressed air and standard electrical power as inputs to produce atmospheric plasma that is highly chemically activated and oxidizes any organic components in paints and other coating materials.

In recent years, North Carolina State University (NCSU) has been a leader in the identification of new applications for AP technology. In order to develop and commercialize several AP-based technologies conceived by himself and others [1] during the course of his doctoral research at NCSU, Peter Yancey founded AP Solutions, Inc. (APS) in 2005. APS has since developed the PlasmaFlux™ coating removal system as well as a number of other AP based products. Since that time, NC State University's Laboratory for Integrated Manufacturing Science and Technology (L-IMST) has performed additional fundamental research on AP technology using equipment developed by APS.

APS's current developmental, working prototype PlasmaFlux™ coating removal system is capable of selectively removing a wide variety of coating materials, weighs less than 60 pounds, uses compressed air as a working gas and runs on 5 kW or less from a 240 VAC power outlet, making it a truly portable and easily-deployed system. Basic proof-of-principle multi-head prototype plasma system configurations have been constructed and tested. The ability to scale the technology is a tremendous advantage both for manual and automated applications, taking into consideration all of the costs associated with media acquisition, storage, handling, and disposal. Elimination of these expenses makes AP an attractive coating removal process.

With the APS PlasmaFlux™ system, the plasma exits as a flowing plume of reactive species that emanate from the plasma nozzle aperture; therefore, line of sight is not required for coating removal. The resulting immersion of substrate parts in the flowing plasma plume allows for coating removal from holes, cracks, or crevices, in honeycomb structures, around fasteners, in overlap joints and corners, and inside tanks and voids. Removal rates greater than a competing laser process have already been demonstrated. AP is a layer by layer removal process capable of stripping to a discrete location within the coating system or completely removing the entire coating system down to the bare substrate. Due to the low-temperature, dry, non-abrasive characteristics of the AP coating removal process, remaining subsurface materials are usually unaffected. The exposed surface is often suitable for immediate recoating. Interaction of AP with dense oxide and solid metal substrate surfaces is self-limiting and does not alter the

substrate profile or geometry, while the process has a demonstrated capability to remove highly metal-laden paints including anticorrosive paints containing 93% zinc solids.

The by-products of the removal process are largely carbon dioxide, water, and inorganic components which can be easily contained using existing technologies. Current grit blast collection systems would readily contain the waste, which would be mainly composed of inorganic pigments and fillers in the coating and any low molecular weight fragments of undigested coating material. In cases where the coating may contain hazardous substances such as chromium, crystalline silica, lead, or cadmium, currently available commercial off-the-shelf (COTS) HEPA vacuum systems could be used with little or no modification. The AP process introduces no additional waste beyond the original coating material. Table 1 contains the desired features that were listed in the statement of need for a media-free removal technology to be developed in this project, along with a corresponding list of benefits offered by the PlasmaFlux™ system.

Different types of plasma-based processes have seen limited use in paint removal applications, with moderate success. Thermal spray has been used to remove paint by injecting glass powder, fibers, and other vitreous materials into plasma for coating onto metal and concrete structures, particularly those with lead based paints [2, 3, 4]. This was demonstrated in an ESTCP program on the viaduct bridge at Rock Island Arsenal, IL and the Kaneohe Bay Hangar Door. This technique does not utilize the plasma directly, but rather as a high temperature source to melt vitreous material for deposition onto the coating. Upon cooling, the difference in expansion coefficient of the coating versus the substrate causes the coating to spall. The process is repeated until all of the coating material is removed. The high temperatures are not appropriate for thin wall metallic structures or other thermally sensitive substrates.

Table 1: Itemized list of PlasmaFlux™ benefits compared to the statement of need.

<u>Desired Features from SON:</u>	<u>Benefits of PlasmaFlux™ Technology</u>
Media-free	Only material requirement is compressed air
Environmentally benign	No media to dispose of, efficient removal process, reduced waste stream
Cost-effective	Inexpensive (media-free, low waste volume) and extremely versatile technology
Applicable to wide range of coatings	Any coating with organic component can be removed
Applicable to wide range of substrates	"Top-down" technique is largely insensitive to substrate type
Capable of preparing substrate for recoating	Same device performs bulk removal, cleaning, and adhesion promotion; does not modify existing substrate surface profile
Nondestructive to substrate condition and profile	Process variables allow for very gentle to very aggressive removal regimes, as applicable
Non-Contact	Treatment at up to one inch from surface
Enable multiple and selective layer removal	Layer-by-layer "top-down" removal
Enable coating removal in air and underwater	Standard PlasmaFlux™ process operates in air, feasibility of underwater system will be evaluated
Achieve comparable rates to existing technologies	Current rates (50 sq ft/hr per nozzle) may be multiplied through higher-power and hybrid systems
Easily deployed into Navy industrial environment	Small and light; Rugged solid-state power electronics design; Modular design for in-field reconfiguration and maintenance
Compatible with ongoing nearby work	Nearby processes are not adversely affected
RFI compatibility	Proper shielding attenuates potential interference
Easily integrated into existing capture technology (APACTS)	Physical size and configuration is similar to a paint sprayer; airflow well within handling capacity of APACTS filtration
Present no limiting environmental or occupational safety/health concerns or hazards	Use with proper exhaust gas and particulate collection system ensures no undue safety or environmental risks. Use with APACTS system for extra protection.
Generate no inherent waste streams to manage other than removed coatings	Reduces amount of solid waste stream by breaking down organic components into vapor
Allow manual or automated application	Handheld pen and robotic system are currently available

In another study, a mild temperature hydrogen plasma created with a microwave source at reduced pressure provided early insight into plasma-based paint removal mechanisms [5]. Standard chemical agent resistant coatings (CARC) consisting of one or two part moisture cured polyurethane military paints with or without an epoxy primer on aluminum and steel were tested in an evacuated chamber with 200-300 °C substrate heating and direct exposure to the hydrogen plasma beam. Up to 50% of the coating weight was lost during treatment, but only with the combination of heat and plasma at sub-atmospheric pressure. Bombardment by atomic species alone including helium, argon, or hydrogen was not effective at removing the coating. The hydrogen plasma was able to react with functional groups in the polymer matrix such as urea, amide, and hydroxyl groups, while inorganic fillers remained. It was speculated that the level of oxygen in the sample may be linked to chemical reactivity.

The effects of pure oxygen plasma were demonstrated while etching powder coating on aluminum [6]. Within two to four minutes of pulsed treatment at low pressure, the polymer matrix was removed and inorganic fillers remained. Although successful, the use of low-

pressure plasma is not practical for large scale applications. The use of an atmospheric non-thermal plasma jet has been reported as successfully removing 30 μm thick polyurethane paint from the surfaces of waste plastics [7]. In this case, dry air and a mixture of nitrogen and oxygen were fed through a jet nozzle for treatment of substrates up to 150 mm from the plasma source.

Plasma is considered the fourth state of matter, which is formed when sufficient energy, such as thermal or electromagnetic energy, is coupled into a gas, such as air, displacing outer valence shell electrons. There are two main types of plasma that can be formed: thermal or “hot” plasma, which is found in lightning, plasma cutters, and stars; and non-thermal or “cold” plasma, which is found in neon lights, fluorescent lighting, and the northern lights or aurora borealis. The PlasmaFlux™ system creates a non-thermal or cold plasma. Cold plasma is useful when it is desired to have the enhanced chemical activity of plasma without the intense heat. Because the PlasmaFlux™ system uses cold atmospheric plasma, it is able to remove coatings from temperature sensitive substrates such as composites and bulk plastics.

The APS PlasmaFlux™ system is specifically engineered to quickly remove polymeric coatings, including those found on aerospace composites. APS has been working closely with Mr. Jeff Kingsley of the AFRL at WPAFB, on a Phase I and Phase II SBIR project to develop an environmentally friendly coating removal system based on the APS PlasmaFlux™ system for the F-22 Raptor and F-35 Joint Strike Fighter programs. In this work, APS has successfully demonstrated rapid removal of pertinent aerospace coatings, with an emphasis on partial removal of coatings from temperature-sensitive substrates. Much of the work for the AFRL contract has been focused on exploring the effects of varying process parameters on coating removal for a number of coatings and substrates. Additional work has been performed to characterize the removal rate, removal pattern, and surface characteristics of treated samples. The highest removal rate obtained so far under these conditions is approximately 50 ft^2 per hour with a single nozzle, for a heavily-loaded RAM coating. Future efforts will focus on incorporating many nozzles into a single head to multiply the single-nozzle removal rate by the number of nozzles in the unit.

While the core PlasmaFlux™ technology and the work performed on the Air Force project provide a strong foundation for the SERDP work, it is important to note several fundamental differences between the two projects. First, the chemistry of the coating stacks involved in the two projects are quite different, which necessitates some preliminary work to estimate etch rates and study any unique effects or challenges with the coating materials targeted for this effort. The second key difference is in the substrate material. A thick steel ship hull, for example, can tolerate a much more aggressive paint removal process than a fiber composite substrate, or even a heat-treated aircraft aluminum substrate. For some naval applications, a number of more aggressive treatment regimes that are unsuitable to aerospace applications may prove useful, with the potential for higher removal rates. A final difference between the two applications is that the coatings of interest in this SERDP project are typically much thicker than the aerospace coatings investigated. However, NCSU and APS have successfully demonstrated removal of coatings in excess of 30 mil, particularly military sealants and baked-on polymethyl methacrylate (PMMA) photoresist films. NCSU has demonstrated effective removal of aerospace sealants from a number of different substrates through work with the In-Service Support Center at NAVAIR. There are a number of benefits to this approach, including the ability to perform

selective/partial removal, decreased solid waste mass due to oxidation of organic components to vapors, and the ability to remove coatings from tight areas and/or parts with complex shapes. An alternative approach to removing thick coatings is a "bottom-up" approach, where the plasma is targeted directly at the coating-substrate interface to release the coating from the surface, while the bulk of the material is lifted mechanically or by other means, thus exposing more of the interface to the plasma. In this way, the treatment time can be significantly reduced, as only a small fraction of the coating mass is broken down by the plasma. Once all of the bulk coating is released, the same plasma can be used to remove any remaining coating residue. For example, APS has successfully demonstrated such a technique to remove two mm thick baked-on PMMA photoresist films from stainless steel flanges used in semiconductor processing.

Technical Approach

As shown in Table 2, a team was assembled comprised of members from academia, industry, and DOD which brought together many strengths offered by each group of individuals who collectively could solve any problem identified during the course of the work. The team's motto was to "Employ science when needed to accomplish engineering objectives".

Table 2: Project team for Atmospheric Plasma Depainting under SERDP WP1762.

Institution	Team Member	Function & Location
North Carolina State University	Dr. Jerry Cuomo, PI	Project Lead Raleigh, NC
	Dr. Stephen Hudak, Technical Lead	
	Dr. Steven Shannon, Associate Professor	
AP Solutions, Inc.	Peter Yancey, President & CTO	Atmospheric Plasma Development Cary, NC
	Dr. Rick Myer, Principal R&D Scientist	
	John Waldrep, Sr. Development Engineer	
Naval Surface Warfare Center (NSWCCD)	Darren Melhuish	Carderock Division Corrosion Research and Engineering West Bethesda, MD
	Jamaal Delbridge	
AFRL/RXSA	Jeffrey Kingsley	Materials and Manufacturing Dayton, OH
NAVAIR Fleet Readiness Center East	Robert Kestler	Science & Technology Lead Cherry Point, NC

Atmospheric plasma has seen tremendous growth during the past decade, but is still at very early stages of development and little is known about either the science or engineering applications. At least one aim of SERDP projects is to gather enough information during the performance period to allow for transition to ESTCP which is the demonstration and validation stage of technology development. Jumping across the "missing middle" or valley of death in transitioning a technology beyond a TRL or MRL level six, is a continuing challenge for all areas of science and engineering. The technical approach consisted of three separate phases of R&D as illustrated in Figure 1. The first phase was essentially a fact gathering mission in order to provide important information for the next and subsequent phases. In addition to identifying, obtaining, and preparing test equipment, materials and paint to be evaluated during phase 1, fundamental information relating to atmospheric plasma was obtained. A Design of Experiments was completed to determine removal rates. Depainted panels were subsequently repainted, then exposed to environmental testing. A variety of analytical methods were used to characterize depainted coupons. The second phase of research was initiated in which a larger area AP system was designed and evaluations initiated. The design and evaluation of hybrid additions were placed on hold due in part to funds being removed from the project during the second year, but also because scale-up activities of atmospheric plasma were successful. The final phase of work

included continued scale-up, integration of a waste collection system, and addressed waste, environmental, operational, and process hazards.

Finally, the acceptability of the minimal waste streams generated by the AP process to Navy, DOD, EPA, and other relevant agencies and regulations was evaluated. Throughout the project, collaboration with DOD partners especially Naval Surface Warfare Center, Carderock Division (NSWCCD) kept the technology focused on the most critical needs of Weapons Systems and Platforms maintenance.

Technical Approach

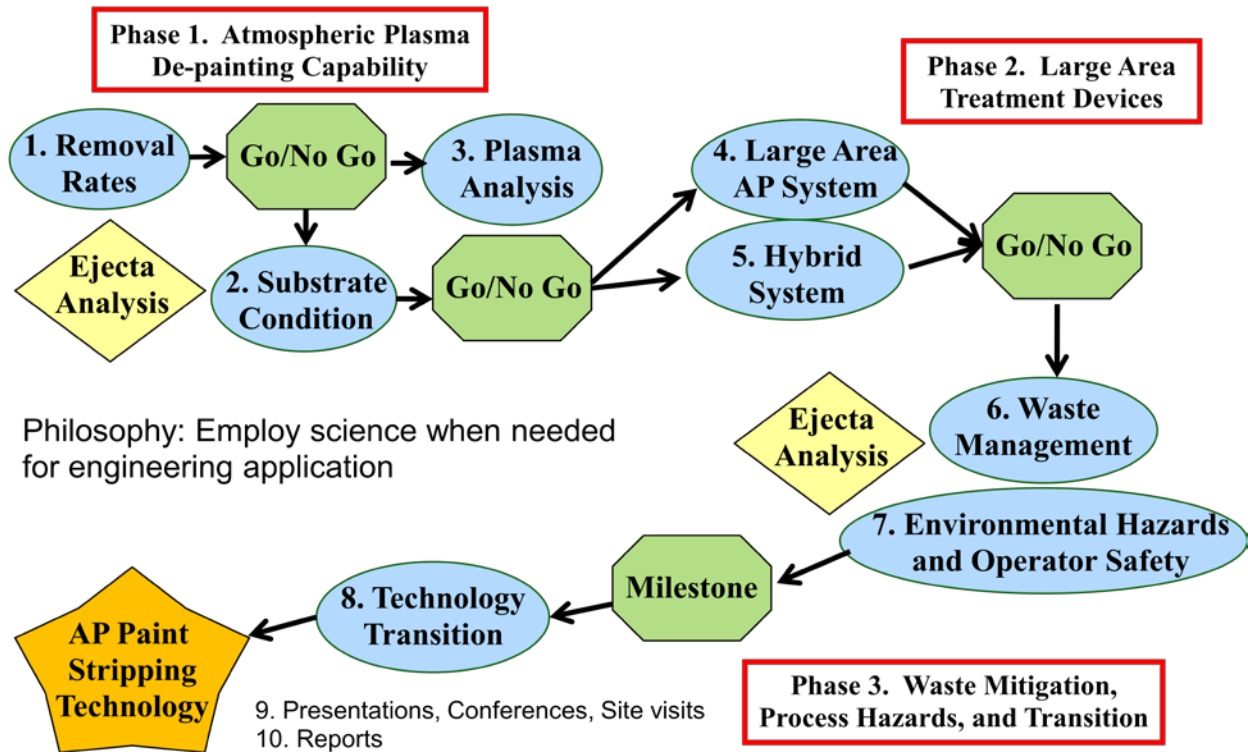


Figure 1: Flow diagram illustrating the technical approach used for atmospheric plasma depainting.

For reference, SERDP maintains a website for project management which contains many of the programmatic details [8]. Since much information is available through this site, information related to budgets, project timelines, other regular or incidental reports will not be contained in this report.

Materials and Methods

Most of the materials used during this research were available for military applications, but not always for civilian use. Paint, for example, might be similar to grades for the private sector, but definitely were specified for military use for example in terms of performance, composition, or application. One obvious reason is to maintain confidentiality for defense purposes such as camouflage or stealth. In the case of underwater coatings, there are numerous methods used to prevent growth of marine organisms on the hull, yet maintain low friction environment while underway. This type of information is restricted and therefore reference is made to relevant MIL standards where appropriate. Paint from several different manufacturers was evaluated early in the research, but down selected due to availability at that time or for other reasons. Above the waterline Freeboard paint was based on MIL-DTL-24441 primer, followed by MIL-PRF-24035 silicon alkyd topcoat. Underwater Antifouling paint was based on MIL-PRF-24441 primer and MIL-PRF-24647 Antifouling topcoat. Steel substrates were DH36 marine steel prepared as specified in SSPC-SP10. In some cases, military approved contractors were used for sample preparation, while other samples were prepared by the project team according to MIL-PRF-23236 and NAVSEA standard item number 009-32.

Rastering of the atmospheric plasma over the surface of test coupons was implemented using robotic action with ShopBot® systems equipped with computer control manipulated using simple G-code commands. Setup typically included some type of vacuum systems for collecting ejecta waste particulate for analysis or disposal after paint was removed from test coupons. In order to evaluate adhesion performance after paint was removed; industry standards were employed such as ASTM G95 cathodic disbondment, B117 salt fog, D4541 pull off adhesion, and G44 variation used by NAVSEA with alternate immersion in sea water at Key West Florida. In addition to physical measurements, a number of common scientific analytical techniques were used throughout the project. These are described in more detail as they are used in the body of the report. Some of the analytical techniques included XPS, FTIR, SEM/EDX, optical profilometry, glancing angle XRD, OES, mass spectrometry, IR and visible photography, thermocouple, sound, EMF, and UV. Sophisticated computer based techniques were used to obtain a variety of different types of information. Design of Experiments was used to obtain relationships and the relevance of the atmospheric plasma parameters for removing paint. Commercial JMP® software available from SAS was employed. Regression analysis, curve fitting and error estimations were made using common methods and Microsoft Excel was often employed.

Although much of the plasma power supply and configuration is considered proprietary to the manufacturer, techniques were utilized to obtain knowledge useful for development of plasma systems. Computational fluid dynamics finite element analysis were initially employed to form a basis for gas flow and to aid in the investigation of plasma generation, heat transfer, and identification of reactive species. Commercial software was used such as Comsol, ANSYS, and Solidworks.

Results and Discussion

Task 1 Determine capabilities of atmospheric plasma to remove Navy paint

1.1 Prepare Experimental Design

Equipment necessary for performing depainting evaluations of Navy coatings was assembled or adjusted as needed at both North Carolina State University (NCSU) and AP Solutions, Inc. (APS). The basic set up, shown in Figure 2 and Figure 3, consists of a power supply about the size of a briefcase typically mounted in an electronics rack for convenience. Air and electrical power are fed to an applicator head which can be manually operated or mounted for robotic manipulation [9]. Both NCSU's standard Buddy® 32" system and APS's 48" Alpha® system utilize servo motors and CNC (Computer Numerical Control) software supplied by the manufacturer or manipulated using G-code by software such as LabVIEW®. The ShopBot Alpha system used by APS had communications problems when using the supplied ShopBot operational software and was replaced with a LabVIEW interface. Upgraded servo motors on the Alpha are capable of speeds up to 1800 inches per minute, while the Buddy is limited to a maximum of 720 inches per minute.



Figure 2: Automated setup for atmospheric plasma depainting at NC State University.

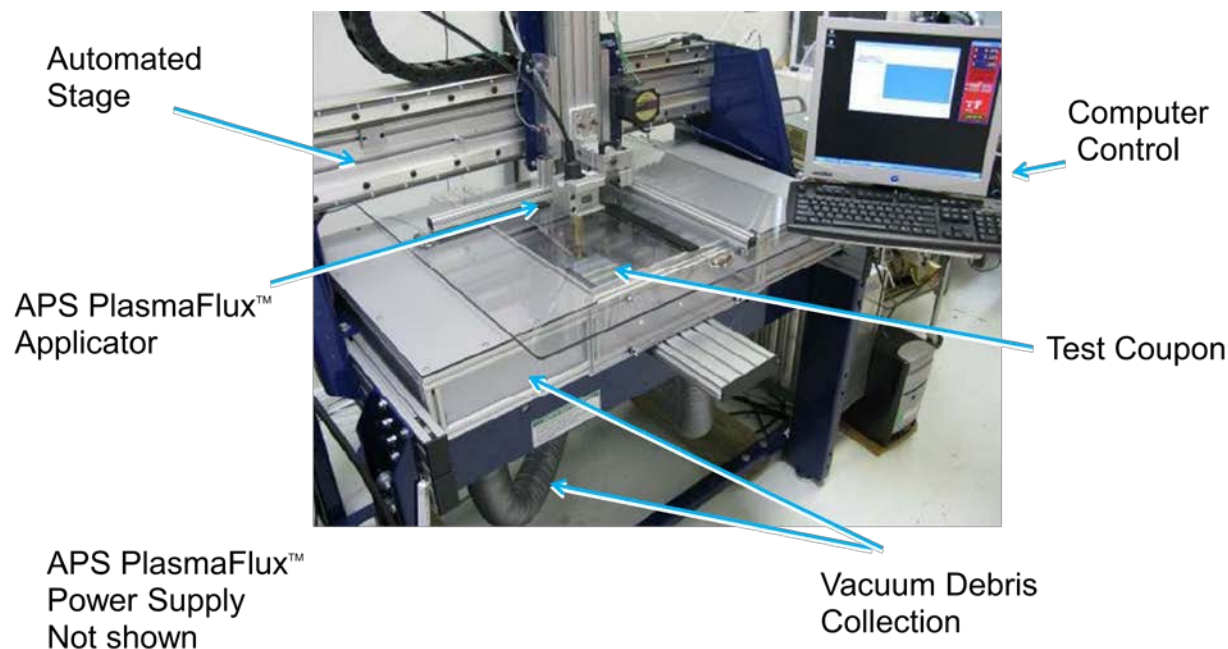


Figure 3: Automated setup for atmospheric plasma depainting at AP Solutions.

Waste is collected through an appropriate container or dust collection device. NCSU acquired an Oskar HEPA filtration system capable of 1500 cfm air filtration. The plasma applicator is fastened to the robotic head for manipulation above test coupons. Debris is contained inside a box which is evacuated by vacuum dust collection for filtration and/or exhaust to the exterior. This set up includes several safety features such as limit switches, interrupt switches, and shutoff devices.

NSWCCD sent several test coupons for quick test trials prior to the preparation of any significant experimental designs. One example is shown in Figure 4. The left side of the photo shows the result of a white silicone based experimental ablative coating which was subjected to marine immersion testing. The surface was covered with fouling on top of the paint. The right side was exposed to atmospheric plasma which removed all material down to the bare metal in a single pass. After paint removal, stains were observed on the coupon which might have been present prior to painting, or created during the marine immersion. This was an interesting observation which demonstrated that atmospheric plasma removed the upper layers of organic material, both from the marine growth and paint application, but left the metal surface in a “clean” configuration without any apparent visual change to the oxide or metal surface.



Coupon subject to immersion testing

After plasma treatment

Figure 4: Test coupon with an experimental silicone ablative white paint subject to marine immersion testing in which the right half was removed with atmospheric plasma.

NSWCCD directed the preparation of an initial set of approximately 80 coupons for a Design of Experiments to remove paint. These samples were prepared to military specifications through a subcontractor. In discussion with the team, it was decided to use the initial set of coupons to narrow down the options regarding the type of paint to be examined, the manufacturer, and the composition. Figure 5 illustrates the composition and geometry of the paint stack which is representative of Freeboard areas of the ship, or above the water line.

As part of the preliminary work, it was understood that paint can be certified either based on a performance standard or composition standard. In either case, paint composition could vary depending on the manufacturer. For this reason, a subset of panels was prepared using paint from three different suppliers - namely International, Ameron, and Sherwin Williams. Surface preparation and painting were performed by the same contractor at the same time in order to provide consistent quality panels. In a typical experiment, coupons were placed inside a box with vacuum debris collection and the plasma rastered across the sample at a defined speed and height from the sample. Photographs shown in Figure 6 were taken after plasma paint removal experiments from each of the three manufacturers. Each stripe on the sample is from a single pass of the plasma. At greater distance of the plasma from the substrate, typically only the top most layer of paint was removed in these experiments. As the distance was decreased, both the top Freeboard paint layer and the second coat of primer were removed leaving only a little if any of the first primer layer which was red in color.

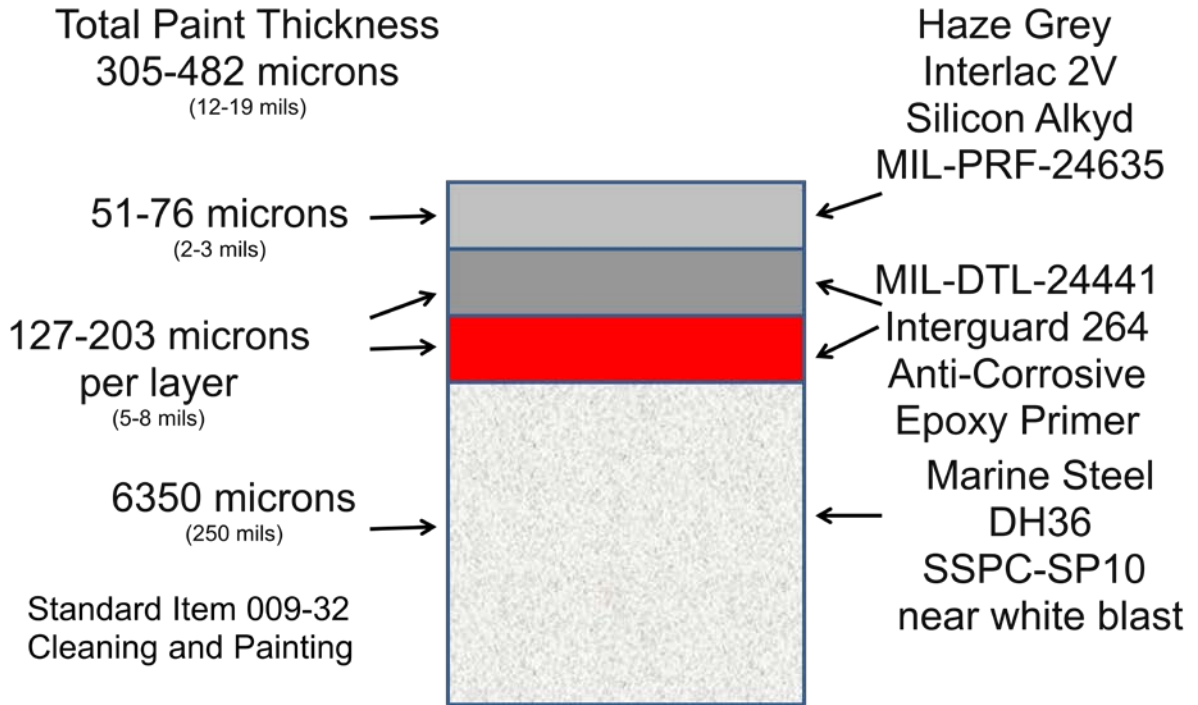


Figure 5: Freeboard (FB) paint schematic typically used above the waterline.

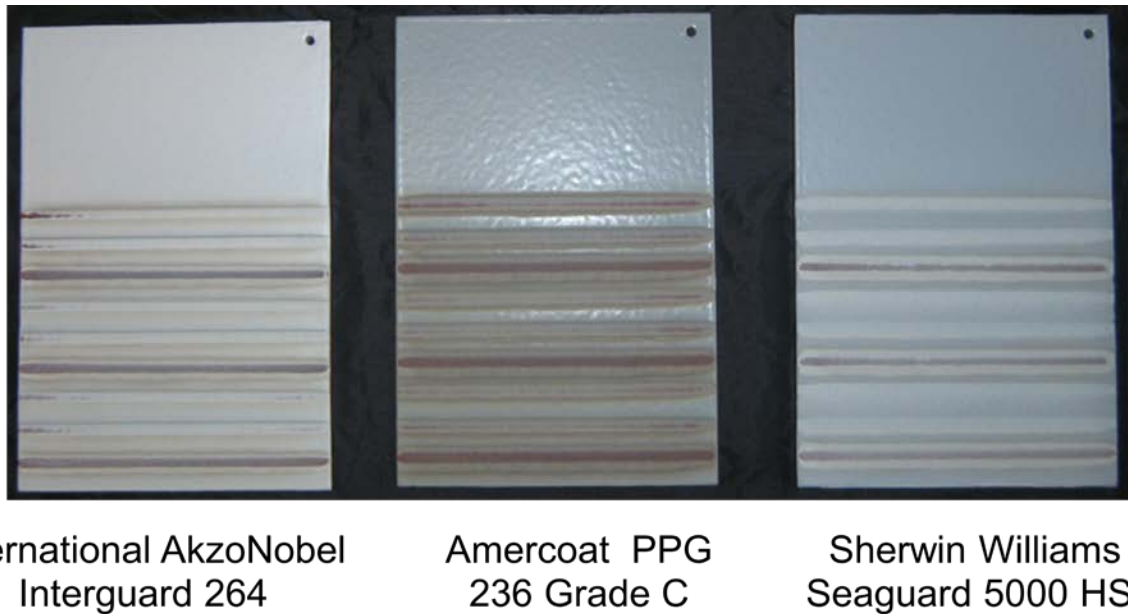


Figure 6: Examples of single plasma pass experiments to depaint coupons prepared using different manufacturers paints.

After each pass of the plasma, the samples were removed from the box, weighed, and then mass loss calculated. Figure 7 contains a graph with results for three different plasma/substrate distances. More paint was removed the closer the plasma was to the substrate which is consistent with the visual appearance of the sample. More Sherwin Williams paint was removed in these experiments. In order to reduce the number of future test specimens, a decision was

made by the team to use the most readily available paint for the duration of the project, namely from International.

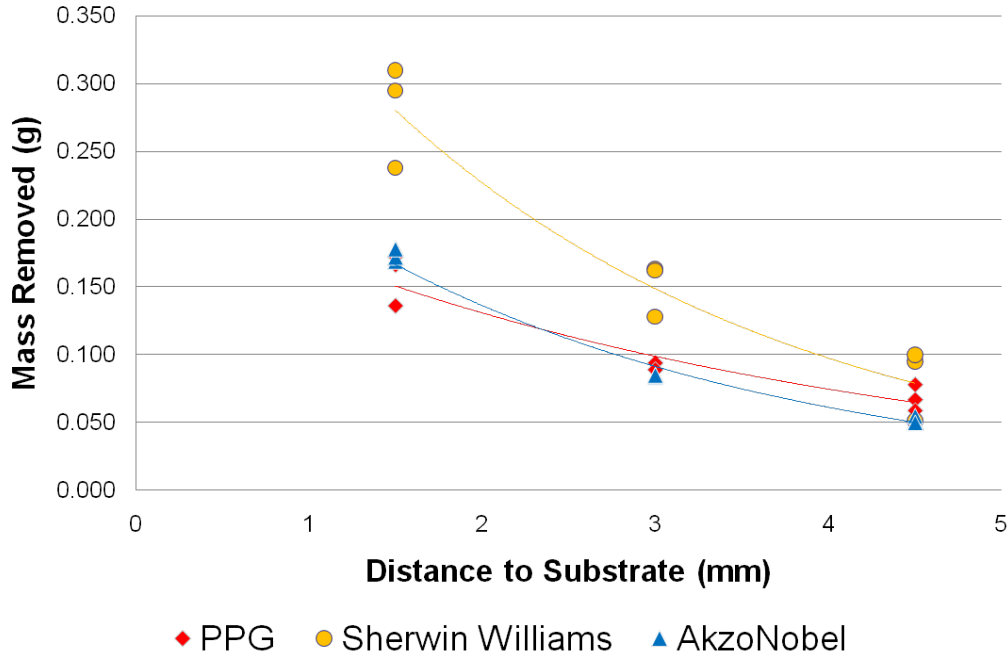


Figure 7: Mass loss versus plasma distance to the substrate from three different paint suppliers.

In another series of preliminary experiments, the plasma direction with respect to the sample surface was varied. The setup is illustrated in Figure 8 with the travel in the plus y direction. The plasma can be adjusted in a push configuration (+ angle) or pulled across the surface (- angle). The atmospheric plasma is an oxidizing media with a flowing stream of active and neutral gas species. Since the primer creates the “bond” to the metal, by breaking this bond the paint can be removed. The question is “How does the plasma reach the primer/metal interface”? In a pull configuration the plasma initially encounters the topcoat material which must be removed prior to reaching the primer layers. In a push configuration, assuming there is metal exposed either from an earlier pass, from an edge, or from prior paint removal, the plasma could directly reach the primer/metal interface.

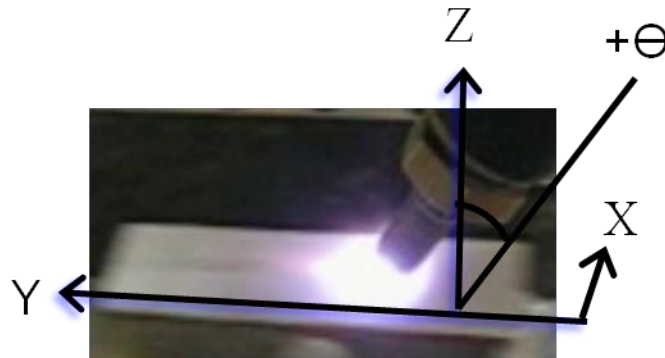


Figure 8: Illustration of coordinates for orientation of plasma to surface direction.

As illustrated in the photograph of Figure 9, pull configurations allowed ejected material to deposit back onto the sample surface. By wiping with a cloth and visual examination, this debris was a combination of dusty inert filler particles, and tacky oxidized paint material. The filler debris was easily removed from the surface, while the oxidized paint was tacky and tenacious. Another interesting feature was a geometric effect of the plasma shape which varied with angle. At 90 degrees, the plasma impacts the surface in essentially a circular configuration. By tilting the applicator, the plasma cone becomes more elliptical in contact with the substrate. This change in geometry alters both the exit distance to the substrate and contact geometry. These effects will be further investigated when multiple nozzles become available.

Data obtained from the angle experiments was run through statistical analysis using commercially available JMP® software from SAS [10]. A portion of the analysis is shown in Figure 10 which contains a graph of mass removed versus angle that was curve fit using a polynomial function. It was interesting to observe that more mass was removed as the plasma was tilted from 90 degrees in either the plus or minus orientation. The data was skewed, however, with more material removed at a given angle in the plus orientation. This is likely due to the “pushing” effect of both active plasma and flowing neutral gas which removed paint, but also could aid in removing the ejected material. In the “pull” configurations, ejected material deposited onto the substrate.

After conducting initial experiments with different types of paint, from different manufacturers, using different experimental conditions, a second paint stack was chosen to represent the most common types of paint for Navy ships. Figure 11 illustrates a typical configuration of paint used below the water line on Navy ships. There is some variation in the types of paint used which is related to performance specifications for the type of ship and expected “dry dock” schedule. Ships may not see dry dock for five, seven, ten, or twelve years or more. One type of underwater paint is intended to prevent marine organisms from attaching during wet docking. These often contain “poisons” such as copper based systems which kill growth, but might accumulate in stagnant waters. Another type of paint will allow a certain amount of marine growth, but once the ship is underway the paint slowly ablates which releases attached organisms. The anti-fouling paint used in this work uses a combination of both mechanisms. The color of the paint layer is commonly altered to ensure complete coating coverage during applications, but also as an indicator of paint wear over time. Ships returning to dry dock may only have a few microns of AF paint remaining. Paint above the water line, conversely may have been increased in thickness over time due to repainting for maintenance, color scheme changes, or cosmetic/performance reasons.

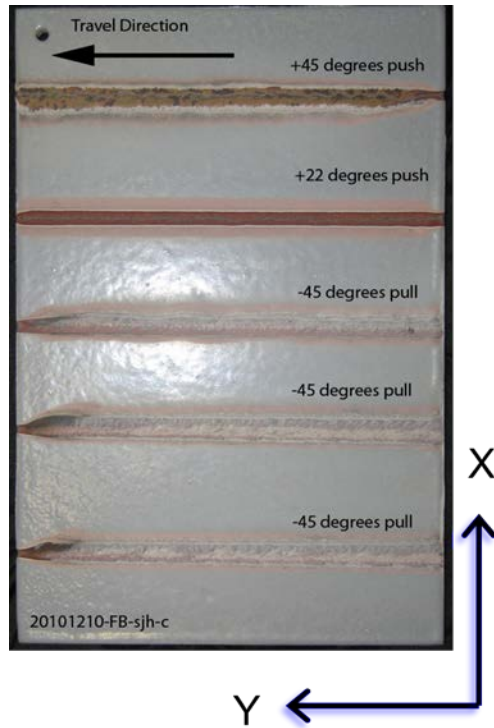


Figure 9: An example FB coupon exposed to various single pass exposures in which the plasma to substrate angle was varied according to Figure 8.

Figure 12 and Figure 13 contain photographs of painted test coupons ready for experimentation. This particular set of AF paint was wrapped with anticorrosive paper prior to full paint cure. As a result, some of the paper stuck to the surface and was removed by vigorous rubbing under running water. In addition, mineral spirits or xylene remaining in the top coat system was outgassed using a prescribed oven aging procedure to cure the paint and partially simulate field aging. In the field, these paint systems can slowly cure for several months if not longer. FB paint did not exhibit this problem. Since some of the coupons would be used for immersion and other performance tests, the back side (and edges) of coupons were also coated.

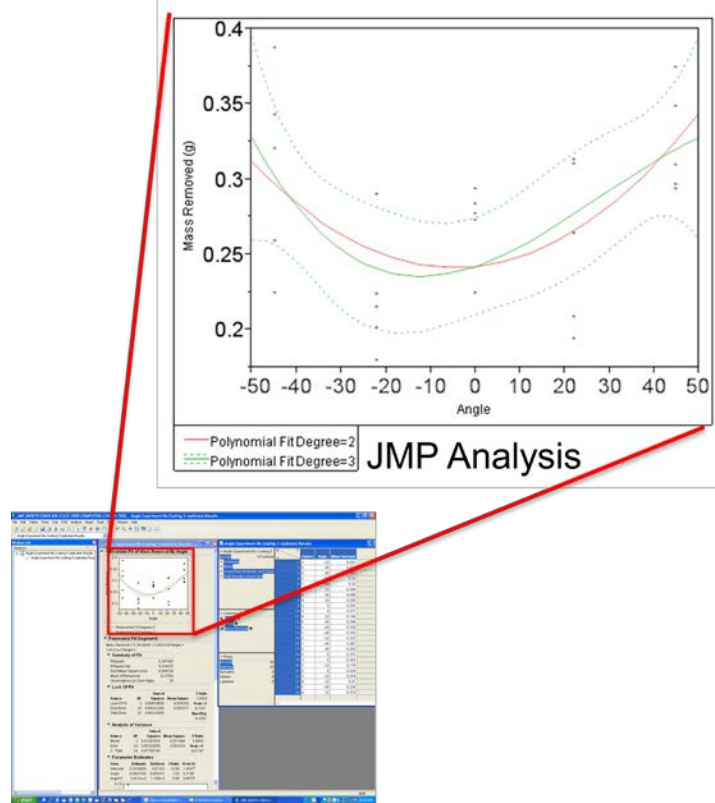


Figure 10: Statistical analysis of mass removed versus angle using JMP software.

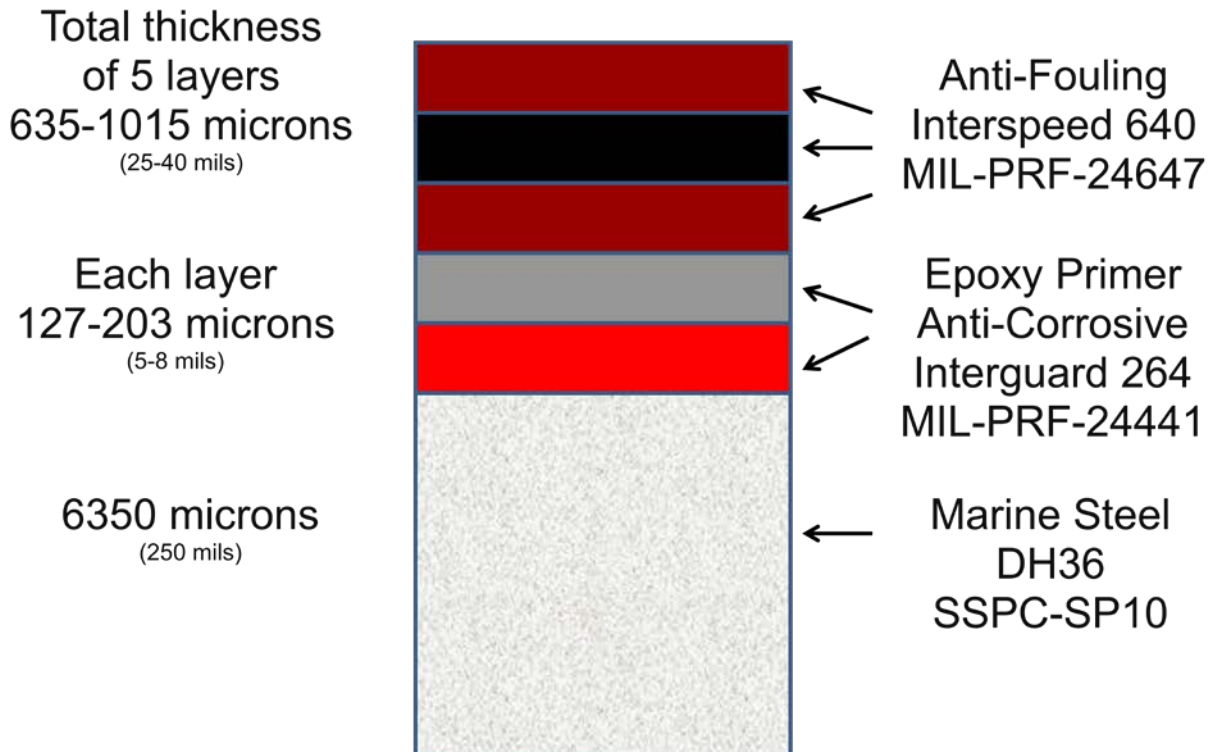


Figure 11: Antifouling (AF) paint schematic typically used below the waterline.



Figure 12: 4”x 6”x ¼” steel painted with Freeboard (FB) ready for testing.



Figure 13: 4”x 6”x ¼” steel painted with Antifouling (AF) ready for testing.

1.2 Perform Experimental Design

The Central Composite Design (CCD) Design of Experiments (DoE) was chosen due to its ability to investigate the main factors considered relevant to paint removal, and the ability to

determine curvature in the relationships between mass removal and the five process parameters summarized in Table 3. This included low and high values of 1) temperature 0:42 °C, 2) speed 30:100 mm/s, 3) air flow 95:135 slm, 4) plasma torch angle with respect to substrate -30:+30 °C, and 5) plasma torch height from substrate 2:4.5 mm and the included center and axial points. Commercially available JMP software from SAS was used to set up the experiment and perform data analysis. The analysis employed was a response surface model using a Least Squares Analysis to determine the statistically significant factors affecting the average mass removal. JMP automatically populates a data table by randomizing the experiments which greatly reduces the influence of irrelevant factors.

Table 3: Factors and limits for CCD DoE.

Factor	Low (-)	High (+)
Temperature	0	42
Speed	30	100
Flow	95	135
Angle	-30	+30
Height	2	4.5

Responses:

- Average Mass Removal of 5 coupons
- Natural Log of the standard deviation of the Mass Removal of the 5 coupons

Total # of runs=31

At each treatment, 5 coupons were measured. 16 runs came from the full factorial experiment, 15 runs came from center points and axial points.

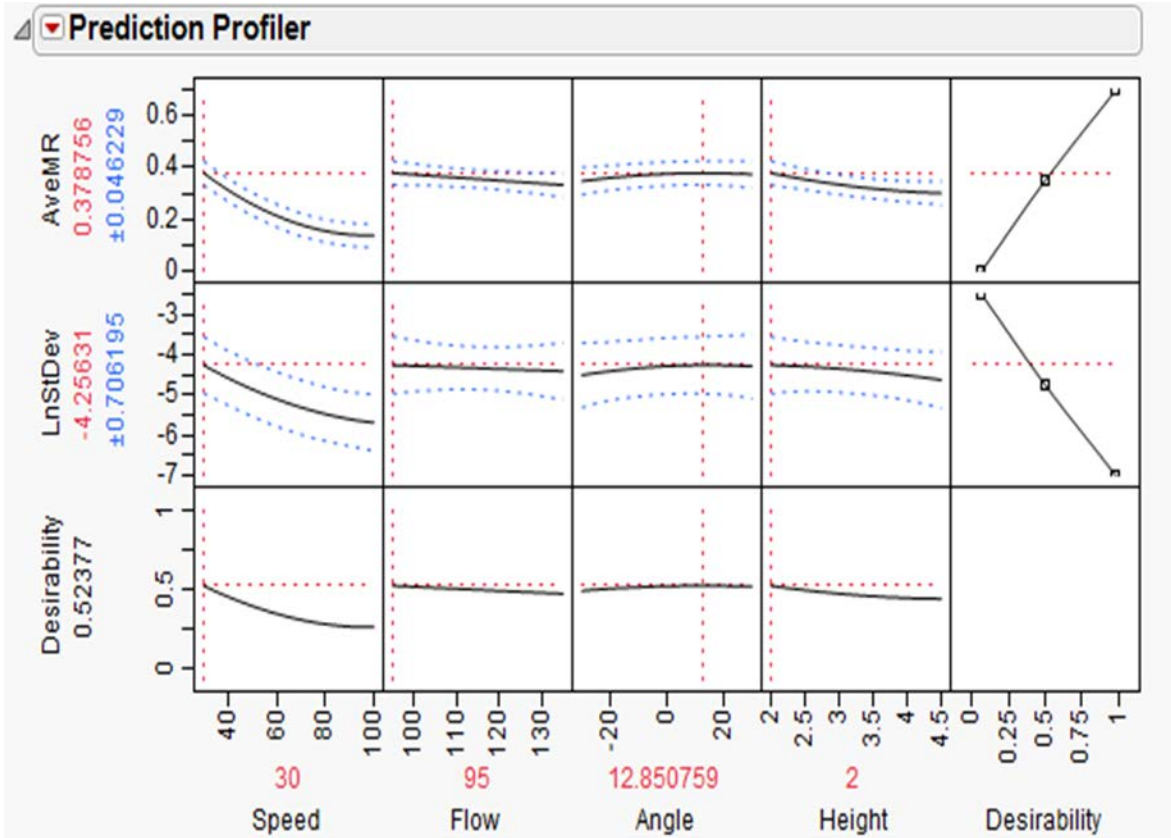
Once the data table was obtained, the experiments were run. For the present experiments, the removal rates were run at AP Solutions. Due to the geometry when the plasma applicator was tilted, the height chosen was based on a perpendicular from the surface to lowest tip of the nozzle. In this case the height was not exactly the same as the distance from the exit to the surface, but since the plasma projects an ellipse on the surface when tilted, it was considered satisfactory. Samples were easy to heat, but cooling presented a challenge. Moisture would condense on the cold samples. To minimize effects, the surface was blown with dry air prior to the experiment.

The data table complete with the results of depainting is shown in Table 4. The next step of analysis was to run a response surface model using least squares analysis to identify what factors were statistically significant in affecting average mass removal. This is done by looking at p values which should be less than 0.05. Other terms can also be left in the model based on experience from the subject matter experts. In other words, it was already known that height, speed, and angle were significant.

Table 4: JMP data table obtained from the CCD DoE.

	Temperature	Speed	Flow	Angle	Height	MassRemoval1(g)	MassRemoval2(g)	MassRemoval3(g)	MassRemoval4(g)	MassRemoval5(g)	AveMR	LnStDev
1	0	100	95	30	2	0.097	0.093	0.101	0.097	0.099	0.0074	-5.8202794
2	0	100	135	30	4.5	0.051	0.058	0.054	0.057	0.054	0.0548	-5.8871451
3	21	65	115	-53.1222	3.25	0.082	0.085	0.085	0.083	0.084	0.0838	-6.6424412
4	0	30	135	-30	4.5	0.208	0.203	0.181	0.206	0.187	0.197	-4.4074628
5	21	3.02401	115	0	3.25	0.576	0.706	0.704	0.593	0.585	0.6328	-2.7152734
6	0	100	135	-30	2	0.048	0.046	0.049	0.046	0.047	0.0472	-6.6424412
7	58.185590	65	115	0	3.25	0.137	0.156	0.144	0.156	0.157	0.15	-4.7074538
8	42	30	135	30	4.5	0.31	0.318	0.312	0.312	0.315	0.3134	-5.7665641
9	21	65	115	0	5.4634280	0.1	0.101	0.101	0.102	0.094	0.0996	-5.7416833
10	42	100	95	-30	2	0.093	0.089	0.092	0.094	0.093	0.0922	-6.2535889
11	21	65	115	0	3.25	0.124	0.126	0.12	0.123	0.133	0.1252	-5.3250178
12	0	30	95	-30	2	0.308	0.314	0.311	0.294	0.284	0.3022	-4.3633402
13	21	65	150.41484	0	3.25	0.133	0.13	0.139	0.133	0.131	0.1332	-5.6570373
14	42	100	95	30	4.5	0.078	0.076	0.078	0.08	0.076	0.0776	-6.3929456
15	21	65	115	0	3.25	0.108	0.13	0.118	0.123	0.126	0.121	-4.7694222
16	21	65	115	0	1.0365719	0.283	0.301	0.288	0.287	0.296	0.291	-4.9179145
17	21	65	79.585151	0	3.25	0.159	0.156	0.158	0.159	0.152	0.1568	-5.8260938
18	21	65	115	0	3.25	0.108	0.093	0.099	0.107	0.119	0.1052	-4.6193699
19	21	126.975	115	0	3.25	0.067	0.066	0.062	0.064	0.062	0.0642	-6.083426
20	42	100	135	30	2	0.091	0.095	0.094	0.086	0.093	0.0918	-5.6369543
21	0	100	95	-30	4.5	0.069	0.07	0.072	0.067	0.065	0.0686	-5.9138181
22	42	100	135	-30	4.5	0.061	0.054	0.054	0.051	0.048	0.0536	-5.3335286
23	21	65	115	53.12227	3.25	0.122	0.117	0.146	0.119	0.114	0.1236	-4.3538743
24	42	30	135	-30	2	0.25	0.27	0.27	0.245	0.262	0.2594	-4.4671125
25	0	30	135	30	2	0.268	0.268	0.282	0.27	0.285	0.2746	-4.7994742
26	21	65	115	0	3.25	0.111	0.112	0.109	0.109	0.107	0.1096	-6.2402547
27	0	30	95	30	4.5	0.258	0.272	0.26	0.266	0.264	0.264	-5.2071566
28	42	30	95	-30	4.5	0.248	0.268	0.258	0.242	0.241	0.2514	-4.4671125
29	21	65	115	0	3.25	0.112	0.105	0.109	0.109	0.113	0.1096	-5.7665641

Once the model was reduced by removing insignificant terms, the residuals versus observation was checked. There were not any unusual trends or patterns; the residual means were equal to zero and the variance in data was constant and random. JMP then calculates the prediction profiler and surface profiler. These are two very useful tools which plot the model from real data. In the software, by grabbing a handle on the graphs and moving one variable, JMP automatically updates the relationships to show the influence in real time. The prediction profiler with optimized values expected for each factor is shown in Figure 14.



JMP’s optimization capability determines factor settings to maximize the average mass removal and minimize the natural log of the standard deviation.

Figure 14: Prediction profiler calculated from the CCD DoE.

Optimized terms from this DoE are shown in red; speed = 30 cm/sec, flow = 95 slm, angle = +12.8 and height = 2.0 mm. The influence of temperature turned out not to be significant in these experiments. Temperature values were selected based on the coldest and hottest days expected in the shipyard. Although this experiment did not show any effect, it could be quite different in a shipyard on a freezing cold day with the wind chill and added moisture effects.

JMP also calculates three-dimensional surface diagrams from each of the significant terms. These are shown in Figure 15. In most cases there seems to be a quadratic relationship. Graph c) confirms that positive angle removes more paint as was observed previously. It was interesting to observe the saddle point relationship between height and speed as seen in e). This helps explain why going too fast may not allow enough time for the plasma to etch the paint, while going too slow the plasma can be wasted by impacting bare metal. From graph f) there is not much relationship between angle and flow.

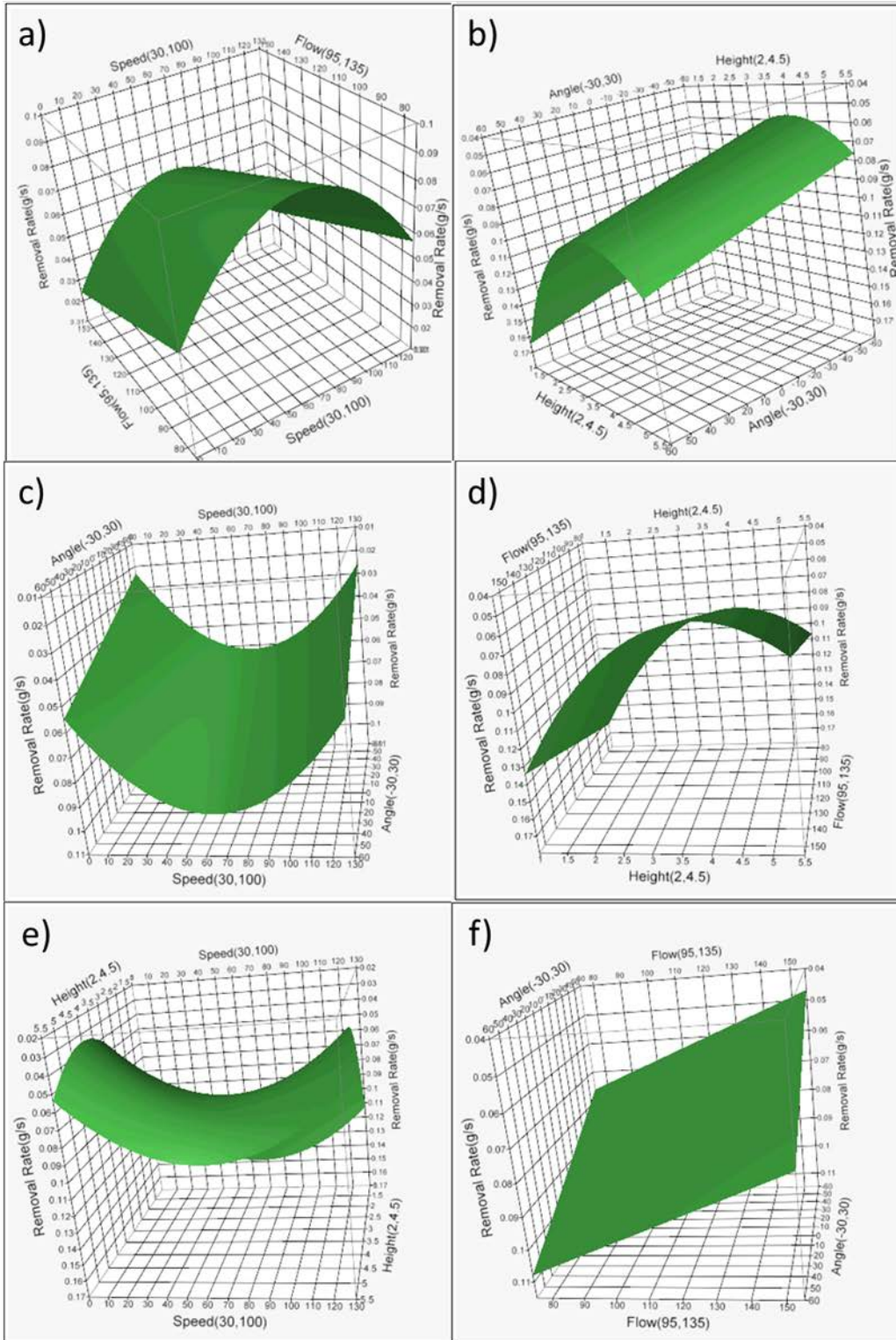


Figure 15: Removal rate response surfaces for the factors a) speed and flow, b) height and angle, c) angle and speed, d) flow and height, e) height and speed, and f) angle and flow.

1.3 Adequate Removal Rates

As discussed in other areas of this report, paint removal rates from current technologies at actual shipyards at best are subject to intense scrutiny, are extremely difficult to determine with accuracy, vary widely from job to job, location to location, ship to ship, time of year, paint type and location, age of the vessel, type of grit and equipment used, type of process, and many more variables. Actual numbers for removal rates are closely guarded by contractors since they are part of the bid process and therefore proprietary. Before jumping to a conclusion that removal rate is the only or most important variable, it should be noted that there are many other variables of significance to a depainting operation. Costs benefit analysis is not a subject of SERDP projects and not performed during this project. However, a brief listing of some significant items is summarized in Table 5.

Table 5: A few factors to be considered for paint removal.

1.	Total cost of manpower
2.	Capital equipment costs
3.	Maintenance costs
4.	Cost and manpower to obtain, store, handle, and dispose of media
5.	Cost of waste collection, handling, storage and disposal
6.	Environmental and operational difficulties of using media for paint removal, such as containment
7.	Ability of other work processes to be performed nearby
8.	Ability to be deployed in a Navy industrial environment
9.	Ability to be manual or automated and ease of use
10.	Training required to deploy and maintain
11.	Capabilities of reaching all areas needing to be depainted
12.	Ability to reach interior and limited access areas
13.	Stability and quality of depainted surface prior to repainting
14.	Repaint adhesion and environmental longevity
15.	Energy costs from start to finish
16.	Total time and cost of the depainting operation

A first approximation calculation was completed by AP Solutions using the figure supplied by NAVSEA of 150ft²/hr. Assuming a 20 mil thickness and a specific gravity of 2, results in 14 kg/hr that must be removed. (The paint out-of-the-can has a density of 14.3 lbs /gal which is 1.7 g/cc, but is higher when VOCs are driven off). According to the DoE results above, a single plasma pen at the current power level yields 0.5 g/s or 1.8 kg/hr (versus 14 kg/hr). This is within a factor of ten, well within reach of the technology.

Table 6: Paint mass on different Navy ships by mass and estimates of time to remove using grit blasting or plasma.

Ship	Total Paint Mass (kg)	Plasma Removal Time (hrs)	Total GB Removal Time (hrs)	# Nozzles for Plasma Removal
Destroyers	7.22E+03	4010.8	515.6	7.78
Aircraft Carriers	3.80E+04	21121.7	2953.7	7.15
Amphibs	1.14E+04	6318.3	850.3	7.43
Cruisers	7.85E+03	4361.2	560.6	7.78

More specifically, data was obtained from the most common types of Navy ships and is summarized in Table 6. Also included in the table is a list by ship type of estimated time to remove paint using grit blasting based on a four man crew operating on an eight hour shift over a period of four days. Two methods were used to calculate paint removal rates. Figure 16 shows that a mass removal of 0.5 g/s using a single nozzle atmospheric plasma source results in 7.78 nozzles needed in order to equal grit blasting. This calculation assumes that all plasma was used to remove all paint to bare metal, which is not necessarily the case. If there is still paint to be removed, more plasma would be needed. On the other hand, if the bare metal is showing, the plasma is wasted. Even with grit blasting and water jet the operator makes adjustments on the fly to go back over areas which were not completely cleaned.

- Assumptions

- 0.5 mm thick at 1.7 g/cc
- 100 mm/s
- 0.5 g/s (1.8 kg/hr)

- Example (Destroyer):

- Grit blasting: $12932 \text{ m}^2 * \frac{1}{25.1 \frac{\text{m}^2}{\text{hr}}} = 515.6 \text{ hrs}$
- Plasma removal: $7.22E3 \text{ kg} * \frac{1}{1.8 \frac{\text{kg}}{\text{hr}}} = 4010.8 \text{ hrs}$
- Equivalent: $4010.8 \text{ hrs} * \frac{1}{515.6 \text{ hrs}} = 7.78 \approx \mathbf{8 \text{ nozzles}}$

Figure 16: Removal rate calculation based on mass per unit time removal.

Most often removal rates are quoted as area per unit time because that is how much of the ship needs to be cleaned and repainted. This obviously does not account for the paint thickness, paint

type, or other variations such as going around rivets, weld lines, steps or other obstacles. A second calculation was completed as show in Figure 17, based on the area removed per unit time indicating that fourteen nozzles would be required to equal grit blasting rates. In a similar manner using the rate of 60 ft²/man-hour (5.6 m²/man-hour) obtained by water jet depainting, only three atmospheric plasma nozzles would be needed. While these calculations are interesting, none of the data including grit blasting accounts for the efficiency of the process.

- Grit blasting: 270 ft²/man/hr (~25.1 m²)
- Assumptions
 - Plasma removes 508 mm² per pass:
 - Length = 101.6 mm
 - Width = 5 mm
 - Velocity = 100mm/s
 - Removal Rate = 0.0005 m²/s (500 mm²/s) = 1.8 m²/hr
- Matching grit blasting rate
 - $\frac{25.1 \text{ m}^2/\text{hr}}{1.8 \text{ m}^2/\text{hr}} = \mathbf{14 \text{ nozzles}}$

Figure 17: Removal rate calculation based on area removed per unit time.

In order to demonstrate the status of the technology for an interim report, a large area was depainted using a single-nozzle atmospheric plasma in preparation for future scale-up experiments. Steel test panels two feet by three feet by 3/8 inch thick were painted with FB and AF paint. As far as coating removal optimization was concerned, it was found that faster treatment speeds and closer interpass spacing resulted in more visibly uniform surface appearance, while maintaining treatment rates similar to those previously attained. For Freeboard samples, treatments in the range of nine inches/second with an interpass spacing of 0.015 inch were found to be effective, giving a treatment rate of 3.4 ft²/hour.

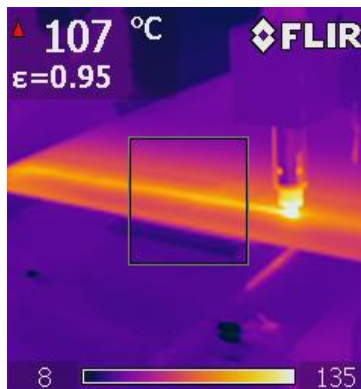


Figure 18: IR photo of surface temperature during removal.

Previous efforts had conducted removal in two “sweeps” over the same area, in part to keep the sample from being over treated. At these higher linear speeds and closer interpass spacing, a

single sweep was found to be effective, without overheating or excessive treatment to the sample. With the large 2' x 3' x 3/8" thick samples, such treatment rates resulted in a fairly uniform surface temperature in the vicinity of the coating removal, after an initial heating up period of a few passes. Figure 18 contains a thermal camera image of the sample during removal, where the surface temperature near the pen stays below the 90-100 °C range throughout a large area treatment. It should be noted that the actual plasma coating removal process can cause significant emission in the same wavelengths that the thermal camera operates, so that the readings at the area where plasma is actively removing are likely to be erroneously reported.

Figure 19 contains a photograph of a large test panel after AF paint was removed, while Figure 20 contains an enlargement of this same panel. This was depainted in less than one hour resulting in a measured production rate of six ft²/hour. As for targeted removal rates, the best information supplied to date supports the conclusion that production rates between 50 and 150 ft²/hour would be an ideal target for atmospheric plasma especially when other factors are considered regarding efficiency of the plasma.

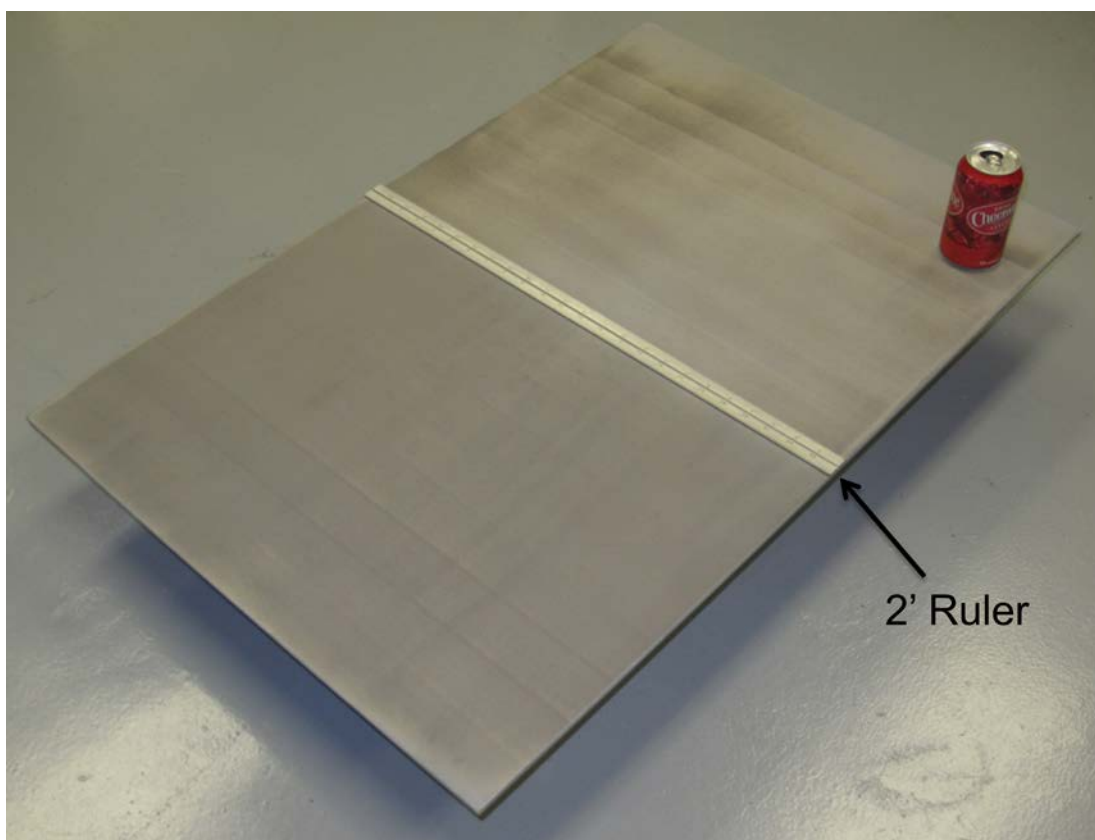


Figure 19: Atmospheric Plasma Depainted FB panel, 2' x 3' x 3/8" (610 mm x 914 mm).

During the large area removal tasks, nozzle wear has been shown to affect the removal efficacy over the course of several hours. In order to ensure uniform removal, the nozzle was replaced every few hours of runtime. Future work will further investigate what factors influence nozzle wear as well as techniques to improve nozzle lifetime, such as cooling jackets (as demonstrated previously) or alternate run parameters.

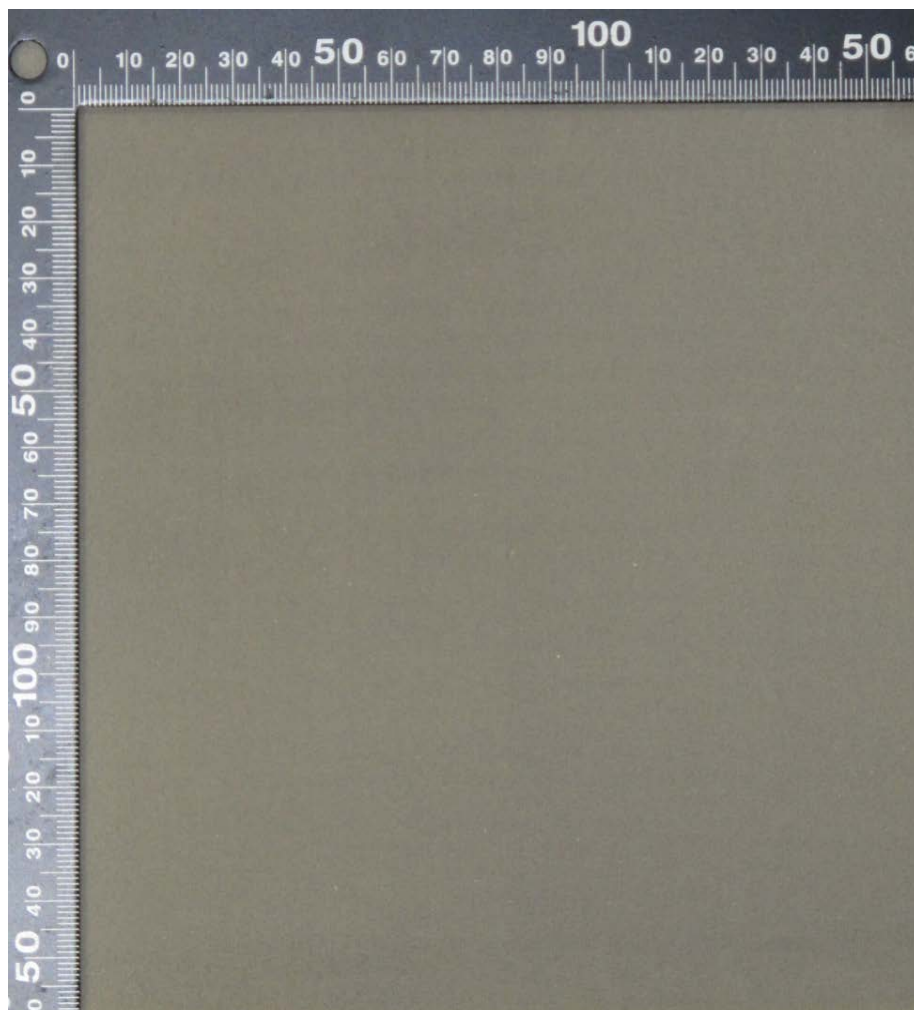


Figure 20: Enlarged area photo from Atmospheric Plasma Depainted FB panel.

Manual trials were also attempted in order to investigate the potential for uniform removal with a skilled operator. The current aggressive configuration of the system (optimized for automated removal at a high rate) resulted in excessive treatment when used manually at comfortable handheld speeds. Less aggressive, lower power configurations will be possible with the improved controls of the redesigned multi-pen power supply and this development is anticipated to improve manual removal results in future work. Based on the information obtained to date, including statistically significant data from Design of Experiments, atmospheric plasma was given a GO for having adequate removal rates.

Task 2 Substrate Condition after Paint Removal

2.1 Obtain Background Information & Prepare Samples

Most of the samples from the DoE were generally unsuitable for further analysis since they contained multiple single pass experiments. Therefore, a series of panels was prepared in which paint was completely removed using atmospheric plasma and grit blasting. Figure 21 has photographs of two such panels. During the April 2011 in progress review, photographs shown in Figure 22 raised a number of questions regarding the different color on the surface when grit blasting was compared to plasma. Although the 20x optical micrographs needed color

correction, the individual layers of paint are clearly visible in the area between fresh paint and the plasma stripped paint. Samples such as these were used in the next task.

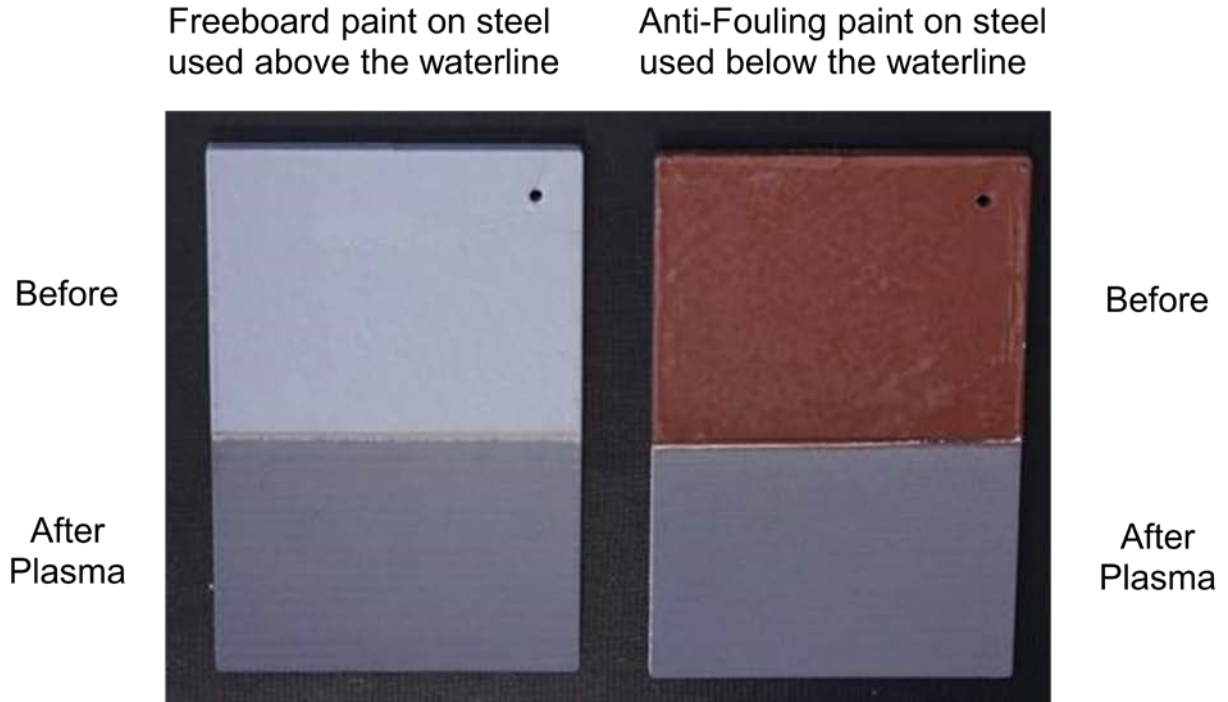


Figure 21: 4 x 6 inch painted steel panels in which the lower half was depainted using atmospheric plasma.

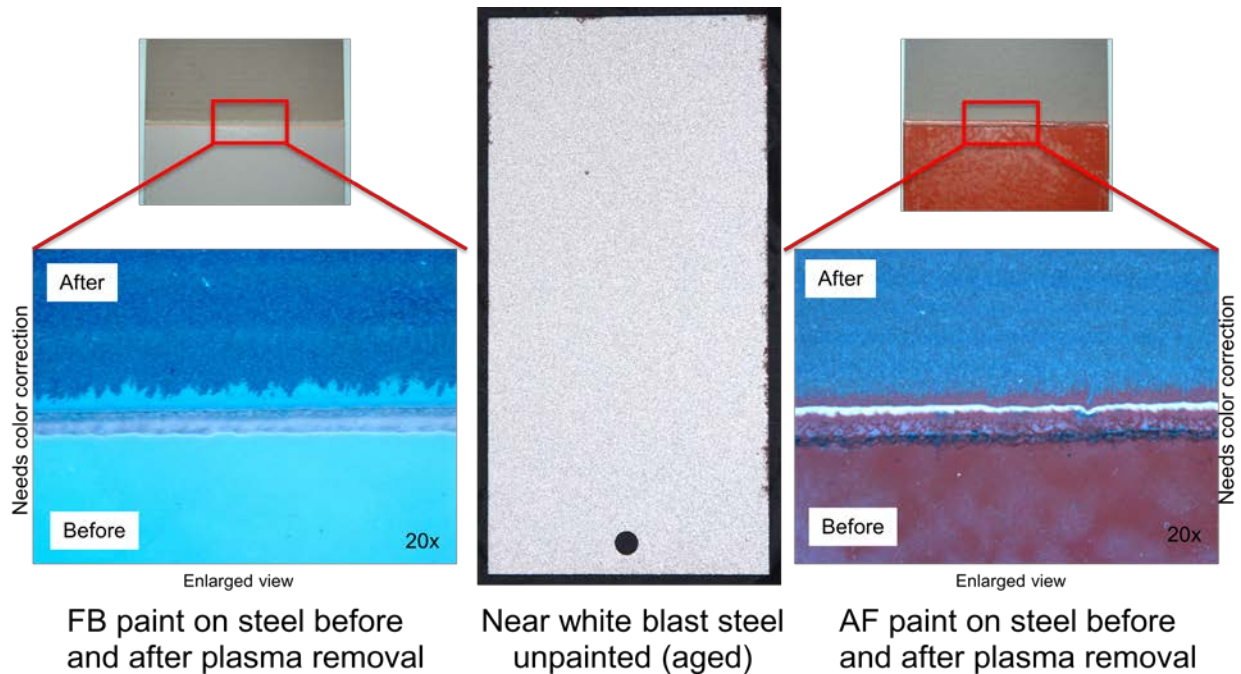


Figure 22: The center photograph is from a control, unpainted, and near white metal blasted steel. Photos on the left and right are enlarged areas showing each layer uncovered by atmospheric plasma.

As a clue to answering the question of why the color was different between grit blasting and plasma, Figure 23 contains photographs of steel having three different surface preparations. The as received surface was contaminated with mill scale, oxides, and debris. Grit blasting to near white metal creates a “near white” bright grey surface due in part to thin oxide layer and metal zero. After plasma depainting, the surface is very clean of organic contaminant, but has a thick oxide layer resulting in a darker gray/blue coloration. The “bluing” of steel is a well known subject often involving the use of acids which is extensively employed to protect machine parts and items like firearms from rapid rusting. Typically the surface is coated with oil to prevent water from reaching the surface. Each of these surface treatments results in different shades of blue/gray due to different thickness and/or composition of the oxide.



A) DH-36 steel
as received

B) Grit blasted,
AF painted, then
plasma de-painted

C) Unpainted DH-36
grit blasted steel

Figure 23: DH36 steel surfaces after three different surface treatments.

2.2 Analyze Treated Samples

2.2.1 Thermal Effects

Plasma is created when electrons in atoms and molecules are moved from their normal ground state to higher energy which creates ions and other active species. Through collisions which occur between particles within the plasma, a variety of additional energetic species are created. These include both positively and negatively charged ions, stable and meta-stable species, radicals, free electrons, and neutrals. One of the more significant parameters is plasma temperature which is an informal measure of the thermal kinetic energy per particle. Owing to their low mass, electrons are easily accelerated by magnetic and electric fields and may come to thermal equilibrium (all moving at the same speed) much faster than the heavier particles. For

this reason electron temperature can be very different (usually much higher) from the temperature of ions, neutrals, and other heavier species. Plasma can be classified as being in non-thermal equilibrium if the electron temperature is vastly different from heavier particles. Thermal equilibrium plasmas such as cutting torches have electrons and heavier particles at the same temperature which can reach thousands of degrees. A plasma is sometimes further classified as being “hot” if it is nearly fully ionized, and “cold” if it is only partially ionized. The properties of plasmas are also dependent on the number of particles involved and therefore the pressure. The atmospheric plasma torch used in this research generates a “cold” or non-thermal plasma from a compressed air source 480-620 kPa (70-90 psi) at relatively high rates of flow, typically around 100 standard liters per minute (slm) which is exhausted to atmospheric pressure. The plasma is comprised of two regions - an active region where plasma, consisting of ions, electrons, and radicals, is generated by an AC high voltage electrode and a downstream afterglow region where the reactive products are delivered to the surface to be treated. Since the flow rates are high, the residence time of neutral gas molecules is sufficiently short that they can be chemically activated (e.g. to neutral atomic oxygen and nitrogen states by electron impact dissociation) before the gas can thermally equilibrate with the energetic electron gas. Maintaining a low gas temperature is desirable as it allows for damage free treatment of temperature sensitive substrates and lowers the electrical power requirements. The pulsed electric field parameters of voltage, pulse frequency, and pulse width provide additional independent process control of the discharge duty cycle to achieve a non-thermal state by reducing the time averaged power density delivered to the plasma. The design details of the electrode and downstream (materials and geometry) and the pulse electric field parameters provide the means of optimizing the delivery of active species.

The question has been raised “How hot is hot and how cold is cold?” To obtain an upper limit estimate of the plasma plume temperature, assume that all of the electrical power delivered to the source is converted to thermal energy of the incoming neutral gas. For every kilowatt of electrical power delivered to a gas flowing at 1 slm an average energy of 14 electron Volts (eV) per molecule is available for driving the physical processes of ionization, excitation, and dissociation of the gas. Thus, if 1 kW of power is delivered to a gas flowing at 100 slm, the average energy per molecule of 0.14 eV (if all the energy were converted to heat) would translate to a gas temperature of 1625 °K (1352 °C). However, since the energy delivered to the plasma is partitioned among the various processes of ionization, excitation, and dissociation, not to mention a significant loss of energy due to plasma (both ion and neutral) recombination processes on the reactor walls, expect the plasma plume temperature to be significantly less than the simplistic estimate above. More detailed theoretical and experimental analysis is underway to understand how the energy is partitioned among the various energy loss channels to guide source design modifications aimed at improving the efficiency of delivering active species to the substrate surface. As a point of comparison, atmospheric DC plasma torches typically run with gas temperatures of 10,000 °K or more.

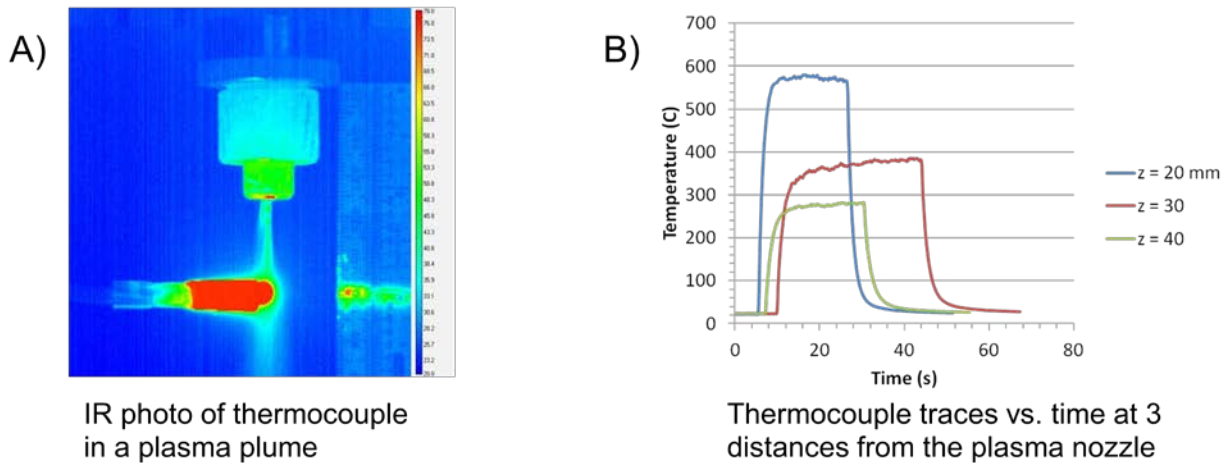


Figure 24: Plasma plume temperature measured using a thermocouple.

As a first approximation at obtaining “plasma” temperature, a K-type thermocouple was placed into the active plasma plume and temperature recorded over time. Figure 24 A) contains a thermogram obtained using an infrared camera from one such measurement. Due to its small size and high conductivity, heat flowed into the thermocouple and rapidly reached equilibrium. The thermogram provided a means to visualize temperature as a function of location. As seen in B), the measured temperature equilibrated rapidly in seconds. Upon exiting the orifice at atmospheric pressure, collisional processes dominate inside the plasma plume. Collisions change both the kinetic energy and chemistry of the species. The mean free path between collisions as the plasma exits the nozzle at constant pressure can be estimated by,

Equation 1. Estimate of mean free path of electrons.

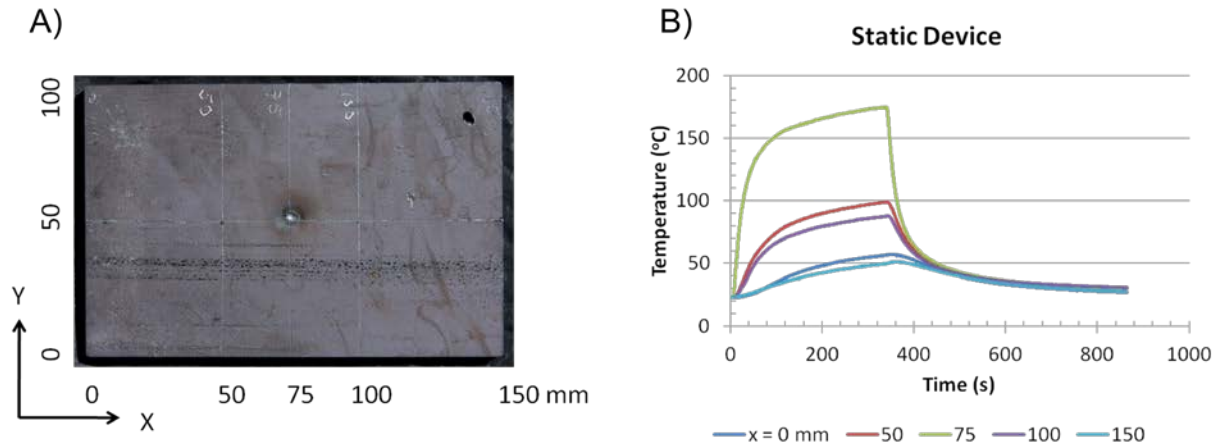
λ (mean free path) = $1/(\text{number} \times \text{cross section})$, assuming Maxwell distribution of velocities:
 or
 $\lambda = k_B T / (pd^2)$

where k_B is the Boltzman constant, T is exit temperature, p is pressure which contains a term for flow, d is the diameter of particles. This approximates to a decrease upon exit of $1/d^2$. In reality the relaxation processes are much more complicated and more likely to assume some form of exponential decay. Measured temperature decreased with distance as $570 > 362 > 271$ °C for the points considered using specific operational conditions. These and other results obtained for the SERDP project using atmospheric plasma for depainting have been concentrated on obtaining a better understanding of the effect of operational and geometric parameters in order to maximize coating removal rate.

What are limitations of the technology? Temperature measured by the thermocouple rapidly decreases back to room temperature once the plasma is turned off. How much of this kinetic energy is transferred through the paint coating to the underlying steel substrate? Measuring the plasma temperature in this manner can be misleading because much of the energy contained in the plasma is not kinetic and therefore not thermal, but chemical. The temperature of the plasma

plume is far less significant than thermal energy transferred to the substrate with gas temperatures of 10,000 °K or more.

The plasma team was asked to define under what conditions the surface temperature could reach 200 °C. As with any energetic process, the longer the energy is applied, the more heat there will be transferred. Even the currently used technology of grit blasting will create a hole in the steel if static and not moved about the surface. Perhaps more important to Navy Ships is the heat transferred into the bulk of the steel which could alter the integrity of the hull. Grit blasting by nature can also damage the surface, but how deep is the penetration and what is considered damage?



Photograph of steel after plasma exposure at position (75,50)

Thermocouple traces measured on the back side the steel during plasma exposure.

Figure 25: Photograph of steel after plasma exposure at position (75, 50).

Figure 25 A) contains a photograph of a 4 x 6 x 1/4 inch (100 x 150 x 6.4 mm) steel coupon. The surface condition was as received from the mill, prior to treatment with the plasma device static at the (75, 50) location 20 mm perpendicular to the steel. The plasma was run in excess of five minutes while traces from thermocouples attached to the bottom of the steel at locations 0, 50, 75, 100, and 150 mm in the x direction and 50 mm in y were recorded as shown in B). A wood block was used to support the sample. The maximum temperature was achieved directly under the plume which reached about 170 °C. There was no significant discoloration of the steel other than directly under the plasma plume. Plasma is an electrically conductive medium. During the five minute exposure, leakage current from microfilaments of the plasma were able to etch the surface of the steel. This worst case scenario illustrated that if the plasma were not moved, temperature still would not become excessive unless left for a very long time, and any damage would be minimized locally.

This example illustrated the localized thermal input provided by the atmospheric plasma in the absence of coating. In reality, steel is covered with paint which is a thermal and electrical insulator. The coating would therefore reduce the thermal flux and electrical conductivity to the substrate

In order to remove paint, the device doing the job needs to move. The plasma device was intended to be continuously moved over the surface. With respect to atmospheric plasma, how does heat flux penetrate once the plasma is in the process of stripping paint? The concept of time average energy density is more appropriate for this application. A more accurate measurement of thermal input with a rastered energy source would require complex Monte Carlo simulations using Fourier's law for heat convection and the Navier-Stokes equations which describe the motion of fluid substances. These equations refer to a velocity field which describes the fluid flow at a given point in time and space. In a recent article by Arnold [11], a proprietary FEM algorithm was developed in an attempt to model the heat flux using atmospheric plasma to predict the local etching behavior over large areas.

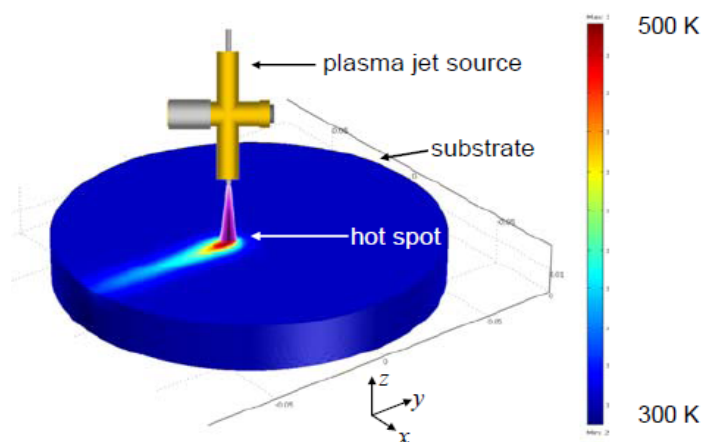
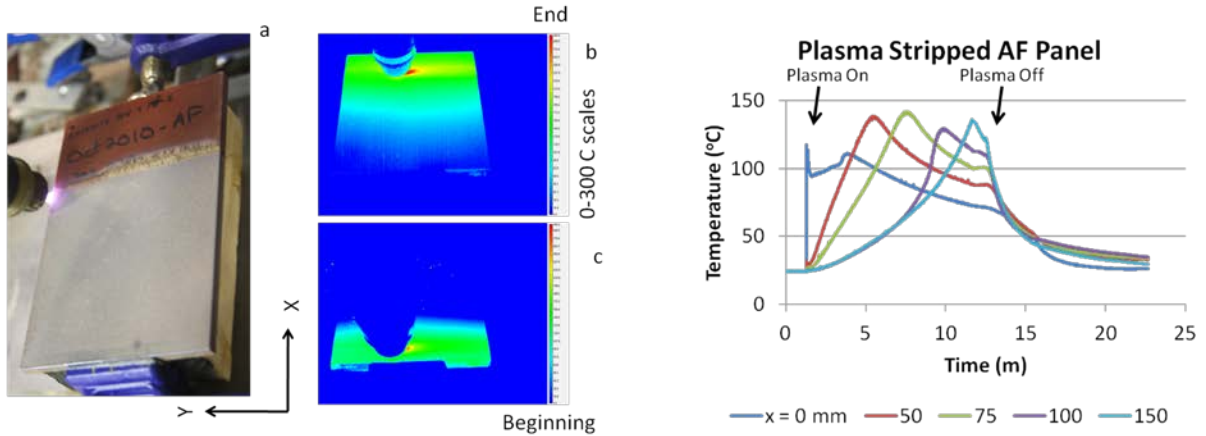


Figure 26: Thermal image model by Arnold using a proprietary algorithm to predict thermal input from plasma in motion.

In their analysis as illustrated in Figure 26, Fourier's law was used in combination with Navier-Stokes to develop a proprietary algorithm. The model was accurate for three back and forth cycles as confirmed using thermal imaging. In the present case, additional air flow surrounding the plasma plume could be used to remove excess heat. Helium has very good thermal conduction and has been used in the lab, but cost would be prohibitive in the field.

Figure 27 contains data from stripping an Antifouling painted panel using atmospheric plasma. For this experiment, the plasma conditions identified by the Design of Experiments as optimum were used. The basic parameters were 30 mm/sec velocity, 20 degree -X angle, 2 mm height, and 93 lpm air flow. The initial spike at the 0 mm thermocouple was due to direct contact with the plasma. As seen in the thermographs b, c, and tracings, d, there was a heat wave moving through the steel panel which reached a maximum temperature of about 140 °C directly under the plasma. The thermal wave began at the near edge and followed under the plasma as it was swept across the sample surface. This type of analysis could be developed further in order to quantitatively identify heat flux. This example essentially had a floating panel with the only dissipation of heat due to convective loss to air. On a ship, the heat sink would be practically infinite. One exception might be on the inside of the ship which might reach a higher temperature. In the present case, the wall thickness was only 1/4 inch (6.4 mm). Real ships have thicker and larger steel surface areas.



- A. Photograph of plasma de-painting in progress
- B. Thermal image near the end of de-painting
- C. Thermal image at the beginning of de-painting

- D. Thermocouple traces at various X locations vs. time.

Figure 27: Dynamic steel temperature measured during plasma depainting in which the plasma was rastered in +/- Y stepped in the X direction.

Due to the interesting result obtained by measuring heat transfer and the potential for escalation during scale-up, in house thermal modeling was performed using COMSOL Multiphysics version 4.2a which included heat transfer and transient analysis modules. This FEA dynamic heat transfer model was developed by Neira [12] for use in modeling heat distribution of electron beam melting of metal and was subsequently altered to fit this project.

A simple definition can be derived from the Fourier law which states than heat spontaneously flows from a region of higher temperature to a region of lower temperature over time approaching thermal equilibrium. Conservation of energy dictates that heat in less heat retained less heat out equals zero. Conductive heat flow occurs in the direction of decreasing temperature since higher temperatures are associated with higher molecular energy. Fourier's law expresses conductive heat flux in differential form as;

Equation 2. Three-dimensional transient heat transfer solution using Fourier's law

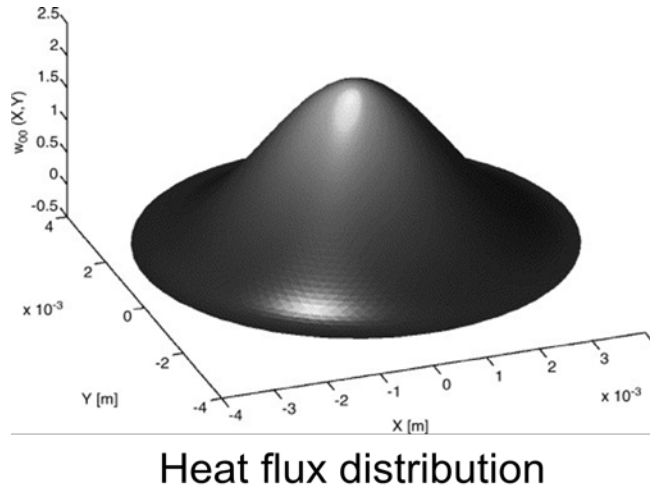
$$\frac{\partial}{\partial x} \left(k \frac{\partial T}{\partial x} \right) + \frac{\partial}{\partial y} \left(k \frac{\partial T}{\partial y} \right) + \frac{\partial}{\partial z} \left(k \frac{\partial T}{\partial z} \right) + \dot{Q} = \rho c_p \frac{\partial T}{\partial t} + \rho c_p V \frac{\partial T}{\partial x}$$

- | | |
|----------------------------|-----------------------------------|
| k = Thermal conductivity | ϵ = Emissivity |
| ρ = Density | T = Temperature |
| C_p = Heat capacity | t = time |
| T = Temperature | V = Rastering velocity |
| | (x, y, z) = Spatial coordinates |

For the purposes of atmospheric plasma, heat input into the surface was provided with a Gaussian distribution as shown in

- Tsai N.S., Eagar T.W., Distribution of heat and current fluxes in gas tungsten arcs, Metallurgical Transactions B, 16B, 1985, p.841.
- Eagar T.W., Tsai N.S., Temperature fields produced by traveling distributed heat sources, Welding Research Supplement, 346s, 1983.

Figure 28, which should very closely approximate real conditions.



- Tsai N.S., Eagar T.W., Distribution of heat and current fluxes in gas tungsten arcs, Metallurgical Transactions B, 16B, 1985, p.841.
- Eagar T.W., Tsai N.S., Temperature fields produced by traveling distributed heat sources, Welding Research Supplement, 346s, 1983.

Figure 28: Gaussian distribution function used as heat source geometry for input to heat transfer model.

This flow model needs to account for movement of the source which then becomes;

Equation 3. Heat source mathematical model used for input to heat transfer model

$$Q^*(x, y) = \frac{q}{2\pi\sigma^2} e^{-(x^2+y^2)/2\sigma^2}$$

Q^* = Heat source moving at a speed v

q = Net heat input per unit time

σ = Distribution parameter of the heat flux

In order to make this model applicable to multiple passes and subsequent overlap passes, Neira included an integration function in the finite element model which accounts for the current position and all previous positions of the heat source as a function of time. In areas where heat

flow continues as input, the temperature will continue to rise. Conversely, in areas where heat is no longer input, it will dissipate according to Fick’s law based on the material properties such as thermal conductivity, heat capacity, the geometry of the sample, and the corresponding thermal properties of the environment. In the present case, wood was used to support the sample and assumed not to alter heat flow at the surface. Loss terms for output of heat away from the sample due to radiation is;

Equation 4. Heat loss due to surface to ambient radiation

$$q = \epsilon\sigma(T_{ext}^4 - T_{plate}^4)$$

While output of heat due to natural convection is represented as;

Equation 5. Heat loss factor as a function of natural external convection

$$h = (T_{ext} - T_{plate})$$

In order to determine q (or heat flux per unit time), a timed static experiment was conducted using thermocouples to measure the temperature drop across a steel sample while exposed to atmospheric plasma for a fixed time. That data was input into Neira’s dynamic heat transfer model which allowed the above experiment to be repeated on a computer. The first model experiment was static by keeping the plasma stationary over the coupon, which resulted in a heat profile as shown in Figure 29. These results compare favorably to those in Figure 25 and were very promising.

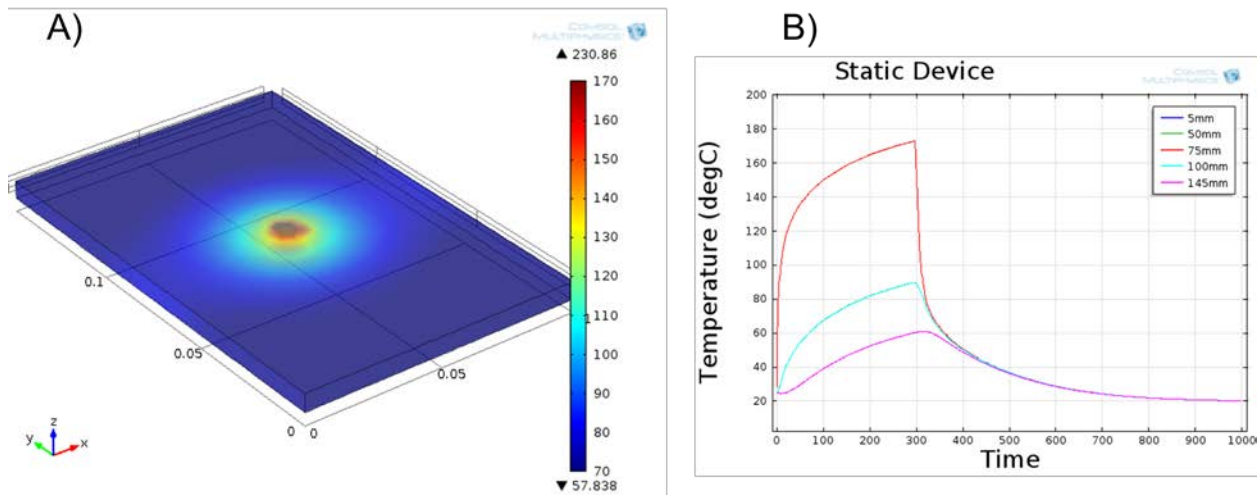


Figure 29: Snapshot of modeled thermogram A) during static plasma treatment at the center position and calculated thermocouple traces at positions X = 5, 50, 75, 100, 145 mm B).

Since the static results were so promising, the dynamic experiment was attempted by rastering the heat source over the substrate using the same velocity profile as before. In this case, the time the plasma was not on the coupon, but was off to the side was accounted for by using an off sample dwell time. The FEA model automatically accounted for time due to distance of the heat

source from the sample. The thermogram model seen in Figure 30 A) at first approximation was similar to that observed using an infrared camera (video obtained but not published). However, upon review of the resulting thermal history shown in B), heat continued to build until the plasma was turned off. After reviewing the shape of the curves and profile, it became clear that additional heat was being lost due to induced convection by the “over spray” of the plasma. In other words, near the active plume heat builds, but just outside of the boundary, high velocity air either from the plasma or something else was aiding in heat removal. Previously, the team had discussed the possibility of adding additional cooling using a hybrid device.

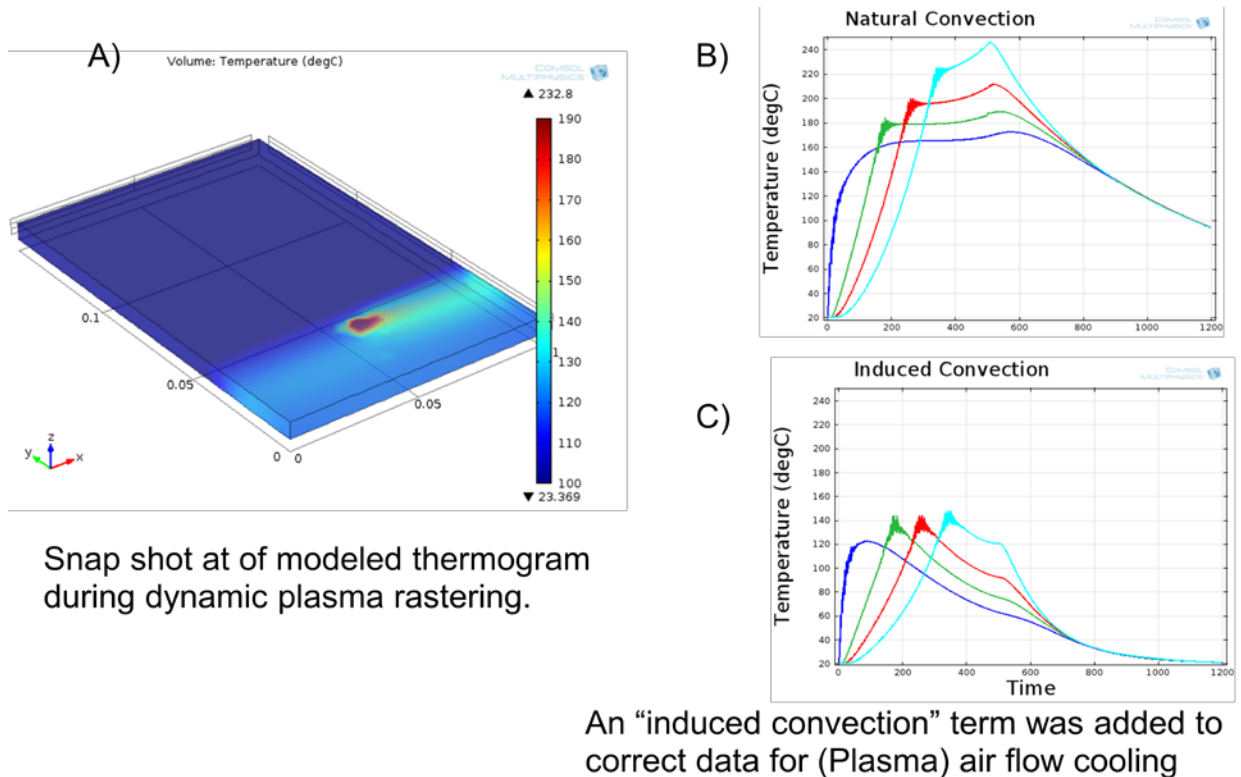


Figure 30: Results of using Neira dynamic heat transfer model to simulate plasma rastering over a surface.

When the model was adjusted for an induced cooling term, the resultant curves as seen in C) once again closely matched those from the previous experiment. In order to confirm that the model closely matched reality, a snapshot was generated from the program at a specific time during the rastering process. The resultant thermogram, as seen in Figure 31, confirmed that the model was accurate.

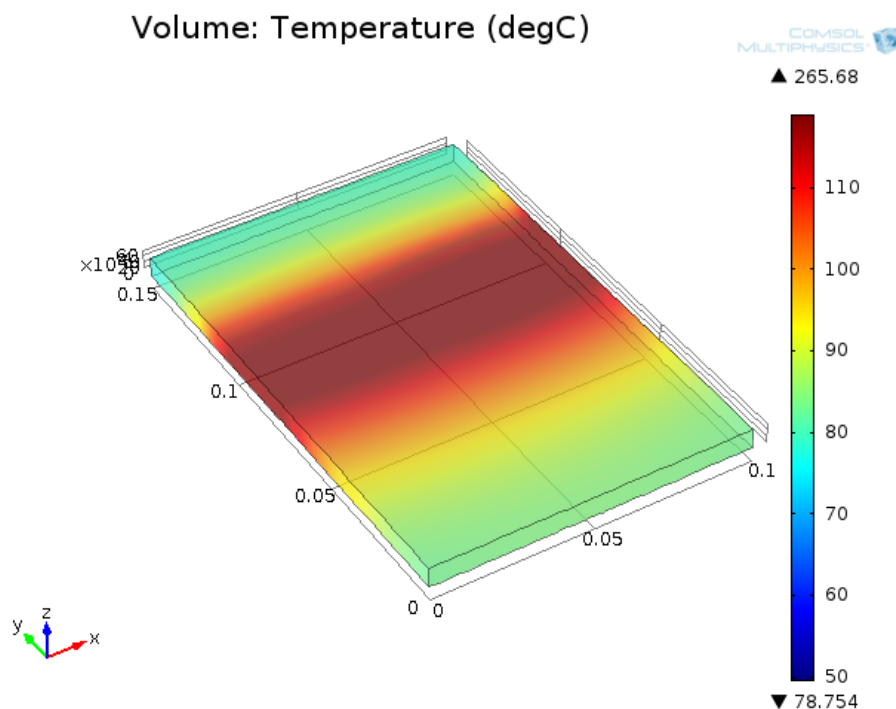


Figure 31: Atmospheric plasma long scan model with induced cooling correction.

The potential use of this model could greatly aid the project. In the case of a real ship, by inputting real parameters into the model, heat build could be predicted. This would be particularly helpful in determining the temperature which might be reached on the inside of the ship. In addition, the model can be adjusted for multiple input sources which have been developed and are under investigation. An interesting experiment which has not yet been attempted would be to input parameters which simulate the near infinite heat sink effects of a large ship. Heat build in sensitive areas also might be modeled as the plasma reaches those areas. In conclusion, the input and dissipation of heat does not appear to be of major concern and could easily be mitigated with external cooling if necessary.

In the case that heat buildup becomes a concern, there are at least two approaches for management using atmospheric plasma - by measurement and control or through hybrid and supplemental systems. The current state of plasma removes paint in localized areas. If the device is static, heat will build. Even though the heat measurements were lower than cause for concern in relation to phase transitions of iron, coupons were sectioned for metallography and evaluated as discussed later in the report. More research is needed to quantify heat flux as a function of plasma parameters and relate that to removal rate. For a small area device, the heat content needs to be monitored and managed. This can occur through various means such as ensuring the device does not become stagnant, using safety shutoffs, or by applying supplemental cooling. The second approach is directed more towards large area devices. In order to provide a viable alternative, plasma needs to be competitive on a production rate scale. This includes consideration of all aspects of the removal process. If a small area system scales appropriately, the problem is solved. If not, phase 2 of SERDP WP1762 was intended to investigate the use of hybrid and alternative systems to complement atmospheric plasma. For example, the current technology uses low frequency which has advantages and disadvantages.

One disadvantage is the possibility of transitioning from stable atmospheric plasma, to a transferred arc plasma which would significantly increase heat input. This could be avoided in several ways. My monitoring and controlling current (or power) the plasma state could automatically be controlled through the power supply to respond to the onset of arc transition. Alternatively using higher frequencies or mixed modes, conditions for plasma ignition and sustainment might be self-tuning and therefore maintain stable plasma.

2.2.2 Substrate Chemistry

Samples from each of the paint systems depainted using grit blasting and plasma were analyzed using XPS. Data obtained from a grit blasted sample is present in Figure 32. Both samples from grit blasting still showed significant evidence of paint residue. Carbon contents were high, as well as Magnesium oxide (MgO) used as filler in the paint. Al and Si were also observed more likely from residual blast media than the steel since Fe concentration was low. However, they might also be remnants of paint. Evidence of residual paint was also found in the O 1s spectrum in which the contribution due to oxygen bonded to carbon exceeded the contribution of oxygen bonded to metal. Also of significance was the presence of a peak due to metallic iron in the Fe 2p region along with peaks from iron oxide. The data made sense since a rather large particle size was used to remove the paint. In the blasting operation any material on the surface is subject to the kinetic energy of the media. In some areas, grit can remove the material, while in other cases, perhaps in the valleys between peaks or due to a hammering action by the grit, paint residue remains. A finer mesh size would be able to reach into the valleys, but would also alter the surface profile and reduce paint removal rates. Oxides of iron can also be removed by the grit exposing metallic iron below the surface.

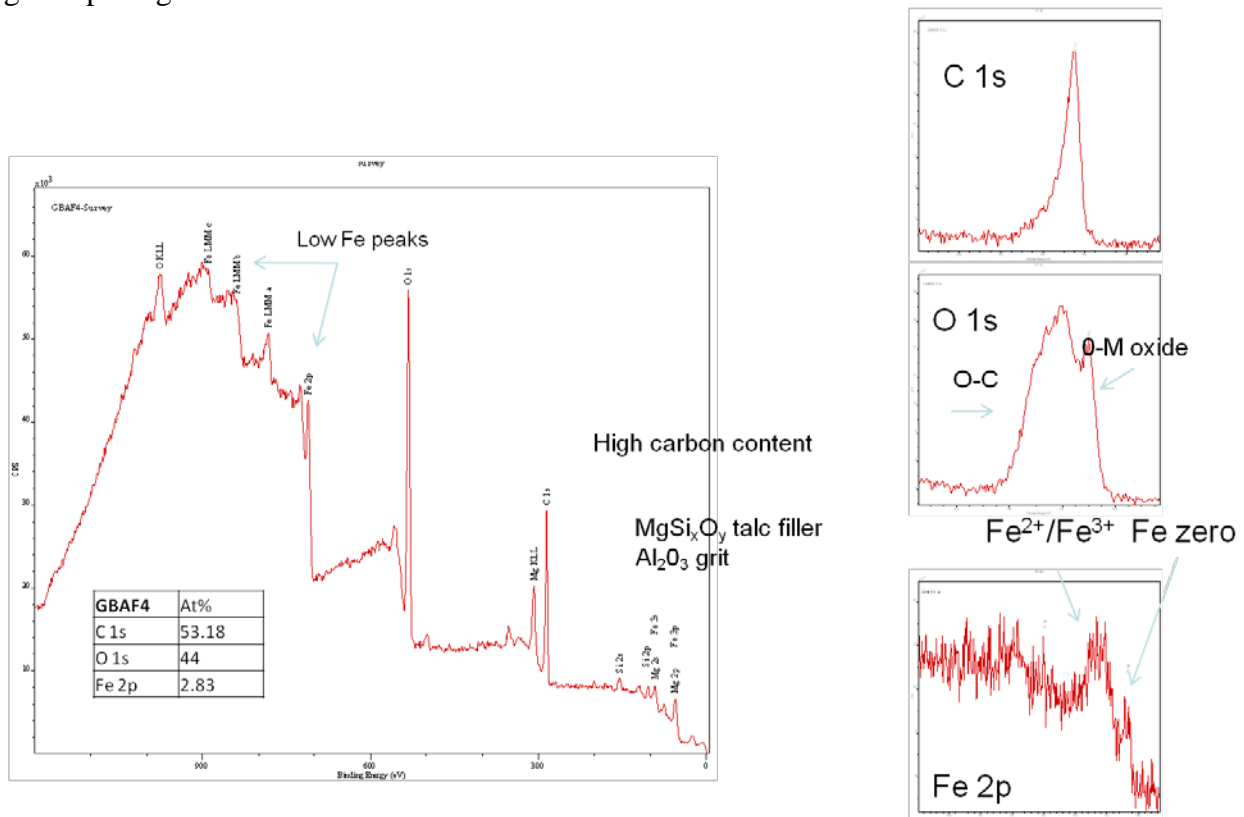
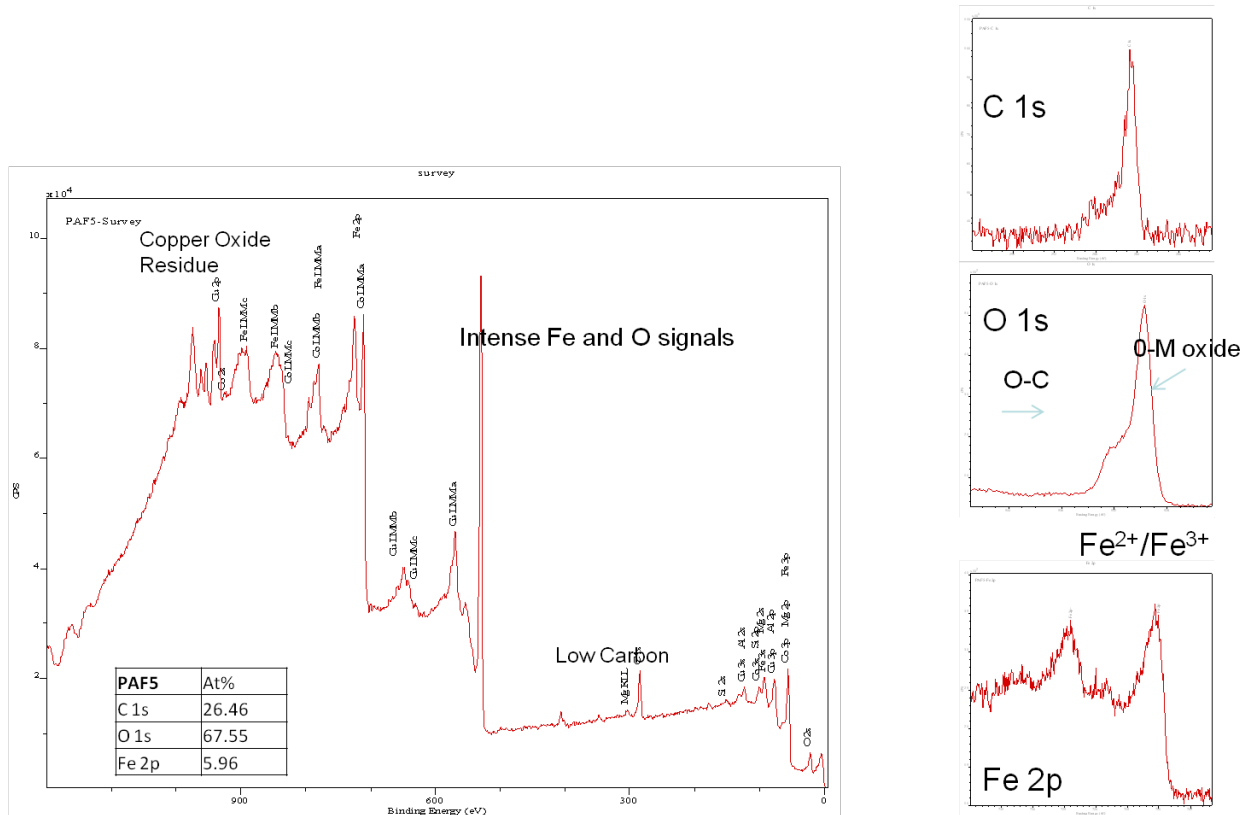


Figure 32: XPS spectra obtained from steel after AF paint was removed by grit blasting.

In contrast to grit blasting, plasma depainted samples were significantly different in a number of ways. Residual carbon as seen in the C1s spectrum of Figure 33, was dramatically lower than the grit blasted samples. Oxygen and iron signals were much stronger. Contribution from organic C-O was dramatically reduced in the O 1s spectra, yet the signal from metallic oxide was strong. Much of the filler residue was removed, but it was interesting that it was still present on the surface. By comparing the O 1s regions with the Fe 2p regions, it is clear that there is a thick layer of iron oxide on the plasma treated sample.



The spectra presented in Figure 34, were obtained from a grit blasted Antifouling panel (had paint residue) that was then treated using plasma. Plasma treatment strips organic material from the surface and at the same time, either revealing the presence of iron oxide, or allowing growth of iron oxide. It was clear that plasma removed paint that grit blasting did not.

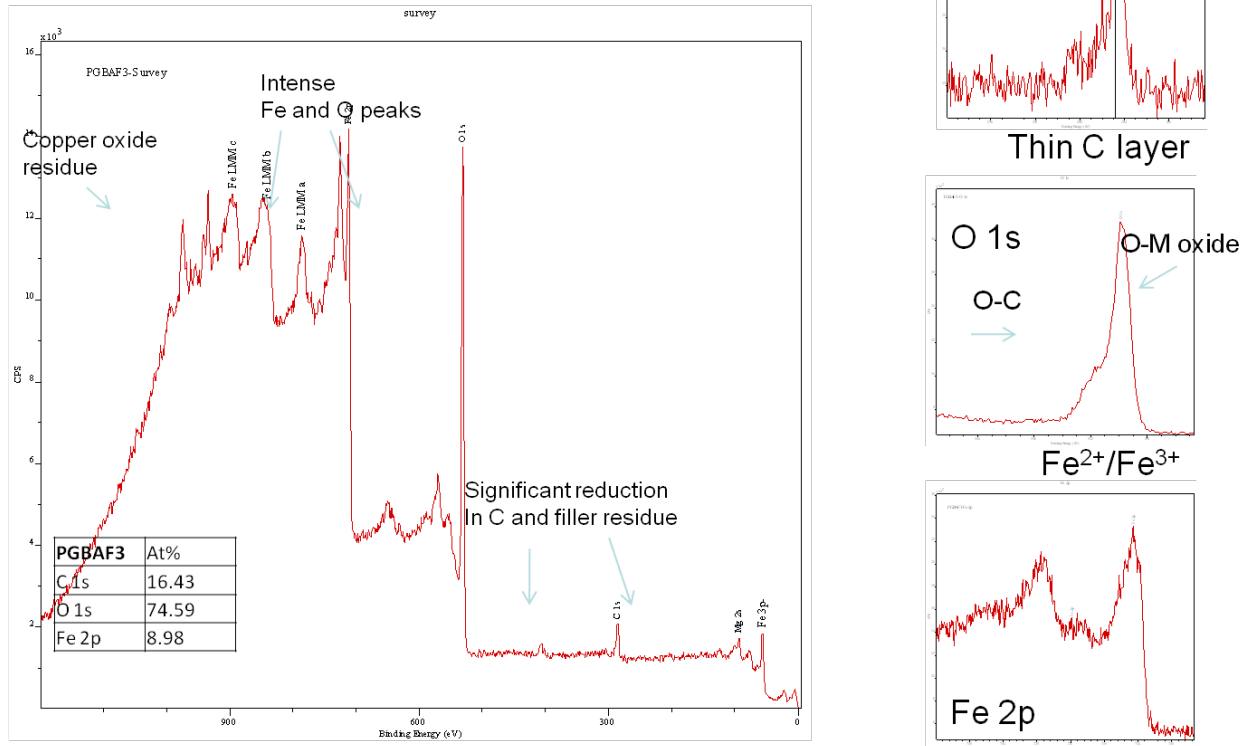
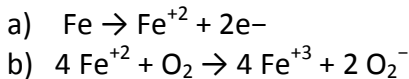


Figure 34: XPS spectra obtained from steel after AF paint was removed by grit blasting, then by plasma.

Grit blasting strips paint and oxide, while leaving behind paint residue, filler residue, media residue, possibly contaminant from recycled or dirty media, and a thin layer of iron oxide with metallic iron under the film. Plasma strips paint, leaves some inorganic filler residue, and a thick layer of iron oxide. Rust back or flash rusting is a common problem with grit blasted surfaces. This is easy to understand with the presence of metallic iron.

Equation 6. Oxidation of iron.



Oxides of iron by themselves can be very stable and tightly adhere to surfaces. Rust which is a hydrated salt of the oxides has less density and adheres loosely to surfaces. The electrochemical processes which result in rust formation start with transfer of electrons from iron to oxygen. If there is no metallic iron to provide electrons, there is no rust. If water cannot penetrate the iron oxide film and reach the metal surface, again there is no rust. An understanding of redox reaction involving iron in the presence of water and oxygen is important since all three are required to form “rust”. Rust consists of hydrated iron(III) oxides $Fe_2O_3 \cdot nH_2O$ and iron(III) oxide-hydroxide ($FeO(OH)$, $Fe(OH)$)

Equation 7. Hydration of iron.

- a) $\text{Fe}^{+2} + 2\text{H}_2\text{O} \rightleftharpoons \text{Fe}(\text{OH})_2 + 2\text{H}^+$
 b) $\text{Fe}^{+3} + 3\text{H}_2\text{O} \rightleftharpoons \text{Fe}(\text{OH})_3 + 3\text{H}^+$

These reactions are accelerated by the presence of salts and acidic conditions. Of key importance are the combined effects of water, oxygen, and electron transport within the electrochemical cell.

Equation 8. Iron hydroxides and reactions evolving water.

- a) $\text{Fe}(\text{OH})_2 \rightleftharpoons \text{FeO} + \text{H}_2\text{O}$
 b) $\text{Fe}(\text{OH})_3 \rightleftharpoons \text{FeO}(\text{OH}) + \text{H}_2\text{O}$
 c) $2 \text{FeO}(\text{OH}) \rightleftharpoons \text{Fe}_2\text{O}_3 + \text{H}_2\text{O}$

Glancing Angle X-ray Diffraction (GAXRD)

In order to better identify the oxides on the surface of grit blasted and plasma depainted surfaces, glancing angle x-ray diffraction (GAXRD) was used. Sample nomenclature is shown in Table 7. Duplicates were analyzed with samples A3 and A5 AF depainted using atmospheric plasma and samples A4 and A5-br depainted using grit blasting. It should be noted that the sample coupons were only 1 cm x 1 cm prior to paint removal. For the plasma depainting this represented a very small surface area over which the intense plume of plasma was rastered. Samples did get hotter than usual, but the temperature was not measured.

Table 7: Summary of samples submitted for glancing angle x-ray diffraction.

Identification	Number	Description
A3	1	Darkly colored sample with rough
A4	1	Bright sample with rough surface
A5	1	Darkly colored sample with rough
A5-br	1	Bright sample with rough surface

Samples were mounted in the x-ray holder such that their surface was parallel to the holder surface and placed in the x-ray diffractometer (Rigaku SmartLab). The x-ray analysis was performed with a Parallel Beam/Parallel Slit alignment due to the rough surface being analyzed. The glancing angle maintained by the source was 1° while a 2θ scan was performed from 20° – 80° . The scan was performed with a step size of 0.1° and a count time of six seconds was captured at each step. The scans were performed with a 40 kV Cu $K\alpha$ beam at 44 mA.

Analysis of A4 and A5-br as seen in Figure 35 and Figure 36 shows only the presence of Fe on the surface. Analysis of A3 and A5 (darker surface) as seen in Figure 37 and Figure 38 shows a different pattern than the bright samples. The presence of Fe is detected but also a mixture of Magnetite and Hematite phases. There are also two very strong peaks that are un-indexed at this time. The darker samples (A3 and A5) are very similar. The other two bright samples (A4 and A5-br) showed no measureable oxide layer on the surface.

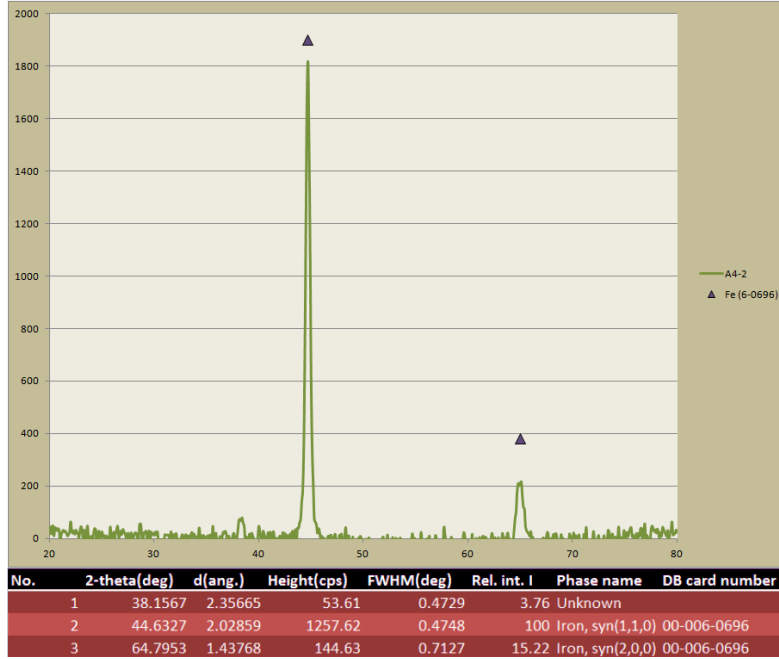


Figure 35: Analysis of grit blasted A4 indicated the presence of iron on the surface.

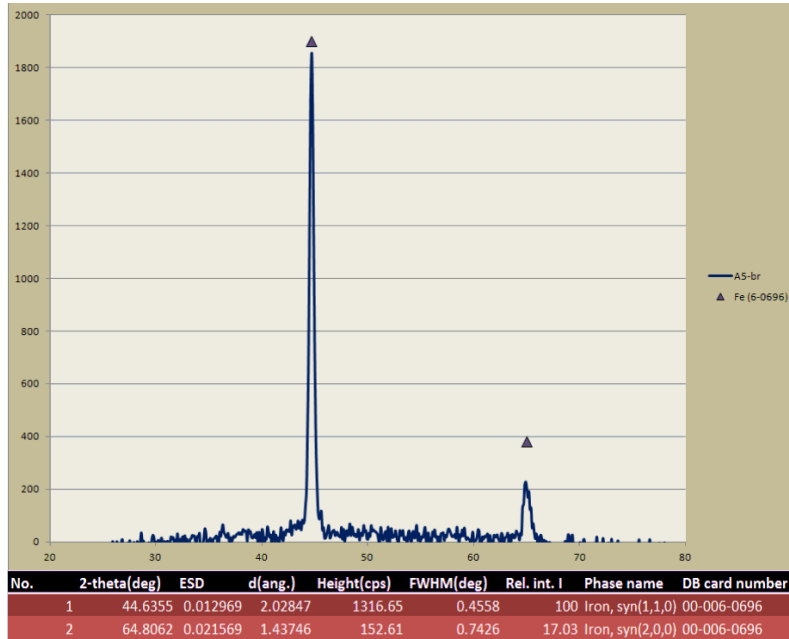


Figure 36: Analysis of grit blasted A5-br indicated the presence of iron on the surface.

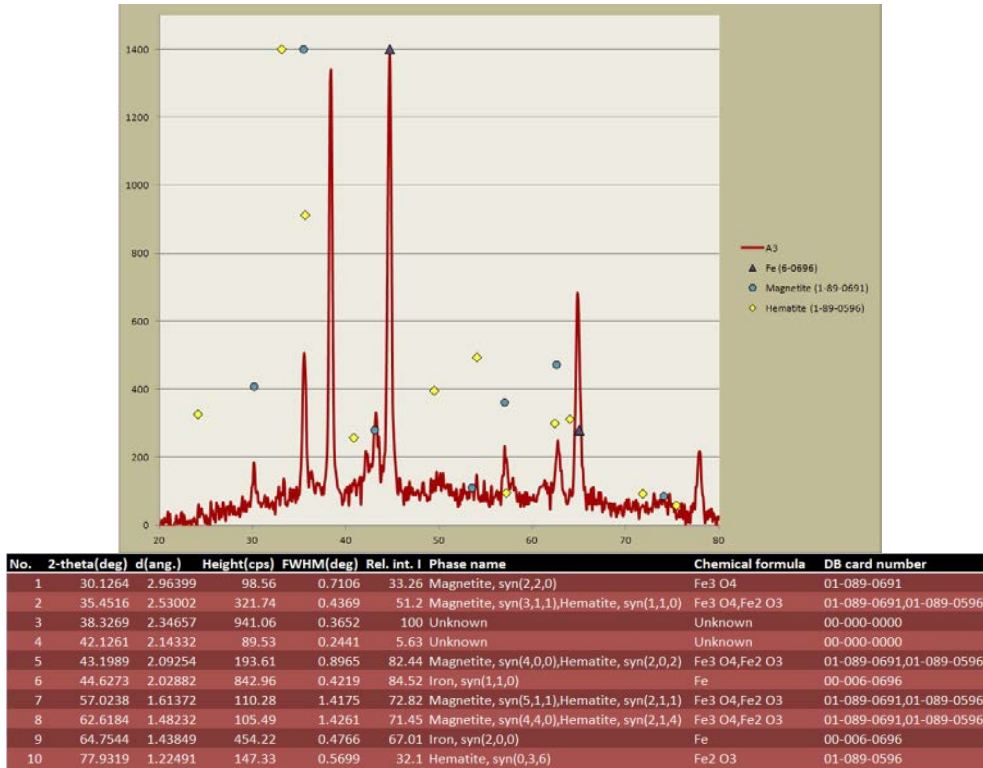


Figure 37: Analysis of plasma deposited A3 indicated the presence of iron oxides on the surface

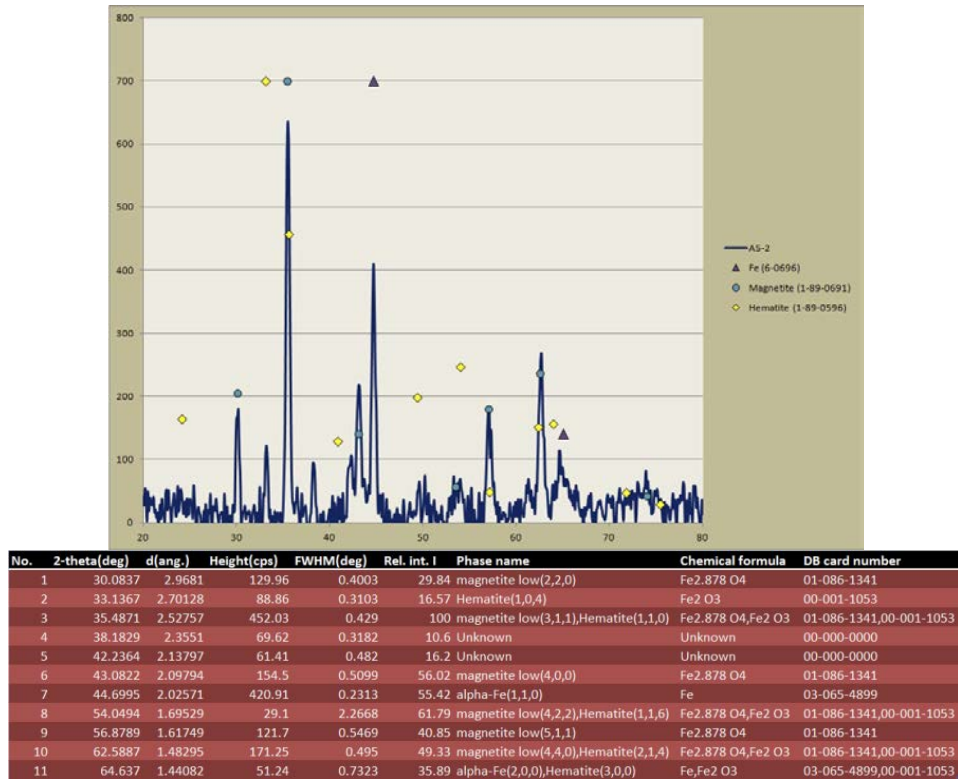


Figure 38: Analysis of plasma deposited A5 indicated the presence of iron oxides on the surface

A summary of the various forms of iron oxide is shown in Figure 39. Color and its absence is the result of visible wavelengths of light (400-700 nm) absorbing, reflecting, and refracting from an interface between media. In the case of films, Snell's law governs the patterns which can lead to a "rainbow" from constructive and destructive interference. The coloration on plasma stripped panels has a grey/blue appearance rather than red/brown. This indicates the absence of rust and the presence of iron oxides. Based on the oxidizing power of the plasma, it seems most likely that iron would fully convert to Fe^{3+} in the form of Fe_2O_3 .

Oxides (Anhydrous)

- [iron\(II\) oxide](#), [wüstite](#) (FeO)
- [iron\(II,III\) oxide](#), [magnetite](#) (Fe_3O_4)
- [iron\(III\) oxide](#) (Fe_2O_3)
 - ◆ [alpha phase](#), [hematite](#) ($\alpha\text{-Fe}_2\text{O}_3$)
 - ◆ [beta phase](#), ($\beta\text{-Fe}_2\text{O}_3$)
 - ◆ [gamma phase](#), [maghemite](#) ($\gamma\text{-Fe}_2\text{O}_3$)
 - ◆ [epsilon phase](#), ($\epsilon\text{-Fe}_2\text{O}_3$)

Hydroxides (Hydrous)

- [iron\(II\) hydroxide](#) ($\text{Fe}(\text{OH})_2$)
- [iron\(III\) hydroxide](#) ($\text{Fe}(\text{OH})_3$), ([bernalite](#))

Oxide/hydroxides (Hydrous)

- Main article: [iron\(III\) oxide-hydroxide](#)
 - ◆ [goethite](#) ($\alpha\text{-FeOOH}$),
 - ◆ [akaganéite](#) ($\beta\text{-FeOOH}$),
 - ◆ [lepidocrocite](#) ($\gamma\text{-FeOOH}$),
 - ◆ [feroxyhyte](#) ($\delta\text{-FeOOH}$),
- [ferrihydrite](#) ($\text{Fe}_5\text{HO}_8 \cdot 4\text{H}_2\text{O}$ approx.), or $5\text{Fe}_2\text{O}_3 \cdot 9\text{H}_2\text{O}$
- [schwertmannite](#) (ideally $\text{Fe}_8\text{O}_8(\text{OH})_6(\text{SO}) \cdot n\text{H}_2\text{O}$ or $\text{Fe}^{3+}_{16}\text{O}_{16}(\text{OH},\text{SO}_4)_{12-13} \cdot 10-12\text{H}_2\text{O}$)
- [green rusts](#) ($\text{Fe}^{\text{III}}_x\text{Fe}^{\text{II}}_y(\text{OH})_{3x+2y-z}(\text{A}^-)_z$; where A^- is Cl^- or 0.5SO_4^{2-})



Crystalline vs. Amorphous?

"Red Rust" is hydrated oxide of iron

Figure 39: Various forms of oxides on iron obtained from sources [13] and [14].

In an experiment which closely approximates what might be happening with plasma, Campo et.al. [15] measured iron oxide composition and thickness changes as a function of temperature and time. Their results are shown in Figure 40. Oxide thickness did not exceed 1 micron until the temperature reached 570°C for at least 200 seconds. The resulting oxides of iron, namely magnetite and hematite, are somewhat protective to low alloy steels. There would certainly be no formation of rust, without the presence of water. FeO was first formed at the metal interface followed by the mixed oxides Fe_3O_4 and Fe_2O_3 , depending upon the conditions.

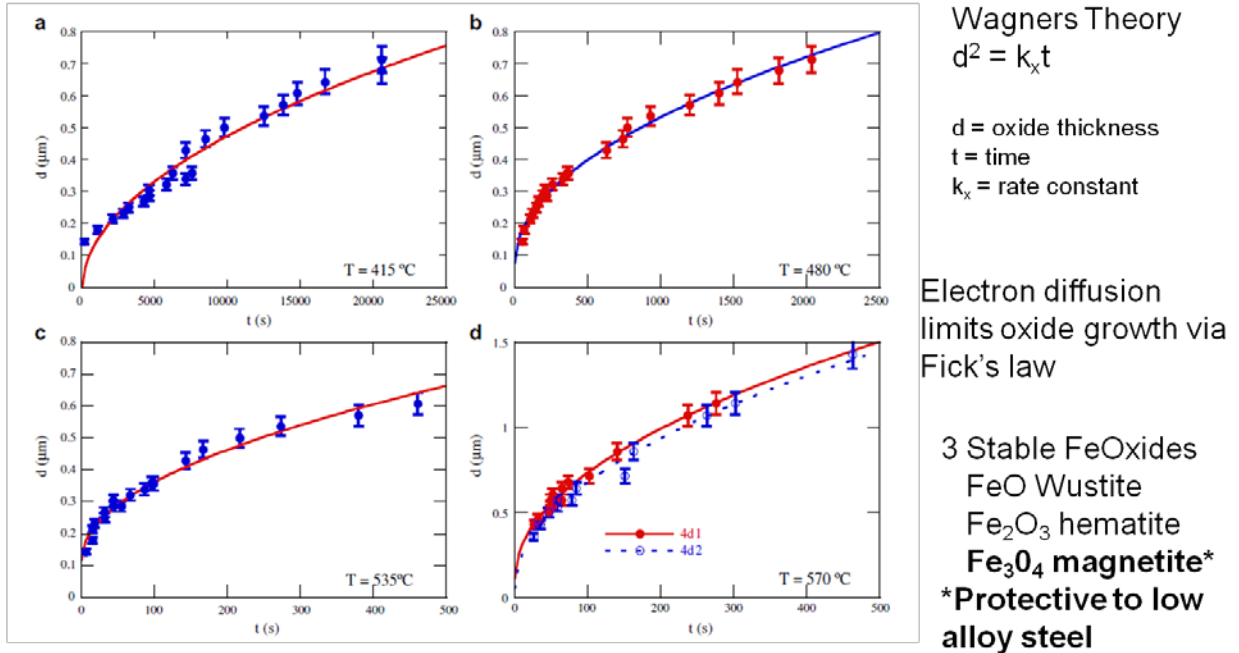


Figure 40: Oxide growth on Fe versus time at four temperatures [15].

Once water finds a way to this surface of plasma depainted samples, will water diffuse through the oxide to the metal, propagate the formation of rust, and if so at what rate? Experiments could be run to evaluate the rate of rust formation on grit blasted steel versus plasma treated steel. This has been previously investigated and reported for the case of water jetting as seen in Figure 41.

It seems when a new technology is being evaluated for an existing application, the common approach is to identify similarities to and difference from the current technology. That certainly seemed the case when water jet was being evaluated versus grit blasting. A significant aspect only associated with water jet paint removal, is the presence and dwell time of water which is almost continuously exposed to the surface.

Figure 42 taken from [16] illustrates how quickly flash rusting occurs on water jet samples. Also observed in the photos is the blue/gray appearance immediately after water jet depainting. As discussed, this is likely due to presence of a thick iron oxide. The various other colors observed such as yellow, yellow green, and brown suggest that a mixture of oxides are present. The photo labeled as “Figure 1” illustrates the conversion of those oxides to “rust”.

Theoretical Basis for Relationship between Flash Rust and Color?

- Progression of rust in the presence of water and oxygen without contaminants
 - Stage 1 - millisecond to second
 - Thin (1-4nm) oxide/hydroxide film
 - Stable/passivating in the absence of liquid water or contaminants
 - Explains why "Light" finishes are achieved with vacuum equipment
 - Stage 2 – after 2-3 hours exposure to near neutral aqueous environment
 - **Most of what we paint over** changes to $\text{Fe}^{II}\text{Fe}^{III}\text{O}_x(\text{OH})_y$
 - **Clear**
 - **Greenish Hue**
 - Stage 3 – exposure to near neutral aqueous environment for ~2 weeks
 - Fragile brownish layer of oxide and hydroxide
 - Leidheiser observed lepidocrocite ($\text{Fe}_2\text{O}_3 \cdot \text{H}_2\text{O}$) as an indicator of the beginning
 - Stage 4 – “in a few days” magnetite begins to form (Fe_3O_4)
 - **Brown**
 - **Black**



Source: T.E. Graedel and R.P. Frankenthal, "Corrosion of High and Low Alloy Steels Exposed to the Atmosphere," *J. Electrochem. Soc.*, Vol 137, No 8, August 1990

12

Figure 41: Progression of flash rusting on iron surface after water jet paint removal [17] [13].

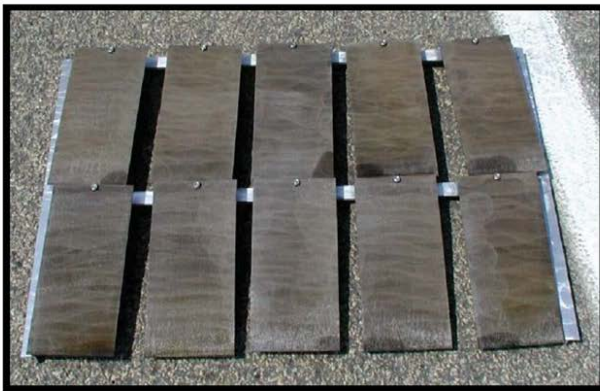


Figure 2. Typical Steel Panels Immediately after Waterjetting



Figure 1. Typical Pre-weathered Steel Panels

Figure 42: Steel panels subject to ultra-high pressure water jet (UHPWJ) [16].

Atmospheric plasma deposited samples randomly stored in our labs have not exhibited anything like the type of rusting shown in these figures. Perhaps it would be prudent to perform an experiment in which plasma deposited surfaces were exposed to different environments. It seems likely that the oxide produced by atmospheric plasma acts to protect the surface from further oxidation.

2.2.3 Surface Topography

One of the objectives of this part of research was to determine if the surface topography changed due to atmospheric plasma depainting. Optical micrographs obtained from grit blasted and plasma depainting Antifouling panels are shown in Figure 43. There were localized areas of blue/gray and red paint flecks remaining on the grit blasted sample. In addition, the overall appearance was “hazy” as viewed optically most likely from organic residue on the surface. The plasma sample had a darker blue/grey appearance. There were still “red” particles remaining, most likely due to copper oxide from the paint. In general, both surfaces had similar overall appearance, with the exception of color differences. Follow-up work using SEM would better help to reveal surface topography since there is much better depth of field. It would be interesting to look for residual blast media, residual paint, filler residues from the paint, and evidence to explain the color difference

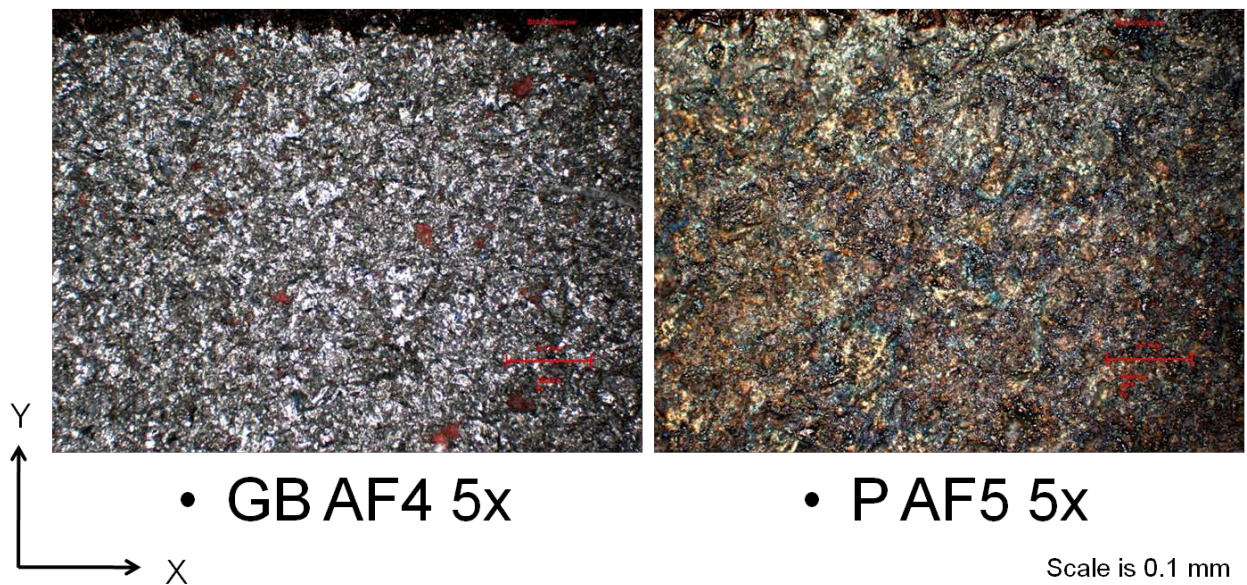
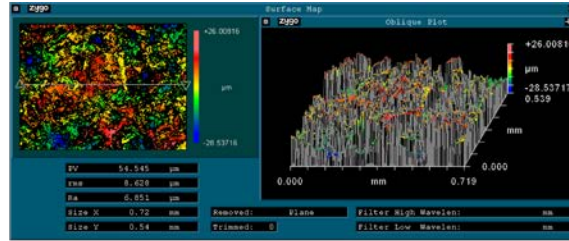


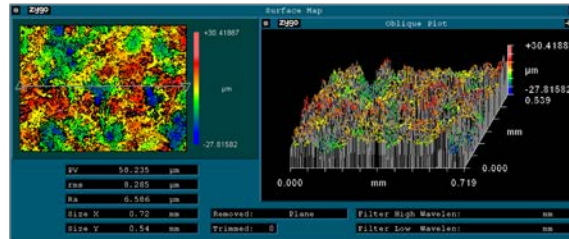
Figure 43: Optical micrographs from steel surfaces painted with AF then depainted using grit blasting (left) and plasma (right).

In order to measure surface topography, optical profilometry was performed using an instrument from Zygo. The optical micrographs obtained from the profilometry are shown in Figure 44. AF paint was removed by GB (grit blasting) or P (plasma). The PGB sample was grit blasted first, then treated with plasma. These were the same samples used for XPS in this report. All samples were very similar and it was difficult to identify any significant differences. There were no obvious differences in surface roughness. It is interesting to note that the grit size used was 36 mesh (0.4 mm), resulting in profiles with peak to valley of 0.050 mm. Clearly smaller particles impacted the surface profile.

GBAF4-10X



PAF5-10X



PGBAF3-10x

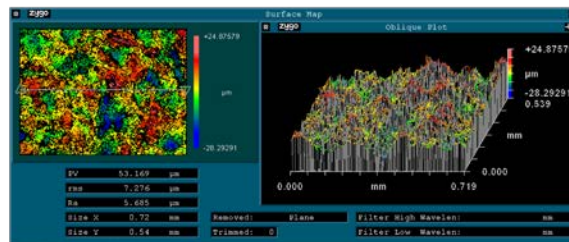


Figure 44: Optical profilometry plots obtained from the surfaces of steel samples painted with AF paint.

Optical profilometry data was easier to interpret by comparing the various measures of surface roughness which are shown in Table 8. This data included both FB and AF types of paint, grit blasted, plasma removed, and grit blasted then plasma treated. In all cases, there were no significant discernible differences. The author does not recall the limit of measurement, but considering visible light was used, precision should be in the sub-micron range. It has previously been shown that oxide thickness is likely on the order of less than one micron, but considering these samples exhibit 50 plus micron roughness, the oxide (trees) are not distinguished from the steel roughness (mountains).

As a final examination to roughness differences, SEM was used which has much higher depth of field than optical techniques. In this case the intent was to determine if atmospheric plasma was creating any changes in the surface morphology. The SEM micrographs are shown in Figure 45. An as received mill scale covered surface and a steel surface grit blasted with 36 mesh aluminum oxide were exposed to atmospheric plasma using similar conditions as in paint removal. It could be argued that there were no discernible differences. The scale of the images is on the same order of magnitude as the Zygo profiles. Certainly the surfaces are quite rough and minor differences if any are difficult to detect. It was concluded that micro scale oxide changes were likely, but macro scale roughness dominated the surfaces.

Table 8: Optical profilometry results from grit blasted depainted surfaces and plasma surfaces.

	GBAF4-10X	GBFB5-10X	PAF5-10X	PFB3-10X	PGBAF3-10X
PV (μm)	54.5	50.1	58.2	65.6	53.2
Rq or rms (μm)	8.6	7.0	8.3	8.1	7.3
Ra (μm)	6.9	5.6	6.6	6.0	5.7

$$R_q = \sqrt{\frac{1}{n} \sum_{i=1}^n y_i^2}$$

$$R_a = \frac{1}{n} \sum_{i=1}^n |y_i|$$

PV = Peak to valley
 rms (Rq) = root mean square
 Ra = arithmetic roughness average

Grit Blasted
AF Red

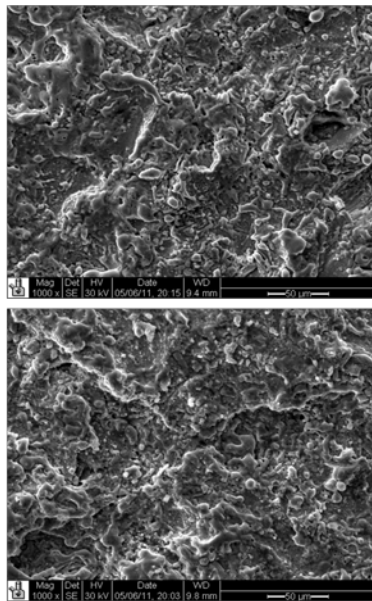
Grit Blasted
Freeboard Grey

Plasma
AF red

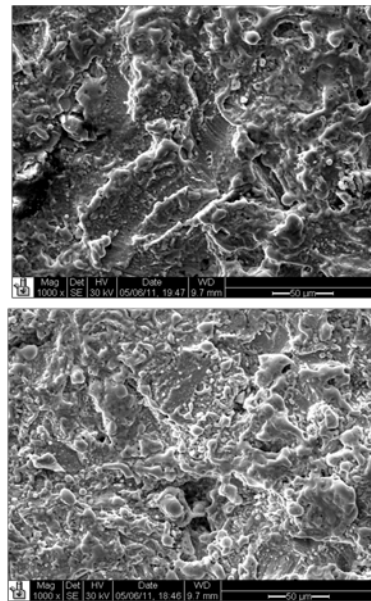
Plasma
Freeboard Grey

Grit Blasted
AF Red
Then Plasma

As Received, Mill Scale



→
Plasma
Treated
→



Grit Blasted 36 mesh Al₂O₃ (0.5 mm)

Scale is 50 micron

Figure 45: Scanning Electron micrographs of as received and grit blasted steel surfaces, which were treated with atmospheric plasma.

2.2.4 Repaint after Depainting Performance Testing

This task was where the rubber meets the road in terms of long term paint adhesion performance of plasma depainted, then repainted coupons. Table 9 summarizes this part of the research. As usual, 4" x 6" x 1/4" steel coupons which were used in other parts of the research were depainted using either grit blasting or atmospheric plasma. Due to concerns at the time about the differences in surface oxide, two sets of atmospheric plasma depainted samples were prepared. Set A was plasma depainted then coated with primer on the same day. Set B was plasma depainted and stored on location under ambient conditions for one week, then along with set A

they were shipped to Carderock. NSWCCD performed the grit blast depainting then transported all samples to a contractor for painting. Set B, therefore was “unprimed” for at least 2 weeks before the first coat of primer was applied. Samples were obtained at various stages of the preparation for future investigation.

Table 9: Summary of environmental performance testing of repainted, depainted test coupons.

Approximately 40 coupons each of AF and FB painted steel were prepared to MIL specification (grit blasted then painted). (3-4 replicates)

- **Set A:** Plasma de-painted then primed the same day at AP Solutions. Shipped to NSWCCD for final painting coats at contractor.
- **Set B:** Plasma de-painted at APS, stored 1 week at ambient, shipped to NSWCCD, all coats painted at contractor.
- **Set C:** Grit blasted at NSWCCD, all coats painted at contractor.

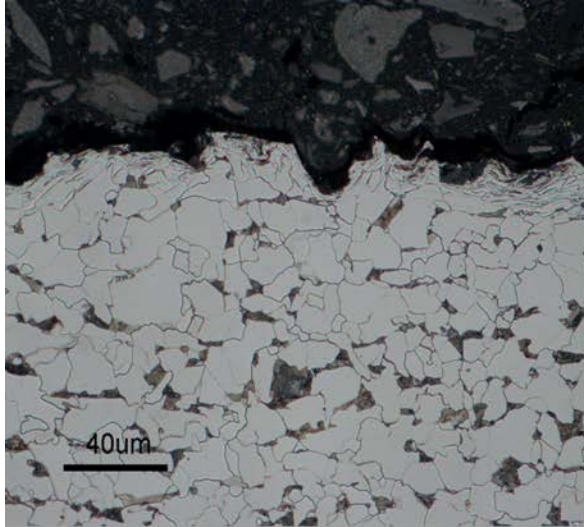
Repainted samples subjected to “Coating Performance Evaluation” tests;

- Analytical evaluations
- ASTM D4541 Pull off adhesion
- ASTM B117 Salt fog
- ASTM G95 Cathodic disbondment
- Navy specific: Key West, FL Alternate Immersion

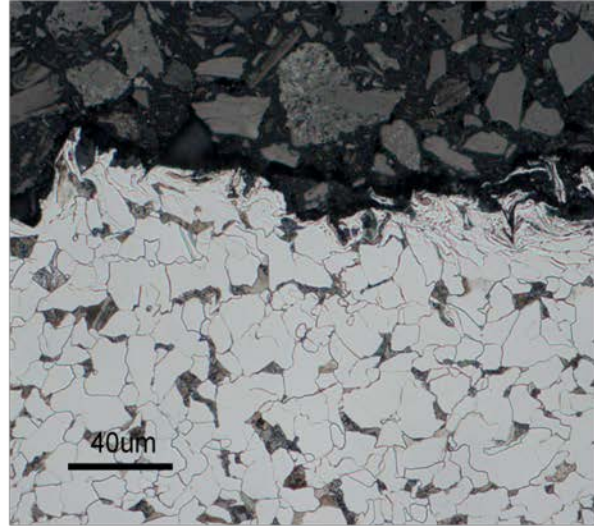
By this time it was known that the oxide thickness and possibly composition on plasma depainted samples was different compared to grit blasting. One question asked was “Does the chemistry of the primer system react any differently to grit blasted steel versus plasma treated steel”? In order to answer this question, depainted then repainted samples were cut in cross section with the paint intact, mechanically polished, etched in Nital and viewed in optical microscopy (all using standard metallographic techniques). The resultant micrographs are presented in Figure 46. There were several interesting features of these samples as summarized below;

- Metallographic cross-sections showed similar morphologies on all samples.
- No observed differences in grain size, structure, or composition.
- Steel grain size was on the order of the surface roughness.
- Oxide thickness was not discernible when comparing atmospheric plasma paint removal with the grit blasted removal on the **repainted** samples.
- Inorganic fillers were clearly visible in the paint layer.

In summary, all samples were similar in appearance.



Plasma De-painted AF Sample
Then Repainted with AF
50X Magnification Etched in Nital

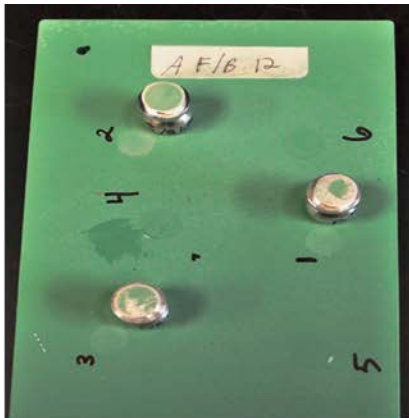


Grit Blasted De-painted AF Sample
Then Repainted with AF
50X Magnification Etched in Nital

Note: FB de-painted/re-painted samples were similar

Figure 46: Cross section optical micrographs obtained from depainted then repainted steel coupons.

Moving on to the different performance tests, the quickest test to complete was pull-off adhesion. Several examples of completed tests are shown in Figure 47. In addition to dry testing, intermittently a sample was taken from one of the other environmental tests, then tested according to ASTM 4541.



Panel A FB 12 Displayed mostly Cohesion and Glue Failures at an Average of 3100 psi



Panel C FB 14 Displayed mostly Cohesion Failures at an Average of 5150 psi

Figure 47: Examples of ASTM 4541 pull-off adhesion from dry samples.

Adhesion results for the FB coated panels and AF coated panels between both surface preparations displayed the mode of failure within the topcoat layers of each panel sets. Since the mode of failure did not occur between the substrate and primer the performance between plasma depainted and grit blasted samples can be considered comparable based on the magnitude of tensile adhesion values. Numerical data from adhesion testing is shown in Table 10.

Table 10: Adhesion Test first and second run comparison ASTM D4541

Panel Designation	Pressure 4 (psi)	Pressure 5 (psi)	Pressure 6 (psi)	Average	Standard Deviation	Type of Failures/ Cohesion (Co), Adhesion (Ad), Adhesive (Y)
A-F/B-12	3384	3308	2984	3225	212	1) Co, 65% C/35%Y; 2) Co, 95% C/5% Y; 3) Co, 85% C/15% Y
A-F/B-13	3136	3340	3260	3245	103	1) Co, 80% C/20% Y; 2) Co, 95% C/5% Y; 3) Co, 100% C
A-F/B-14	2264	2936	2828	2676	361	1) Co, 5% C/95% Y; 2) Co, 95% C/5% Y; 3) Co, 90% C/10% Y
B-F/B-12	4744	6104	6920	5923	1099	1) Co, 60% C/40% Y; 2) Co, 85% C/15% Y; 3) Co, 85% C/15% Y
B-F/B-13	5872	5308	5708	5629	290	1) Ad, 20% B/C, Co ~70% C /10% Y; 2) Ad, 15% B/C, Co, 80% C /5% Y; 3) Ad,25% B/C, Co, 65% C, 10% Y
B-F/B-14	5704	5060	5996	5587	479	1) Ad, 10% B/C, Co ~90% C; 2) Ad, 100% B/C; 3) Co, 95% C/ 5% Y
C-F/B-12	5200	4476	5528	5068	538	1) Co, 80% C/20% Y; 2) Co, 75% C/ 25% Y; 3) Ad,10% B/C, Co~90% C
C-F/B-13	5056	5352	5428	5279	197	1) Ad, 5% B/C, Co~85% C/ 10% Y; 2) Ad, 5% B/C, Co, 75% C/ 25% Y; 3) Co, 90% C/ 10% Y
C-F/B-14	5192	5560	5032	5261	271	1) Ad, 5% B/C, Co, 90% C, 5% Y; 2) Ad, 10% B/C, Co, 85% C/ 5%Y; 3) Ad, 15% B/C, Co, 70% C/ 15% Y
A-A/F-12	4776	4124	3792	4231	501	4) Co, 70% C/30%Y; 5) Co, 60% C/40% Y; 6) Co, 30% C/70% Y
A-A/F-13	3396	3576	3756	3576	180	All 3 Spots had 100% Y ~ Glue Failures
A-A/F-14	4976	4944	4484	4801	275	4) Co, 70% C/30% Y; 5) Co, 60% C/40% Y; 6) Co, 70% C/30% Y
B-A/F-12	4572	4084	4004	4220	307	4) Ad, 95% B/C, Co, 5% C; 5) Ad, 95% B/C, Co, 5% C; 6) Ad, 100% B/C
B-A/F-13	4572	4124	3408	4035	587	4) Ad, 85% B/C, Co ~15% C; 5) Ad, 90% B/C, Co ~10% C; 6) Ad, 100% B/C
B-A/F-14	3716	4728	4068	4171	514	4) Ad, 5% B/C, Co ~20% C, 75% Y; 5) Ad, 100% B/C; 6) Ad, 100% B/C
C-A/F-12	4180	4024	3948	4051	118	4) Co, 15% C/85% Y; 5) Ad, 95% B/C, Co~5% C; 6) Ad, 95% B/C, Co~5% C
C-A/F-13	4668	4352	4556	4525	160	4) Ad, 90% B/C, Co~10% C; 5) Ad, 85% B/C, Co ~15% C; 6) Ad, 70% B/C, Co~30% C
C-A/F-14	4312	4336	3812	4153	296	4) Ad, 90% B/C, Co ~10% C, 75% Y; 5) Ad, 85% B/C, Co~15% C; 6) Ad, 100% B/C

Results from Salt Spray Fog AF & FB coated panels ASTM B117:

Results for the Freeboard coated panels displayed no significant coating performance differences between the plasma depainted panels (Set A-F/B and B-F/B) and the grit blasted panels (Set C-F/B). More importantly within all the sets of panels (Set A, B, C), the epoxy primer coating system were intact for the most part after testing concluded. Results for the underwater hull Antifouling coated panels displayed no significant coating performance differences between the plasma depainted Antifouling panels (Set A-A/F and B-A/F) and the grit blasted Antifouling panels (Set C-A/F). More importantly, all sets of panels (Set A, B, C) of the MIL-PRF-24647 Type II anticorrosive epoxy primer coating system were all intact after 3,000 hours salt spray (fog) testing concluded.



Panel B F/B 11 Displayed Corrosion Sites (Dark Areas) within the Scribe Line, & Moderate Lifting of Coating along Scribe Line Edges



Panel C F/B 8 Displayed Corrosion Sites (Dark Areas) within the Scribe Line, & Moderate Lifting of Coating along Scribe Line Edges

Figure 48: Example test coupons subject to B117 salt after 3,000 hours.

Results from Cathodic Disbondment AF & FB coated panels:

In this project, the cathodic disbondment test seemed the most aggressive and likely test to identify performance differences of plasma versus grit blasting. Knowing that the oxide thickness was different, and potentially the chemistry as well, the impressed potential was expected to readily identify any weakness in the primer/steel adhesive bond. Photographs of samples during the test are shown in the Figure 49 and completed samples in Figure 50.

The top coated layers of the AF system, Copper Ablative Antifouling, and of the FB system, LSA Alkyd, exhibited complete disbondment. However, both epoxy primer systems for AF and FB systems were intact throughout with no disbondment. But more importantly there were no performance differences between the plasma depainted panels (Sets A & B) versus the media grit blasted panels (Set C). Both surface preparation methods performed similarly. Both epoxy primer systems for AF, Interguard 640 Red, MIL-PRF-24647, Type II and FB, MIL-DTL-24441, Type III F150 systems remained intact after 60 days exposure with no disbondment.

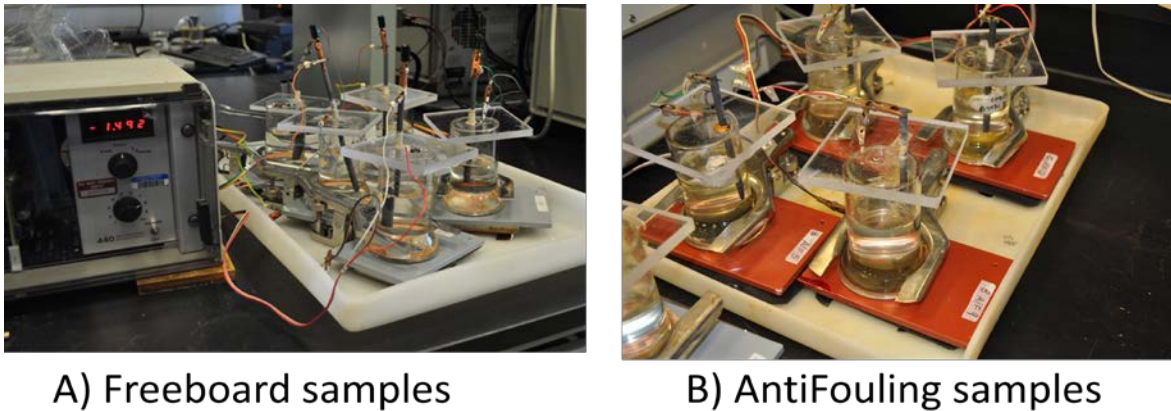


Figure 49: Photographs from test specimens during ASTM G95 cathodic delamination testing.

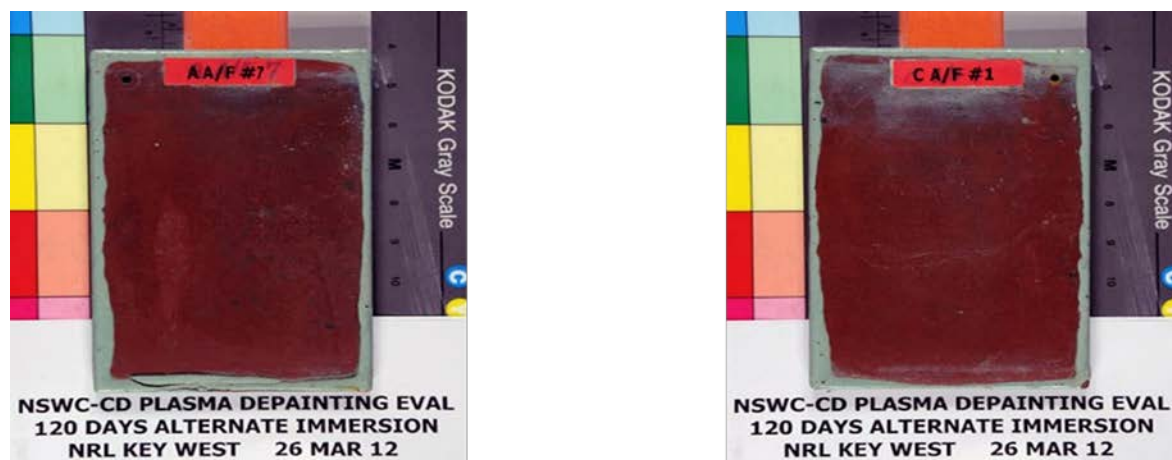


Panel A A/F 4 Exposed in ASTM D1141 Artificial Seawater for 60 Days has Epoxy Primer in-tact

Panel C A/F 8 Exposed in ASTM D1141 Artificial Seawater for 60 Days has Epoxy Primer in-tact

Figure 50: Examples of coupons after cathodic disbondment testing for 60 days according to ASTM G95.

Example coupons from alternate immersion testing at Key West, FL after four months are shown in the photographs of Figure 51. Natural seawater immersion results for the FB coated panels and Antifouling AF coated panels displayed no significant coating performance differences between the plasma depainted panels (Set A-F/B and B-F/B) and the grit blasted panels (Set C-F/B). There were no significant damages on any of the panels after four months of testing at NRL Key West, FL. Environmental Performance Summary. No significant differences in performance have been observed to date, when comparing plasma depainted or plasma depainted then aged, with grit blasted.



Panel A A/F 7 Displayed No Coating Performance Damage

Panel C A/F 1 Displayed No Coating Performance Damage

Figure 51: Example test coupons from alternate immersion testing at Key West, FL after four months.

2.3 Satisfactory Substrate Condition

Based on all the analytical testing performed and especially the long term environmental adhesion performance testing, the substrate condition after plasma depainting was considered satisfactory and therefore given a GO.

Task 3 Characterize Atmospheric Plasma Plume

3.1 Spectroscopic Studies

In general, the objective of plasma diagnostics is to gain a fundamental understanding of the physical processes that occur in the plasma from non-intrusive observations. One of the more common diagnostic techniques in low pressure plasmas is the electrostatic Langmuir probe which provides a convenient means of measuring electron temperature, plasma density, and plasma potential. Unfortunately, these probes cannot be used at atmospheric pressure since the insertion of probes is highly disruptive to the plasma equilibrium and an electrostatic probe theory has yet to be established at high pressure. There are a number of non-intrusive optical probing techniques for measuring plasma density, most notably Thomson scattering [18] and interferometry [19]. Thomson scattering provides a means of measuring the local electron density. However, even after many years of its use, Thomson scattering remains a very difficult and expensive technique. Optical emission spectroscopy (OES) has become the diagnostic of

choice for atmospheric plasma research as it is implemented with relative ease, has the potential for measuring the density and temperature of the electrons, and can be used to measure localized molecular and atomic species concentrations and temperatures.

Summary of Available Spectroscopic Techniques

The goal of spectroscopic diagnostics in the context of the coating removal process is to determine how the spatial profile of active species varies as a function of source parameters, such as input power, gas flow, and source geometry, and to determine how these processes and design parameters can be changed to scale the process to production mass removal rates. Since the active species (atomic oxygen and nitrogen) are created by an energetic electron population it is also important to be able to measure spatial profiles of ne and Te.

Optical Emission Spectroscopy

One of the advantages of optical emission spectroscopy is the ease with which the data can be acquired. Light emission from the plasma plume is passed through a grating spectrometer which provides a line integrated measurement of the emitted radiation as a function of wavelength. Air plasmas have a rich spectrum in the visible range (390 nm to 750 nm) due to the atomic and molecular forms of nitrogen and oxygen. Atomic oxygen is critically important to the coating removal process as it is responsible for converting the coating to the principal by-products of carbon dioxide and water. Atomic nitrogen plays a significant role in the removal process by transporting chemical energy to the substrate surface where energy is released via recombination. Since the coating that is being removed contains inorganic and some metallic constituents (for example, copper and zinc in naval coatings or chrome in aircraft coatings) it may be possible to observe the atomic emission from these constituents as they interact with the plasma afterglow. Metallic emission in the plasma plume may provide a means of monitoring the removal process where, for example, an observed change in the emission spectrum is used as an indicator of the plasma removal process transitioning to a different layer in the coating stack.

Spectral Line Identification

The first step in spectral analysis is the identification of the various spectral features that are observed. Commercial spectral line packages are available from PLASUS [20] and Ocean Optics [21] which provide databases for spectral line identification and software packages for curve fitting the results. These licensed packages cost approximately \$5,000 per copy. One of the most comprehensive spectral line databases is maintained by the National Institute of Standards and Technology (NIST) [22]. This free online database includes detailed spectroscopic data and references to the original data; however, the data is in HTML format which can be inconvenient to work with. Another public domain database has been made available by MU, Department of Physical Electronics at Masaryk University in the Czech Republic [23]. This database provides a simple user interface to perform line identification, curve fitting, and temperature determination.

Species Concentration Mapping

To obtain a quantitative measure of the species density, a careful analysis of spectral line widths, absolute intensities, and relative intensities must be performed. By performing this analysis at various points in the plasma, it is possible to measure how the plasma plume evolves as the reactive species flow toward the substrate.

Actinometry

If the atomic species concentration were simply proportional to the emitted line intensities, the mapping of active species would be a simple task; unfortunately, this is not the case, so actinometrical techniques have been developed for mapping specific atomic concentrations of interest [24]. In this technique, an inert gas, such as Ar, is introduced in the plasma and the relative emission intensities of the active species and the actinometer (argon) gas are measured. Provided the actinometer and the active species satisfy certain requirements, the ratio of their emission line intensities is approximately constant [25]. Trends in the active species concentration can be estimated by monitoring the ratio of the line emission intensity of the active species to that of the actinometer.

Optical Absorption Spectroscopy

In optical absorption spectroscopy (OAS) a calibrated light source is directed across the plasma and the amount of transmitted light is measured. The line integrated number of absorbing atoms is inferred by measuring the decrement in transmitted power. Continuous light sources that were traditionally used in the past have been replaced by coherent sources such as tunable dye and diode lasers where specific transitions can be excited.

OAS provides an accurate measurement of atomic concentrations when the atoms being probed are in their ground state. It has recently been reported that OAS has been used to determine the atomic to molecular ratio in oxygen helicon discharges by measuring the absorption of the central atomic oxygen line at 777 nm [26]. It seems unlikely that atoms in a plasma containing an energetic electron population will be in their ground state. In this case, active spectroscopy techniques such as Laser Induced Fluorescence (LIF) must be used for an accurate accounting of the competing processes of absorption, stimulated emission, spontaneous emission, and non-radiative quenching. This technique was recently used in mapping OH radicals in high pressure discharges [27].

Stark Broadening Technique – n_e and T_e measurement

Stark broadening of spectral lines has been shown to provide a relatively simple method of simultaneously measuring the electron density and temperature in atmospheric pressure microwave plasmas [28]. In this technique, two different Stark broadening models are used to relate the observed Full Width at Half Maximum of the $H\beta$ (486.13 nm) and $H\gamma$ (434.05) lines to distinct values of n_e and T_e . Hydrogen is introduced into the plasma as a minority species, typically less than 1% by volume, which is a very desirable feature of this technique as the small concentration of hydrogen minimizes any impact hydrogen may have on operation of the plasma source while also minimizing the optical depth of the hydrogen lines. Stark splitting of degenerate levels has also been used to measure the electric field strengths in dielectric barrier discharges [29].

Relative Line Intensity Techniques - T_{gas}

One of the most common spectroscopic techniques in atmospheric pressure plasmas involves measuring the relative intensities of the first negative system of molecular nitrogen lines [30] [31] [32]. In this technique the theoretical relative line strengths of rotational transitions are fitted to the measured spectrum using the nitrogen rotational temperature as a free variable.

Implementing this technique requires the use of a higher resolution spectrometer to be able to resolve the separation of the rotational transitions.

Microwave Interferometry

Microwave interferometry can be used to more directly measure the electron density of a plasma by observing the phase shift imparted on a microwave beam traversing the plasma. This technique could be used as an independent check of the density obtained spectroscopically. Interferometry has been used for wavelengths ranging from the microwave range up through soft X-rays to span a range of densities from a low of $1,010 \text{ cm}^{-3}$ to $1,021 \text{ cm}^{-3}$. A commercial microwave interferometer operating at fifteen GHz is available at a cost of about \$30,000 and is capable of measuring densities as high as $1,013 \text{ cm}^{-3}$ [33]. There are difficulties in implementing this technology in atmospheric torch discharges due to the small size of the discharge compared to the interferometer wavelength, and densities reported in some atmospheric discharges may require a higher frequency source than what is commercially available at the present time. Millimeter wave or laser interferometry techniques may become more viable in the future as inexpensive commercial sources become available.

Spectroscopic Measurements of Plasma Plume

In order to be able to form a recommendation on the most promising spectroscopic technique for the SERDP program, an Ocean Optics Jaz Spectrometer was used to obtain spectra from a plasma pen operating under the nominal conditions used in the DoE (dry air, 70 psi, 115 slm). The spectra were obtained for a pen in free operation, i.e., without the plume impinging on a substrate, in order to identify the species exiting the plasma pen under the nominal operating conditions.

The Ocean Optics spectrometer used in this experimental survey consisted of two modules with spectral ranges of 200 to 500 nm and 500 to 800 nm (lines /mm, CCD detector). The spectra from the two modules are joined at 500 nm to display the complete spectrum on the same scale. A typical spectrum obtained roughly two mm from the nozzle exit is shown in Figure 52. The optical emission spectrum of the plasma pen ranges from 200 to 800 nm. The short wavelength portion of the spectrum shows the characteristic molecular spectrum including the first negative and second positive series. Details of the N_2 second positive series are shown in Figure 53. The optical emission spectrum of the free jet plasma pen from 300 to 400 nm shows the second positive N_2 bands.

It was encouraging to see the strongest emission line centered at 777 nm, identified as the neutral atomic oxygen triplet. Another triplet set, identified as neutral atomic nitrogen, is also observed. The limited resolution of the Jaz spectrometer precludes its use in determining plasma density and temperatures from these features. Moreover, the short wavelength wings of the band heads indicate a significant broadening of the rotational band structure which is far greater than what one would expect from instrumental or thermal broadening. One possible mechanism for this broadening is the excitation of vibrational states due to the volume recombination of the atomic species. Such broadening would preclude the use of the nitrogen rotational bands as a diagnostic tool. More investigative work is needed to identify the source of this observed broadening.

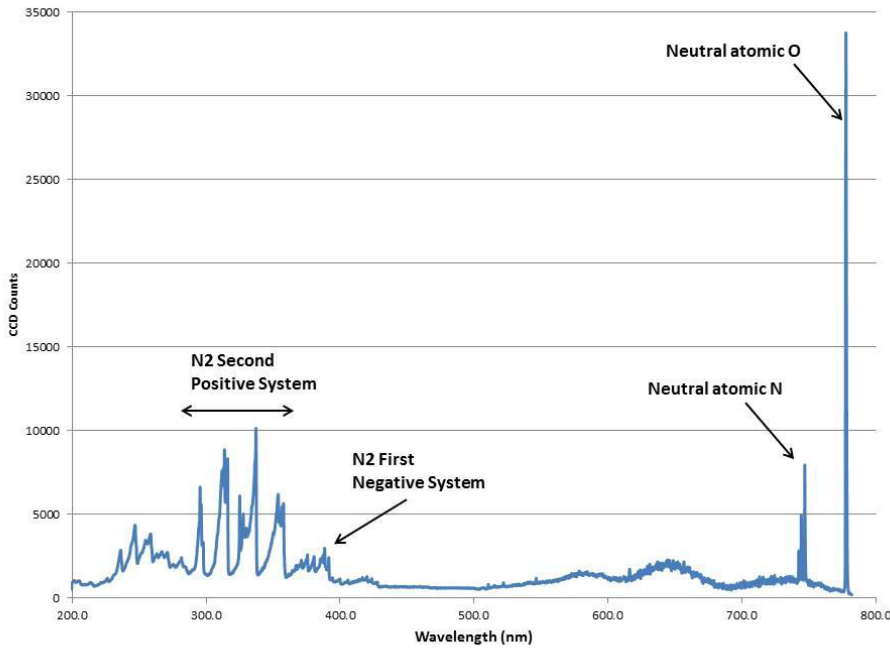


Figure 52: Optical emission spectrum of the plasma pen ranging from 200 to 800 nm.

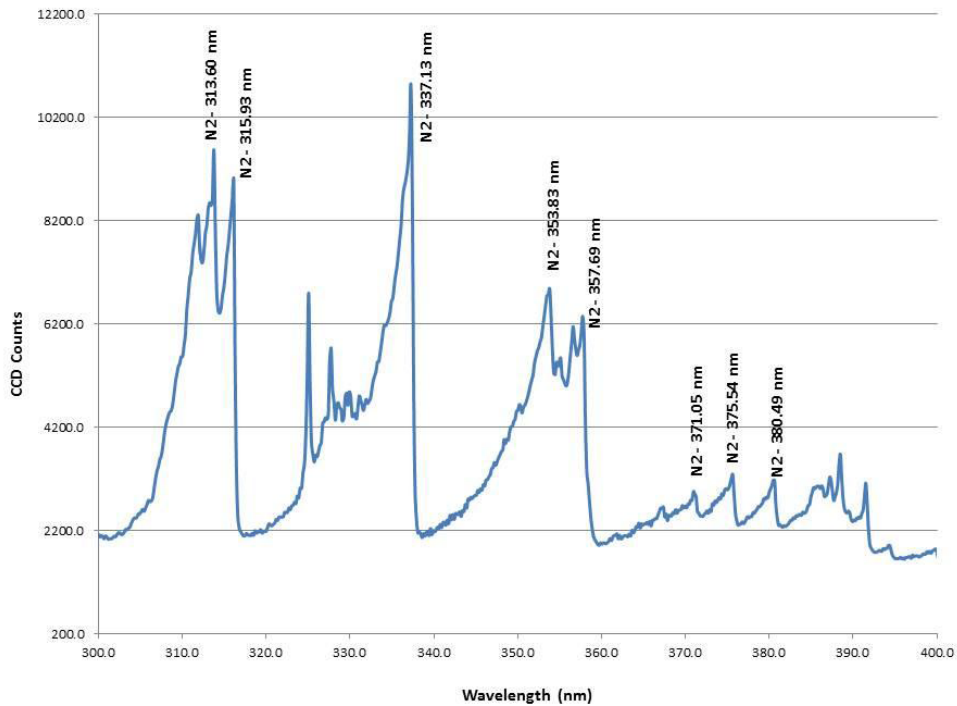


Figure 53: Detail of the optical emission spectrum of the free jet plasma pen from 300 to 400 nm showing the second positive N₂ bands.

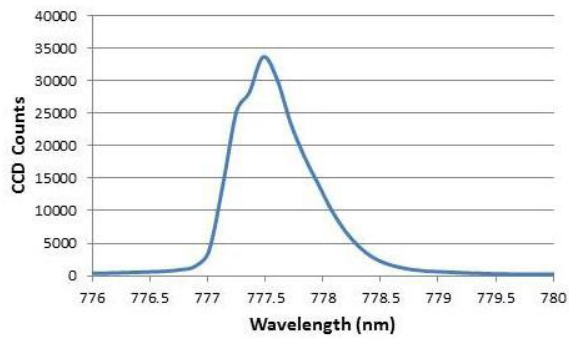


Figure 54: The triplet neutral atomic oxygen lines cannot be resolved by the current Ocean Optics spectrometer.

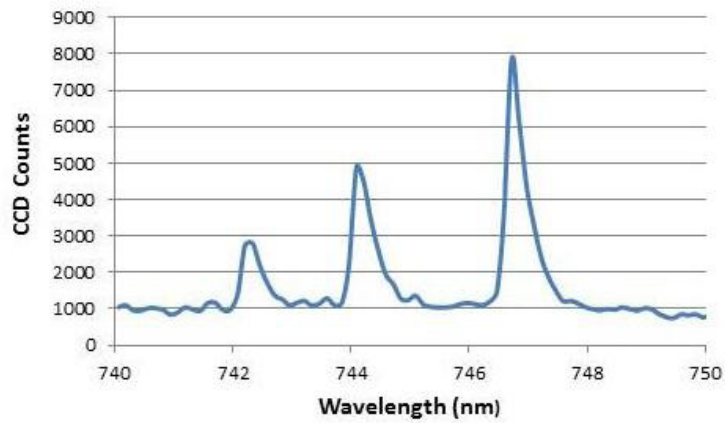


Figure 55: The triplet neutral atomic nitrogen lines are easily resolved by the current Ocean Optics Spectrometer.

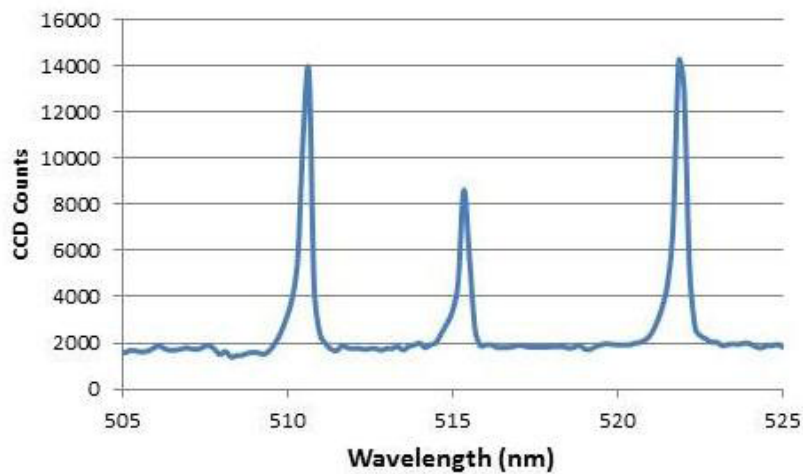


Figure 56: Detail of neutral copper emission lines captured by fast acquisition capability of Ocean Optics spectrometer.

The strength of the atomic emission lines are found to decrease with distance away from the pen nozzle while the three emission bands are found to increase. These bands appear to be a mixture of N₂ and O₂ lines, but have not been identified in this brief study. The fact that these bands increase in strength with distance from the source suggests that the emission may be due to excitation (collisional or recombination) of molecular gas that is entrained in the downstream afterglow plasma.

The fast response time of the Jaz spectrometer allows for real time monitoring of the plasma discharge. For example, when conditions are such that the plasma is not stable, a number of sharp atomic emission lines are found to appear sporadically in time in the range of 505 to 525 nm. These lines have been identified as the neutral atomic copper (Figure 56). Unstable operating conditions are correlated with the appearance of arcs attached to the source electrode which may lead to excessive heating of the electrode. The appearance of these lines can be used to remotely monitor the plasma source to determine when unstable plasma conditions may exist. An intelligent control system can potentially be programmed to vary the input electrical power or gas flow to restore stable plasma operation. Work is continuing at APS to use this diagnostic capability as a real-time process control tool during the removal of coatings to detect the transition between the various layers of paint and primer.

The optical emission spectrometer used to obtain the spectra shown above was configured for maximum optical range (200 nm to 800 nm) and is limited to a resolution of 0.5 nm. Nevertheless, the spectrometer can be used as a real time monitor of optical emission, not as an absolute measurement, but rather as an indicator for the presence of specific species, in particular, metal or inorganic species.

The optical techniques briefly summarized here will require the use of a spectrometer with a spectral resolution of 0.05 nm or less. This can be done most cost-effectively by reducing the spectral range of the Ocean Optics spectrometer modules while optimizing the slit size and grating for maximum resolution. The cost for an optimized spectrometer, with a reduced spectral range of approximately 50 nm, is \$4,600.

Of the techniques outlined here, Stark broadening (electron temperature and density) and actinometry (active species mapping) appear to be the simplest to implement and most likely to succeed with a modest effort and an optimized spectrometer. Gas temperature measurements using the rotational spectrum would be desirable, but given the complication of the observed broadening there is less likelihood for success in using this technique with the plasma pen. OAS would also be of great interest since it may provide a more direct measurement of the atomic species concentrations which are critical to the coating removal process. However, OAS represents a significant investment in cost (approximately \$20,000 for a diode laser) and effort since it is a more difficult measurement technique to develop given the potential complications of having a high concentration of excited atomic species. A more careful analysis and further discussions with the commercial vendors is necessary to determine which lines would be best for applications at atmospheric pressure before committing to the cost and difficulty of implementing this technique.

Additional OES Research

NCSU performed additional optical emission spectroscopy (OES) characterization using a Beta version of the Plasma Flux[®] 5000 system purchased from Atmospheric Plasma Solutions, Inc. This version of the PF5000 was an early model which APS claims has been upgraded significantly. OES is commonly used to characterize atmospheric pressure plasma devices, primarily as it is a non-perturbing technique [34]. Characterization was performed with an Ocean Optics 4-channel S2000 spectrometer with an analog to digital converter model ADC1000-USB with a manufacturer specified pixel resolution of 0.5 nm and a calculated FWHM of 0.72 nm. The spectrometer captures spectra across the wavelength range of 200-1050 nm with each channel acquiring a different subset range as shown in Table 11 which can be spliced together forming a single spectrum. The signal was acquired with Ocean Optics developed SpectraSuite software. The integration time and number of averages for each channel were controlled such that the total acquisition time totaled five seconds with background subtracted from each channel. Positioning and movement of the plasma torch was controlled by a three-axis CNC PRS standard model BT32 commonly referred to as a ‘ShopBot Buddy’ manufactured by ShopBot Tools, Inc. with a measured precision of <5 μm .

Table 11: Actual and spliced wavelength ranges for the S2000 Spectrometer.

Channel	Actual Wavelength Range (nm)	Spliced Wavelength Range (nm)
1	194.65-522.42	200-400
2	394.45-725.95	400-600
3	595.03-895.87	600-800
4	794.53-1055.71	800-1055

The spatial resolution of 1.35 mm was achieved using an inline disk with a pinhole of diameter one mm. The optics and torch were aligned such that an axial position of zero mm entails the field of view passing unobstructed below the tip of the nozzle with increasing positive values represent increased distance from the nozzle. Radial position of zero mm corresponds to the physical centerline of the torch as shown in Figure 57. Higher spatial resolution of 100 μm was attempted and deemed unsuccessful due to extremely high signal attenuation, and the device was diffraction limited.

A single broadband compiled spectrum acquired at an axial and radial position of zero mm is shown in Figure 58. Peaks identified included NO- γ transition in the 200-300 nm range [35], N₂ second positive system and N₂ first negative system covering the 300~450 nm range [36], Cu I lines at 510.24, 514.95, and 521.54 nm, and various atomic oxygen and nitrogen lines in the 740-875 nm range [37].

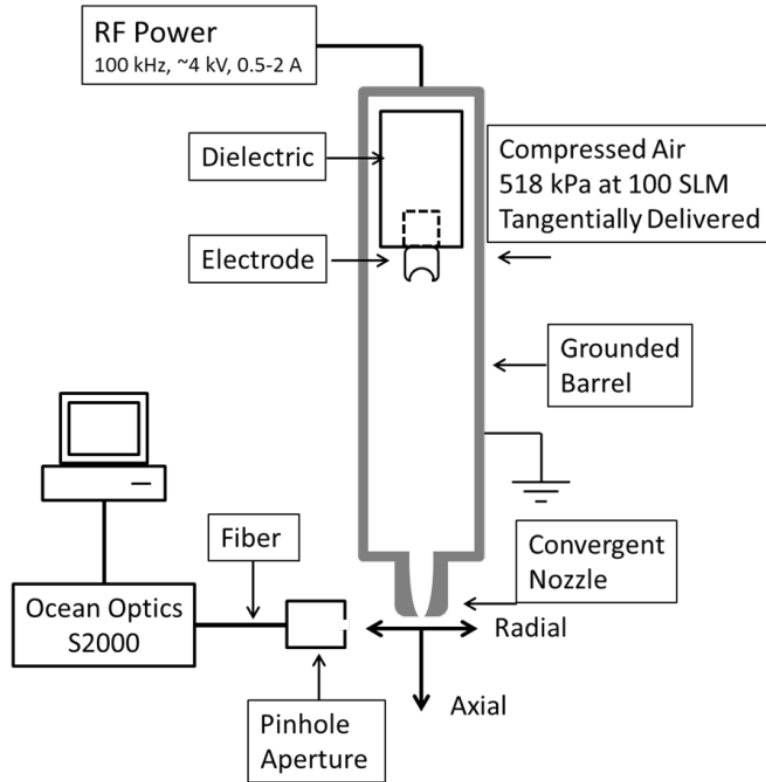


Figure 57: Diagram of the OES characterization setup indicating the various aspects of the plasma torch, the radial and axial directions with the intersection denoting the 0,0 point, and arrangement of the computer controlled 4-channel Ocean Optics S2000 spectrometer connected via fiber optic cable to a pinhole aperture.

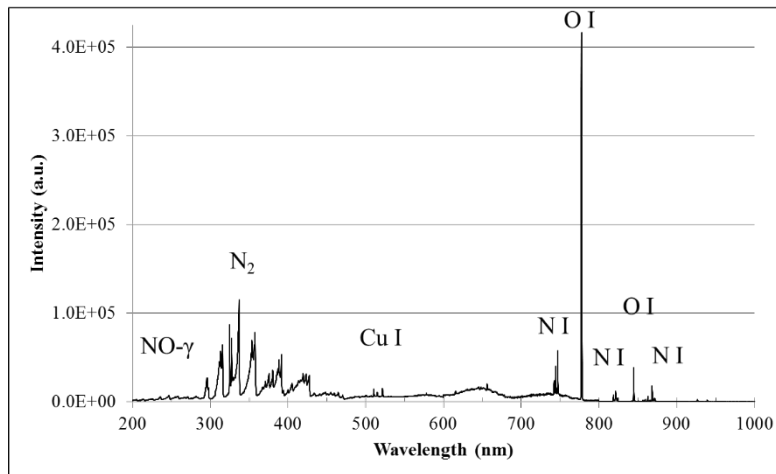


Figure 58: A broadband OES spectrum of the plasma torch with several peaks identified.

An expanded view of the nitrogen first negative system, $N_2^+ B^2\Sigma_u^+ \rightarrow X^2\Sigma_g^+$, and nitrogen second positive system, $C^3\Pi_u \rightarrow B^3\Pi_g$, is shown in Figure 59: OES N2 second positive system and N2 first negative system bands and two Cu I lines with the prominent band heads labeled, with a

more comprehensive list given in Table 12 as well as two atomic Cu I lines located at 324.92 nm and 327.57 nm.

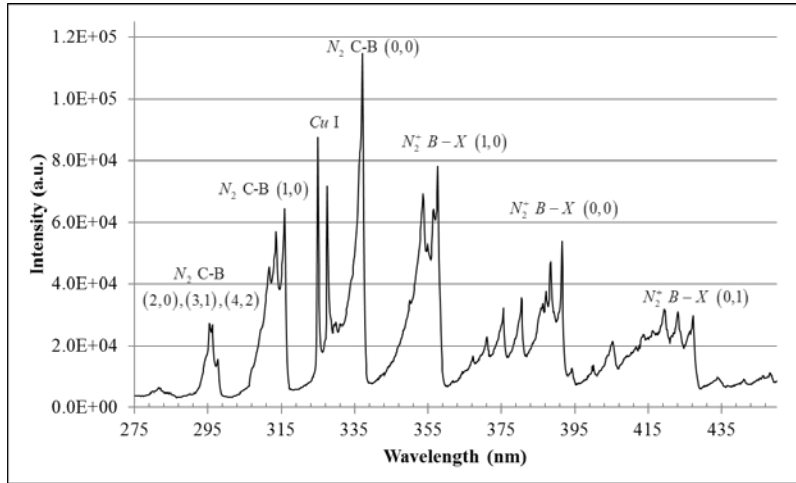


Figure 59: OES N_2 second positive system and N_2 first negative system bands and two Cu I lines.

The trio of Cu I lines are shown in Figure 60, atomic N I in Figure 61, atomic O I 777.4 nm line in Figure 62 and several atomic N I lines and atomic O I line in Figure 63. It is also possible to calculate the electron temperature of the plasma using the Cu I emission lines, present in the plasma torch emission, with the Boltzmann plot method. [38] [39]

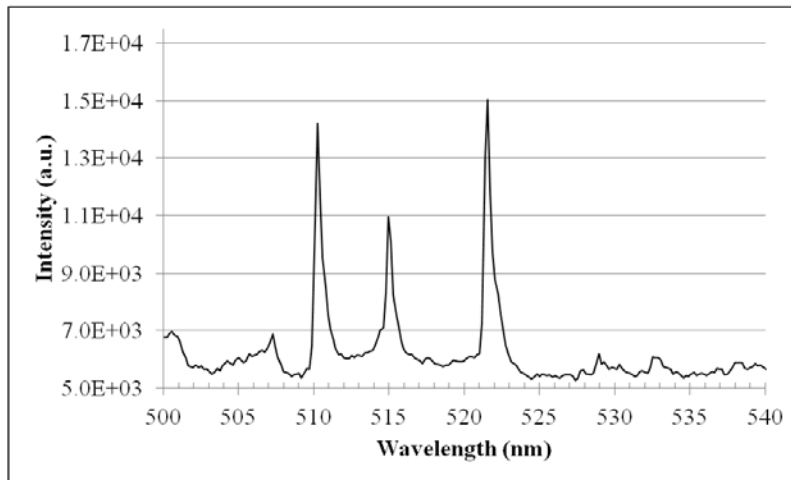


Figure 60: OES spectrum of Cu I lines.

Table 12: Wavelengths of the various N_2 second positive system and N_2 first negative system bands adapted from Reference [40].

N_2^+ $B^2\Sigma_u^+ \rightarrow X^2\Sigma_g^+$ (First Negative System)		N_2 $C^3\Pi_u \rightarrow B^3\Pi_g$ (Second Positive System)	
Band (v'-v'')	Band Origin (nm)	Band (v'-v'')	Band Origin (nm)
0-0	391.1	0-0	337.0
1-0	357.9	1-1	333.8
2-1	356.1	2-2	330.9
3-2	354.6	1-0	315.8
4-3	353.5	2-1	313.5
2-0	330.5	3-2	311.5
0-1	427.5	4-3	310.2
1-2	423.3	2-0	297.6
2-3	419.6	3-1	296.1
3-4	416.4	4-2	295.2

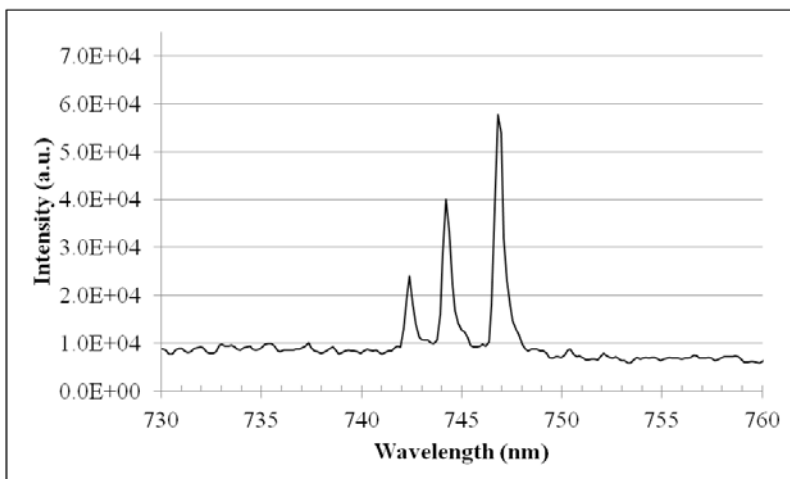


Figure 61: OES spectrum of atomic N I lines.

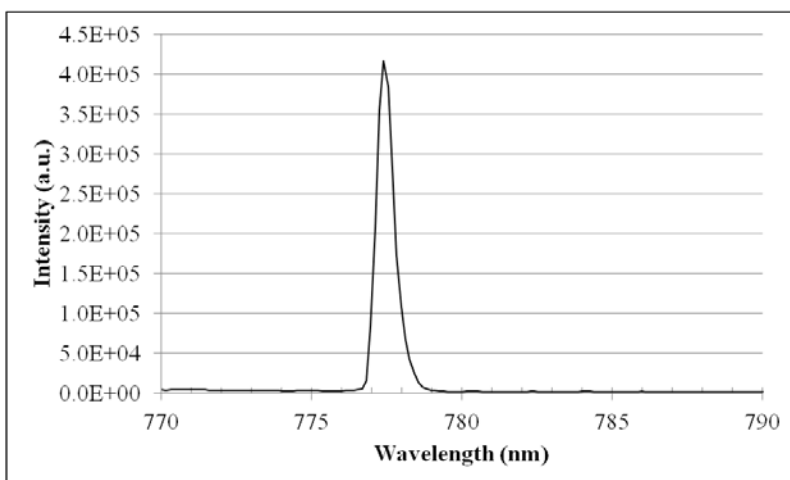


Figure 62: OES spectrum of O I line.

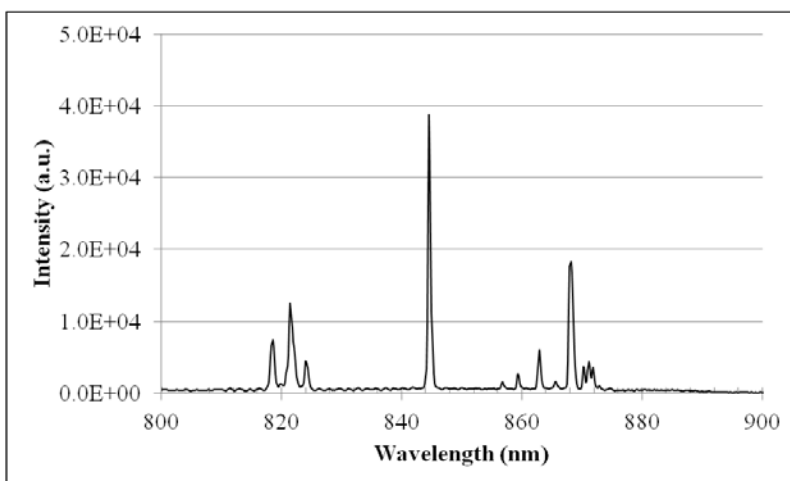


Figure 63: Atomic N I lines with the exception of the intense atomic O I line at 844.54 nm.

Spatially resolved OES was performed in two parts. The first part was at an axial position of zero mm spanning a radial range from -3.0 mm to + 3.5 mm, and the spectra were acquired at 0.5 mm increments and are shown in Figure 64. The second part were radial spectra acquired from -3.0 mm to +3.0 mm in 1.0 mm increments at axial positions of 1, 2, 3, 4, and 5 mm and are shown in Figure 65, Figure 66, Figure 67, Figure 68, and Figure 69, respectively. These spectra indicate a slight radial asymmetry with respect to the centerline of the torch that is assumed to arise from flow irregularities at the nozzle exit and a sharper distribution of the atomic species when compared to the molecular nitrogen bands, and it is currently assumed that this is related to the de-excitation and recombination of the atomic species. Intensity ratios were taken between the most prominent atomic line, O I 777.4 nm, and the nitrogen second positive system and nitrogen first negative system where the 777.4 nm atomic oxygen line intensity is normalized by

the N₂ Second Positive System band head (0,0) (337nm) (\blacklozenge) $\left[\frac{I_{777nm}}{I_{337nm}} \right]$ and N₂ First Negative

System band head (0,0) (391 nm) peaks (■) $\left[\frac{I_{777nm}}{I_{391nm}} \right]$ at an axial position of zero mm as shown in

Figure 70 indicating the intensity of the O I 777.4 nm line relative to the molecular nitrogen bands intensities and the inverse shown in Figure 71 indicating the intensities of the molecular nitrogen bands relative to the O I 777.4 nm line. From these two figures the relative intensity of atomic oxygen rapidly decreases sharply while the relative molecular nitrogen intensity increases.

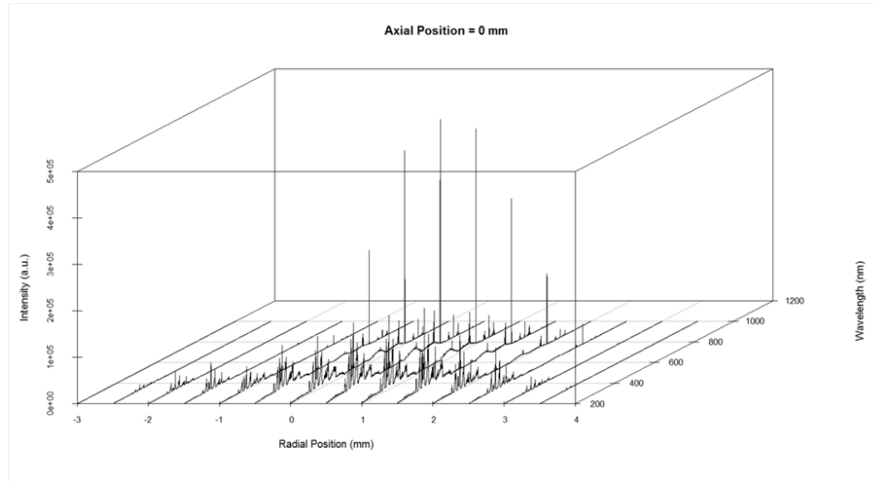


Figure 64: Radial OES spectra acquired at an axial position of 0 mm.

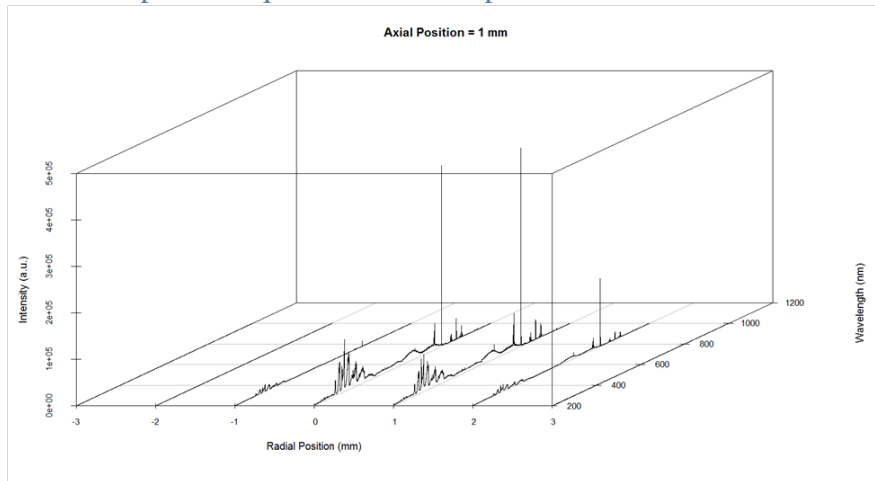


Figure 65: Radial OES spectra at an axial position of 1 mm.

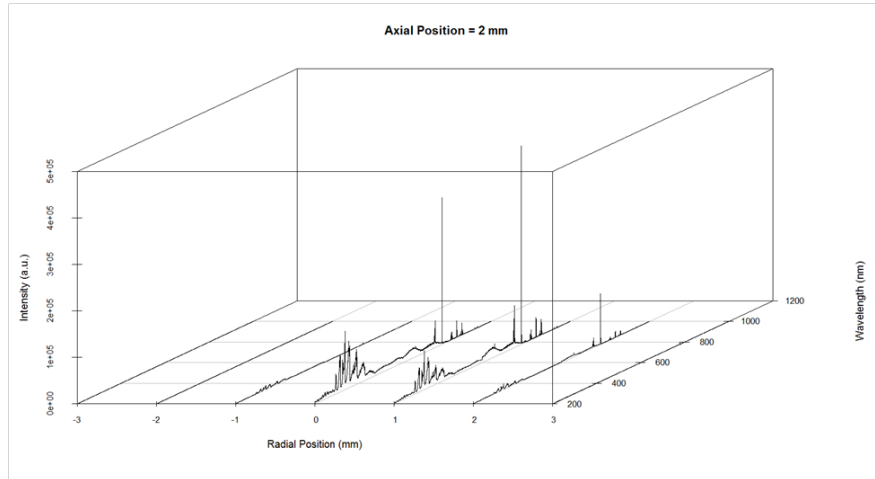


Figure 66: Radial OES spectra at an axial position of 2 mm.

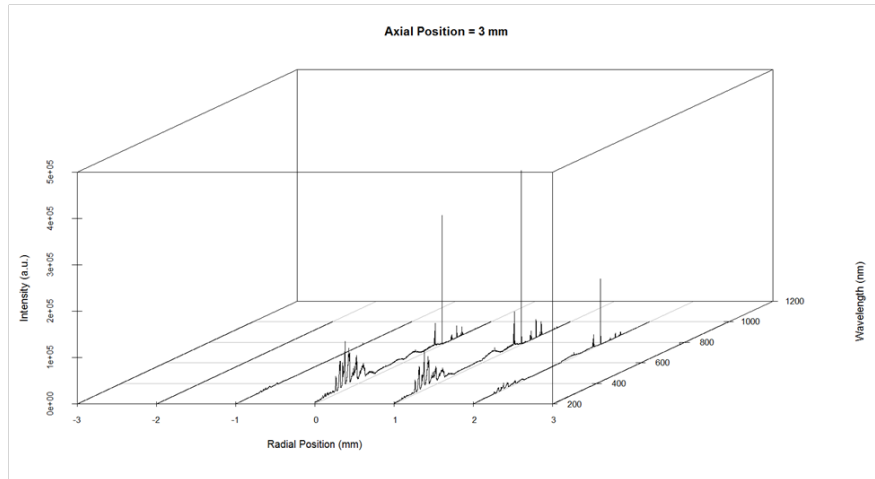


Figure 67: Radial OES spectra at an axial position of 3 mm.

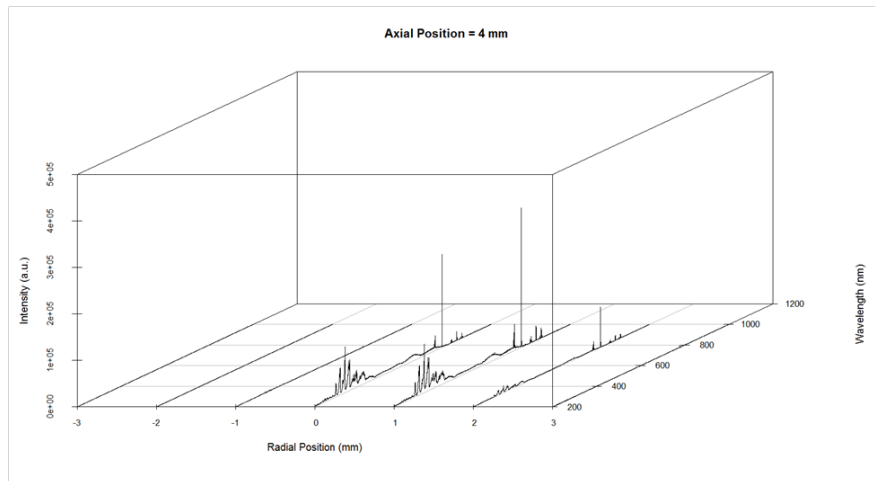


Figure 68: Radial OES spectra at an axial position of 4 mm.

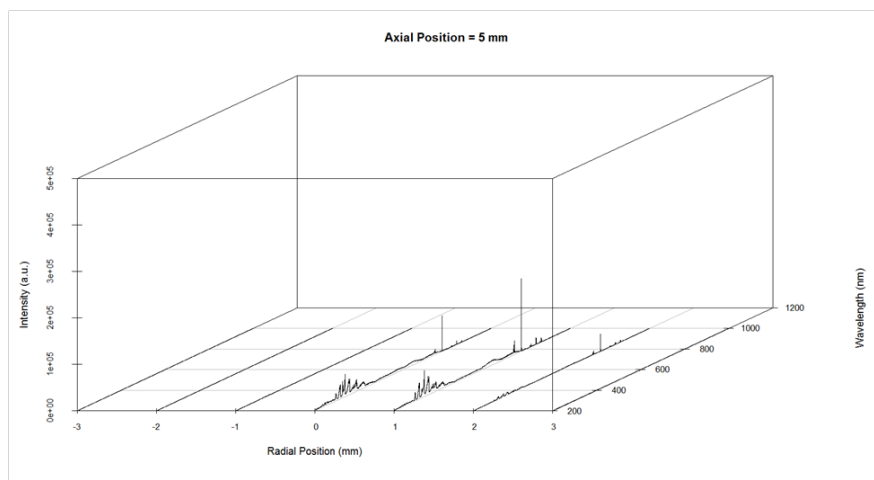


Figure 69: Radial OES spectra at an axial position of 5 mm.

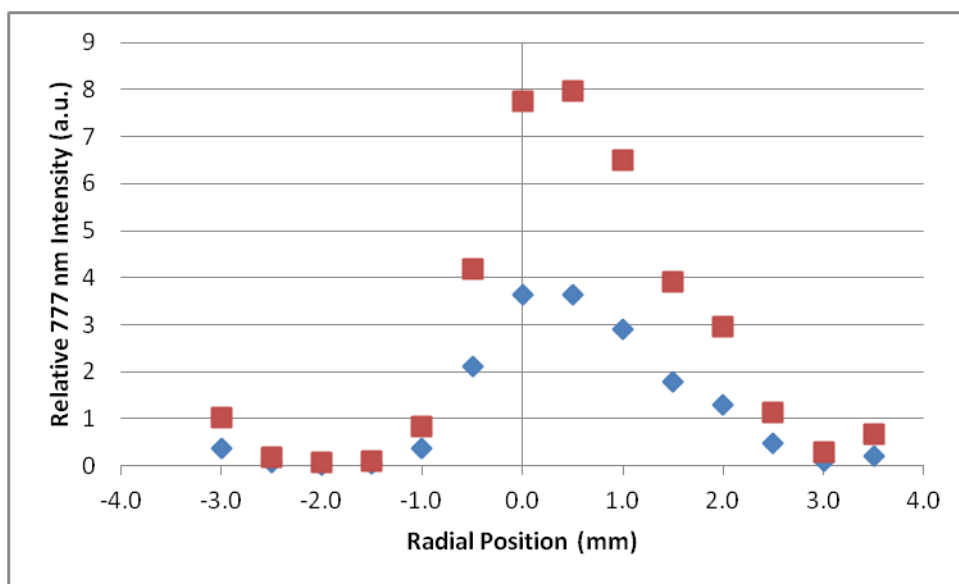


Figure 70: The radial distribution of the intensity of the 777 nm atomic oxygen line normalized to the N2 Second Positive System band head.

The center points of these radial profiles were compiled into an axial spectra distribution shown in Figure 72 with an apparently similar decrease of intensity, with respect to distance from the nozzle, for both the molecular and atomic species. However, relative atomic oxygen intensity decreases at a faster rate than the relative molecular nitrogen band heads as indicated in Figure 73 and Figure 74.

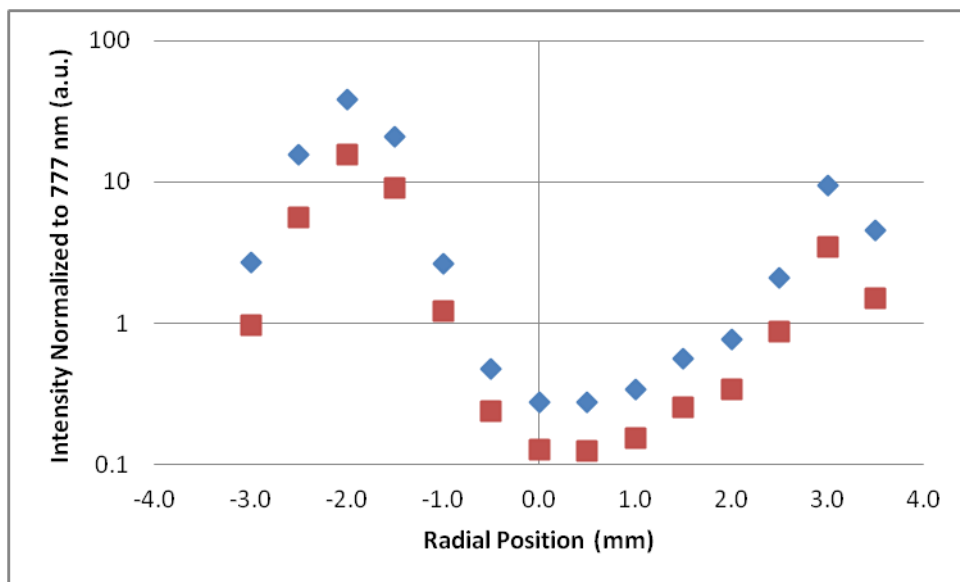


Figure 71: Radial distribution of the intensity of the N₂ Second Positive System band head.

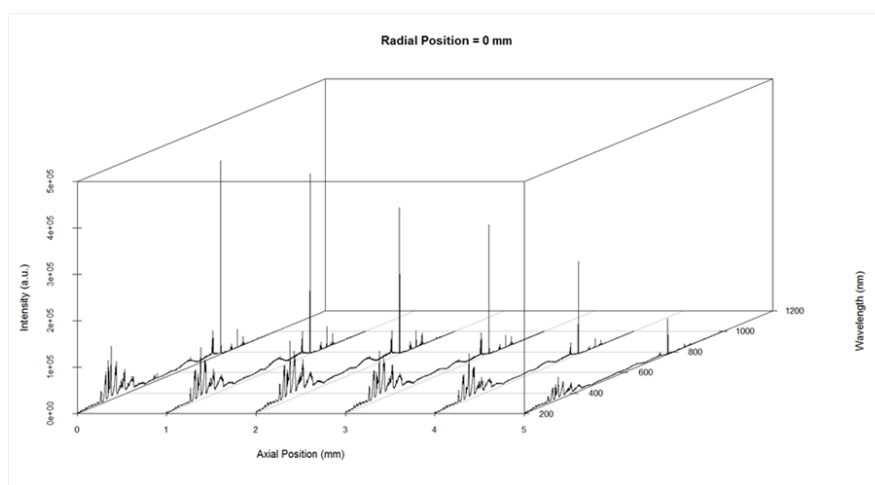


Figure 72: Axial OES spectra at a radial position of 0 mm.

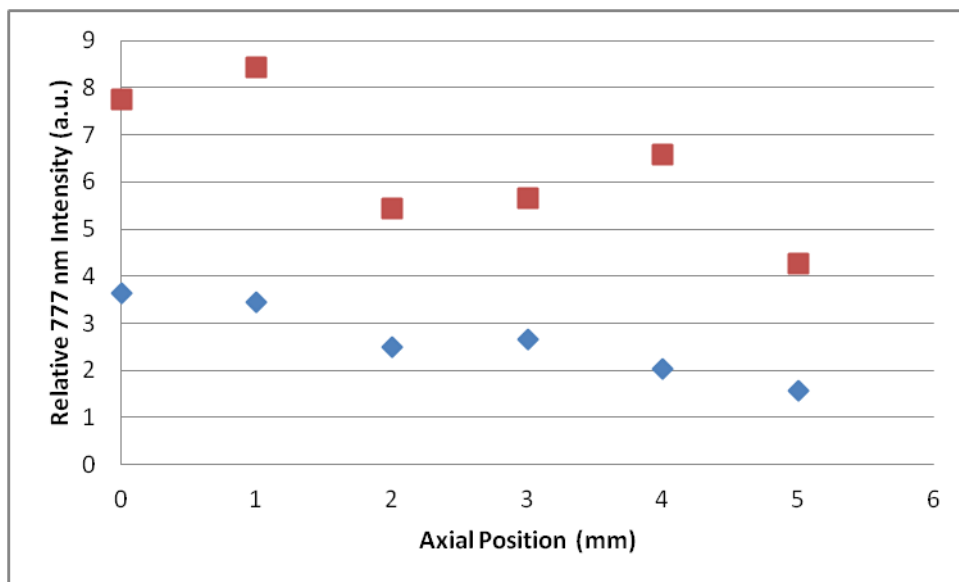


Figure 73: The axial distribution of the intensity of the 777 nm atomic oxygen line normalized to the N₂ Second Positive System band head.

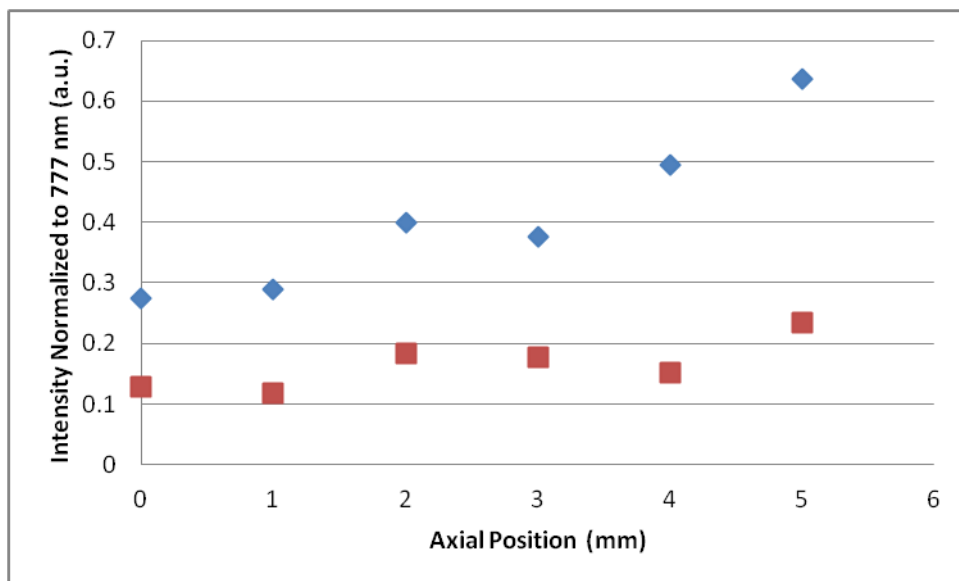
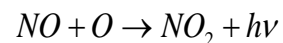


Figure 74: The axial distribution of the N₂ Second Positive System band head.

Another significant molecular species typically found in atmospheric air plasma is the NO_x group of compounds that is responsible for the ubiquitous greenish yellow glow [41]. It has been determined that the reaction constitutes the majority of the afterglow [42].

Equation 9. Oxidation of nitric oxide to nitrous oxide.



This nitrogen and oxygen chemical process produces a quasi-continuum emission spectra over a wavelength range of 400-900 nm. A maximum occurs near 620 nm arising from electronically

excited NO_2 molecules, while the long-wavelength range from 700-1200 nm is a result of the ‘thermal’ radiation of NO_2 molecules caused by collisional E-V excitation (molecular ${}^1\text{B}_2\text{-X}^2\text{A}_1$ electronic transitions), and the short-wavelength range from 400-600 nm is the ‘recombination’ radiation emitted by the $\text{NO}+\text{O}$ reaction. [43] The NO_x continuum is also denoted by a strong negative temperature dependence such that the intensity decreases with decreasing gas temperature, that generally correlates to farther distances from the plasma generation or nozzle, which agrees well with the rate of $\text{NO}+\text{O}$ radiative recombination [43]. It is assumed that this continuum is present in the afterglow region of the plasma torch given the similar plasma chemistry, apparent coloration, and the appearance of a broad continuum in the emission spectra as shown in Figure 75 [44]. These spectra were obtained in a separate experiment with a spatial resolution of approximately three mm, at a step size of two mm, and the number of averages and integration time normalized to three seconds. A qualitative comparison of the atomic O I 777.4 nm line to the ‘area-under-the-curve’ of the 400-600 nm range produced by Equation 9 is shown in Figure 76.

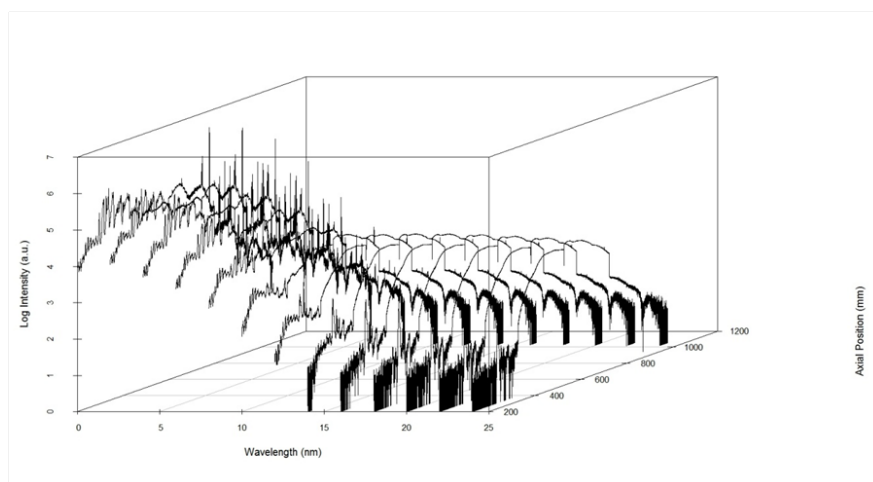


Figure 75: The log intensity of spectra over a wider axial range showing a decrease in the atomic and molecular nitrogen intensities and an increase in a broadband continuum.

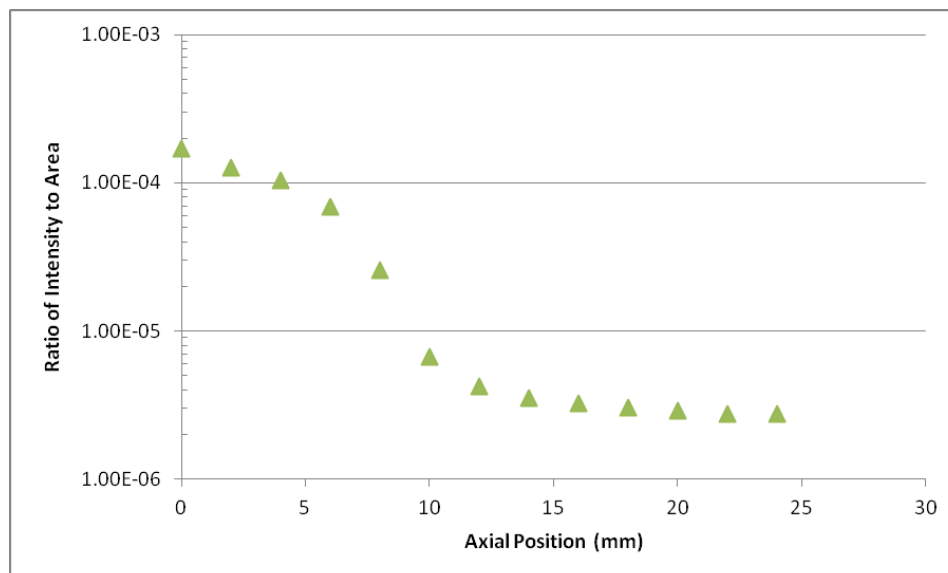


Figure 76: The ratio of intensity/area as a function of axial position.

3.2 CFD Modeling

The purpose of Computational Fluid Dynamic (CFD) modeling is to gain a more detailed understanding of the physical phenomena involved in generating plasma at atmospheric pressure and transporting the reactants to a surface where the coating removal process occurs. The ultimate goal of this effort is to learn how atmospheric plasma technology may be scaled to achieve production coating removal rates. The atmospheric plasma used in the coating removal process is clearly separated into two distinct regions which are characterized by different physical characteristics - the active region and the afterglow region.

The active region of the plasma pen is where an intense electric field generates the plasma and creates the reactive species required for the coating removal process. As the plasma exits the nozzle, the ionized flow transitions from subsonic to supersonic flow. The CFD model used in the active region should incorporate the following physics:

- Multiple species plasma fluid equations explicitly conserving mass, momentum, and energy
- Self-consistent electric field (Maxwell solver coupled to fluid equations)
- Chemical kinetics (source and sink of reactive species, volume and surface reactions)
- Flow transition from subsonic to supersonic

Plasma modeling is, for the most part, still considered a highly specialized field limited to the academic community. Specialized CFD code has been developed by academic researchers, but these are generally not openly available. We have only considered commercial software vendors in this study since application support is likely to be a key factor in establishing a CFD capability. Only three commercial vendors were found who offer a plasma modeling capability as a standard product. These models were not generally applicable to the unique plasma conditions in the active region of the plasma pen where compressible flow dynamics is augmented with a minority species which is electrically conductive.

In the afterglow region the plasma expands into a field free region. As the plume expands away from the nozzle, the plasma density and conductivity decreases rapidly and the flow decelerates from supersonic to sonic. Under these conditions conventional CFD models may be applicable. As in any modeling effort, it is unlikely that all of the relevant physical effects can be included in one model so the physical phenomena need to be carefully selected to capture the essential physics while maintaining tractability of the model. In order of importance, the afterglow plasma model should include the following:

- Multiple species fluid equations conserving mass and momentum and using an equation of state for closure,
- Flow transition from supersonic to sonic,
- Realistic treatment of fluid –surface interface (boundary layer) including turbulence and heat transfer,
- Chemical reactions including volume and surface reactions, and
- Particulates entrained in the plume due the removal process.

Most of these physical phenomena can be handled by the commercial CFD packages. Ideally, a three dimensional capability is required to incorporate the critical coating removal parameters such as pen height, angle, and raster speed. Particulate modeling will be an important consideration in developing a particulate collection system but would be of secondary importance in any initial modeling effort. Modeling of the active region would not be attempted with the commercial packages but might be handled very effectively by a careful implementation of the FAST3D package available through the Naval Research Laboratory described briefly below.

Commercial CFD packages

Commercial CFD packages, such as FlowEFD and FloXpress, are offered as an add-on feature to conventional CAD software packages like SOLIDWORKS and ProE. These CFD packages provide the simplest fluid models (in viscid, laminar, incompressible flows) and mostly serve as three-dimensional flow visualization tools, although some useful engineering problems can be competently modeled when these packages are coupled with a heat transfer calculation. Most commercial CFD packages offer full three-dimensional automatic meshing tools which create the model grid directly from CAD design files. Free-form grids are widely used to enable the modeling of very complex geometrical objects. Adaptive gridding is also offered where the grid resolution is changed during the simulation to maintain accuracy as complex flow patterns evolve. The inclusion of more realistic fluid phenomena such as viscosity, turbulence, and compressibility leads to increasingly more complex packages and increases in cost. In some cases, lower cost versions of a product offering are possible by reducing the geometric detail to Cartesian (fixed) grid or a reduction in the number of spatial dimensions.

ANSYS, Inc. 275 Technology Drive, Canonsburg, PA 15317
Available on 5/31/2011 at: <http://ansys.com/>

ANSYS, Inc. appears to be the market leader in commercial CFD software. The more general term of multi-physics modeling applies to the ANSYS packages since the modeling capabilities

cover such a diverse range of disciplines. Those capabilities specifically relevant to modeling the plasma plume include the interaction of fluids with moving surfaces (or in our case a moving source of fluid and stationary surface), chemical kinetics, turbulence, particulates, and heat transfer.

A computer system with a minimum of sixteen GB of RAM and multiple dual-core processors is required to run this software optimally. Purchase price for a CFD module with heat transfer is typically over \$50,000 and scales more or less linearly with the number of dual-core processors included in the license. ANSYS does offer lease options for approximately \$20,000 per year for a single seat, single dual-core processor. For contracts funded by the federal government, like SERDP, it is possible to get a GSA discounted rate which is typically 40% of the commercial rate.

Kinema, Inc.

During the search performed for this study, a 2000 press release was found on the web that states that ANSYS had acquired a small company called Kinema for its plasma modeling capability. The ANSYS representative that we contacted was not aware of Kinema or its acquisition by ANSYS. Attempts to contact Kinema personnel via phone and email were not successful so it appears the acquisition of Kinema's modeling capabilities did not result in an ANSYS plasma module.

Computational Particle Fluid Dynamics Software, LLC
10899 Montgomery NE, Suite A, Albuquerque, NM 87111
Available on 5/31/2011 at: <http://www.cpf-d-software.com>

CPFD's Barracuda engineering software package is a specialized CFD package which is dedicated to modeling fluid-particle flows and chemical reactions in industrial-scale fluidization applications. Barracuda is most commonly applied to fluidized applications where the solids volume fraction span the range from almost fully dilute up to densely-packed. This type of software package would be useful in modeling the plasma plume/substrate interaction especially in view of the nanoscale particles that are ejected in the coating removal process. Electrostatic charging of the fluidized particles and its effect on particle motion can be accounted for with this software package. Typical cost of the software package is \$50,000 per seat.

COMSOL, Inc.

Available on 5/31/2011 at: <http://www.comsol.com/>

The COMSOL Group also provides multiphysics modeling packages, though not quite as extensive as ANSYS. Comprehensive physics models are developed by integrating several specialized modules in a single package. For example, to model interaction of the plasma plume and a painted substrate, a package would include (at a minimum) the base system, which includes a preprocessor for mesh generation and a post processor for visualization, the CFD module, and a heat transport module. Cost for the entire package would be \$30,000 including a SOLIDWORKS interface for model generation from SOLIDWORKS files. COMSOL is unique in that they do offer a Plasma Module as a standard product which costs an additional \$10,000; however, it does not appear that the Plasma Module runs concurrently with the CFD module so the flow of plasma is not linked with a compressible fluid model for the neutral species.

ATK Mission Systems: MAGIC 8560 Cinderbed Road, Suite 700, Newington, VA 22122
Available on 5/31/2011 at: <http://www.mrcwdc.com/magic/index.html>

The fundamental engine of ATK Mission Systems' software suite MAGIC is a multidimensional electromagnetic Particle-in-Cell (PIC) code which provides a self-consistent treatment of kinetic plasma processes. The applications of this code appear to be primarily in the field of pulsed power devices where particle dynamics and electromagnetic field evolution is advanced on relatively short time scales. Despite the inherently time intensive nature of PIC simulations, some researchers have reported some success in modeling the interaction of an atmospheric plasma torch with a surface [45]. From the posted 2009 price list, a twelve month lease of the two-dimensional and three-dimensional packages costs \$22,500. The purchase price for the same package is \$44,500.

CFD Online: <http://www.cfd-online.com/>

CFD Online claims to be the largest and most popular CFD site on the Internet. The site does not appear to be frequently updated; many of the links were found to be obsolete. The most useful resources on this website include several discussion forums and a free CFD reference in the form of a CFD-Wiki. Two public domain or relatively inexpensive CFD software suites were found from this site including the codes supplied by the Open Channel Foundation and the Naval Research Laboratory CFD Computations Group.

Open Channel Foundation
<http://www.openchannelfoundation.org/>

The Open Channel Foundation (OCF) provides access to an extensive offering of engineering software that originates within academic and Federal Agency research labs. The software offered is either free or at prices significantly lower than commercial packages. A search for the keyword "CFD" returns a number of CFD related software. The most general package is a highly integrated, digital computer program called STARS (SStructural Analysis RoutineS), which was developed by K.K. Gupta of the NASA Dryden Flight Research Center. STARS contains much of the relevant physics including compressible subsonic and supersonic flows, general geometry and boundary conditions, and heat transfer. STARS has its own automatic two-dimensional and three-dimensional unstructured grid generation and interfaces with pre- and post-processing software. The source code is in Fortran. The compiled software runs on Windows-32 and Windows-64 based PCs. The cost for the STARS module is \$2,000 and is available to US citizens only.

Naval Research Laboratory
FAST3D CFD Package – Flux corrected transport algorithms
<http://lcp.nrl.navy.mil/cfd-cta/CFD1/#TestCas>

FAST3D is another general CFD package made available to US citizens by the Naval Research Laboratory. This package provides a software suite for modeling multidimensional reactive flows in complex geometries. The FAST3D package includes a complex geometry grid generator

(GRIDVCE), a parallel flow solver FAST3D, and a visualization package PLOT3D. FAST3D is a general purpose CFD package for solving time-dependent, compressible flow problems in three dimensions with moderate flow speeds ($0.2 < M < 5.0$) based on the high resolution Flux Corrected Transport (FCT) algorithms invented and developed at the Naval Research Laboratory [46]. The software is extremely well documented, including a user's manual, sample problem code listings (Fortran), and guidelines for incorporating user-specified, time-dependent source terms and chemical reactions in the flow.

Recommendations for CFD Modeling

Aside from the public domain code options, the lowest cost point of entry to CFD modeling may be through the ANSYS offering of a software lease at the GSA discounted rates. This would provide access to a very powerful multi-physics package and application support. The public domain/low cost federal agency codes are available at lower cost (or no cost), but the lack of applications support may be an issue.

To ensure the success of any CFD modeling effort, it is recommended that the problem be carefully formulated before deciding on any particular software package. The basic steps in formulating the problem include, but are not limited to, the following:

1. Define the problem geometry including the flow field and surfaces where fluid interactions are important. The fluid source function must include some realistic model of the plasma plume (orientation relative to the substrate, gas temperature, chemical energy contained in reactive species, flow velocity, etc.). Most of these parameters are not known in detail, but will have to be estimated based on measurements of test case situations against which the model may be calibrated.
2. The initial flow variables at every point in the computational domain should be defined including the number of chemical species and the relevant chemical kinetics for each species. Appropriate boundary conditions need to be specified and applied at the solution domain boundaries. The coating removal process involves a moving boundary. The CFD package should allow for moving boundaries to capture the effect of gross surface morphology changes as the coating is removed.
3. User defined sources and sinks of the various species either due to volume or surface reactions need to be incorporated. One example of this would be the introduction of new species (e.g. ejecta) at a material surface based on a chemical kinetics model of the paint/plasma plume interaction.
4. The spatial grid parameters defining the computational domain must be specified as an initial input to the automatic meshing routine.
5. Define the post processing requirements including the frequency, spatial locations, and physical variables that should be output, either numerically or graphically. User defined metrics, such as mass removal rates, should also be defined.

We suggest that these five general features of defining the CFD problem relevant to paint removal be determined via a group discussion following the completion of the Design of Experiment Task. Defining the goals of the effort with a complete understanding of what questions we wish to answer with CFD modeling will ensure an efficient use of the team's resources.

NCSU recently obtained access to the ANSYS multi-physics modeling software. The purpose of this task was to assess the capabilities of the ANSYS software for simulating the atmospheric plasma coating removal process. The ANSYS software combines modeling capabilities from a variety of disciplines including structural mechanics, heat transfer, fluid dynamics, and electromagnetics into a single unified package. The use of common geometrical model and meshing capabilities enables the user to combine whatever analysis packages are needed for a specific project. An initial review of the extensive ANSYS documentation package indicates that ANSYS contains most, if not all capabilities for modeling the atmospheric plasma coating removal process. Following is a brief description of the key physical phenomena which need to be incorporated in a simulation of the AP coating removal process and the identification of ANSYS modeling capabilities which can enable the inclusion of these phenomena.

ANSYS FLUENT Model Capabilities

Fluid dynamic phenomena are at the heart of the AP coating removal process since a stream of activated gas is directed at high velocity toward the surface being treated. ANSYS offers two Computational Fluid Dynamic (CFD) solver packages that can be applied to simulating this process - ANSYS FLUENT and ANSYS CFX. These two solvers differ mainly in the methods of discretizing and integrating the fluid flow equations and in their equation solution strategies. The ANSYS FLUENT appears to be more flexible in that it offers several solution approaches to cover a wide range of incompressible and compressible, laminar and turbulent fluid flow problems. The difference between the two packages appears to be largely one of user preference. We have decided to focus on ANSYS FLUENT at this point; however, this does not preclude the use of ANSYS CFX in the future since the two modules appear to be readily interchanged.

In any model development effort, one generally begins with the simplest geometric configuration and physical phenomena that is representative of the experimental configuration. At each stage of development the model needs to be benchmarked against experimental observation to test the accuracy and predictive capability of the model. More realistic geometries and inclusion of more physical phenomena may be incorporated in a progression of models of increasing complexity. The key to success will lie in being able to capture the essential physics while minimizing the complexity of the model. Model complexity translates to computer memory usage, CPU speed and execution time; the model should remain tractable so that useful information can be obtained with a reasonable commitment of resources.

Compressible Fluid Flow

The atmospheric plasma generated by the APS system is a weakly ionized, highly collisional plasma where the flow dynamics is dominated by the neutral gas in which the plasma is entrained. Large variations in the gas pressure and density become significant at the high velocities attained by the compressed air flow in the plasma pen. The importance of compressible effects is characterized by the Mach number which is the local ratio of the fluid velocity to sound speed. Compressible effects are negligible at subsonic speeds ($M \ll 1$) and become more important as M approaches unity. Supersonic flows ($M > 1$) may give rise to localized shock structures which pose significant challenges in a discretized model.

Modeling compressible flows requires the solution of the conservation equations of mass, momentum (3 components), and energy. The Navier-Stokes equations and the ideal gas law form a closed system of coupled equations which give rise to numerical instabilities that require multiple solution strategies to achieve a converged solution. ANSYS has taken advantage of the significant progress made in the last two decades in dealing with these numerical instabilities. In addition, ANSYS has full multigrid solution capabilities which can be used to optimize the solution initialization for more rapid convergence.

High Reynolds Number Flow

The Reynolds number, Re , is the ratio of inertial force to viscous forces for a set of flow conditions,

Equation 10. Description of Reynolds number.

$$Re = \frac{\rho VL}{\mu},$$

where ρ is the fluid density, V is the fluid velocity, L is a characteristic length of the flow (e.g. nozzle diameter, length of boundary layer, surface roughness), and μ is the dynamic viscosity. The Reynolds number for the flow exiting the plasma pen is in excess of 5000 so one would expect the fluid flow to exhibit chaotic behavior over a wide range of spatial and temporal scales. Under these circumstances, the Navier-Stokes equations are replaced by a simplified set of equations which describe the average flow field supplemented by a “turbulence model” which represents the effects of the turbulence scale flows.

Selection of an appropriate turbulence model is one of the key elements of the CFD modeling process. ANSYS provides a collection of turbulence models that includes those most commonly used in industrial applications where the need to capture the physics of a specific application is balanced against computational resources and time. There are several models which appear to be suited for specific aspects of the plasma pen flow, such as eddy viscosity models for free shear jet, wall bounded mixing length theories for the plasma plume-substrate region, or Reynolds Stress Models where features such as streamline curvature stabilizes against turbulent behavior. A review of the literature will be required to determine which turbulence model is best suited for our application.

Heat Transfer to the Substrate

ANSYS has the capability of calculating the substrate surface temperature during the coating removal process by calculating the heat conduction from the fluid through the material wall interface and the conduction of heat away from the surface within the material. Heat transfer from the plasma plume occurs by two mechanisms - direct thermal contact of the fluid with the substrate surface and thermal energy delivered to the surface by chemical reactions occurring on the surface. In ANSYS, heat flux at the substrate surface is introduced to the material via a thermal boundary condition that drives a thermal analysis package to calculate conduction away by the surface. Chemical energy can also be introduced through a “Species boundary condition” for inclusion of surface reaction mechanisms. The transport of chemical energy from the plasma pen to the substrate may be possible through the implementation of the ANSYS Chemkin (Chemical kinetics) package and multiple fluid species. Increasing the number of fluid species will lead to increased computation time due to the increase in the number of equations that need to be integrated.

Plasma Pen Rastering

The plasma pen rastering motion complicates the CFD model in that the fluid flow is inherently unsteady. This adds an additional iterative process where the solutions are advanced in time as the position of the pen relative to the sample substrate is changed. Execution time for the model will be increased since a change in the pen position relative to the substrate requires the grid to be continually updated. ANSYS can handle this situation through its dynamic and sliding mesh features. Execution time to time-advance the solutions and periodically update the grid could be significantly increased with this capability.

Particulate Production

Inorganic solids from the coating removal process are released as particulates that must be safely collected. A waste capture system will be an important feature of an AP coating removal system. A CFD model of the plasma/substrate flow pattern with particulate generation could be used to assist in the design of a waste recovery manifold. ANSYS does have a particulate generation capability; however, some investigation is required to determine if this capability is compatible with compressible flows and the implementation of turbulence models. Overall, ANSYS seems to provide the capabilities needed to model the plasma plume/substrate interaction. Estimates of the impact of including these various phenomena will be made as the modeling activity progresses to determine future computational requirements.

Fixed Flow Analysis CFD Model

An ANSYS “seat” was installed on a desktop computer that meets the minimum system requirements for RAM, disk storage, and CPU speed. This computer is adequate for familiarizing APS and NCSU personnel with the capabilities of ANSYS; however, with demands for increased modeling capabilities, such as increased memory or processor speed due to increased mesh size or inclusion of additional physical phenomena, it may be necessary to transition the model to a higher performance workstation.

Once issues associated with the software license and hardware incompatibilities were resolved, progress was made in going up the “learning curve” with the aspects of executing an ANSYS project including user interface, model importation and editing, mesh generation and refinement, solution setup, and initialization and selection of solution strategies. User training is a significant consideration. Although the interface is easy to use, there are multiple opportunities for running the software incorrectly. The ANSYS software seems very stable and not prone to frequent crashes. The process of developing a model in ANSYS generally involves the following steps: Geometry, Mesh, Setup, Solution and Post processing.

Geometry

To get started with setting up a basic CFD model, a SOLIDWORKS model of a converging/diverging nozzle is generated as shown in Figure 77. A simple converging/diverging nozzle is used to generate a supersonic flow. This was imported into the ANSYS Design Modeler module. A converging/diverging nozzle similar to this will eventually be used as a means for launching supersonic plasma at a flat surface. The simple model here was used just to gain familiarity with obtaining solutions for the simplest flow situations - steady, viscous, laminar flow for the case of incompressible and compressible fluid.

Meshing

The next step after importing a geometry model in ANSYS is the process of generating the mesh on which the model equations will be discretized. For the most part, the mesh generation step is automatic, though the process of refining the mesh does require input from the user that will be model specific. The mesh shown in Figure 78 is a volume filling tetrahedral mesh used to discretize the Navier-Stokes equations filling the interior volume of the nozzle. This mesh was refined once for finer resolution, resulting in a mesh consisting of approximately 5000 tetrahedra. Computation time generally increases with the number of nodes or cells used in the discretization process as well as the specific solution method chosen. Fine meshing minimizes discretization errors at the expense of increased computation time and RAM requirements.

Setup and Solution

In the Setup step, the model information such as materials properties, boundary conditions, solution methods, and convergence criteria are established. The solution process is started with an initial “guess” of the solution derived from the selected boundary conditions. The incompressible flow problem was found to be very easy to set up and execute with a converged solution obtained after 20 seconds of execution time. Contours of axial fluid velocity in the converging/diverging nozzle are shown in Figure 79. Note: fluid accelerates then decelerates through the Venturi nozzle. Also note the boundary layer at the wall surface while the fluid velocity vector is shown in Figure 80. The axial velocity contours show an increase in the velocity as fluid enters the nozzle throat and then decreases as the throat expands. This is the expected result so the next step was to turn on compressibility.

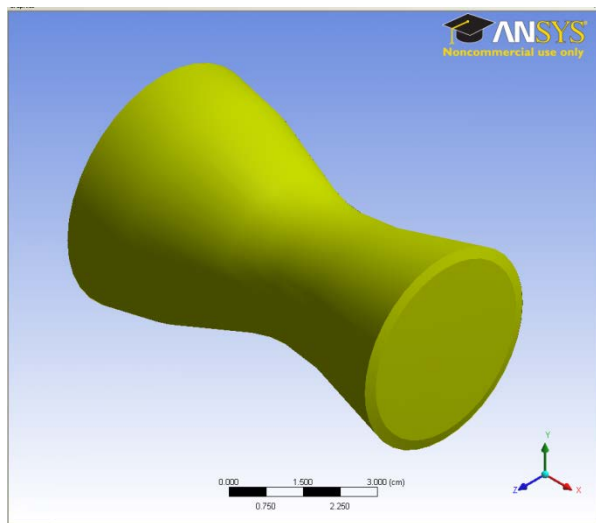


Figure 77: A simple converging/diverging nozzle is used to generate a supersonic flow.

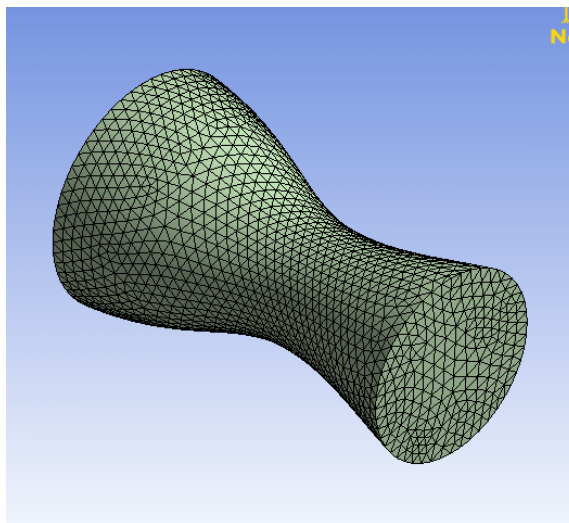


Figure 78: Volume filling tetrahedral mesh used to discretize the Navier-Stokes equations.

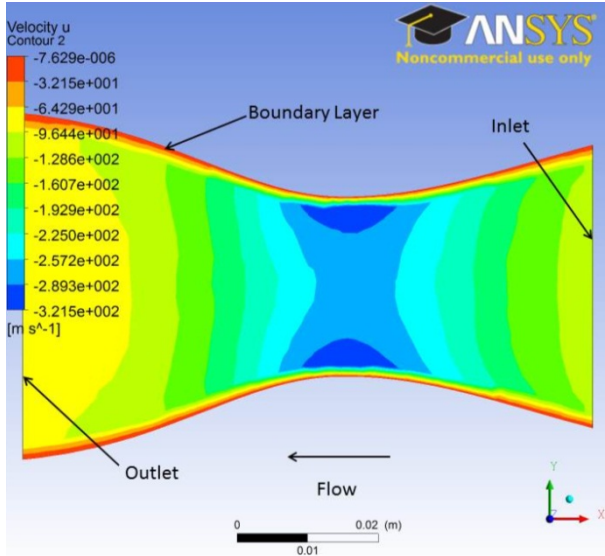


Figure 79: Velocity contours for incompressible fluid in converging/diverging nozzle.

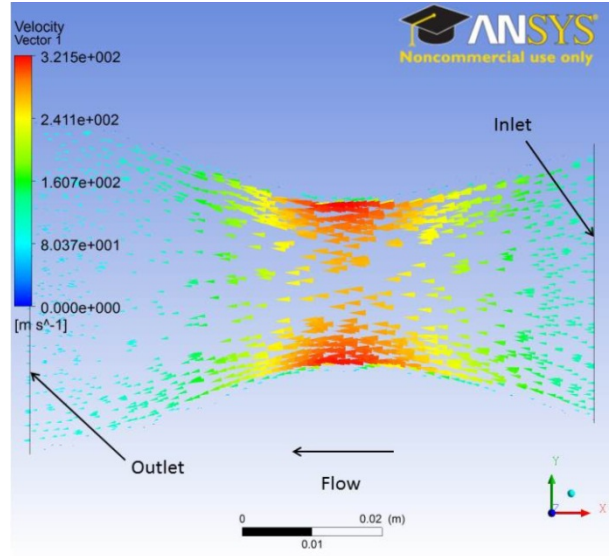


Figure 80: Velocity vector plot for incompressible flow in converging/diverging nozzle.

Compressible Flow Model

Compressibility is turned on in ANSYS by simply specifying “Ideal Gas” for the fluid and adding the energy equation to the system of equations. However, initializing the solution and choosing the best method of solution for a compressible flow problem is not straight forward. Manual initialization of the flow problem resulted in extremely slow convergence or, in the worst cases, divergence of the solution. Fortunately, ANSYS does provide a “Solution Steering” option for initializing the compressible flow solutions. The fluid velocity and density contours for compressible flow through the nozzle are shown in Figure 81. A simple converging/diverging nozzle is used to generate a supersonic flow. Fluid is sonic ($M=1$) at the throat so fluid accelerates continuously from right to left. Density contours for compressible flow in Figure 82, show reduced density from right to left as fluid density accelerates.

Notice that as the fluid flows from right to left, the fluid velocity increases continuously with the concomitant reduction in the fluid pressure. Even with the “Steering Solution” method, convergence to a solution is relatively slow, requiring over a minute to execute.

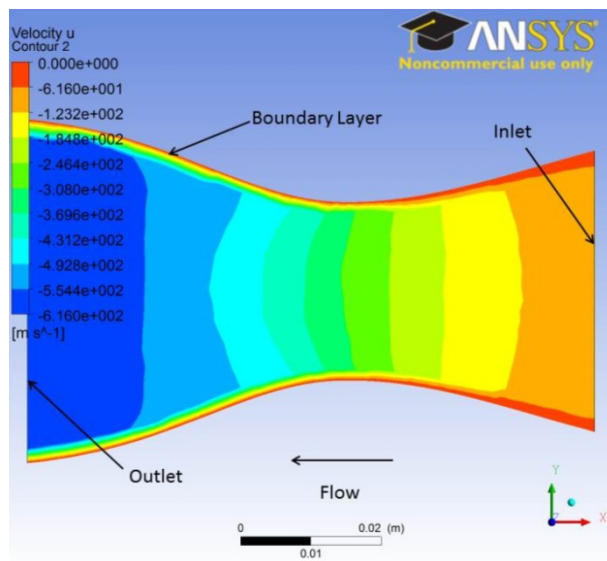


Figure 81: Velocity contour for compressible flow.

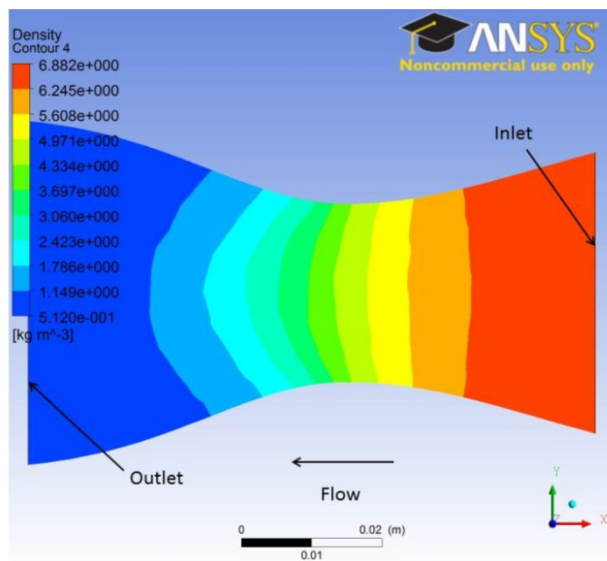


Figure 82: Density contours for compressible flow, flow from right to left showing reduced density as fluid accelerates.

Work Status

Work intended to complete this task included a study of exit nozzle shape on the plasma plume structure, as well as a realistic model of the plasma pen operating at a standard set of conditions (e.g. 135 slm at 500 kPa). A simple experiment was intended which consisting of a neutral gas jet striking a plate. Results were to be compared to measurement of pressure profiles versus predictions of the CFD model.

- Gain an understanding of physical phenomena generating plasma at atmospheric pressure (internal to plasma source)
- Understand transport mechanics of reactants to a surface (external to plasma source)
 - ◆ Active region with intense electric fields and reactive species
 - ◆ After glow region of reduced activity
- Design flow transitions as desired from subsonic to supersonic.
- Attempt to understand these effects on coating removal, ability to control near surface interactions, and ejecta removal
- Use this knowledge to aid in scale-up of plasma designs
- After literature review, ANSYS was selected for evaluation.
- CFD work has been suspended due to budget constraints, time to complete, ANSYS accessibility, and man-hours needed.

Due to budget, time, manpower constraints, and considering the overall objective of the project and value of each task, it was decided to put the remainder of this task on hold.

3.3 Photographic and Electrical Studies

Due to the lack of access to electrical components in the power supply and applicator head and proprietary content, the Plasma Flux system was not available for taking electrical measurements and other modifications for exploring the capabilities of atmospheric plasma. In response, Dr. Hudak used literature and patent sources to design an in-house system referred to as the Plasma

Vortex design. Several different sources were also available to provide power for this system. One such supply unit used in this research was an AIR-DBD-5000 Plasma Power Supply manufactured by AP solutions that was originally intended for a dielectric barrier discharge (DBD) type plasma. With slight modifications to the configuration, the supply was re-purposed for torch style research. The device has a usable frequency range of ~ 30-160 kHz. This device differs from the standard devices in that the step-up transformer is a separate exterior device.

This ‘in-house’ plasma torch was dubbed the Plasma Vortex and a schematic is shown in Figure 83. The side, front, and rear isometric views of the actual device as manufactured are shown in Figure 84 with the individual components shown in Figure 85.

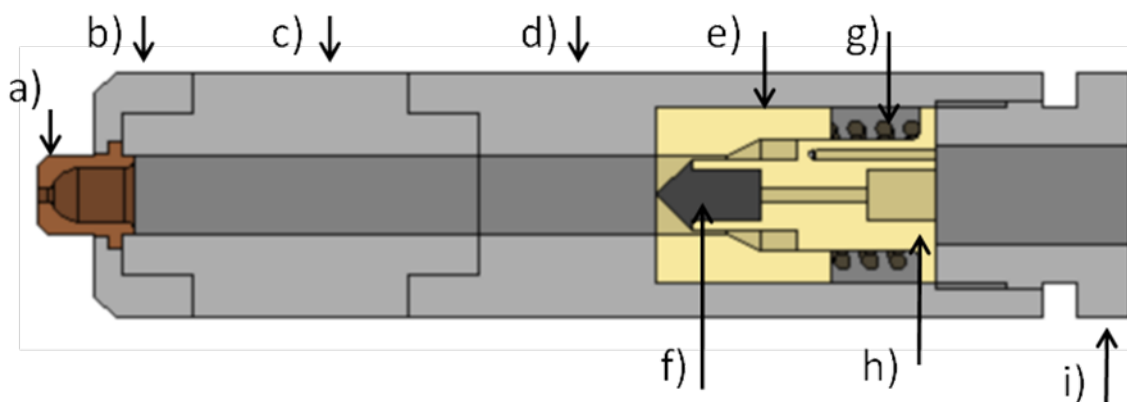


Figure 83: A schematic drawing of the Plasma Vortex torch with components of a) nozzle, b) nozzle retaining nut, c) barrel length extender, d) primary barrel, e) dielectric spacer, f) electrode, g) spring, h) dielectric electrode holder and gas delivery, and i) end cap.

The Plasma Vortex has many features suitable as a research tool. Since it is modular in construction, many of the components can be changed in both material and geometry with minimal effort. The nozzle (a) is easily modified or replaced by different designs. The electrode (f) can and has been made of different materials such as copper, graphite, Ni alloys, brass or other materials, and the geometry is easy to configure. Conical, hemispherical, cylindrical and hollow versions have already been manufactured. The barrel length (c) is easily adjusted with a different insert. Due to the spring design (g) and dielectric spacer (e) electrode gap distance (e) to (d) can easily be adjusted.

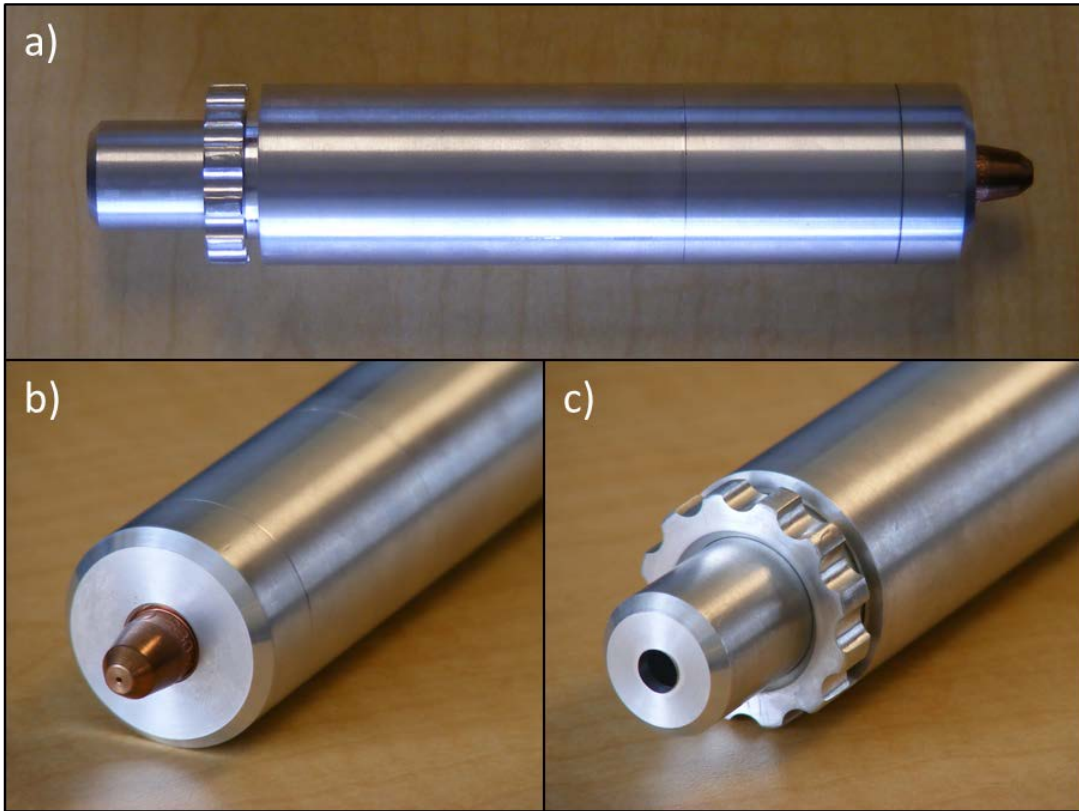


Figure 84: The Plasma Vortex shown in a) side view, b) front isometric, and c) the rear isometric view.



Figure 85: Major components of the disassembled Plasma Vortex.

Figure 86 contains photographs of various plasma plumes generated from torch type designs. Photos A) and B) are from the Plasma Flux system, while all the others are from the Plasma Vortex. In each case a different configuration was used by varying the geometry or materials and inputs to the applicator such as power or flow.

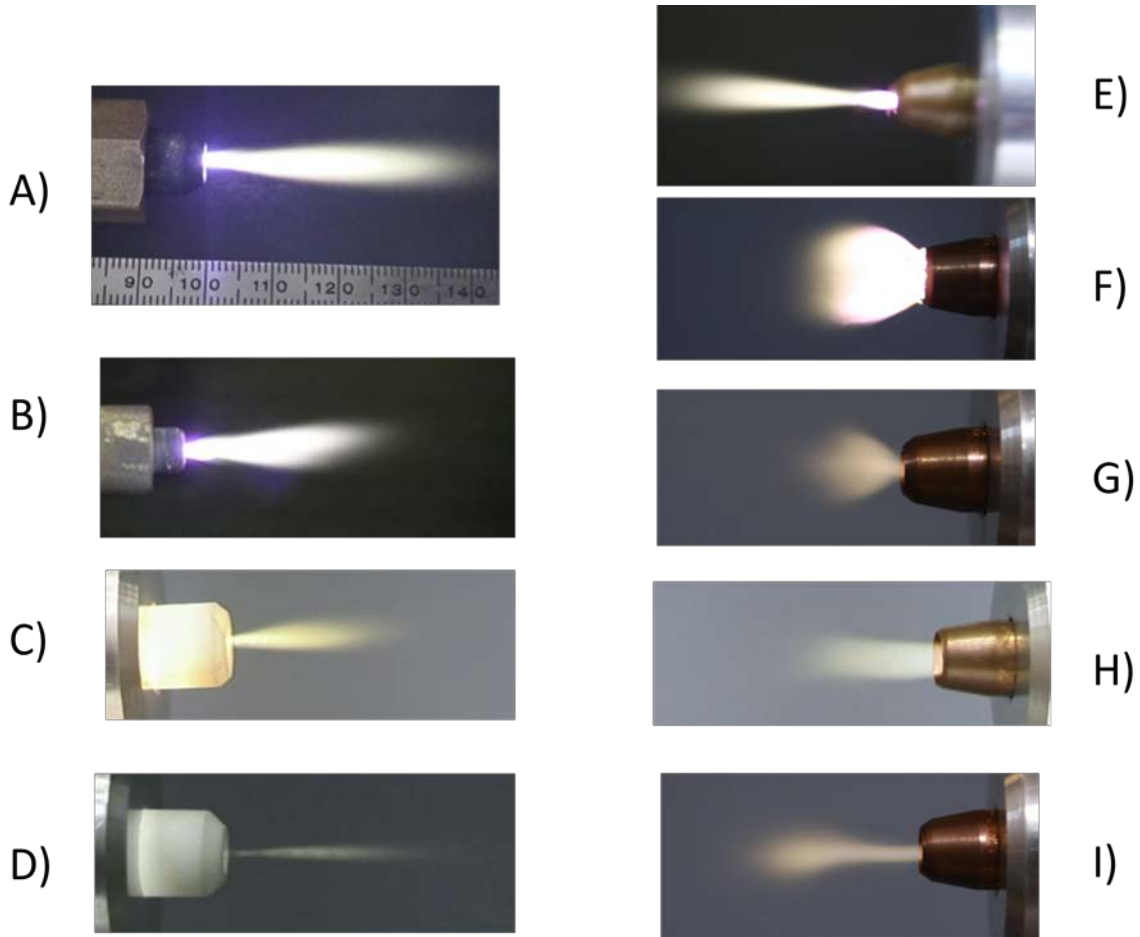


Figure 86: Plumes created by various flow, power, frequency, nozzle geometry and materials.

As stated previously it was not practical to make electrical measurements on the PF5K so measurements were conducted using the Plasma Vortex. Typical current and voltage spectra for the described torch are shown in Figure 87 depicting a periodic waveform. The I/V waveforms are nearly in phase with each other indicating a resistive type of plasma discharge. From these data, it was calculated that the RMS power is 598 W and the resistance across the plasma is 2 k Ω . One notable feature is the voltage spike during the initial rise or drop in potential. This feature has been hypothesized as a result of the increased potential needed to begin the gaseous breakdown process for either the primary arc column or one of the secondary arcs. As well, it could simply be an artifact of the power supply capacitor discharging. Further characterization and analysis is needed; however, this work will be left to the manufacturer as it may involve proprietary information.

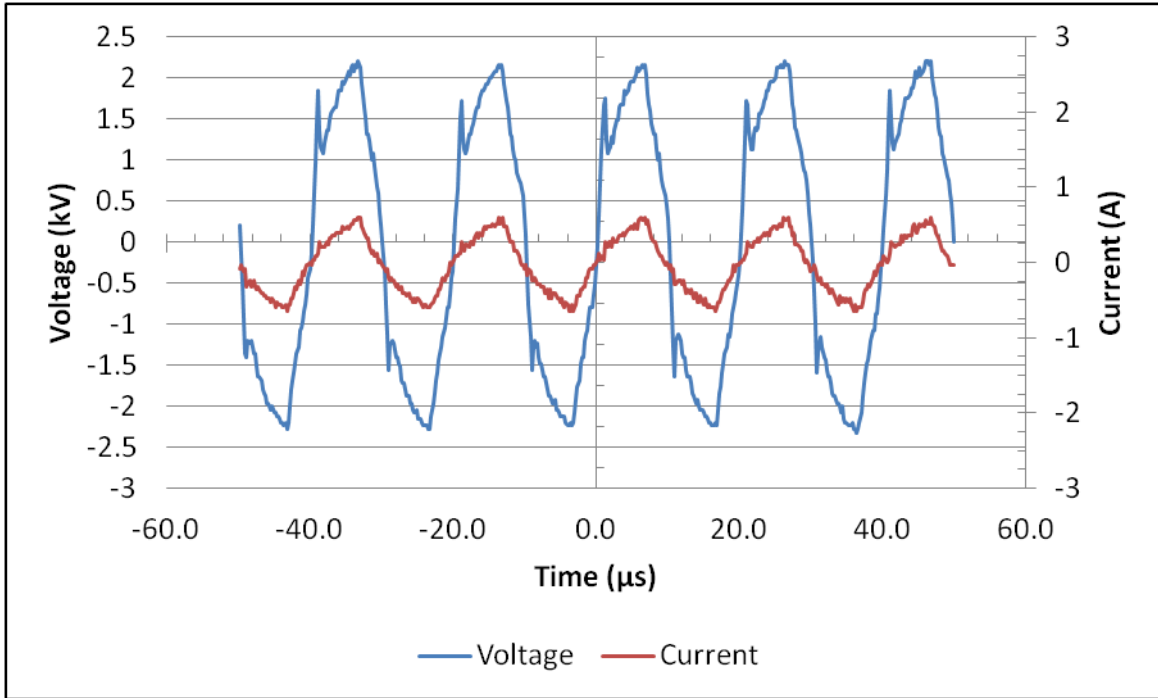


Figure 87: I/V characteristics of the Plasma Vortex operating at 50 kHz and 50 slm with a RMS power of 598 W and resistance of 2 kΩ.

Another feature of the Plasma Vortex is the ability to perform computer simulations, such as fluid flow modeling. An example of one such experiment is shown in Figure 88. This particular example, which is also available as a video, illustrates how the air velocity near the electrode is high, which decrease as it travels down the barrel, then accelerates rapidly at the nozzle exit. Without having to manufacture and test, a wide range of conditions can be generated and optimized.

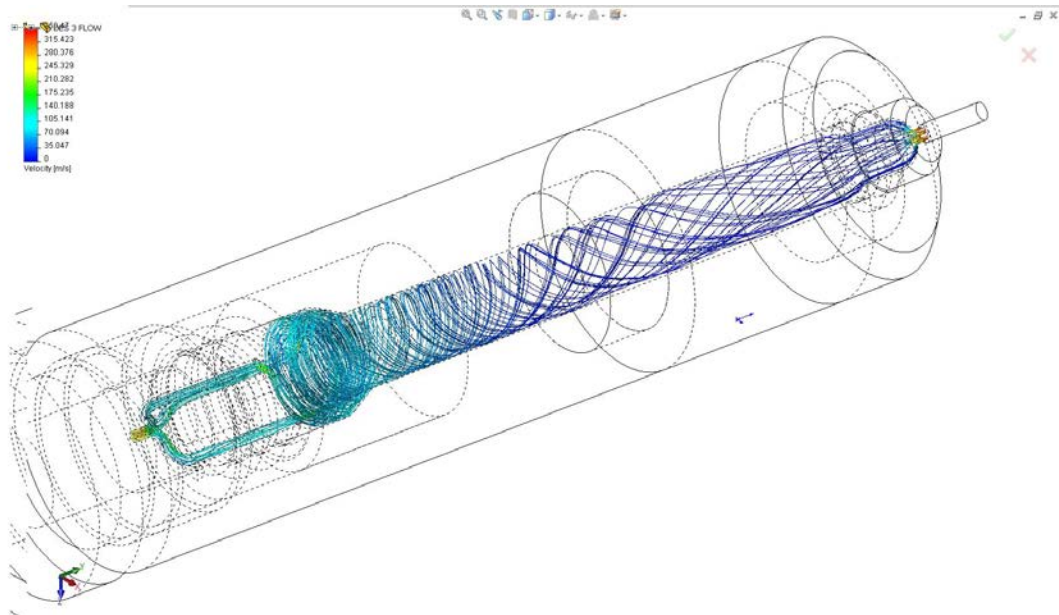


Figure 88: Fluid flow modeling from the SOLIDWORKS model using FloExpress software.

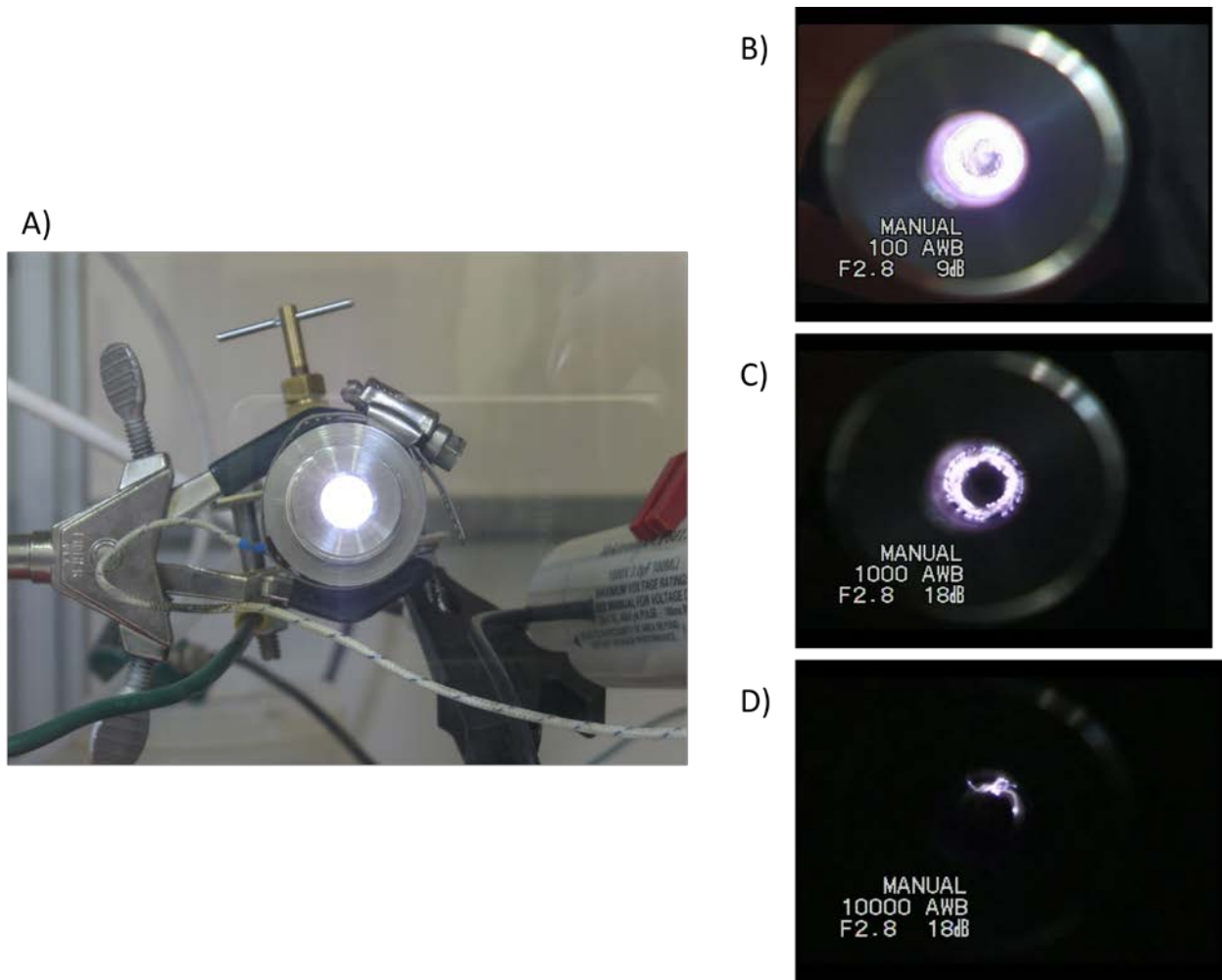


Figure 89: Operation of the Plasma Vortex with free exhaust expansion.

Another feature of the Plasma Vortex allowed for operation in partially assembled condition in order to investigate characteristics of the plasma. As seen in Figure 89, the plasma is generated inside the barrel of the device. A high speed camera was used to record plasmas and the shutter speed slowly increased to a maximum of 10,000 frames per second. Under normal operation as seen in A), the intensity and frequency of the plasma renders it unobservable by eye. Slowly increasing the shutter speed of the camera effectively reduces intensity and captures fewer cycles of the VHF. Using 30 kHz excitation and a 1/10,000 second shutter speed, the image shown in D) would contain only three cycles of the waveform used to generate plasma.

A practical example of this technique is illustrated in Figure 90. In A) the actual voltage of a 120 kHz generator was displayed (in blue). By using a pulse generator synchronized to a high speed CCD, the shutter on the camera could be tripped at any given point in the waveform. The overlay in A) shown in red are discrete points where the shutter was triggered and an image captured. In the case of the IR camera, the shutter was limited to about one millisecond. However, by using a high speed camera, pico-second time frames may be captured. These results indicate it is possible to observe the plasma generated during a specific part of the

waveform. This information is very valuable in designing plasmas systems, especially with today's digital and semiconductor technology.

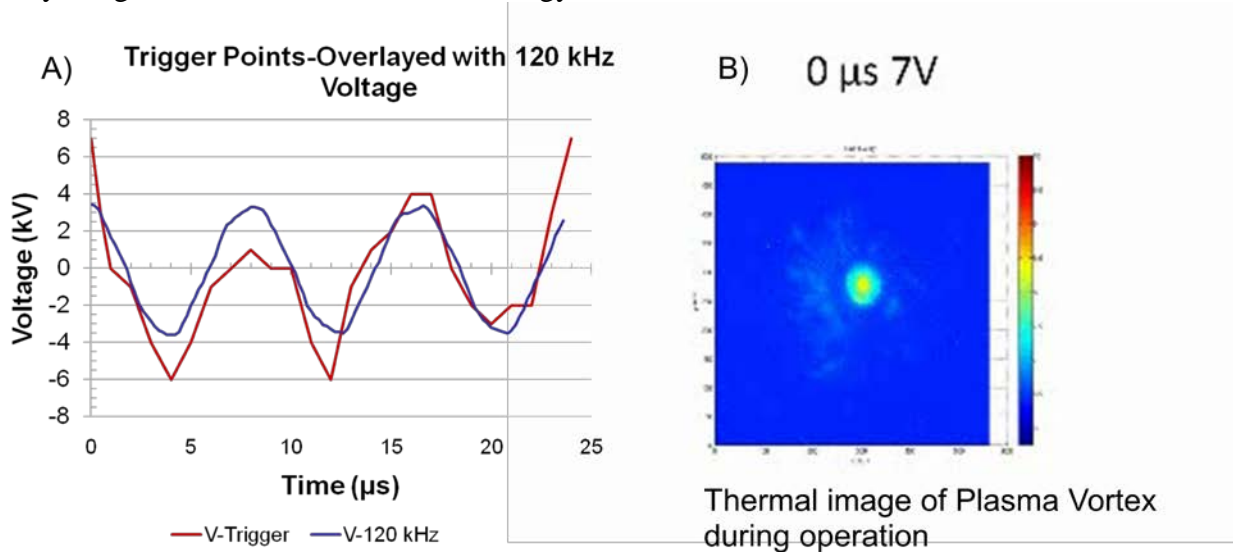


Figure 90: Example of use of high speed photography coupled with a pulse generator to trigger the shutter on a high speed infrared camera.

One of the discoveries made independently at NCSU is the observation or generation of mach discs. Figure 91 shows a series of photographs illustrating mach discs in the plasma plume. A), D), and F) were generated using the Plasma Vortex using different stimulation conditions and nozzle designs. The shape of the plasma plume, the position of the mach discs, and the shape of the mach discs can be controlled using fundamental principles of fluid flow. The image in E) is from the Plasma Flux used in this research. The image in B) is an infrared photo of the Plasma Flux. The graph in C) contains a plot of temperature in C versus distance from the exit along Line 1 shown in B). Although the true temperature of the plasma is not known, since its emissivity is not known, what the thermal plot shows is a maximum temperature at each of the mach discs and a slow decay as the distance from the nozzle increases. The phenomenon of mach discs is well known and further information can be found at www.aerospaceweb.org.

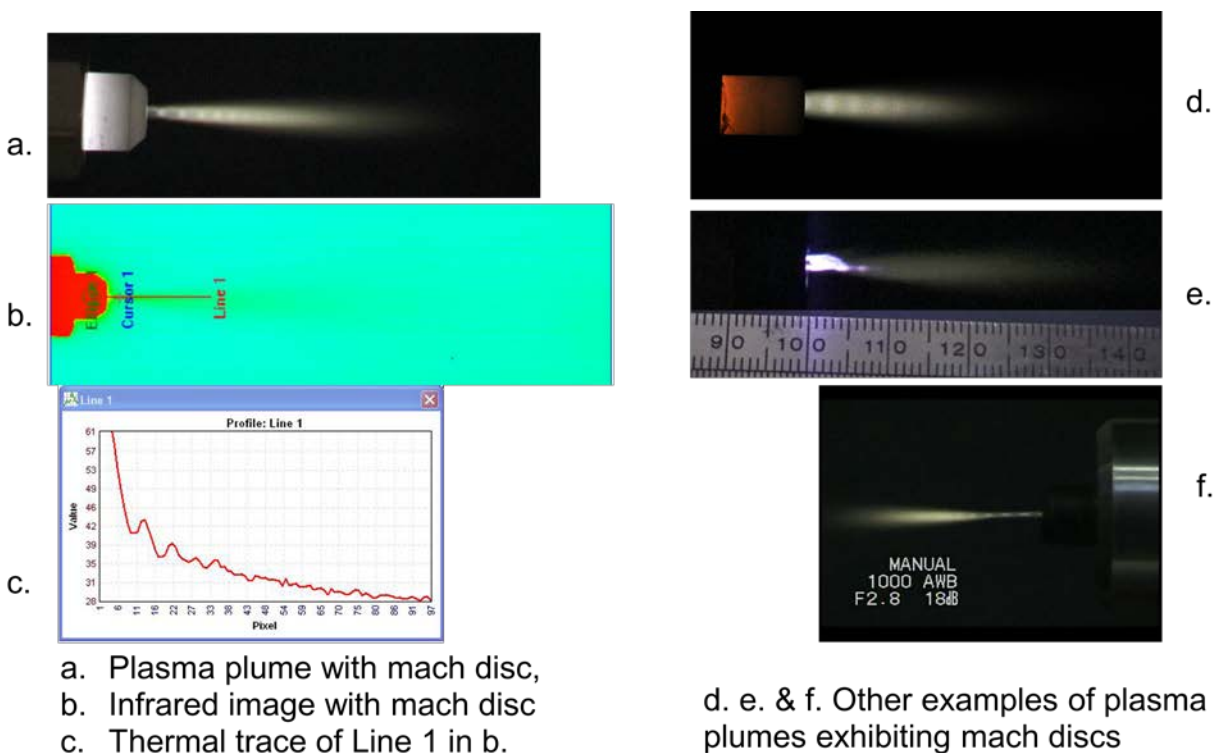


Figure 91: A series of photographs showing the presence of mach discs in plasma plumes.

Task 4 Large Area Plasma Removal System

4.1 Design Large Area Plasma System

4.1.1 Multi-Nozzle Plasma

Design Criteria and Assumptions for Plasma Pen:

The base for the multi-pen design concept undertaken in this task was the single nozzle pen geometry which has been used successfully to remove Navy coatings during Year 1 and Year 2 testing. The internal geometry of the successful single pen was translated into a four-nozzle array based on a monolithic block instead of four discrete pens. The design presented in this report replicates the internal geometry of the current Navy coating removal system and should thus be better suited to the task of removing coatings. As mechanical design considerations were taken into account during the three-dimensional CAD layout, a center-to-center nozzle spacing of 1.25" (31.75 mm) was found to be suitable to allow for all necessary connections and voltage creep requirements. An improved power supply design was also in progress. The multi-pen work for this task investigated the effects of scaling up the single nozzle applicator that was studied extensively during this SERDP project.

With the center-to-center nozzle spacing established, a modular system can be used to stack adjacent modules into an array of any size while maintaining a constant nozzle-to-nozzle distance. The design presented here incorporates connection hardware that maintains a constant spacing of 1.25" (31.75mm) between nozzles. The initial testing was of a 1x4 (1 row of 4

nozzles) linear nozzle unit. An existing multi-pen power supply was retrofitted with this pen for testing. It was thought that the 1x4 module would allow sufficient freedom to test the initial concept and show a scaled removal rate in order to meet the goals of this project within the allotted schedule. These results provided baseline information in order to guide further scale-up work

The three-dimensional CAD model of the 1x4 nozzle module was designed and modeled and is presented in Figure 92. The model presented is made up of three such 1x4 modules, although initial testing used only one. The applicator shows a safety shield on top and a waste collection vacuum hood on the bottom with a high temperature flexible polymer hood that sweeps over the surface, a design that has been previously demonstrated to be effective in directing ejecta into a vacuum hose. Air and power lines are fed into the top of the unit, and all cabling was bundled within a flexible coaxial shielded umbilical that runs back to the power supply. The safety shield and vacuum hood can be scaled to whatever size array is chosen, such as the 1x4 unit that was tested. Figure 93 shows the same design viewed head-on looking into the plasma nozzles. The hardware attachment points for stacking the pens also allow for handle/mounting brackets to easily accommodate particular raster patterns.

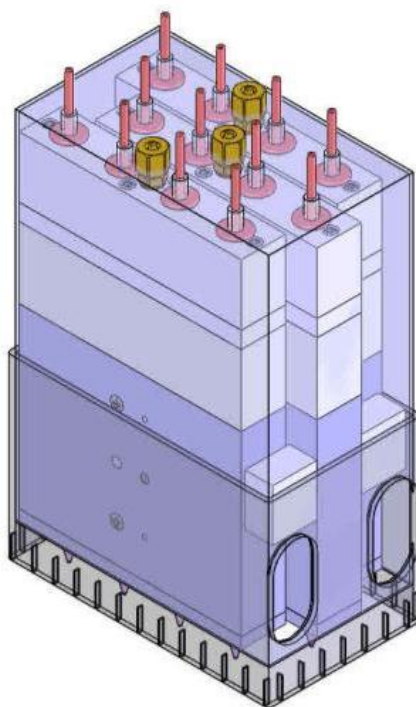


Figure 92: A multi-nozzle configuration utilizing the existing internal pen geometry.

This applicator consists of three individual 1x4 modules mounted together with equidistant spacing and incorporates an ejecta collection system and safety shield.

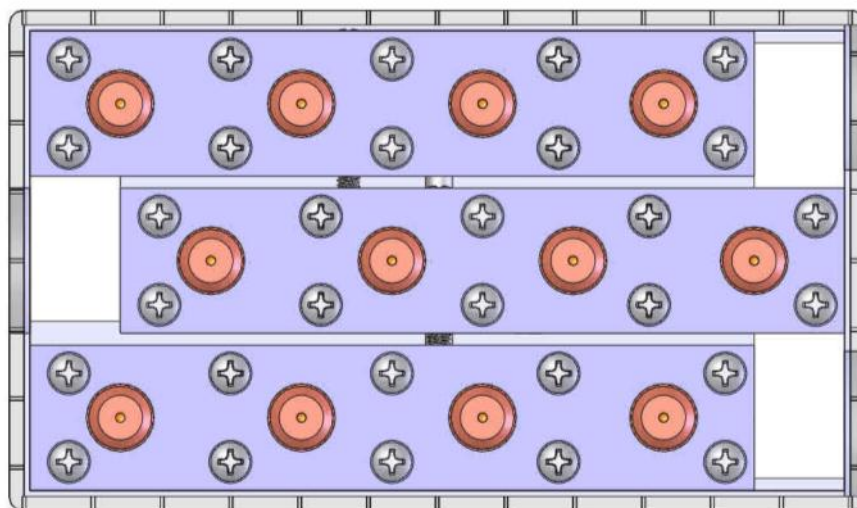


Figure 93: Nozzle arrangement for a twelve-nozzle (3x4) configuration. Three individual 1x4 modules are visible, as well as the vacuum shroud.

Logic and Calculations:

Performing larger-scale removals of 4" x 6" samples demonstrated that the results from the single pass DoE cannot be scaled up in such a way as to allow for accurate prediction of multi-pass removal rates. While Antifouling single-stripe removal showed topcoat-only removal rates of up to 13 ft²/hr (1.21 m²/hour) for a single stripe (0.14" (3.56 mm) wide stripe at 3.9 in/s (100 mm/s)), the actual best treatment rate achieved for removal to bare metal was ~3.3 ft²/hour (0.31 m²/hour), not including time spent off the sample for the robot to change direction and ramp up the speed. The best Freeboard removal rate was on the order of 1.9 ft²/hour (0.18 m²/hour). It is important to note that, due to the compressed schedule of testing, multi-pass removal rates have not been systematically optimized, and these rates were preliminary. If the grit-blast target rate is 150 ft²/hour (13.9 m²/hour), then these non-optimized rates would correspond to a necessary scaling of 46 nozzles for Antifouling and 80 nozzles for Freeboard. Based on material data and the volumetric model, it is estimated that a 1x4 module will weigh approximately 2.6 pounds (1.18 kg), while the entire 3x4 module shown above, including safety shield and vacuum shroud would weigh less than nine pounds (4.1 kg). This does not, however, account for cabling and vacuum hose, which must be routed in such a way as not to significantly hinder movement

APS has identified the desirable design criteria for a prototype multi-pen plasma head. Based on data from recent un-optimized multi-pass testing, perhaps as many as 80 nozzles might be required in order to match one cited rate for grit blasting removal, 150 ft²/hour (13.9 m²/hour). Prior to a full scale-up effort, a DoE study was recommended to optimize multi-pass removal rates. Using the above information, an external three-dimensional CAD model of a large area plasma coating removal head was designed, drawn, and created consisting of multiple plasma pens in a single housing. This large area head utilizes existing plasma pen designs integrated into a single housing that can be easily tested at different angles, heights, and sweep patterns if desired by the operator. Consideration was given to the future inclusion of additional nozzles if needed, as well as incorporation of an ejecta collection system.

4.1.2 VHF Plasma Applicator

Summary

This section of the report summarizes efforts by Dr. Steven Shannon in developing a novel atmospheric plasma applicator for paint removal during 2012. This effort was motivated by the prospect of utilizing a novel atmospheric source design as a large area applicator for paint removal. Efforts focused primarily on source design and characterization including electrical, chemical, and preliminary removal rate studies (focusing primarily on removal rate dependence on power levels and gas composition.) The source developed exhibits unique electrical and optical characteristics that presented a unique operating regime when compared to state of the art atmospheric systems such as dielectric barrier discharge, pulsed DC, microwave, or AC blown arc discharges. The discharge did not appear to produce streamers or arcs, but instead remained as a steady state glow located at the end of the inner coaxial power feed.

Electrical analysis was carried out by coupling electrical measurement of system impedance at RF frequencies to a global high frequency plasma model. Plasma impedance was determined by comparing the loaded and unloaded impedance of the coaxial source RF input; this termination impedance was combined with a simple high frequency global model to estimate an electron density of approximately 10^{11} cm^{-3} at 400 W delivered power in air.

Optical emission characterization of the source shows a monotonic increase in emission with respect with power; the relative intensity of the peaks from excited species, however, remains constant over a power range from 300 to 600 W. This unique source geometry presents a possible pathway for high gas throughput, large area, high power density processes such as surface modification, air purification, media removal, and chemical surface treatment.

Preliminary paint removal experiments yielded mass removal rates of up to 20 mg/sec for a single applicator design running at approximately 800 W of input power. These preliminary results are very encouraging given the current TDR level of this technology; it is reasonable to expect similar performance improvements seen by current state of the art systems as the TDR level increases and this source is designed around the specific application of media removal through appropriate applicator design and material selection.

Introduction

Advances in the application of atmospheric plasmas have come primarily from the development of a broad array of source technologies that seek to maintain the unique conditions found in a non-equilibrium plasma at these higher pressures. Atmospheric plasmas are driven at a wide range of frequencies ranging from DC to GHz. Most rely on either sustained arc-type discharges such as plasma torches [47], periodic breakdown to afterglow formation such as plasma jets [48] [49], dielectric barrier discharges [50], ion trapping [51], or wave heating systems such as microwave resonant cavity based plasma jets [52]. Many of these systems rely on helium [53] and its metastable states to sustain the discharge.

One of the primary challenges in producing atmospheric plasmas with higher power densities has been the transition point between the formations of a glow or streamer dominated discharge to that of an arc discharge. Glows and streamers tend to operate under conditions that are not in thermal equilibrium, thereby providing the novel chemistries that have made atmospheric plasmas so compelling for an array of applications. As power density is increased, the stable operating regime of the plasma transitions from a non-equilibrium glow to an arc-driven discharge. Under these conditions, the plasma tends to operate more in thermal equilibrium, presenting a very different interaction with surrounding material both chemically and energetically [54].

In order to push this transition to an arc-driven discharge out to higher power densities, several strategies have been employed. The most common strategy is to provide current isolation between surfaces of differing electrical potentials in order to mitigate arc formation via charge buildup and subsequent field reduction. This technique is most famously utilized in the class of atmospheric plasma sources referred to as dielectric barrier discharges (DBD's), where a narrow gap parallel plate system with insulating layers over the plasma facing electrode surfaces generates glows and streamers at atmospheric pressure while preventing the transition to an arc discharge. Another strategy is to terminate the potential between surfaces prior to arc formation, thereby terminating the accelerating potential before an arc can form. These pulsed systems have generated a tremendous amount of interest, particularly in combustion and biomedical applications due to their non-equilibrium gas phase chemistries [55] [56] as well as their unique ability to propagate beyond the electrodes of the system via photo ionization, forming what is commonly referred to as a "plasma needle" or a "plasma bullet" [57].

A third means for mitigating arc formation follows a similar strategy to these pulsed systems by minimizing parasitic electrical elements in the source design and modifying the potential between electrodes at a time scale much higher than the characteristic time for instabilities to manifest in the system; this is the mechanism that we seek to employ in the source detailed in this work. Electrical characterization of atmospheric air discharges have measured instabilities timescales on the order of 200 ns, primarily due to ionization thermal instability [58]. By driving the plasma with an RF power source with a frequency that is much lower than this timescale, a mitigation pathway can be achieved that prevents the amplification of the instability to the point of arc formation, and thus loss of the discharge's non-equilibrium properties.

In this report, a coaxial plasma source driven at 162 MHz is described in detail. Plasma sources that operate in this frequency range have had tremendous success, particularly in the area of material deposition and etching, where VHF systems have exhibited an increased ability to dissociate feed gases and generate higher electron densities and lower sheath potentials than their lower frequency counterparts; these sources have tended to operate at much lower pressures [59] [60]. This source employs a low loss, low-Q structure that provides power coupling to the plasma with minimal parasitic capacitance. The period of the RF drive (6 ns) is much shorter than the characteristic timescale for ionization thermal instability. This structure presents an electrical pathway for instability mitigation by operating in a regime where the discharge resistance measured at the drive frequency increases with increasing electron density, thereby providing negative feedback to the system that mitigates the growth of this instability.

Source Design

The NCSU atmospheric VHF source is powered by a 3.5 kW 162 MHz generator (Advanced Energy Ovation 35162). The generator has a characteristic termination impedance of 50 Ω and is connected to the source by a 50 Ω high power coaxial cable. A directional coupler, capable of measuring magnitude and phase between the forward and reflected RF waveforms is located at the output of the generator. Source matching is accomplished via tuned stub matching, where the RF input to the source is fed into the inner conductor of a coaxial feed with an inner conductor diameter of 2.25 cm and an outer conductor diameter of 5.25 cm; the dielectric insulator between the inner and outer coaxial elements is air, giving the coaxial structure a characteristic impedance of 51.7 Ω . The source coaxial feed splits from the RF input to a grounded termination and an open termination. The length of the grounded termination and open termination are determined by the power and air flow that are used to sustain the atmospheric glow. The grounded termination effectively serves as a shunt element for a coaxial matching network, while the open circuit acts as a series element. The atmospheric discharge is initiated at the end of this series element, and acts as the load impedance for this coaxial matching network. Process gas (in this case ambient room air) is fed into the coaxial structure from the grounded end and flows between the inner and outer conductor inside of the coaxial source, effectively serving as the dielectric insulator of the shielded coaxial structure. Gas flow can be set between 2 L/s and 10 L/s using a needle valve at the inlet of the coaxial source. Air is fed into the assembly slightly off axis in order to promote a cyclonic flow pattern inside the coaxial structure. The end of the inner conductor of the series leg is flared to a diameter of 3.5 cm for the last 3.8 cm of the series leg. Figure 94 is a schematic of the source configuration, along with a photo of the final source assembly housed in an enclosed fume hood and a down-barrel photograph of the source operating at 500 W with ambient air flow of 5 L/s.

Plasma ignition is initiated with a low flow (~ 1 L/s) helium gas injection. Upon ignition, the gas is transitioned to a helium/room air mix, immediately followed by a transition to ambient room air only. The ignition and transition steps are initiated at 300-400 W delivered power depending on the desired power level that creates a match with the generator impedance. When a steady state ambient air discharge is established, the power is increased to the desired set point. With proper tuning of the shunt and series lengths, reflected power levels as low as 5% have been achieved.

After ignition and stabilization of the ambient air discharge, a diffuse glow is observed in front of the flared end of the electrode. No plasma is observed in the region behind the electrode surface. After prolonged runs in excess of 20 minutes at power levels of 500 W and air flow of 5 L/s, the outer shield of the structure is cool to the touch. The flared end of the electrode does heat up, and approaches temperatures of around 75 $^{\circ}\text{C}$, measured with a Ryobi Tek4 infrared temperature monitor after the plasma is turned off. During normal operation, no pitting or discoloration is observed on any surface in direct contact with the plasma.

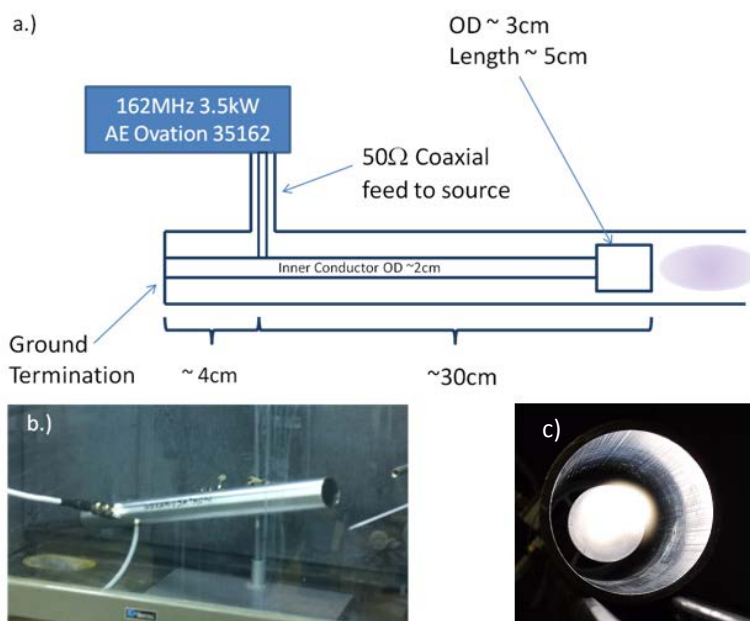


Figure 94: Coaxial source schematic; (a) photograph of the assembly (b) and image down the barrel of the assembly during a 500 W, 5 L/s ambient air discharge (c).

Characterization of the glow is carried out via electrical and optical measurement of the system. Optical emission of the plasma region is measured across the visible spectrum with a Verity Instruments 2048LC spectrometer with integrated linear CCD array, providing an instrument resolution of approximately 2 nm. Source impedance measurements are made using the onboard directional coupler meters on the Advanced Energy Ovation 35162 RF generator; this provides both magnitude and phase information, enabling source impedance measurement during operation. Discharge current is measured using a small B-loop probe housed in a thin ceramic tube along the inside diameter of the outer cylindrical housing. The probe is connected to a Tektronix TDS 2024 oscilloscope for waveform analysis. A summary of these diagnostics is illustrated in Figure 95. Source characterization (without plasma) is done via one-port measurement of the source assembly taken at the end of the RF cable normally connected to the RF generator using a Hewlett Packard 8753B network analyzer.

Paint removal rates were conducted on prepared steel samples with battleship FB grey paint. The samples were manually rastered below the plasma source at approximately 10 cm/sec at various applicator-to-substrate distances. Gas flow was nominally 5 slm. Air, nitrogen, and carbon dioxide were used as feed gases to study air chemistry impact on removal rate. Power was varied from 300 W to 800 W to study discharge power impact on removal rate. Painted samples were weighed before and after treatment; the difference in pre and post measurements are assumed to be due to paint removal and are normalized to treatment time and reported as mass removal rate in this report.

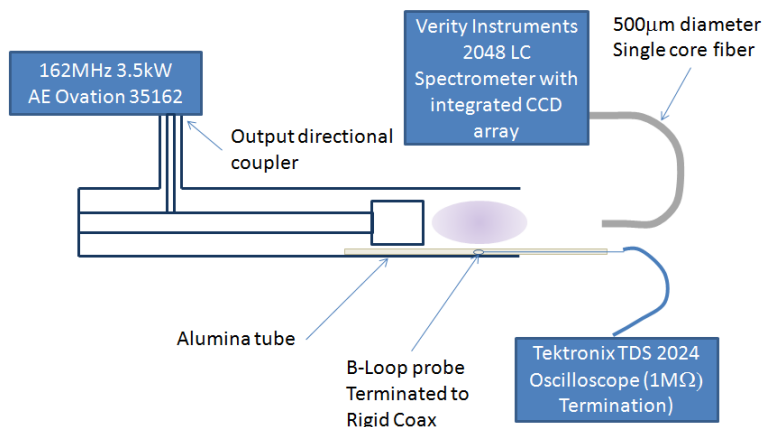


Figure 95: Electrical and Optical Diagnostics Used to Characterize the Coaxial VHF Source.

Electrical Characterization

The simple electrical structure of the coaxial drive provides a unique opportunity to study trends in system impedance in order to estimate plasma conditions and trends with respect to power and flow. By measuring the vacuum impedance of the coaxial structure, and solving for the necessary plasma load termination impedance of the series leg to achieve the measured magnitude and phase of the reflected power from the source (relative to the forward power from the generator), an estimate of the plasma impedance can be made. These electrical parameters are measured as a function of process set point and used with a simple global plasma model to estimate the electron number density in the discharge.

The impedance of the system was measured by the reflected power and load phase measured at the generator output. Using this impedance measurement along with lossy transmission line theory, the impedance of the plasma can be calculated. The equation used to calculate the impedance along a transmission line is:

Equation 11. Plasma impedance along a transmission line.

$$Z = Z_0 \frac{Z_L + Z_0 \tanh(\gamma l)}{Z_0 + Z_L \tanh(\gamma l)}$$

Where Z is the measured impedance, Z_0 is the characteristic impedance of the transmission line, Z_L is the load impedance the line is terminated to, γ the propagation constant of the line, and l the length of the line. Due to the cylindrical electrode at the end of the inner conductor, the load impedance is actually the combination of the plasma impedance in parallel with the capacitance of the gap between the electrode and the outer wall. For this calculation both the transmission line properties of the power cable and the coaxial structure of the device were used. An equivalent circuit model for the plasma is then used to estimate the electron density from the calculated plasma impedance.

The plasma model uses a simple equivalent circuit to represent the electrical characteristics of the plasma, consisting of a bulk plasma impedance in series with the capacitive reactance of the surrounding sheath. The plasma impedance is composed of the vacuum capacitance of the plasma region in series with a resistive and inductive term that depend on electron density and

electron neutral collision frequency. This equivalent circuit representation is commonly used to study the electrical response of RF discharges [61], and has recently been applied to discharges under atmospheric pressure conditions [62]. A circuit schematic is illustrated in Figure 96. The real portion of the plasma impedance is given by:

Equation 12. Real portion of plasma impedance.

$$R_p = \frac{R_B X_B^2}{R_B^2 + (X_B + X_L)^2}$$

where R_B is the DC resistance of the plasma, X_B is the vacuum reactance of the plasma region, and X_L is the plasma reactance. The DC resistance of the plasma R_B is given by:

Equation 13. DC resistance of plasma.

$$R_B = \frac{L\nu n_e}{Ae^2 m_e}$$

where $L = 5$ cm is the axial length of the plasma (estimated based on visual observation), m_e is the electron mass, $A = 9.6$ cm² is the area of the powered electrode surface, n_e is the electron density, e is electron charge, and ν is the electron-neutral collision frequency, estimated using the polarization cross section for charged specie collisions with neutral species [63],

Equation 14. Cross section for charged species.

$$\nu = n_g \sqrt{\frac{\pi\alpha e^2}{m_e \epsilon_0}}$$

where n_g is the neutral gas density (estimated at room temperature ambient air at atmospheric pressure) and $\alpha = 0.021$ nm² is the polarizability constant for air. Although some gas heating is expected, the earlier observation of minimal surface heating after extended operation suggests that this is relatively minimal and is ignored in this analysis. Using Equation 14, collision frequencies on the same order of magnitude (approximately 10^{11} s⁻¹ - 10^{12} s⁻¹) used by other groups to model atmospheric discharge are obtained. [64] Although polarization scattering does present a collision frequency that does not vary with electron temperature, it will be shown later in this work that the emission spectra of the plasma suggests the electron temperature is very constant over the range of conditions studied, and that any electron temperature dependence in collision frequency not accounted for by Equation 14 is therefore negligible.

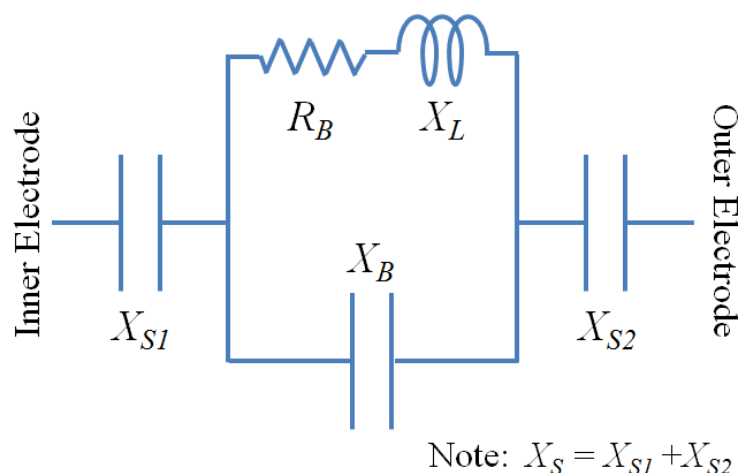


Figure 96: Equivalent circuit used to obtain plasma density n_e and sheath reactance X_s .

The reactive portion of the plasma impedance is made up of the capacitive sheath terms in series with the reactive component of the bulk plasma impedance. The vacuum reactance of the plasma X_B is the difference between the no-load termination of the coaxial structure X_0 and the sheath reactance X_s . The sheath is modeled as two series vacuum capacitors defined by their effective surface area and sheath thickness ($OD\pi L$, and s respectively, where OD is the outer diameter of the coaxial structure). The no-load termination X_0 is measured in the absence of a plasma via one-port measurement of the source impedance using a Hewlett Packard 8753 network analyzer at the end of the cable that is normally connected to the RF generator; the termination impedance measured at this point is then transformed to the open end of the coaxial assembly using Equation 11 and solving for Z_L . The bulk plasma reactance is modeled as an inductor,

Equation 15. Inductor model of bulk plasma reactance.

$$X_L = \frac{\omega R_B}{\nu}$$

and the imaginary term for the total discharge impedance is given by

Equation 16. Imaginary part of the plasma discharge impedance.

$$X_p = X_s + \frac{X_B R_B^2 + X_L X_B (X_L + X_B)}{R_B^2 + (X_L + X_B)^2}$$

In reviewing Equation 8 to Equation 15, the two plasma parameters that determine the termination impedance $R_p + iX_p$ are n_e and s . Measurement of the plasma loaded impedance of the coaxial structure at the generator output, transformed to the plasma termination provides R_p and X_p . Using Equation 8 to Equation 15 for R_p and X_p provide a system of equations from which the two unknowns for the system, n_e and s , can be extracted. Similar high frequency models have reported good correlation to plasma conditions for VHF atmospheric plasmas under different conditions (gas, geometry, power density, etc.).

Measurements of the source impedance loaded by a plasma discharge were made at fixed coaxial lengths as a function of dissipated RF power. The source was ignited at 300 W using an initial

helium flow that was transitioned to ambient air flow of 5 L/s. Power was swept from 300 W to 600 W for constant flow; reflected power magnitude and phase was recorded at each power setting. The plasma impedance was calculated using Equation 11 accounting for the additional shunt impedances imposed by the grounded coaxial termination and flared electrode end on the plasma (series) leg. A summary of the plasma impedance with increasing power is shown in Figure 97. Again using Equation 8 to Equation 15, the electron density and sheath thickness can be estimated. A summary of the calculated electron density and sheath thickness is shown in Figure 98.

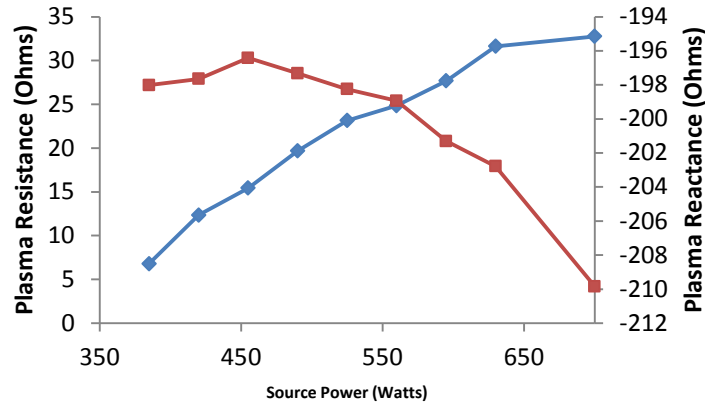


Figure 97: Plasma resistance R_p (\diamond) and reactance X_p (\blacksquare) measured as a function of delivered power for ambient air flow of 5 L/s.

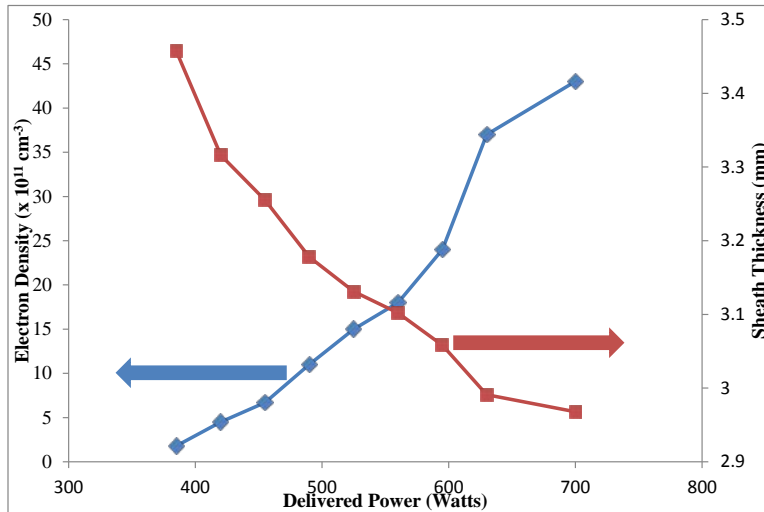


Figure 98: Electron density (\diamond) and sheath thickness (\blacksquare) estimations made from electrical measurement of source impedance as a function of delivered power to the source.

To determine the presence of thermally driven instabilities such as ionization thermal instability, a B-loop current probe was shielded from the plasma via a thin ceramic tube and inserted down the coaxial device along the outer wall so as to minimize plasma perturbation. The current probe

was a shielded rigid coaxial structure. The inner conductor of the rigid coax was looped and soldered to the grounded outer shield, forming a loop structure approximately six mm in diameter. The probe was connected to a Tektronix TDS 2024 oscilloscope where the induced potential generated by the time varying current in the plasma discharge interacting with the B-loop diagnostic was measured. Measurements of current were taken along the length of the device and were greatest in magnitude when the current probe was in line with the plasma body (i.e., the cross sectional area of the probe was facing the center axis of the coaxial discharge). The measured current decreased to near zero when the B-loop normal vector was aligned perpendicularly to the normal vector from the barrel capacitor and peaked when the B-loop normal vector was parallel with the capacitor normal vector. The probe was calibrated using Faraday's law to determine the induced potential generated by a time varying magnetic field of magnitude B passing through the loop of the probe, $\varepsilon = NBA\omega$, where ε is the induced potential, N is the number of turns ($N = 1$ for this probe configuration), A is the cross sectional area of the probe (12mm^2), and ω is the natural frequency of oscillation ($2\pi \times 162$ MHz). The induced magnetic field was correlated to plasma current using Ampere's Law, $B = \mu_0 I / 2\pi r$, where μ_0 is the permeability of free space, I is the RF current amplitude, and r is the distance from the loop probe to the center of the plasma (1.5 cm). The calculated relationship between current at 1.5 cm and induced potential agreed well with measurements made using a $50\ \Omega$ terminated Bird Truline model 1908 coaxial directional coupler housing, where one of the directional couplers was replaced with the B-loop probe to measure current near the $50\ \Omega$ termination. Although this calibration is an approximation based on the rough dimensions of the plasma, it does highlight the resolution of the probe compared to current signatures attributed to thermal instabilities by other groups, where mA ranges are reported. The plasma current trace is a near perfect 162 MHz sinusoid for all powers and flows studied, and shows no evidence of streamers or arcing such as spikes or irregularities (dips, humps, etc.) that have been identified in previous efforts [65] [66]. A representative waveform trace is illustrated in Figure 99.

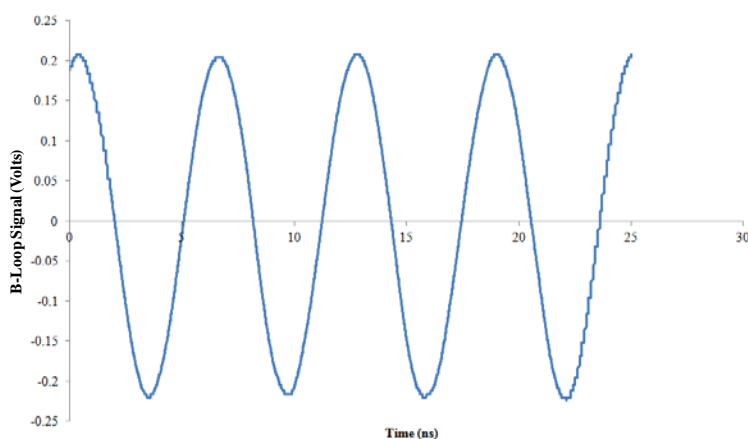


Figure 99: Representative B-loop measurement of current waveforms produced in the coaxial plasma source. 1 Volt is approximately equal to 0.1A induced current on the loop diagnostic.

The absence of thermally driven instabilities and arcs is believed to be due to the plasma impedance response to increasing electron density. Staack et. al. presented a very straight forward explanation for the propagation of ion overheating instabilities in atmospheric plasmas

[58]. In this work, the progression from increasing electron density heating the background gas (and thereby reducing the gas particle density), which increases the E/n ratio for a DC discharge, increasing electron temperature and thereby increasing ionization rate and thus electron density (further feeding this chain from the beginning), was illustrated as a straight forward mechanism with positive feedback that drove this instability in atmospheric systems. At very high frequencies such as 162 MHz, a similar analogy can be made, but in this case, negative feedback is observed. The analogy is as follows: assume that through some perturbation an incremental increase in electron density δn_e is generated in the coaxial discharge. Similar to the ionization thermal instability, this results in a reduction in background gas density.

Additionally, this results in an increase in the real portion of the plasma discharge impedance R_p . This increase in R_p decreases the RF current driving the plasma discharge assuming that the delivered power is constant since $P = I^2 R_p$, where P is the delivered power to the system and I is the RMS current amplitude through the discharge. On first order, the electron density tracks with RF current and sheath thickness with the equality $s_0 e \omega n_e A = I$, where s_0 is the sheath thickness of the capacitive discharge. Reviewing the plasma parameters summarized in Figure 98, s_0 is a relatively slowly varying parameter compared with electron density as a function of P (and hence I^2) and is therefore not a significant contributor to the change in I . Therefore, the introduction of δn_e reduces I and introduces negative feedback to the time dependence of δn_e , effectively restoring the electron density established by the global particle and energy balance of the discharge. Taking a nominal discharge impedance of $(24.9 - j198) \Omega$ that was measured at 560 W, 5 L/s gives an RC time constant of 0.1 ns, much shorter than the measured characteristic frequency of thermally driven instabilities such as ionization overheating, which are 10's of nanoseconds.

This negative feedback, coupled with the much faster time response of the system, is believed to be the mechanism that supports a volume glow in this source; effectively, the plasma load acts as a ballast at these high drive frequency conditions for atmospheric discharges. Varying frequency in Equation 8 to Equation 15 show that as frequency is decreased, the electrical response of the system reverts back to a regime where increasing electron density reduces bulk plasma resistance, thereby introducing a positive electrical feedback that cannot counteract instabilities induced by changes in δn_e . This frequency dependence is illustrated in Figure 100. Additionally, the reduction in gas density that follows the introduction of δn_e has minimal impact on the RF impedance of the discharge, even for reductions as high as 10x.

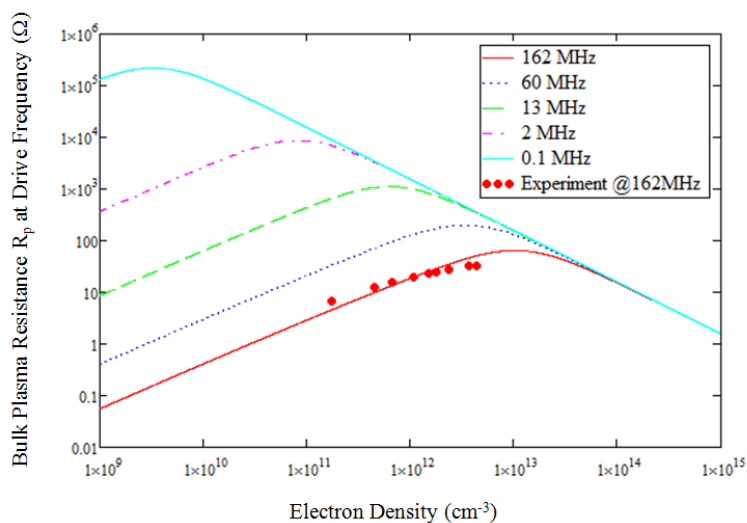


Figure 100: Response of bulk plasma resistance R_p at the RF drive frequency as a function of electron density for various frequencies.

Also included are the measured real impedance and calculated electron densities for the conditions studied at 162 MHz drive (denoted by the symbol ●).

Optical Characterization

Visible spectra were acquired using a Verity Instruments 2048LC Czerny Turner spectrometer with approximately 2 nm line resolution over the visible spectral range of 200 nm to 800 nm. Integrated spectra was obtained via light collection at the open end of the coaxial barrel (no spatial resolution). Spectra were obtained for ambient air discharges as a function of applied 162 MHz power from 300 W to 600 W for ambient air flow of 5 L/s and as a function of flow from 2 L/s to 10 L/s for constant delivered power of 500 W. The spectrometer was not calibrated with a black-body light source. Although this inhibits quantitative comparison of emission peaks for a given condition, relative intensities as a function of plasma condition still lend some insight into plasma composition. Spectra obtained as a function of air flow from 2L/s to 10L/s did not yield any significant trends in either integrated spectra or axially resolved spectra, indicating minimal plasma emission dependence with respect to the flow range studied.

As a function of power, the spectra monotonically increased in intensity, as shown in Figure 101. When the spectra is normalized for each power condition such that the area under the spectra for each case is equal, it is observed that the overall shape of the spectra does not change as a function of power and that the relative composition and temperature of the plasma appears to remain relatively constant over the studied power range. This monotonic spectroscopic response indicates little or no change in electron temperature over the range of conditions studied, further validating the earlier assumption that the electron-collision frequency is constant over this range of conditions. Figure 102 is an overlay of the integrated emission spectra as a function of delivered power; the emission peaks of dissociated species of interest for air plasma applications including NO, OH, and O are highlighted.

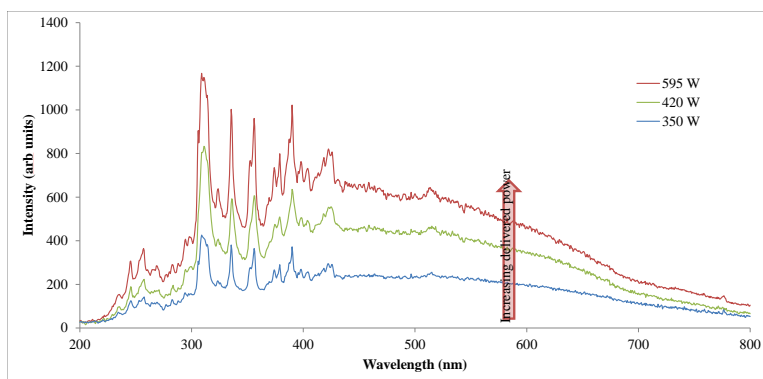


Figure 101: Integrated spectra as a function of delivered power from 350 W to 595 W.

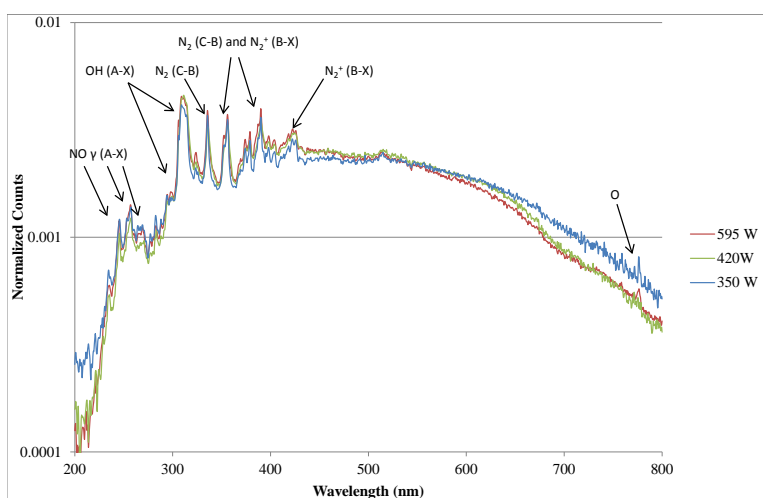


Figure 102: Normalized spectra as a function of delivered power. Species of interest, including NO, OH, and O are highlighted.

Removal Rates

The VHF applicator was evaluated for paint removal to determine if the non-thermal discharge characteristics provide any intrinsic benefit for this application. Applicator power, gas composition, and electrode-to-substrate gap were varied in order to elucidate mechanisms for removal and source to substrate interaction.

Steel substrates (6" x 4") were primed and painted with battleship FB "haze grey" paint and weighed. The painted surfaces were exposed to the plasma at the end of the VHF applicator. The substrate was rastered underneath the active plasma region at an approximate rate of 5 cm/sec. The substrate was rastered in order to remove paint without exposure of the metal substrate; this allows for an accurate estimate of removal rate by minimizing the exposure time over bare metal, where material removal would be negligible. Time of exposure was recorded. Samples were then weighed after exposure. The weight difference, normalized to time of exposure, was then used to estimate mass removal rates for the experiment.

Removal rates for the process conditions run were relatively flat as a function of air flow. The dynamic range of the air flow was limited to 10 cfm due to the delivery system available for this experiment. These results are consistent with optical and electrical measurements of the plasma discharge that showed little systematic change with respect to air flow. Figure 103 summarizes removal rate trend with respect to air flow for two power levels.

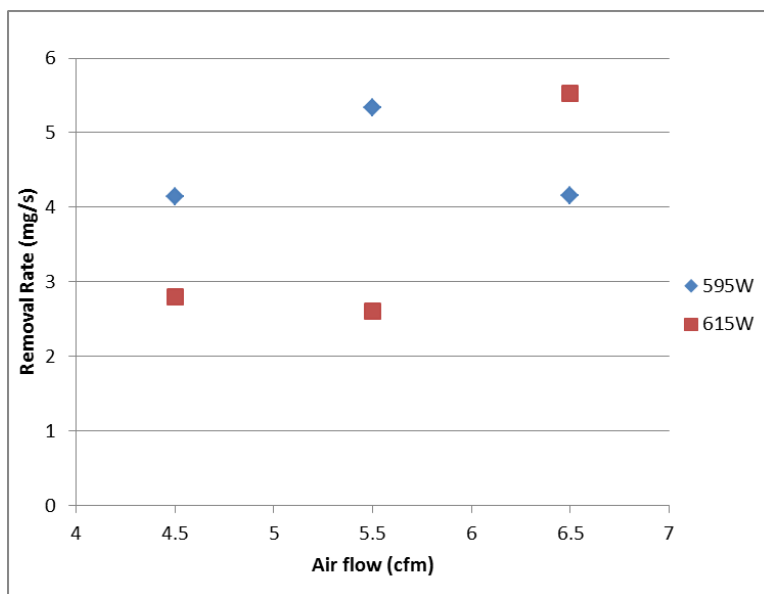


Figure 103: Removal rates as a function of air flow at two power levels. Applicator was positioned 0.76 cm from the painted surface. The VHF electrode was recessed 1.5 cm from the end of the applicator.

Removal rates for the process conditions run were relatively flat with respect to power but appeared to be strong functions of distance from the active plasma region to the painted surface. These results are consistent with results reported with other applicators and suggest strong removal rate dependence with respect to ROS and RON species in the plasma region. These results are summarized in Figure 104. Removal rates for the process conditions run appear to be weak functions of gas composition. Power sweeps were conducted at constant applicator gap of 0.76 cm for air, carbon dioxide, and nitrogen each of which appeared to have comparable removal rate. A similar dependence on removal rate with respect to oxygen content using the VHF plasma are expected to be consistent with that observed in the gas composition carried out on the plasma torch. However, the repeatability of the preliminary experiments run on the VHF applicator makes a one-to-one comparison difficult.

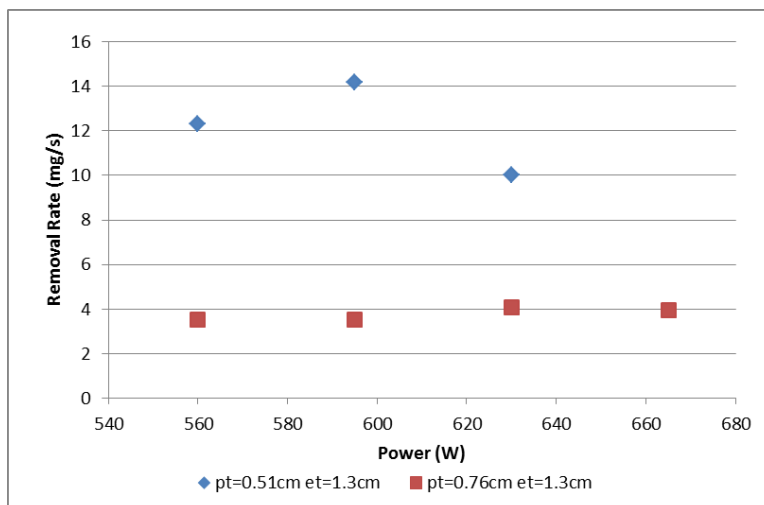


Figure 104: Removal rates as a function of power for two applicator-to-surface gaps. Note the significant increase in removal rate as the gap is decreased.

Conclusions

A novel, large area, high power density, non-equilibrium atmospheric air plasma source has been designed, built, and characterized. Non-equilibrium chemistries driven by electron number densities around 10^{11} cm^{-3} have been reported. This plasma source is based on a coaxially driven system driven at 162 MHz where the gas feed to the plasma region is fed through the dielectric break between the powered and grounded electrodes of a cylindrical coaxial system. The high frequency drive is believed to generate a plasma load ballasting effect that introduces a negative feedback mechanism that inhibits the formation of thermally induced instabilities. This configuration serves as both the source assembly and matching network for the system. Preliminary removal rates of haze grey substrates yield modest removal rates, and improvements are expected as the TDR of this technology continues to mature. This work was supported by SERDP, a grant from Advance Energy, and NCSU funding.

4.1.3 Alternative Large Area Plasma Concepts

Early in the project, there were at least two additional plasma designs being considered which made it at beyond the drawing board at least to the test staging. These designs were made by Dr. Hudak based on literature sources and patent examination. The first concept was based upon an expansion of the idea that if a single nozzle is useful, then many nozzles would be more useful. There are more than a few examples in the literature related to the use of micro-plasmas which contain many tubes or nozzles. Most of these systems are inductive type setups and require the use of noble gasses such as helium or argon for activation.

A schematic of the shower head concept is illustrated in Figure 105. The business end of the applicator would typically be enclosed and outfitted with exhaust capability for collecting debris. The combination of individual plasma jets, operated on a head with random orbit capabilities would act in a manner similar to one large plasma and provide uniform area treatment. A single cell prototype was manufactured and plasma was generated at low frequency and low power.

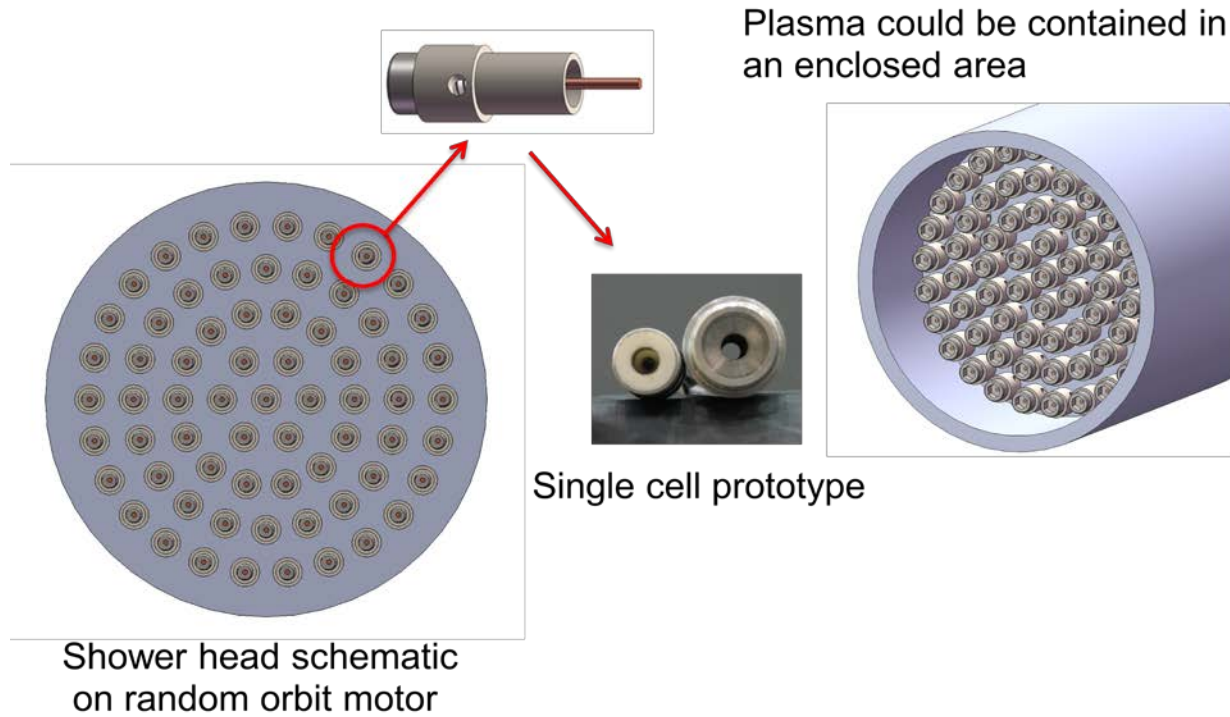
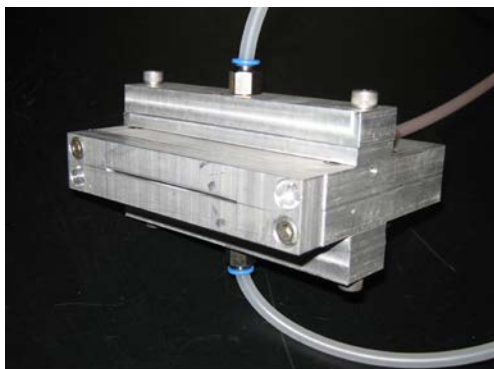


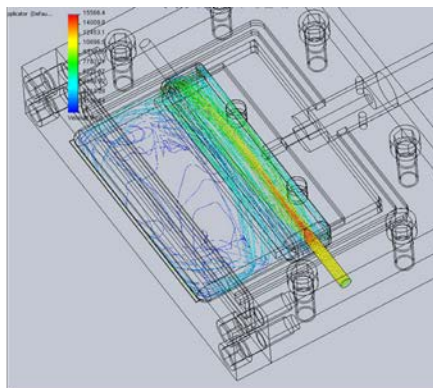
Figure 105: Schematic diagram of a shower head design plasma concept and an actual individual cell.

There would be significant development still needed, especially with respect to the power delivery. Pulsed signals would have to be controlled to each of the individual cells to maintain a constant supply of current. Cross talk between individual nozzles would need to be addressed and solved. This is not impossible but would require significant electrical engineering so the concept was eliminated from consideration.

Another concept based partly on patents from APJet, (who has a working model) is illustrated in Figure 106. The idea behind this type of device is to generate plasma over a wide area using an elliptical interior design. Generation of plasma is controlled by a combination of factors which include internal geometry, air velocity, power, pulse frequency – duration - waveform, and the materials of construction. A prototype was manufactured which fired, generating a weak plasma. Also due to the stage of development and progress in other areas, this design was dropped from consideration.



Linear array plasma concept



FloXpress model of flat plate with one channel gas supply

Figure 106: Depainting brush head concept using atmospheric plasma.

4.2 Fabricate and Test Large Area Plasma Device

Multi-nozzle Module Construction

The foundation for the multi-nozzle pen design concept undertaken in this task was the single nozzle pen geometry which has been demonstrated to successfully remove Navy coatings of interest. The internal geometry of the single pen was translated into a four-nozzle array based on a monolithic block instead of four discrete pens. This new applicator was constructed during this period and used in conjunction with an existing power supply designed for a previous four-nozzle applicator. An improved power supply design was under development. The effects of scaling up the single nozzle into a multi-nozzle array were investigated.

Individual parts for the build were fabricated and assembled as designed in the previous task. The manufacturing was carefully monitored to maintain critical tolerances in order to minimize pen-to-pen variation. As the build and assembly proceeded, some parts were reworked for improved manufacturability or performance. The most significant change to the design was the addition of a gasket to mitigate potential leaks from two mating faces within the assembly. The final four-nozzle assembly was found to work with existing facilities at up to four times the standard single pen air flow condition ($4 \times 135 \text{ slm} = 540 \text{ slm}$), but future testing may require facility upgrades to allow for testing higher flows. The air compressor at the APS facility being used for this project is rated for over 2000 slm at the pressures required for these applicators; however, some of the air plumbing and flow control/monitoring components would need to be upgraded to handle the full capacity of the compressor.

Air and power lines were fed into the top of the unit, and all cabling was bundled within a flexible coaxial shielded umbilical that runs back to the power supply. A basic cable bundling and shielding scheme was found suitable for this early testing, but investigation of a better cabling solution is underway. In order to achieve the desired goal of coating removal within the limited timeframe and budget, minimal work was completed under this project to electrically characterize the output of nozzles. The careful control of the mechanical manufacturing of applicator was found to provide sufficiently uniform plasma output for these early removal tests.

The hardware attachment points built into the design served both to allow stacking multiple four-nozzle units, as well as to allow for handle/mounting brackets to easily accommodate particular raster patterns. For this testing, an adjustable mounting bracket was designed, constructed, and used for removal testing. This fixture allows for adjustment of the array angle (α) described later in the report. Fixtures for the ShopBot robotic stage were also fabricated for routing air and electrical lines. The mounting fixture was found to be suitably rigid to enable effective removal at appropriate speeds (approximately 7 in/s) without observable flexure or oscillation during removal tests. A design review of the vacuum/safety shield was conducted, stock was purchased, and work was begun on the design. Initial testing showed that the system operated adequately without the metal enclosure, but only a shielded cable was used for final testing. High-voltage standoff was already designed into the fixture, and the standard ventilated enclosure was used for the testing with minor modification, so it was decided that the shroud would not be needed for these tests. In light of the discussions concerning waste collection after the Norfolk shipyard tour, it was decided that the integrated waste collection feature of the prototype would be addressed later in the project.

Initial test firings of the system demonstrated that all four nozzles could be fired simultaneously with a total input power of ~ 7 kVA. Figure 107 shows an image of the four plasma plumes in operation. Once the plasma system was constructed and shown to successfully generate plasma, testing focused on investigating multi-nozzle paint removal with some temperature measurements taken. The test setup did not allow for in-situ measurement, so a more complete thermal analysis may require dedicated testing. Results of the removal testing are summarized below.

Coating removal trials with large area plasma system (two-nozzle)

This task focused on a small optimization study using a two-nozzle system to remove AF coatings. It was found that although the four-nozzle design was operational as illustrated in Figure 107, power was not equally divided to each nozzle. This task was expected to provide a good base upon which to build future work with larger areas and more nozzles. Furthermore, in conjunction with the large area (2' x 3', 610 mm x 914 mm) single-nozzle removal, this task was intended to emphasize the ongoing scale-up effort to scale to multi-nozzle systems, while investigating and anticipating technical issues.

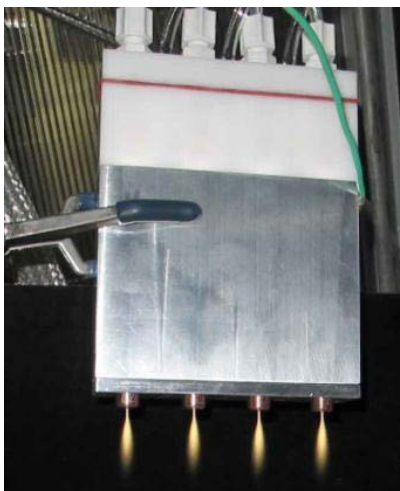


Figure 107: Four-nozzle plasma in operation.

Array Angle Determination

The additional dimension of complexity added by concurrently using multiple nozzles necessitated that certain terms be clearly defined. A Glossary of Terms for Multiple Nozzles is included in Appendix A. The four-pen apparatus constructed has four nozzles in a linear array, with an inter-nozzle spacing of 1.25 inches (31.75 mm). If removal is conducted with the array at 90° to the coupon (Figure 108 a), the removal swaths are separated by an inter pass spacing between nozzles (Δx_n) of 1.25 inches. By changing the angle of the array (α) relative to the coupon, the swaths can be brought closer together. In Figure 108 b, the array is at an angle of $\alpha = 23.6^\circ$, resulting in a Δx_n spacing of 0.5 inches (12.7 mm) between swaths in the array. Equation 17 shows how to calculate the resultant Δx_n spacing if the array angle (α) is known.

Equation 17. Plasma spacing of four nozzle plasma as a function of angle.

$$\Delta x_n = 1.25 * \sin(\alpha)$$

If there is a particular Δx_n spacing that is desired, Equation 18 can be applied to determine the appropriate array angle.

Equation 18. Desired spacing calculated based on array angle.

$$\alpha = \arcsin\left(\frac{\Delta x_n}{1.25}\right)$$

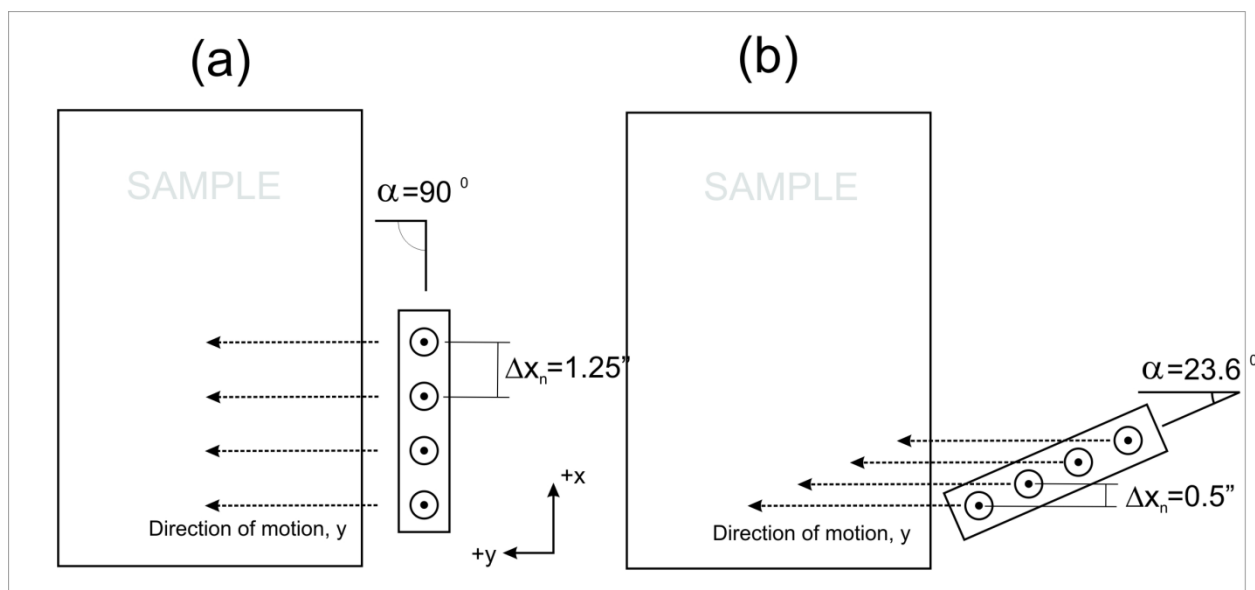


Figure 108: Four-pen array and coupons. A) Array is at a 90° angle to the coupon, removal swaths are separated by 1.25". B) Array is at a 23.6° angle to the coupon, removal swaths are separated by 0.5".

Single-Pass Removal

All single-pass removal tests were conducted using certain standard conditions as follows: Total flow to all four nozzles was 270 slm; height above sample was 0.079 inches (2 mm); speed of removal was 3.937 in/s (100 mm/s). All of these tests were done on the Antifouling coating system.



Figure 109: Removal swaths from the first four-pen removal test. The white areas are chipped paint; this paint was missing prior to plasma treatment. Scale is in 1/8" increments.

The first removal was conducted with all four pens firing. All four pens removed into the second topcoat layer, and some of them removed a small amount of the third topcoat layer (see Figure

109). The total mass of paint removed was 0.43 g. This is very close to the same amount of paint typically removed by a single pen at the same height, speed, and a similar per-nozzle flow (60 slm as opposed to 67.5 slm), which resulted in an average of 0.421 g.

Electrical simulation and measurements of the power supply showed that the overall power of the system was limited such that four high-power pens (similar to the single pen used in previous testing) could not be supported with this particular power supply design without a major redesign. As a result, in order to improve per-pen removal capability, the outermost nozzles (1 and 4) were electrically disconnected, so that only nozzles 2 and 3 would fire. This particular system was also limited to a total airflow of about 270 slm for stable plasma output. Lower operating frequencies (~65 kHz) were also beneficial for this system to achieve maximum output power, ~4 kW total for the two-nozzle configuration. This power level gives the same per-nozzle power level as the previous single-pen design, as was desired for this test. A new power supply design being developed will be capable of supporting higher total output powers (>10 kW) and flows to fully test four-nozzle and larger systems.

Two removals were conducted at an array angle of 90° using two active nozzles at the above settings; one of these is shown in Figure 110. Average mass removal was 0.936 g, which means each pen was removing approximately 0.468 g of paint, which is greater than the single-pen mass removal of 0.421 g at this condition (same height, speed, and a similar per-nozzle flow of 60 slm as opposed to 67.5 slm). Further testing would be required to verify that this ~10% increased per-nozzle removal rate is maintained across a wider range of samples and conditions.

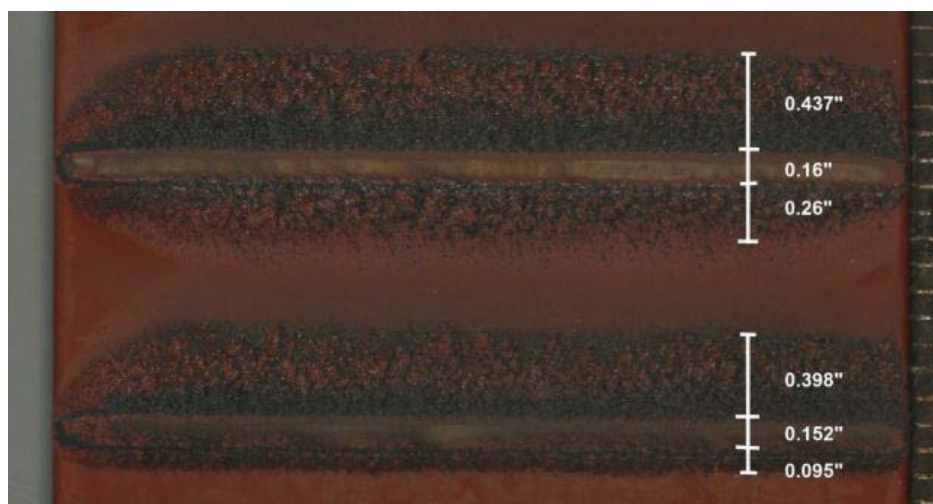


Figure 110: Widths of removal features from a two-nozzle removal conducted with an array angle of 90°.

For each swath, the three regions are, from top to bottom: overspray, removal, overspray. Scale on right is in 1/8" increments. To determine which other array angles might produce interesting results, the widths of the various removal features were measured using calipers. These widths were then used as guidelines for choosing angles which would result in varying degrees of overlap of the two removal swaths. The angles then selected were: 35°, resulting in minor overlap of overspray regions; 26°, resulting in near-complete overlap of overspray regions (but little to no interaction with removal regions); 6.9°, resulting in two side-by-side removal regions;

and 3.2°, resulting in partial overlap of the removal regions. The average total and per-nozzle removal masses for each of these angles are shown in Table 13. Total flow to all four nozzles was 270 slm; height above sample was 0.079 inches (2 mm); speed of removal was 3.937 in/s (100 mm/s).

Table 13: Average total and per-nozzle mass removed for various array angles.

Array Angle	Δx_n (in)	Total Removal (g)	Per-nozzle removal (g)
N/A (Single)	0.000	0.421	0.421
90°	1.250	0.9355	0.467
35°	0.717	1.026	0.513
26.1°	0.550	1.146	0.573
6.9°	0.150	1.145	0.5725
3.2°	0.070	0.8735	0.436

As the results in Table 13 indicate, the per-nozzle removal at all angles except for 3.2° was significantly higher than for a single pen. The angled removals also noticeably outperformed the 90° condition. One potential contributing factor is that air was still flowing through nozzles 1 and 4, and this additional airflow could have pushed away paint that would have otherwise re-deposited in the overspray regions. At 3.2°, the overlap of the actual removal regions meant that less paint (particularly the more-easily removed topcoat) was coming in direct contact with the plasma, so the removal amount dropped sharply. A thermal camera (FLIR i40) image of the sample after the second sweep of the 3.2° treatment (about 7 s after treatment) showed a maximum surface temperature of ~66 °C across the 4"x~0.75" removal swath. It should be noted that only a single repeat of each condition was performed. A more complete statistical analysis would require further testing. Further removal and thermal testing is recommended, particularly in the between 6.9° and 26.1° (Δx_n of 0.15 to 0.55 inch), where there may be an optimum per-nozzle removal rate.

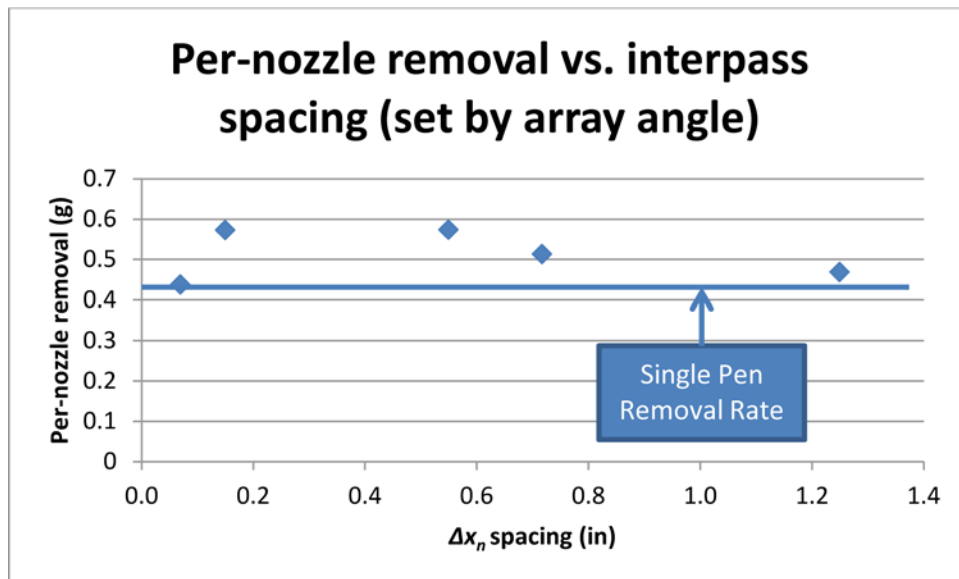
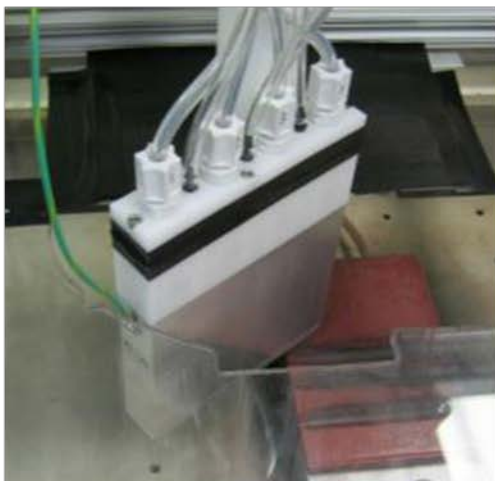


Figure 111: Per-nozzle removal masses for various array angles.

Photographs of the four-nozzle applicator with only two nozzles operating is shown in Figure 112. The offset angle of 3.2° is shown in (b) with the nozzles active during a depainting experiment.



(a) 4-nozzle applicator installed in Shopbot jig above AF sample for paint removal



(b) Image of AF paint removal in progress using 2 nozzles at an angle of $a = 3.2^\circ$

Figure 112: Interaction of two plasma nozzles on an Antifouling coating surface.

Multi-pass Removal

Based on the preliminary single-pass two-nozzle removal tests described above, a number of multi-pass removals were performed to see the effect of the interactions between the multiple passes required to treat a larger area. All multi-pass removals were conducted with only nozzles 2 and 3 firing, a total airflow of 270 slm, and a height of 2 mm. All removals were also two-sweep – the pen was swept across the entire area being removed using standard single-pen removal interpass spacing (Δx), then removal was paused for 30 seconds or more, and then the pen was swept over the entire removal area again, at a slight offset (Δx_o) so the exact same area was not treated twice. It should be noted that most of the multi-pass removals conducted have used this same two-sweep or a three-sweep method employing an interpass spacing (Δx) plus a small offset (Δx_o) between sweeps. Two different speeds were tested, 6 or 7 in/s (152.4 or 177.8 mm/s).

It was found that good removal occurred when the interpass spacing was set to double the nozzle-interpass spacing ($\Delta x = 2\Delta x_n$), and the offset was half the nozzle-interpass spacing ($\Delta x_o = \frac{1}{2}\Delta x_n$). When all four pens are used, the interpass spacing should be four times the nozzle-interpass spacing, ($\Delta x = 4\Delta x_n$) and the offset should remain the same. The best removal attained during this testing had an interpass spacing of 0.08" (2.032 mm), offset of 0.02" (0.508 mm) and a speed of 6 in/s (152.4 mm/s). When the same spacing was maintained and the speed increased to 7 in/s (177.8 mm/s), small amounts of primer remained on the sample. Figure 113 shows the resulting removal swaths for the above conditions. From left to right, the features correspond to: pre-existing single pen single pass removal; multi-nozzle multi-pass removal with too-wide interpass spacing; and successful multi-nozzle multi-pass removal – 0.08" interpass spacing, speed 6 in/s. Thus, this preliminary removal data shows that two nozzles can effectively remove Antifouling coating to bare steel at a treatment rate of between 6.0 and 7.0 ft²/hr (0.557 m²/hr). It

is expected that with further time spent on optimization of the multi-nozzle multi-pass treatment, this rate may be further increased. Nonetheless, the results of this initial test (between 3 and 3.5 ft²/hr per nozzle) compare favorably with the previously-demonstrated single-pen removal rate of up to 3.3 ft²/hr.



Figure 113: Multi-nozzle multi-pass removal on an Antifouling coupon.

More work could be completed with the existing prototype, including removal testing with a larger number of samples and using Freeboard coating in addition to Antifouling, in order to gain a better understanding of coating removal variability across a range of parameters. It is expected that with further testing and optimization of the treatment parameters, higher multi-pass removal rates could be achieved. Thermal measurements using either static thermal camera measurements or in-situ thermal probes would provide a clearer picture of the effect of multiple nozzles on surface heating. Multiple modules may be produced of the current design to test eight or twelve nozzles, although additional hardware and facilities would be required for full testing.

The upcoming higher-power power supply design should allow for full power, full airflow testing of four nozzles concurrently and potentially higher power levels. Improved applicator design may also increase removal rate and/or efficiency. The vacuum/safety shield design may be fabricated and tested in future work

Multi-nozzle Removal

A small DoE was conducted to investigate a wider range of conditions which might be suitable for two-pen removal on the Antifouling coating. Conditions were selected based on results from the previously-reported multi-nozzle removals, as well as some additional preliminary multi-

pass, multi-nozzle removals. Three angles (1.4, 1.8, and 2.3 degrees) and three speeds (5, 6, and 7 in/s (127, 152.4, and 117.8 mm/s)) were tested in a full-factorial design with two repeats. The three angles correspond to nozzle-inter pass spacing of 0.03, 0.04, and 0.05 inches (0.76, 1.02, and 1.27 mm) respectively.

All multi-pass removals were conducted with only nozzles 2 and 3 firing, a total airflow of 270 slm, and a height of 2 mm. Electrical parameters for each removal were held the same. Because the power supply was of an older design than that used for other testing, the power level was set to a similar level (~2 kW) to standard conditions. The frequency used was 65 kHz; operating bus voltage was 290 V. All removals were also two-sweep – the pen was swept across the entire area being removed using standard single-pen removal interpass spacing (Δx), then removal was paused for one minute, and then the pen was swept over the entire removal area again, at a slight offset (Δx_o) so the exact same area was not treated twice. It should be noted that most of the multi-pass removals conducted used this same two-sweep or a three-sweep method employing an interpass spacing (Δx) plus a small offset (Δx_o) between sweeps. Since it was found that good removal occurred when the interpass spacing was set to double the nozzle-interpass spacing ($\Delta x = 2\Delta x_n$), and the offset was half the nozzle-interpass spacing ($\Delta x_o = \frac{1}{2}\Delta x_n$), these spacings were set based on the nozzle-interpass spacing generated by each angle.

The conditions tested generated area treatment rates ranging from 3.75 to 8.75 ft²/hr (0.348 to 0.813 m²/hr) (Table 14). The fastest treatment rate that was fully successful (removed to bare metal over the entire treated area, no primer remaining) was 7 ft²/hr (0.650 m²/hr), occurring at an angle of 1.8 degrees and a speed of 7 in/s (Figure 114). The two faster rates left some primer, a small amount in the case of the 7.5 ft²/hr rate samples and more in the case of the 8.75 ft²/hr samples (Figure 115). Samples treated at slower treatment rates tended to be over treated, showing thin oxide formation (Figure 116). The two nozzles tended to have slightly different removal efficacy, such that one would either under- or over-treat more than the others. Because the new power supply under development had improved controls and monitoring, it was anticipated that future work would allow for better power-balancing between multi-nozzle systems.

Table 14: Conditions used for two-nozzle DoE.

	Treatment Rate (ft ² /hr)	Speed (in/s)		
		5	6	7
Pen Orientation Angle	1.4	3.75	4.5	5.25
	1.8	5	6	7
	2.3	6.25	7.5	8.25

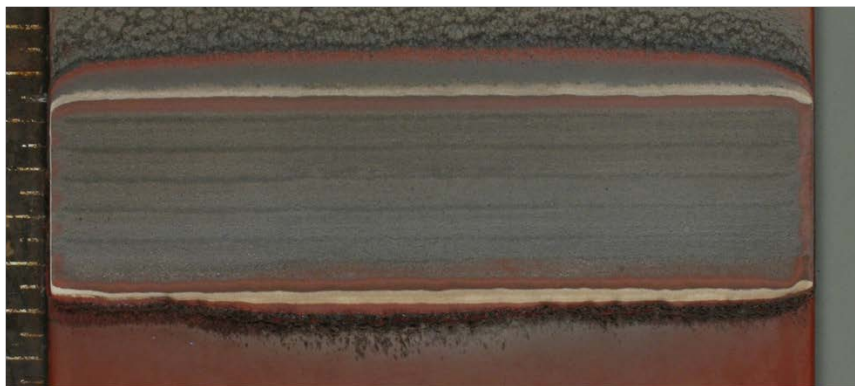


Figure 114: Sample SER-AF-187, which was treated at a speed of 7 in/s with an array angle of 1.8 degrees. (Treatment rate 7 ft²/hr).

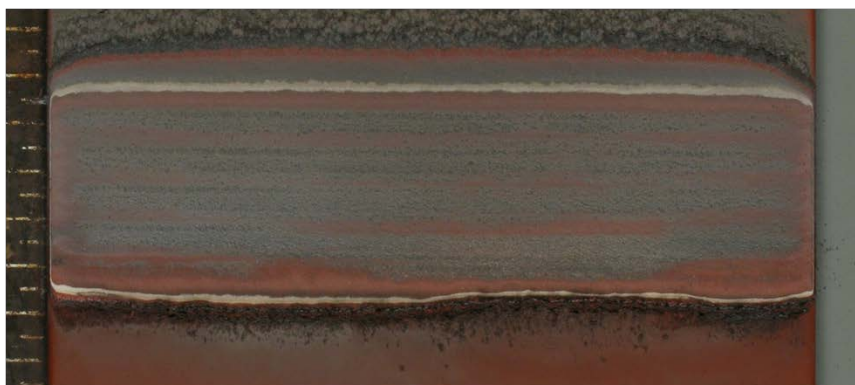


Figure 115: Sample SER-AF-195, which was treated at a speed of 7 in/s with an array angle of 2.3 degrees. (Treatment rate 8.75 ft²/hr).

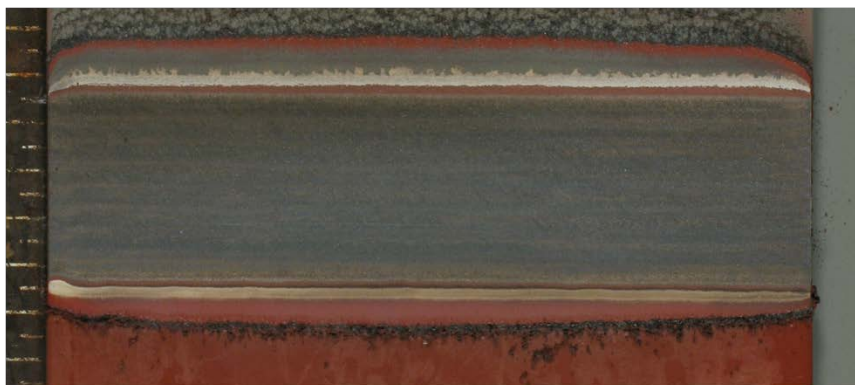


Figure 116: Sample SER-AF-199, which was treated at a speed of 5 in/s with an array angle of 1.4 degrees. (Treatment rate 3.75 ft²/hr).

Power Supply Improvements:

AP Solutions developed a rugged, high power, atmospheric plasma power supply which was capable of driving an array of plasma pens, as in the multi-nozzle approach reported here or in a

master/slave configuration with combined outputs to power a single, higher power plasma pen. This new power supply design is an extension of the PlasmaFlux™ power supply which incorporates the design improvements listed in Table 15.

Table 15: Listing of design improvements for atmospheric plasma high power supply.

Parameter	Legacy Power Supply	New Power Supply	Improvement
Input Voltage	220 VAC, 1 ϕ , 60 Hz	480 VAC, 3 ϕ , 60 Hz	Compatible with dry dock power
Full Power Output	2 kW	10 kW	> 4 times power density
Output Voltage	2.2 kV RMS	2.5 kV RMS @ full power	
Output Current	1 A RMS @ full power	1 A RMS @ full power	
Switching Frequency	90 to 120 kHz	100 to 200 kHz	Expanded frequency range for process flexibility
Regulation	Unregulated	Constant Current or Power	Precise, repeatable control
Multi-Pen	No	Yes	Can drive a single higher power pen or multiple pen arrays

The new power supply design operates at more than four times the power density (10 kW); however, the overall power supply dimensions are the same as the legacy PlasmaFlux™ power supply. More efficient power switching components allowed for the new power supply to operate with lower switching losses resulting in lower operating temperatures for increased reliability of the power components. Water cooling of the switching transistors was used to allow higher overall energy density of the power supply. For compatibility with Navy dry-dock facilities, the new power supply operates off either 208 VAC or 480 VAC input power and uses COTS components wherever possible to meet the necessary regulatory and safety requirements. The PCB design was performed to ensure compliance with the applicable commercial safety standard UL61010-1. During the construction of the four-pen system, some defects in the original PCB were found. These defects prevented the system from operating safely. The defects in the PCBs were identified and corrected by APS engineers. Using the corrected PCBs, the power supply was able to successfully fulfill all of the stated design goals. Initial bench (low power) testing using only one active single pen as a prototype was conducted to confirm operation of the system components. The power supply design was finalized with the incorporation of an optimized power control scheme which enabled improved plasma initiation and more efficient power transfer to the plasma than the legacy power supply.

Multi-nozzle Removal

With the manufacture and initial electrical testing of the four-nozzle system, complete, full-power removal testing began using up to four nozzles on 4" x 6" Antifouling samples in order to establish a baseline for the performance of the new system. This testing began with single-pass mass removal trials with one or multiple nozzles, as well as multi-pass removal with four nozzles, in order to compare with previous baseline data. Future work will continue the scale-up momentum with refinement of the treatment parameters and treatment of larger areas.

Single-Pass Mass Removal Trials

Single-pass removal tests were conducted with active plasma firing from one, two, three, or four nozzles. Air was flowing through all four nozzles of the array regardless of how many nozzles had plasma firing. All tests were conducted on the Antifouling coating stack. Conditions for all runs were: array angle (α) of 3.2° (Δx_n of 0.0698 in), speed of 100 mm/s, height of 2 mm, and air flow of 350 slm. The treatment array angle, speed, and height were selected to match previously-obtained baseline data for the previous multi-nozzle system with two full-power nozzles. The new power supply allowed removal at higher flow rates than the previous system (270 slm total), which has previously been found to improve Antifouling removal rates. Flow rate may be further investigated in future removal trials. Figure 117 contains a photograph of all four nozzles active during a single pass removal experiment.



Figure 117: Four active nozzles driven by the new power supply during a single pass experiment to remove Antifouling paint.

Figure 118 and Table 16 contain the data obtained from the one to four active nozzle mass removal experiments. The total mass removal was found to increase as more nozzles were activated. This was not unexpected since more nozzles equates to more plasma and more paint removed. This trend in total mass removed increased in progression from one to two to three to four nozzles. Of interest, however, was that the mass removal per nozzle increased significantly from one and then two nozzles. The mass removed held steady from two and three nozzles, and dropped off as the fourth nozzle was brought online. If each nozzle were infinitely separated from its neighbor, then the paint removal would simply be a sum of the individual nozzles and mass removed/nozzle would be consistent. By bringing the plasmas closer together it was anticipated that there would be a synergistic effect of multiple plasma streams active in overlapping areas. This combined effect should remove more paint per unit time, which was observed from one to two nozzles.

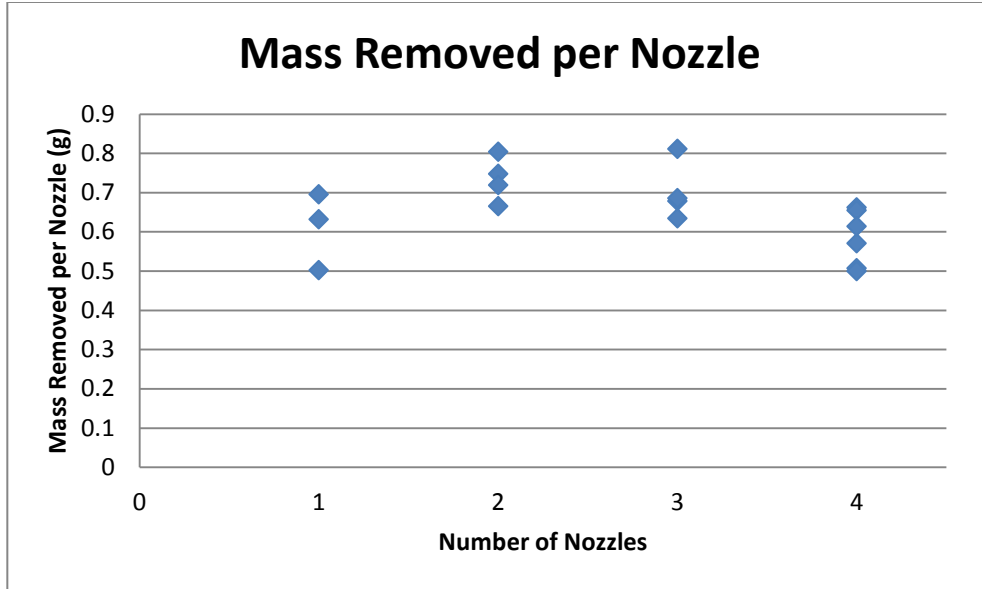


Figure 118: Mass removed per nozzle for different number of active nozzles in a single-pass experiment.

Table 16: Total and average Antifouling paint mass removed using one, two, three, or four active nozzles with the new power supply and four-pen array.

Number of active nozzles	Total mass removed (g)	Average mass removed per nozzle (g)
1	0.6097	0.6097
2	1.4675	0.7338
3	2.107	0.7023
4	2.5013	0.6253

At some point, however there is either no more paint to remove or the plasma streams are not working synergistically. From an electro-physics perspective, since each plasma stream could be considered independent, care must be taken to ensure there is no cross talk (electrical discharge, break down, exchange) between plasma plumes. Plasma by its nature is electrically conductive. If there is cross talk between plumes, not only is the power not used effectively for removing paint, but the power supply must compensate for this change in impedance and adjust power accordingly. The new power supply and nozzle configuration manufactured by APS did a good job at controlling the plasma. What this experiment demonstrates is that additional plasma plumes do in fact work synergistically, but there is a diminishing return. It must be pointed out that all of these experiments are operated in “free flow” whereby the collective plumes exhaust freely to the air (high pressure to atmospheric pressure). In addition, the plumes were in a linear configuration so the only overlap was along a single axis. It is speculated that once a confinement system such as a waste collection shroud is added, the plumes would be more contained and able to work even more synergistically in the same volume of space. There should be more synergy with two-axis arrays, for example a honeycomb hexagonal configuration. The interior of such array would be nearly 100% plasma, while the exterior would be exposed to air

on the outside and plasma on the inside. Clearly, there is much to learn about multiple plasma plume configurations as they relate to paint removal.

A photograph from one of the four-nozzle single-pass experiments is shown in Figure 119. The plasma stripped paint to bare metal in a single pass. The conclusion reached was that by the time the fourth nozzle reached the surface, the paint was gone and so there was no additional mass to be removed. This same effect would be expected with any type of top down mass removal method, even for grit blasting.

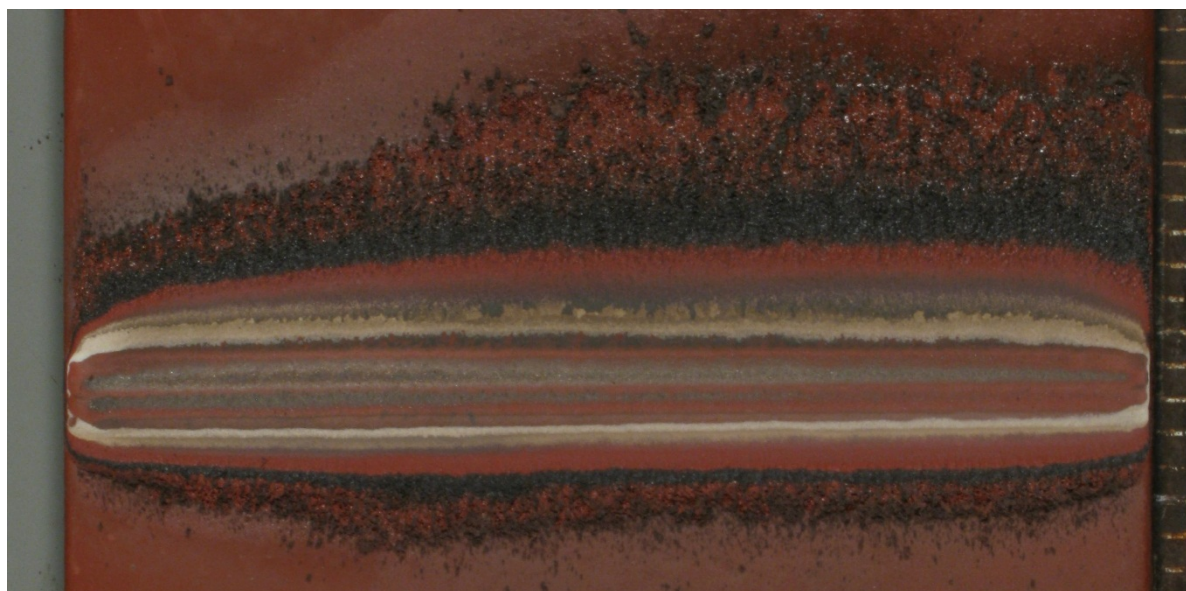


Figure 119: Photograph of Antifouling sample after a single-pass experiment with four active nozzles and the new power supply. (Mass removed was 2.649 g, or 0.6623 g per nozzle).

Also of interest, as can be seen in the photograph, is that each layer of the paint is visible. The author does not recall specifically the stack for this sample, but it appears to be metal/red primer/grey primer/red AF/black AF/red AF. Notice that each layer is in a pristine condition as if cut with a microtome. There is some feathering on the upper side likely due to the exhaust created by the plasma plume. The color of each layer is visible. On the surfaces outside of the plasma exposed region are what at first would seem to be charred material. Waste generated by plasma has been referred to as ejecta throughout this project. Analysis by microscopy and EDAX has shown this material in particular is removed paint which has been deposited outside of the active plasma area. One goal of these experiments is to remove the paint as quickly as possible. In that mode of operation, not all of the paint is completely broken down into mineral form. Some of the paint is still intact and/or adhering to filler particles. In addition, some of the material has a tacky texture which indicated incomplete oxidation. Also specific to Antifouling paint, is the presence of copper from the paint which has a catalytic chemistry by nature. The copper might be participating in a chemical reaction which occurs in the highly active plasma plume. The ejecta material is subsequently removed and further broken down in the next pass of the plasma.

Single-pass removal testing with four full-power nozzles showed mass removal rates of up to 2600 mg/s on Antifouling coating stacks, with an average of ~2500 mg removed or ~625 mg

removed per nozzle. Previous baseline data for the same array angle and speed ($\alpha=3.2^\circ$, $s = 100$ mm/s) yielded an average removal of only 437 mg per nozzle (874 mg total) on similar Antifouling samples. This represents a per-nozzle mass removal improvement of greater than 40% over the previous system.

Because these runs were conducted at 100 mm/s speed over ~100 mm wide samples (+/- 5%), the removal masses reported here can also be used as mass removal rates for comparison to other testing (i.e. 2500 mg removed translates to approximately 2500 mg/s mass removal rate for a single pass). It should be noted that the first pass over an untreated sample generally achieves a significantly higher removal rate than subsequent passes, due to the larger volume of coating available at the surface to be removed. Furthermore, the mass removal rate further decreases as the metal substrate is revealed. Because removal to metal is a requirement, the mass removal rate becomes less important than the treatment rate for larger area, multi-pass removal, as discussed in the following section.

Multi-pass Removal Rate Trials

The single-pass trials indicated that the mass removal rate for the new system was considerably higher than the previous system had achieved. Because single-pass tests do not provide good data to calculate a real removal rate, multi-pass removal trials also were completed as part of the baseline testing. Preliminary multi-pass removal testing with four nozzles was completed using the same array angle ($\alpha=3.2^\circ$) as the single-pass settings and previous multi-pass data with the previous system, in order to provide comparison baseline data. Figure 120 shows the four-nozzle applicator during a multi-pass treatment.

Table 17: Comparison of current and previous single- and multi-pass removal results.

	Four Nozzle Improvement	Current result Four Nozzle		Previously reported result Two Nozzle	
	Per Nozzle	Total (four nozzle)	Per nozzle	Total (two nozzle)	Per nozzle
Single-pass removal (mg/sec)	43%	2501.3	625.3	873.5	436.8
Multi-pass removal (ft ² /hr)	46%	20.5	5.1	7	3.5

A full DoE will be completed in the next section; however, this preliminary data has given promising indications of improved performance. Single-sweep multi-pass removal was conducted at different interpass spacing and speeds with the goal of achieving full removal to metal without significant primer remaining. As can be seen in Table 17, this goal was achieved with removal at a treatment rate¹ of 20.5 ft²/hr (1.9 m²/hr), which actually resulted in some

¹ Treatment rate is calculated based on scan speed, s , interpass spacing Δx , and number of repeat sweeps, n , using the following formula: Treatment Rate = $s * \Delta x / n$

This maintains consistency with single-nozzle removal results, and accounts for the fact that each nozzle spends equal time over the sample. Production rates, on the other hand, must account for time spent off of the sample, which varies with the type of setup.

excess treatment of the sample, indicating that even higher treatment rates are possible while maintaining full coating removal.

Thus, with further optimization, it is expected that rates higher than 20.5 ft²/hr (1.9 m²/hr) can be achieved with the new four-nozzle system. The per-nozzle treatment rate attained in these trials was 5.125 ft²/hr/nozzle. The highest successful treatment rate attained during two-nozzle DoE multi-pass removal trials was 7 ft²/hr, or 3.5 ft²/hr/nozzle. This preliminary result represents a per-nozzle increase of greater than 40% in comparison to earlier two-nozzle DoE results of 3.5 ft²/hr per nozzle for the same coating stack.



Figure 120: Four active plasma nozzles over the Antifouling coating surface during a multi-pass experiment.

Four-Nozzle Removal

This task consisted of a group of studies using the four-nozzle system to remove Naval coatings, with a focus on Antifouling coating, which had been determined to be the primary target at that stage in the project. The task provided a good base upon which to build future work with larger area removals and more nozzles. Much of the work of this period was carefully planned to gain understanding of the four-nozzle coating removal process in order to lay the foundation for upcoming eight-nozzle removal work.

The Antifouling samples used in this work were repainted samples prepared at NCSU. Once the 77 samples were received, they were unpacked and allowed to continue curing for a few days. Samples were inspected for obvious visual defects. Coating thicknesses were measured at five points across each sample using an ElektroPhysik MiniTest 740. Any sample that had a ≥ 10 mil variation across it was rejected. Samples were photographed front and back, and then isopropyl

alcohol was used to wipe pre-existing markings from the back of each sample. A new ID number was applied to the back of the sample, and the back was re-photographed.

Coating thicknesses of these repainted samples were, on average, 15.5% greater than thicknesses of the original Antifouling samples, which were used for all single-pen tests to date. The original samples were 19 mils average dry film thickness, in comparison to 22.5 mils average for the repainted samples.

Multi-nozzle Geometry

The geometry of the eight-nozzle array is such that completely matched nozzle-interpass spacing for all nozzles would occur at an array angle of 10.89° , which corresponds to a nozzle-interpass spacing of 0.236" between each adjacent nozzle. Work with single- and multi-pen removal has shown such wide spacing to be ineffective for complete removal to metal. In order to achieve a narrower spacing, the array must be turned to a smaller angle so that the removal swaths from each of the four-pen modules are brought closer together, but a larger gap is left between the swaths from the two modules. In order to provide even coverage over the sample, this gap between the two modules' swaths may be subdivided into so-called subpasses. The planned raster pattern for the eight-nozzle array would result in each of the two four-pen arrays removing alternating swaths, with each swath consisting of multiple subpasses. Thus, there will be several small Δx movements followed by a larger Δx movement as the front array is moved past the area which the back array has already treated. The angles selected for the DoE described below correspond to angles at which an integer number of passes will fit in each removal swath – three subpasses for 3.96° , four for 3.00° , and five for 2.42° .

In order to properly test these multi-pen sweep patterns, a precise method of controlling the array angle in the robotic treatment stage was required. A permanent raised straightedge was installed on the sample stage's baseplate, parallel to the Y-axis (fast axis of motion). A sine bar can be set to an arbitrary angle in reference to the straightedge. The pen array is adjusted to match the sine bar angle by pushing the sine bar into place against the pen body and tightening the retaining clamp. By using a 5" long sine bar and precision gauge blocks, angles can be set to better than 0.1 degree precision for the purposes of this testing.

Height Investigation

To determine the effect that height above sample had on removal with the multi-nozzle system, single-pass tests were conducted at two array angles: 3.00° and 80° ; and four heights: 0.079, 0.118, 0.157, and 0.197 in (2, 3, 4, and 5 mm). The large angle was selected because it minimized between-nozzle interactions and allowed each nozzle to leave a distinct, measurable removal swath (Figure 121). The smaller angle was selected to provide significant overlap of the four removal swaths, and to match the central angle used in the full-factorial DoE (described below). At both array angles, the test conducted at 0.079 in (2 mm) height removed 15-20% more mass than tests conducted at any of the higher conditions. Results from the 80° tests showed that the removal swath left by each nozzle did increase in width by about 20% for heights above 0.079 in (2 mm), as measured using calipers. Figure 121 shows a sample treated at 80° ; the individual removal swaths are clearly visible. However, the "depth" of removal decreased as height increased – coating thickness measurements (within removal swaths) post-treatment were thicker on samples treated at higher heights (corrected for initial

coating thickness). The conclusion was that of the four heights tested, 2 mm was the most likely condition to yield removal to metal, although the influence of height would need to be explored with the eight-nozzle system and larger samples to see how this effect scales.



Figure 121: A sample treated by a single pass with an 80 degree array angle.

Each removal swath is distinct, and its width easily measurable. The sample is 4" (100 mm) wide and scale markings on edges are at 1/16" (1.588 mm) increments.

Antifouling DoE

A Design of Experiments (DoE) was conducted to investigate a wider range of conditions which would be suitable for four-pen removal on the Antifouling coating. Conditions were selected based on planned 8-pen geometry and results from the previously-reported multi-nozzle removals, as well as some additional preliminary multi-pass, multi-nozzle removals. Three angles (2.42, 3.00, and 3.96 degrees) and four speeds (2.953, 3.937, 5.906 and 7.874 in/s (75, 100, 150 and 200 mm/s)) were tested in a full-factorial design with two repeats. The three angles correspond to nozzle-interpass spacing of 0.05275, 0.0655, and 0.0864 inches (0.76, 1.02, and 1.27 mm) respectively. Table 18 details the conditions used in this DoE and their respective treatment rates.

Table 18: Conditions tested in this DoE

		Speed, in/s (mm/s)			
Treatment Rate, ft ² /hr (m ² /hr)		2.953 (75)	3.937 (100)	5.906 (150)	7.874 (200)
Array Angle α (degrees)	2.42	15.577 (1.445)	20.768 (1.929)	31.149 (2.894)	41.535 (3.859)
	3.00	19.342 (1.797)	25.787 (2.396)	38.678 (3.593)	51.575 (4.791)
	3.96	25.47 (2.366)	33.957 (3.155)	50.931 (4.732)	67.913 (6.309)

All multi-pass removals were conducted at a height of 0.079 (2 mm) with electrical parameters for each removal held the same. Pen output power was approximately 2.5 kW per pen, resulting in a total power level of up to 10 kW. Unlike most of the multi-pass removals conducted to date for SERDP with fewer nozzles, these removals were single-sweep – the array was swept across the entire area being removed only once. Each removal consisted of six passes, resulting in a total treated area of 5 to 8.3 in² (0.0032 to 0.00535 m²) (array angle dependent).

While the conditions tested generated treatment rates which ranged from 15.577 to 67.913 ft²/hr (1.447 to 6.309 m²/hr), only treatment rates of 20.768 ft²/hr (1.929 m²/hr) or less resulted in near-complete removal to bare metal. Treatment rates of 25.787 to 38.678 ft²/hr (2.396 to 3.593 m²/hr) resulted in some exposed bare metal, while treatment rates greater than 38.678 ft²/hr left significant amount of primer remaining over the entire treated area. Figure 122 shows a sample that received the most aggressive treatment (angle of 2.42°, speed 2.953 in/s (75 mm/s), treatment rate 15.557 ft²/hr (1.445 m²/hr)). Figure 123 and Figure 124 show samples which were treated at rates of 19.342 and 20.768 ft²/hr (1.797 and 1.929 m²/hr), respectively.

A small amount of primer remains in the area treated by the first and second passes (lower portion of image), but by the fifth and sixth passes (upper portion of image) oxide formation is becoming noticeable. The sample is four inches (100 mm) wide, and scale markings on edges are at 1/16" (1.588 mm) increments.

Another trend that can be seen across the samples is that the first pass has clearly weaker removal than subsequent passes, and oxide formation becomes more prevalent on later passes. A similar trend had been observed with one- and two-nozzle systems. Previous work has also shown a plateau effect, where initial passes are reduced efficacy, but then through the bulk of the sample, removal will stabilize. This further supports the decision to move to larger samples for additional work, as such edge effects will be reduced. Optimizing the treatment regime for larger samples may require speed “ramping” to account for these effects. A positive side effect

of such an adaptive treatment (increasing speed over time) will be a net increase in the treatment rate.

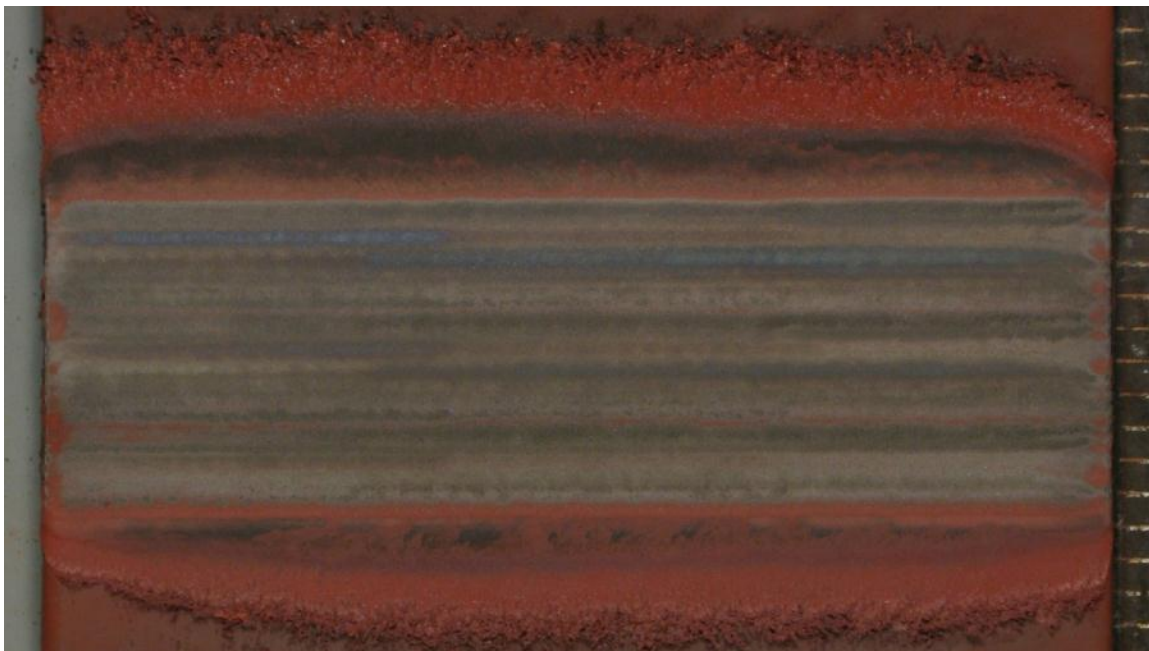


Figure 122: Antifouling sample treated with conditions: angle of 2.42° , speed 2.953 in/s (75 mm/s), treatment rate $15.557 \text{ ft}^2/\text{hr}$ ($1.445 \text{ m}^2/\text{hr}$).

An important observation with the four-nozzle removal of Antifouling coating is the formation of ejected material left on the surface after a pass. Before four-nozzle removal trials had been conducted, there was concern that with multiple interacting nozzles, the buildup of the combined ejecta of all of the nozzles could hinder removal. The ejecta left by one pass on the sample must be removed by a subsequent pass, and if a large buildup occurs, each subsequent pass could become increasingly less effective. Fortunately, with the raster patterns used in this work, this was not found to be a significant issue. Instead, as discussed above, the removal efficacy is seen to actually increase in subsequent passes. Further work with the eight-nozzle applicator will be necessary to ensure that this trend continues with larger systems.

Overall, the most effective removal to metal occurred with the smallest array angle ($\alpha = 2.42^\circ$) tested. Also, as would be expected, the higher treatment speeds (i.e. higher treatment rates) resulted in less oxide formation. As discussed above, the angles that were chosen for this work correspond to angles believed to be best for rastering the upcoming eight-nozzle applicator. This method provides an easy way to adapt and compare the current work to the eight-nozzle applicator. Naturally, the doubling of the number of nozzles (from four to eight) and transitioning from one row of nozzles to two is a significant change to process and will likewise require significant further work to understand and optimize. At this time, however, the evidence would indicate that small angles and faster scan speeds are a promising path forward with the eight-nozzle applicator.

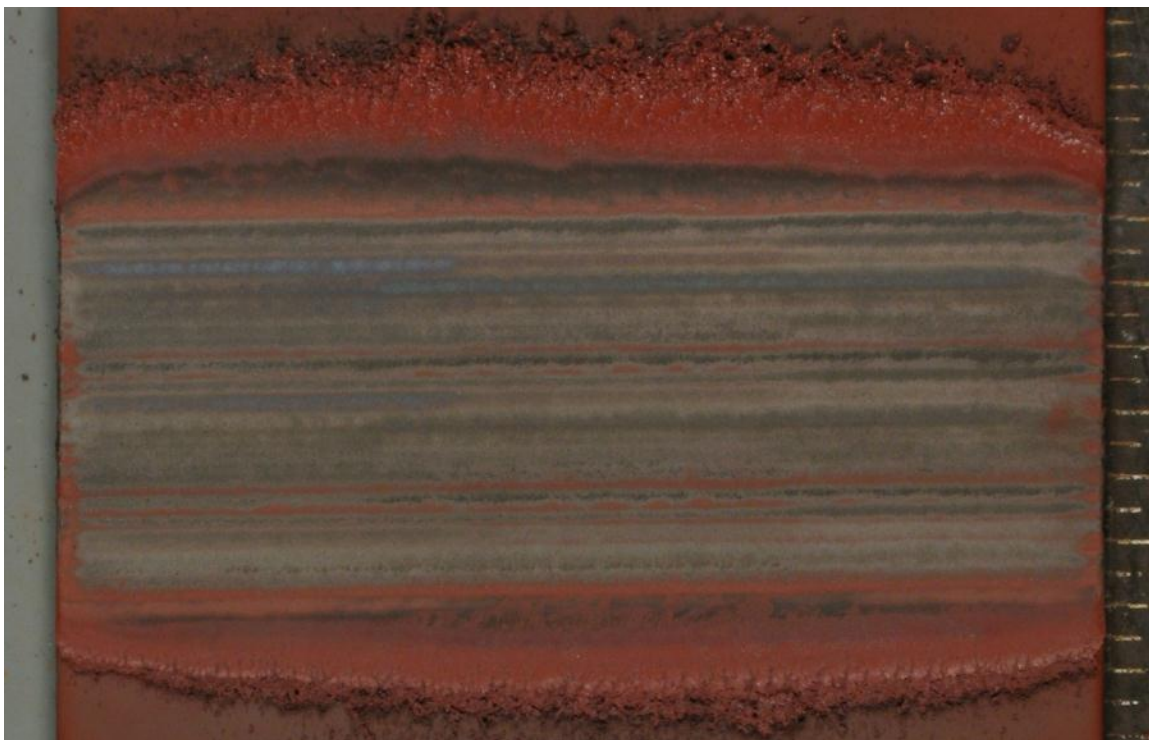


Figure 123: Antifouling sample treated with conditions: angle of 3.00°, speed 2.953 in/s (75 mm/s), treatment rate 19.342 ft²/hr (1.797 m²/hr).

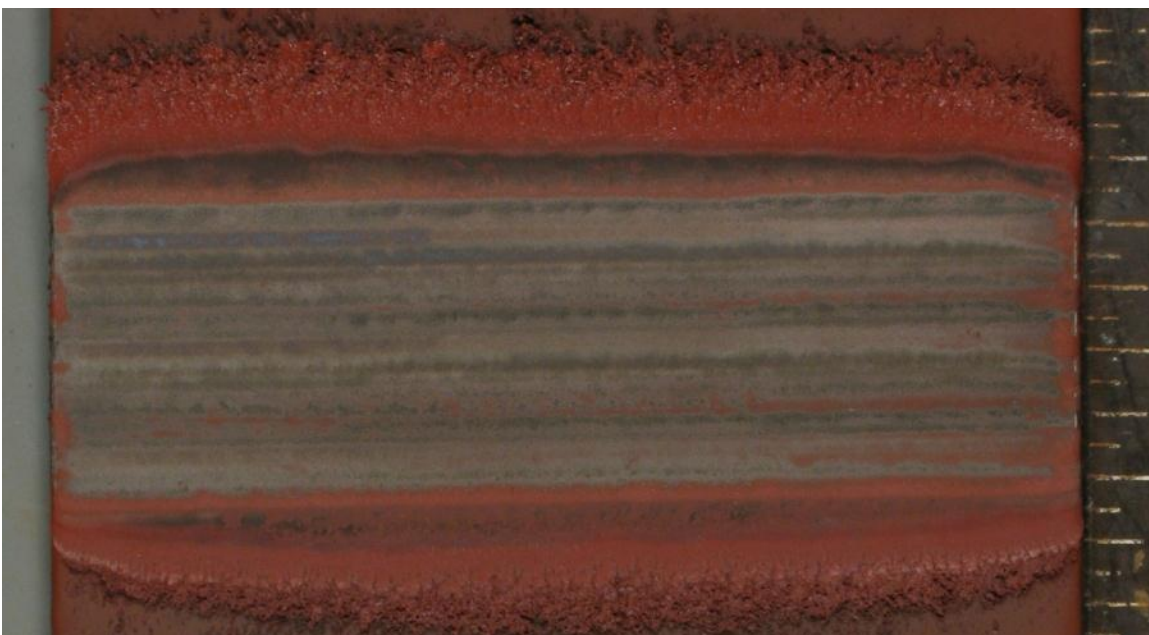


Figure 124: Antifouling sample treated with conditions: angle of 2.42°, speed 3.937 in/s 100 mm/s, treatment rate 20.768 ft²/hr (1.929 m²/hr).

FREEBOARD DoE

Following completion of the Antifouling DoE, a subset of the conditions used was repeated as a smaller Freeboard DoE in order to provide comparison data to the Antifouling. Past work with

fewer nozzles has shown that the conditions needed to successfully remove Antifouling and Freeboard paint are rather different. As an example, the single pen conditions used to successfully remove Antifouling for Task 2 (for depaint and repaint study) resulted in an effective interpass spacing of approximately double those found to be effective for Freeboard, although the Freeboard treatments allowed for a faster ultimate scan speed. Based on the knowledge that Freeboard coatings had previously required more aggressive treatment, the two smaller angles from the Antifouling DoE (2.42 and 3.00 degrees) and the three slower speeds (75, 100, and 150 mm/s) were chosen and implemented in a full-factorial arrangement.

None of the condition combinations tested in this investigation was able to completely remove Freeboard to metal across the entire treatment area. Conditions resulting in up to 25.787 ft²/hr (2.396 m²/hr) did result in some bare metal showing, however. In order to attain complete removal of Freeboard, it is likely that the array angle would need to be further decreased, or a second sweep added to the treatment. Although the Freeboard coating is not the primary target at this time, future work will further investigate scaled-up plasma arrays on this coating system.

Recommendations for Further Research

Based on the multi-nozzle work to date, there are a number of recommendations for further research. The primary recommendation is to continue the scale-up work with the construction and testing of the eight-nozzle version of the applicator. Other recommendations are provided below, as well as an updated analysis of the scale of system required to meet Navy target rates. The synergistic effect of multi-nozzle systems has been shown throughout the scale-up effort of this project, and the next scale-up step of manufacturing an eight-nozzle system. It is believed that the increased number of simultaneous nozzles will further increase the per-nozzle removal rates achievable. More careful manufacturing tolerances are also expected to improve uniformity and overall reliability of the system.

Adaptive processing (speed ramping)

As discussed previously, the multi-pen system removal efficacy for removing to bare metal is lowest on the first pass and increases with subsequent passes. While automatic feedback is outside of the scope of the current work, adaptive treatment parameters may be used (to simulate future human or automated feedback) to increase the treatment speed over the course of a large sample run. This will have the added benefit of increasing the overall treatment rate.

Larger sample size (reduced edge effects)

While a great deal can be learned from removal on the smaller 4" x 6" samples, the multi-nozzle applicators are large enough that edge effects may be significantly affecting the results. Previous work has shown diminished removal rates at the edges. Thus, it is expected that larger area samples are likely to show improved removal rates and uniformity. On the other hand, the logistics of large samples necessarily limit the number of samples that can be run, and therefore can limit the amount of useful data for studies such as this. It was determined that the optimum sample size for the next set of tasks was 6" x 12" (152.4 to 304.8 mm).

Temperature studies

The current setup with 4" x 6" samples does not allow for ready access to the sample surface in order to monitor temperature, and real-time temperature measurements have not been

incorporated at this time. However, previous work has shown a strong correlation between high levels of surface oxidation and high surface temperatures, so an attempt has been made with work up to this point to control over-oxidation while still achieving removal to metal.

In preparation for scale-up work, additional larger panels 2 x 3 feet 3/8 inch thick were prepared using FB and AF paint (Figure 125).

Interlac 665 Haze Gray FB painted panel



FB and AF Panels loaded for Transport



Figure 125: 2' x 3' x (3/8inch) Panels Prepared for Scale-up Work.

Eight-nozzle Geometry

The geometry of the eight-nozzle array is such that completely matched nozzle-interpass spacing for all nozzles would occur at an array angle of 10.89° , which corresponds to a nozzle-interpass spacing of 0.236" between each adjacent nozzle. Work with single- and multi-pen removal has shown such wide spacing to be ineffective for complete removal to metal. In order to achieve a narrower spacing, the array must be turned to a smaller angle so that the removal swaths from each of the four-pen modules are brought closer together, but a larger gap is left between the swaths from the two modules. In order to provide even coverage over the sample, this gap between the two modules' swaths may be subdivided into so-called subpasses. The planned raster pattern for the eight-nozzle array would result in each of the two four-pen arrays removing alternating swaths, with each swath consisting of multiple subpasses. Thus, there will be several small Δx movements followed by a larger Δx movement as the front array is moved past the area which the back array has already treated, as shown in Figure 126.

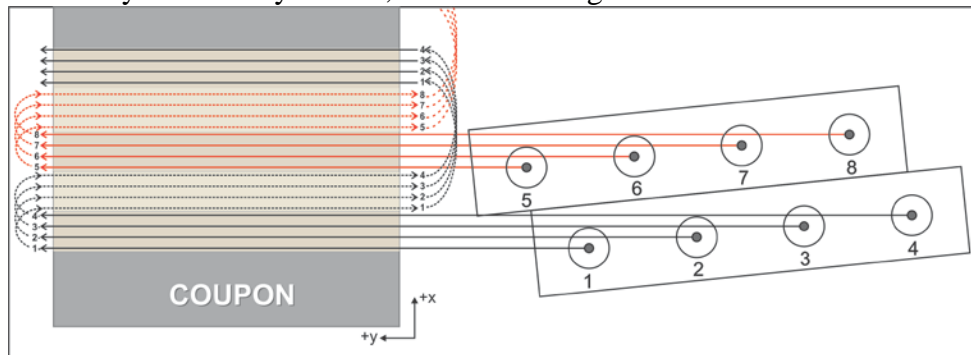


Figure 126: Illustration of the path of travel for the eight-nozzle array conducting a removal with a normal pass and an additional subpass: angle array is 5.82° .

Note that the array is moved by a smaller Δx once, then a larger Δx motion occurs to move the front four nozzles (black lines) past the area already treated by the back four nozzles (red lines). For the angles used in this work, two, three, or four small Δx movements (2 to 4 subpasses) occur before the larger Δx movement, with the size of each determined by the array angle.

This task emphasized the momentum of the ongoing scale-up effort to intelligently scale to multi-nozzle systems, by building on the results of the previous successful demonstration of a full-power four-nozzle treatment system. In moving from a 10 kW to a 20 kW system, much of the supporting mechanical hardware had to be upgraded in addition to the new applicator and power supply sub-assemblies.

Scaled-up Subsystems

Testing of the scaled-up eight-nozzle system required upgrades to the APS power supply and associated sub-assemblies, enabling safe and stable delivery of 20 kW to the control module. The semiconductor components and internal wiring required for this increased power capacity are typically used in fairly large industrial installations and require a greater degree of safety, conditioning, monitoring, and e-stop circuitry. This preparatory work was a significant subtask in order to manufacture the eight-nozzle system and also represents a significant step toward the industrial type of system that would be required to perform coating removal work on Navy platforms.

Based on the successful prior testing of a four-nozzle module, applicator and cabling subassemblies were manufactured and assembled for the eight-nozzle module. In order to provide optimum performance and uniformity of the scaled-up system, improved QC procedures were established and followed for these subassemblies. Necessary upgrades were also made to the air supply hoses, waste collection, multi-channel controller, and water-cooling subsystems to accommodate the scaled-up system.

Large Area (eight-nozzle) Plasma System Features

A 20 kW, eight-nozzle power supply was manufactured and tested for the large area plasma coating removal system. The underlying design features the ability to drive individual pens at higher power (>2.5 kW per nozzle possible) with independent control of each plasma pen in the eight-pen array. Preliminary baseline electrical testing was conducted on each channel of the eight-nozzle array to ensure safe and consistent operation. The new eight-pen plasma system is an extension of the PlasmaFlux™ power supply design which incorporates the design improvements listed in Table 15 above. Based on the success of the previously-demonstrated four-nozzle system implementation, a new system with double the power was manufactured in addition to the other scaled up subsystems described in the previous section. The new system was intended to have the same overall design and features as the four-nozzle system with the minimum set of improvements needed to ensure successful testing of a full-power eight-nozzle system to achieve the scale-up goals of this project. Figure 127 shows the final assembled eight-pen power supply.



Figure 127: The 20 kW plasma power supply manufactured for task 4.2.4.

Figure 127 shows the completed eight-nozzle plasma system enclosed in a standard 18" wide equipment rack. The power supply is approximately 42 inches tall and 20 inches deep. Space optimization was not of primary concern when building this prototype. It is possible to reduce this size by about 2/3 with a concerted effort to minimize volume.

Figure 128 shows the new eight-nozzle system under full power operation. Ten samples were treated at a variety of different processing conditions similar to the initial conditions under which the four- nozzle system was first tested. Preliminary results indicate satisfactory removal rates for an eight-nozzle system. The upcoming work for Task 4.2.5 will further test the performance and coating removal capabilities of the new system.

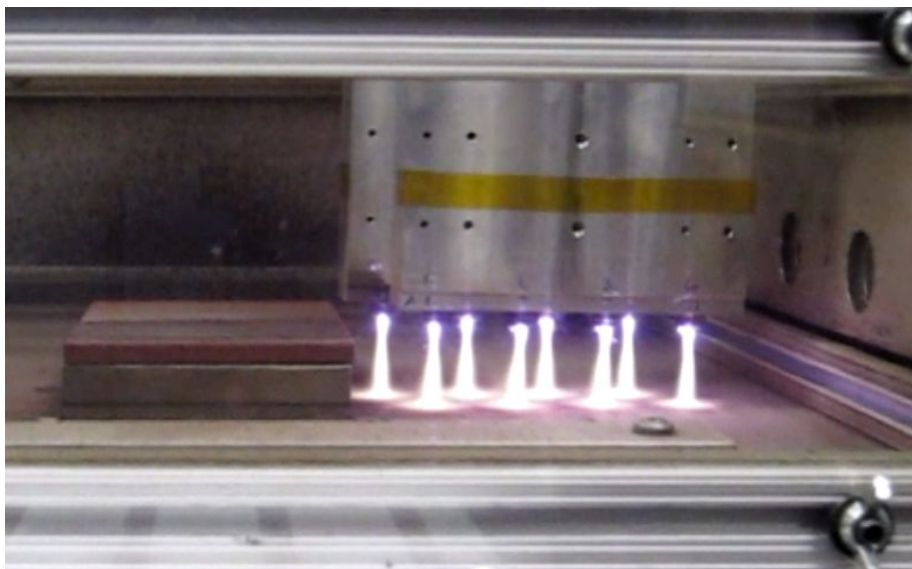


Figure 128: Photograph of eight-nozzle plasma applicator operating at full power.

Introduction

Upgrades to Supporting Subsystems

As testing of the scaled-up eight-nozzle system proceeded, several upgrades to the system were needed to support further testing to improve removal quality and provide a safe working environment. The transition to 6" x 12" samples required the construction of a new custom sample stage and the removal of the old waste collection chamber (which was built onto the X-Y table). This waste collection enclosure was replaced with a larger enclosure that encompasses the entire XYZ stage. Significant effort was required to ensure proper ventilation and sealing of the enclosure to provide a safe environment for removal testing of the larger samples. A silicon window was added to the enclosure for taking thermal images using a FLIR i40 thermal camera, which was calibrated with a 100 °C reference through the window. By manually taking images during the treatment, the surface temperature can be approximated, though future work with thermocouples embedded in the stage is recommended for more accurate data. Further effort was required in order to ensure that the fixtures holding the larger eight-nozzle applicator and samples were properly aligned and would sufficiently maintain their alignment throughout sample treatment with rapid movement, airflow, and other environmental changes.

Experimental results and conclusions

Due to the complexities of eight-nozzle removal, a number of different types of removal were attempted during this task, with varying results. All samples presented in this report are of the most recent batch of 6" x 12" Antifouling samples.

Some testing was conducted with the eight-nozzle head oriented at $\alpha=90^\circ$, such that the removal stripe of each nozzle interacted minimally with those of its neighbors, with one such sample shown in Figure 129. The sample shows eight discrete swaths (one for each nozzle) stacked vertically in the image—each nozzle was rastered up the sample until it met the removal swath left by the adjacent nozzle. As expected, this did not yield very uniform removal, leaving primer residue at the bottom of the swath, and overt treating at the top of each swath, with

sample temperatures as high as 224 °C observed. Some primer was also left in the area between adjacent nozzles' swaths.

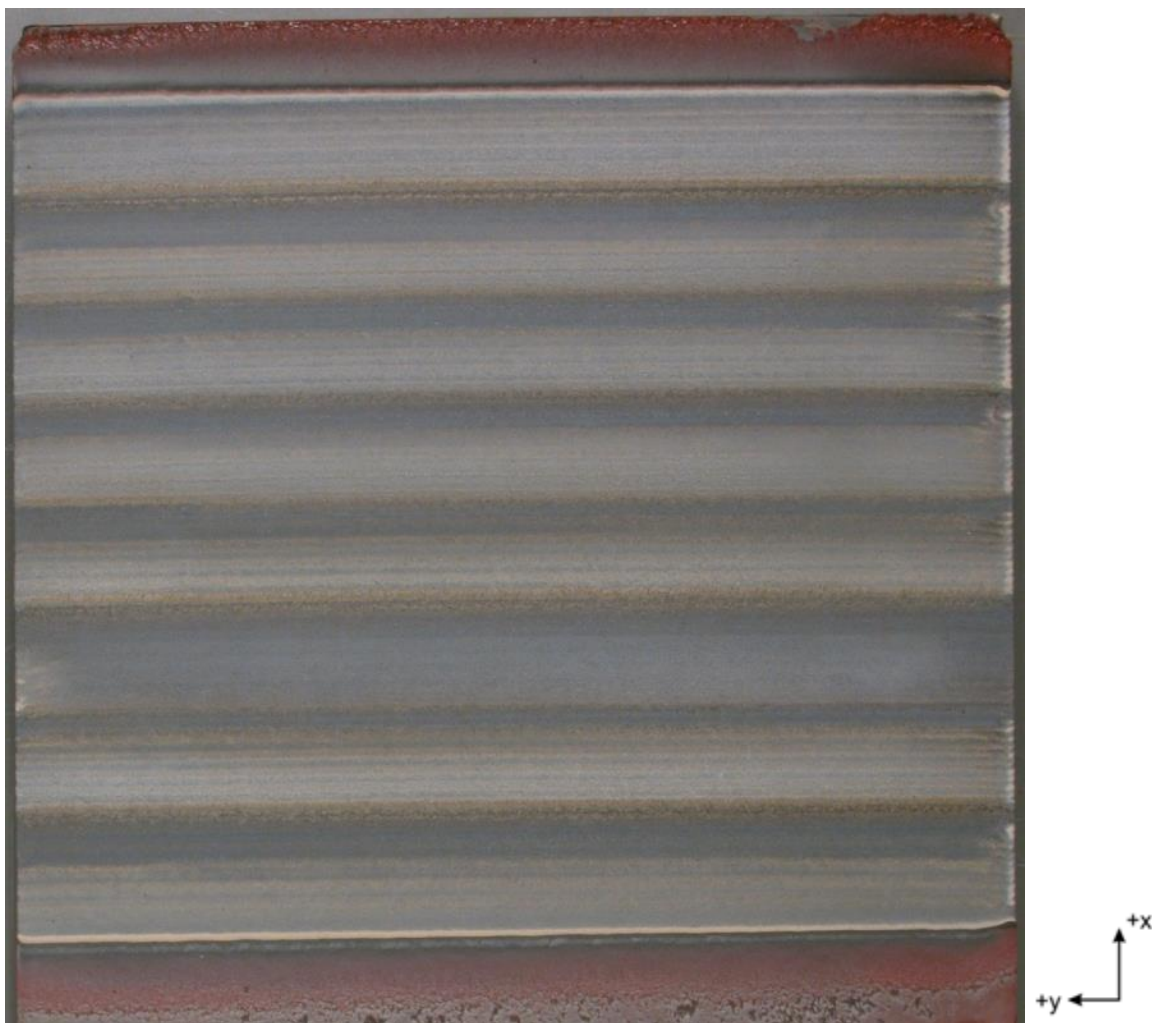


Figure 129: A treatment at $\alpha=90^\circ$, with a treatment rate of 19.7 ft²/hr. Note the high degree of both over treatment and under treatment in different areas.

Another set of experiments conducted removal at smaller angles. Figure 130 shows one such sample that was run with $\alpha=3.0^\circ$. Generally speaking, this method appears to more successfully expose bare metal at higher speeds, most likely benefitting from the much closer spacing of each nozzle's path and thus much greater interaction between them. Sample temperatures were also lower than the 90° tests, with this sample having a maximum observed temperature of 165 °C. However, at this early stage in testing, it appears that the eight-nozzle system will require further tuning and balancing of the power between nozzles in order to further increase the uniformity and removal rate. This particular removal achieved a high degree of bare metal at a 25.8 ft²/hr treatment rate but also has some areas of both overtreatment (oxidation) and under treatment (remaining primer).



Figure 130: A treatment at $\alpha = 3.0^\circ$, with a treatment rate of $25.8 \text{ ft}^2/\text{hr}$.

This removal yielded significant bare metal exposure, but some primer remains in addition to some areas of increased oxidation. Another promising type of removal was also conducted where the angle was set to very small angles, close to $\alpha = 0^\circ$, to allow for maximum interaction between the nozzles' swaths. Figure 131 shows one such removal with a $\alpha \sim 0^\circ$ and a treatment rate of $37.8 \text{ ft}^2/\text{hr}$, with a maximum observed temperature of 127°C . This type of treatment yields a lead-in and lead-out area of $\sim 1''$ that only receives partial treatment, then a central region with the full treatment. In the case of the sample shown, this central area is about $3'' \times 6''$. As can be seen in the figure, there is primer remaining in the initial part of the central area of treatment (toward the bottom of the image), occupying up to 40% of the area, but the remaining primer percentage diminishes as the treatment continues until it is as low as 10% at the top portion of the treatment.

Removal conditions with such small alpha angles result in considerable overlap of each nozzle's treatment area, which may reduce the removal efficiency. Thus, further adjustments to angle and other run parameters are expected to yield better removal rates in upcoming work. For

comparison, the four-nozzle removal work of 4.2.1 and 4.2.3 previously yielded treatment rates of up to 20.8 ft²/hr (~5.2 ft²/hr per nozzle) on Antifouling samples with trace amounts of primer remaining, as discussed in previous reports. The highest successful treatment rate attained during two-nozzle DOE multi-pass removal trials (Task 4.2.2) was 7 ft²/hr, or 3.5 ft²/hr per nozzle. Single nozzle results were on the order of 3.3 ft²/hr for Antifouling removal to metal. With further optimization, the eight-nozzle removal is expected to exceed these previous results and continue the forward momentum of the scale-up effort.



Figure 131: A treatment at $\alpha = \sim 0^\circ$, with a treatment rate of 37.8 ft²/hr.

This removal yielded ~60-80% visible bare metal in the active central region. It should be noted that the transition from four nozzles to eight nozzles represents a major change in treatment geometry from a one-dimensional type array (one row of four nozzles) to a two-dimensional array (two rows of four nozzles each) and thus represents a significant increase in the number of treatment variables which affect removal. While this particular task was limited in time and scope, it did lay a foundation to explore the processing techniques which will yield high quality removal with a multi-nozzle system. With further refinement of the low angle types of setup and with additional techniques such as adaptive processing and non-linear treatment, removal rates approaching 50 ft²/hr are expected to be possible. This would allow for treatment of 150 ft²/hr with 24 nozzles total.

Engineering specifications of the scaled-up system

The modular approach employed for the multi-pen design has maintained many of the properties of the single nozzle system studied earlier in this project. The single pen measured 1.25" diameter by ~8.5" length (excluding cabling), while the four-nozzle module maintains this 1.25" distance between nozzles, and allows for two-dimensional arrays at this spacing. The four-nozzle module measures ~5" W by 1" D by 8.5" length (excluding cabling). An assembled eight-nozzle applicator weights approximately 3 kg, versus approximately 0.35 kg for a single pen, excluding cabling and fixtures.

As previously discussed, the power requirements have changed for the new four- and eight-nozzle systems, allowing for higher power systems more compatible with Navy shipyard requirements. Per nozzle airflow requirements have remained similar, with the range of 100-120 slm per nozzle typically used in current eight-nozzle work. With the transition to a higher power density power supply, the eight-pen system uses water cooling, rather than the forced air cooling used with earlier one-, two-, and four-nozzle systems. The move to a larger eight-nozzle applicator and larger 6"x 12" samples has also necessitated an upgraded waste collection system enclosure, larger sample stage, and upgraded fixture to hold the larger samples and applicator securely and with the proper orientation while the pen is moving.

Task 5 Hybrid Module Construction and Evaluation (cancelled)

5.1 Design Hybrid Module (cancelled)

Task 6 Technologies for Waste Stream Management

6.1 Lab-Scale Manual System

Waste collection had not been a focus of this program since early work with the single pen systems. Perhaps a major reason was that there just is not that much waste generated, especially when compare with the large amount of waste generated from grit blasting or water jetting. In addition, any waste that has been generated was easily collected using common vacuum cleaner type devices and there have been no problems with operator or equipment contamination. Existing waste collection systems that have been used in the laboratory work have only needed small enclosures that fit on the robotic sample stages.

Early in the project, qualitative evaluation of the waste composition from a single-nozzle plasma exhaust found that particle counts exceeded the maximum reading of the meter (although this may have been due to a high background particle count for the laboratory air). NO_x and CO were also detected, especially in the "worst case" scenario tested in which the ventilation equipment was shut down. NO_x was detected at levels of 0.5 ppm vented, 1.2 ppm non-vented, while CO was detected at a level of 2 ppm non-vented and not detected while the ventilation was running. In the rare occasion when plasma has been fired without ventilation, some plasma operators have reported being able to smell NO_x even after a brief firing. The human odor threshold for nitric oxide (NO) is between 0.3 and 1 ppm (CDC), and the human odor threshold for nitrogen dioxide (NO_2) is 5 ppm.

As a result, there has not been a need to further develop any containment systems for small area treatments. The conclusion was reached that, depending on the need of a specific depainting application, perhaps there might be a need for specific adaptors to be developed for that application. This could be compared to a common shop vacuum type system in which there are various adaptors attached to the end of the hose. Provided the operator received sufficient instruction regarding any potential hazards, adaptation for use in small areas was considered unnecessary at this time.

6.2 Automated Large Area System

Media-free removal technology and vaporization of organic paint components results in much smaller mass of waste than media-based technologies which means that collection systems are well within the current capabilities of Navy processes. As has been previously discussed, the plasma removal process does yield some solid waste. Most of the particulate matter that becomes airborne as dust is from fillers in the paint which do not become oxidized because by their inherent nature they are already oxidized. Other larger particles may contain small fragments of paint still adhering to filler particles and some very small droplets of tacky residue due to partially oxidized organic species may redeposit away from the plasma plume. All of the waste material collectively has been referred to as “ejecta” in this project. If not completely broken down, some of this ejecta can deposit slightly ahead of the plasma applicator, such that it is treated on subsequent passes. This can be compared to grit blasting where if some paint is not removed during the first pass, and operator can go back over an area to ensure complete paint removal. Atmospheric plasma can be operated in the same manner to ensure all areas have been cleaned. Solid waste re-deposition has not yet been shown to significantly hinder removal on the sample surface. However, as removal rates increase with scaled up samples, there has been a trend in increasing amounts of build-up of ejected solid material including on the underside of the plasma applicator. Other raised surfaces near the removal site may also have some material deposited during large area aggressive removal conditions. This material is relatively loosely adhered and can be knocked off such as with a puff of compressed air or use of a wooden dowel. Thus far, the appearance of the buildup on the applicator has not been seen to have a significant effect on paint removal. Larger sample tests should provide a better idea if this will present an issue for scaled-up systems, and more localized waste collection designs (such as vacuum shrouds) would be expected to pull this material away from the site before it could re-deposit.

A commercial off the shelf (COTS) Oskar Environmental Model SPC-G3 portable fume filtration system was evaluated for the purposes of waste management scale-up. This system commonly used for welding exhaust features a 3 HP motor (230V, 7.5 Amps, 60 Hz, 3450 RPM), with three-stage filtration and dust drawers, as well as an externally-mounted 2.5” deep HEPA filter. The system has a rated flow of 1200 cfm. The system also has an infrared remote control, a reverse pulse cleaning system, and two articulated standing fume arms (6” diameter, 10’ length) with 13” diameter conical fume funnels installed on the end of each. There are two 6” diameter and one 8” diameter inlet ports, and the HEPA-filtered exhaust port is ~30” wide by 24” high. A small steel enclosure was fabricated to attach a 6” duct to the exhaust, which was expanded to 12” to allow venting of exhaust gases to outside. The standing arms were also removed in order to use the 8” inlet for this work.

As a first step, the COTS filtration unit (“Oskar”) was adapted to the current lab-scale waste collection system, as shown in Figure 132. The existing waste collection system featured a

smaller fume collection unit in conjunction with the inner waste collection chamber shown in the diagram. The waste collection chamber sits atop the XYZ table, with a central chamber of ~18" by ~22" into which small samples can be mounted. A transparent sliding window is fitted around and moves with the plasma applicator. The sliding window effectively cuts the usable area within the chamber in half and so is only useful for samples up to approximately 6" by 12". At the left and right sides of this chamber are vacuum plenums which draw exhaust out of the chamber and down into four inch flexible ducts which feed into a fume collection unit. The existing fume collection unit featured a 2 HP motor and five micron single-stage filtration, with a five inch inlet. For the current work, this fume collection unit was replaced with the Oskar filtration unit, which provided higher power, a larger (less restrictive) inlet, and improved filtration (down to the HEPA level).

The new waste collection system was tested on Naval coating removal. The system was found to work well for solids collection, such that significant amounts of the solid wastes did not escape the inner chamber. However, this system was found to lack adequate vapor-phase filtration for indoor use without exhausting outdoors. Further work will be needed to address this issue to make this system appropriate for lab-scale work. This system could be made to work by ensuring the unit is sealed from exhaust gases leaking out of the fume collector chassis and venting the exhaust directly outdoors.

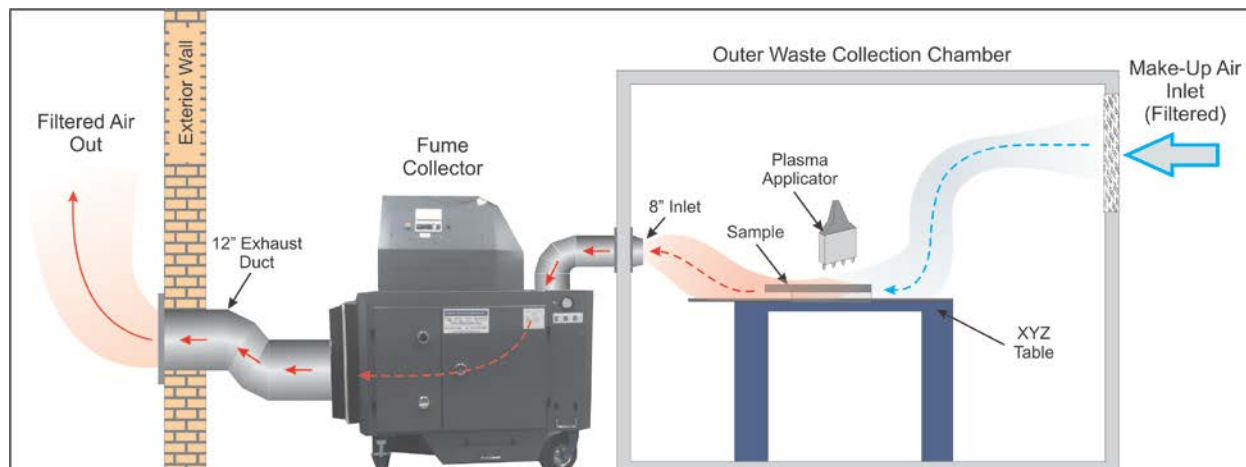


Figure 132: Large area waste collection system.

Summary of Available Waste Collection Technologies

In addition to the work with adapting the waste collection systems, other available technologies for collection of solids and gases were investigated as summarized below.

Welding Fume/Solids Collectors

Commercially available fume collectors generally consist of a portable (wheeled) body with one or more hinged extraction arms. These collectors extract solid particulate matter from the waste stream, with many claiming to remove particles as small as 0.5 μm . While several brands of these devices include carbon filters, they do little to extract VOCs and do not mitigate the NO_x produced in coating removal. They are readily available and relatively inexpensive as a filtered solids-collection solution, although a custom vacuum shroud or chamber is required, and vapor-phase waste must be either separately treated or exhausted away from operators.

Examples:

Oskar Air Products – Model Name: Giant*

(<http://www.oskarairproducts.com/products/filter-units/giant/>)

*the fume collector currently in use is a model similar to this model

DIVERSI-TECH Inc. - Model Name: FRED

(<http://www.diversitech.ca/product-line/dust-smoke/fred-02-02c.aspx>)

Miller - Model Name: Filtair

(<http://www.millerwelds.com/products/fumeextraction/product.php?model=M00328>)

Chemical/solvent vapor collectors

These systems also consist of a portable (wheeled) body; some have similar extraction arms to the welding fume collectors. Some brands offer filters designed to remove particular types of chemical/solvent vapors; others contain very large amounts of activated carbon. In order to prevent clogging from particulate matter, such a system would need to be installed downstream of a particulate filtration system. However, these systems have a much lower flow rate than welding fume collectors. These vapor collectors also do not remove NO_x. The use of media and the low flow rates mean that such systems are likely not practical for use with atmospheric plasma coating removal.

Examples:

Sentry Air Systems

(<http://www.sentryair.com/heavy-dutyindustrialchemicalfumeextractor.htm>)

Fumex: (<http://fumeextraction.fumexinc.com/item/all-categories/chemical-and-solvent-extraction-2/g3-00?&plpver=10&origin=compare&filter=0&CTypeID=2>)

NO_x Management

NO_x is a pollutant, contributing to the production of acid rain and can also cause severe respiratory damage to workers exposed to it. There are several technologies used in NO_x abatement: standard catalytic converters, Selective Catalytic Reduction (SCR), and NO_x adsorption. Standard catalytic converters have been used for decades in automobile emission control systems to mitigate the release of NO_x compounds, as well as carbon monoxide and unburnt hydrocarbons from gasoline-engine exhaust into the atmosphere. A typical design features a high-surface-area ceramic core coated with a catalytic material. When the engine exhaust passes over the catalyst, the NO_x compounds are reduced (to O₂ and N₂), while the carbon monoxide and hydrocarbons are oxidized (to carbon dioxide and water). Standard COTS catalytic converters are designed specifically for the exhaust composition of gasoline engines and also require several minutes to “warm-up” to become effective. This technology might be useful for atmospheric plasma coating removal but would likely require a custom design suited specifically for the exhaust of the atmospheric plasma process.

SCR uses a catalyst and a reductant (typically ammonia) to convert NO_x to N₂ and H₂O. This reaction requires a temperature from 225 to 450 °C to operate. The majority of these systems are very large and geared towards industrial installations, such as power plants or industrial diesel generator sets. Smaller units are made for diesel-powered vehicles, but these still require high temperatures and continued addition of the reductant to function. Additionally, it is possible for

the SCR reaction to become “poisoned” by certain compounds, which can reduce the effectiveness of the catalyst; however, these would be filtered out by earlier stages of filtration.

NO_x absorbers, which are also sometimes referred to as Lean NO_x Traps (LNTs), use zeolite as a molecular “sponge” to collect NO_x while an engine is running under lean conditions. The trap can be purged/regenerated by then briefly running the engine in rich conditions. However, this technology is typically used specifically for combustion engine exhaust and is still experimental and thus expensive and only works at temperatures between 150 and 500 °C.

Examples:

SCR: Peterbilt (http://www.peterbilt.com/pdf/PACCAR_SCR.pdf)

LNT: BASF (http://www.basf.com/group/corporate/en/brand/BASF_LNT)

In preparation for scale-up activity and expectations for field demonstration, planning was performed in which current grit blasting methodology could be applied to atmospheric plasma depainting. Figure 133 contains a diagram representing the components of a grit blasting operation. Those items which normally would involve the grit would be replaced or modified for use with atmospheric plasma as needed. Starting with the air compressor, the size and specifications might be greatly diminished depending on the demands of the plasma equipment. Dried air would still be needed for the plasma and for the operator if used in confined spaces.

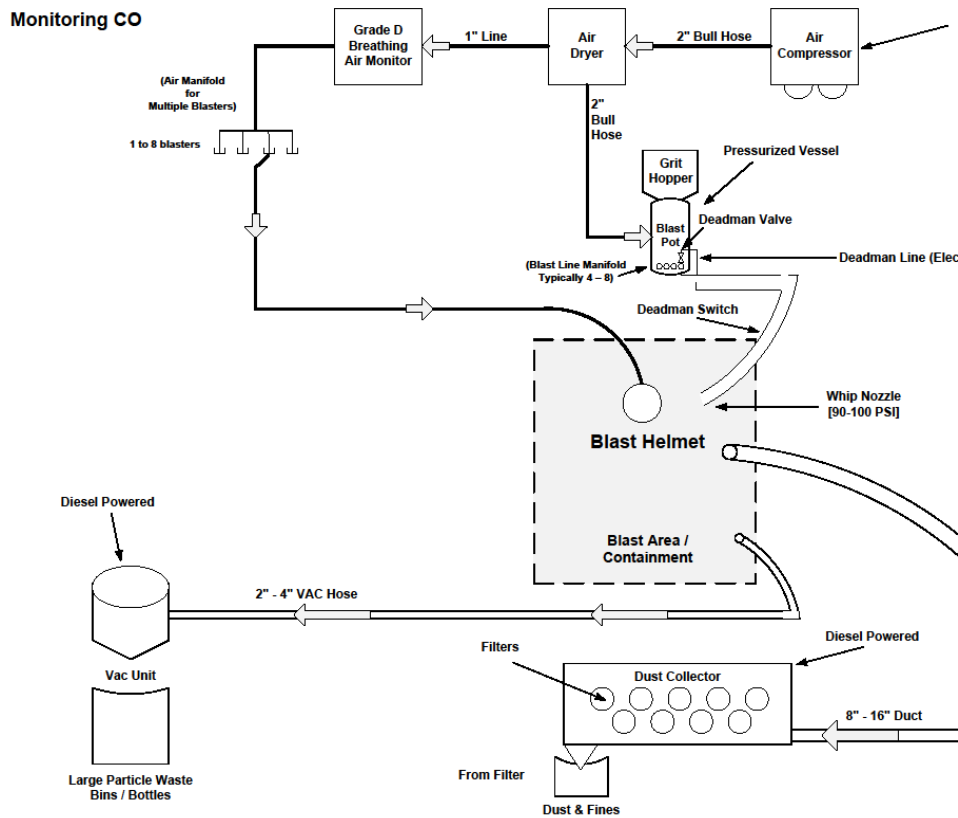


Figure 133: Schematic diagram of a single operator grit blasting operation.

If operated outdoors, it is unlikely the operator would need demand air, but that would depend somewhat on the collection system for waste of the plasma system. The grit hopper, blast pot, and associated equipment would be replaced with the plasma system. The large particle waste bins would not be needed since there would be no media used. However, the dust and fines collection would likely need some modification for connection to the plasma system. In summary, the flow diagram would be very similar to grit blasting. As for the costs and benefits in making any needed changes; that would be a subject of future evaluation. It could be argued that elimination of the huge volume of grit along with the associated collection, storage and disposal methods needed justifies consideration of plasma for further investigation.

6.3 Hybrid Modules (cancelled)

Task 7 Quantify Risks for Environmental Hazards and Operator Safety

From previous work using atmospheric plasma interacting with various organic compounds, carbon dioxide and water have been identified as significant by-products of chemical reactions. Therefore it seemed prudent to calculate the total amount in mass of by-products which would be generated from typical Navy paint on the most common classes of vessels. Table 19 contains the results of these calculations. There were several assumptions made in order to simplify calculations. First, all paint was assumed to be in the form of hydrocarbon (only hydrogen and carbon). Starting mass was calculated from MIL specifications. Oxygen was not included in the initial mass, but would come from air and be part of the waste mass. Real paint systems have complex chemistries which add elements such as nitrogen, oxygen, and silicon. In another part of this research, polyethylene was used as a model compound to test this theory, and was compounded with varying amounts of TiO_2 in order to simulate paint formulations. A second assumption did not account for any changes which might occur to inorganic fillers when exposed to atmospheric plasma. There are numerous different types of fillers including hydrates, carbonates, silicates, and carbon black, which might change upon exposure to the aggressive oxidizing environment of atmospheric plasma. Another assumption was made in calculating the filler content from manufacturer's data sheets, which often include only the filler amount in paint formulations and not the dried and cured product. The average thickness of each paint layer was determined from MIL specifications, which subsequently provided the ratio of organic to inorganic content.

Table 19: Calculation of CO₂ which would be generated using atmospheric plasma to remove paint from Navy ships assuming all paint is converted to CO₂ and H₂O.

Ship	Total Surface area (m ²)	Total Paint Mass (kg)	Total CO ₂ (kg)	Total Solids (kg)
Destroyer	12,900	7,219	5,920	5,335
Aircraft Carrier	74,000	38,019	32,930	27,542
Amphibs	21,300	11,372	9,610	8,315
Cruisers	14,000	7,580	6,440	5,532

Assumptions

- Paint composition is $-(CH_2)_x-$
- 100% $CH_2 \rightarrow CO_2 + H_2O$
- Inorganic content
 - Primer: 83.88%
 - AF: 82.82%
 - FB: 36.40%

For Comparison

- 5.48mt CO₂ /car per year
*<http://www.epa.gov/oms/climate/420f05004.htm>

As seen in Table 19, since paint is heavily loaded with inorganic fillers, it was not surprising that after depainting, the waste mass was approximately 75% of the original paint mass. This is quite significant compared to current operations. For grit blasting, waste solids are 100% original paint mass plus all the grit necessary to remove the paint. In the case of water jet, assuming all the water was separated from the waste, there would still be 100% of the mass remaining for disposal. Considering that huge amounts of both grit and water are required, the use of atmospheric plasma with only air as the media represents a tremendous opportunity for savings. At the minimum, this represents a 25% decrease in waste product needing to be disposed.

More striking was the amount of gas produced. Water would be generated in vapor form and most likely diffuse from the operation unless condensed to liquid in collection equipment. Due to their surface area, aircraft carriers have the most paint. Using these figures, after plasma depainting, the resultant carbon mass of waste generated is 27,542 kg of CO₂. In order to put this into perspective, the EPA calculates that the average car in the US generates 5.45 mt. Therefore stripping paint from an aircraft carrier with atmospheric plasma generates about the same amount of CO₂ as five average cars in the USA (1 mt = 1000 kg). This insignificantly small amount could be collected during waste removal but would likely not be worth the effort. This is such a startling fact that it is worth repeating. The amount of CO₂ generated using atmospheric plasma to strip paint from an entire aircraft carrier is approximately the same amount as generated by five automobiles in a year.

The purpose of Task 7 was to identify those aspects of atmospheric plasma depainting which could potentially be harmful to operators of the system and the resultant waste products which could be harmful to the environment and/or operators. Identification of operational hazards is

discussed later in the project since it was necessary to build and test the plasma system while researching various hazardous forms such as solid, liquid, gas, thermal, irradiative, sound, and physical. At the beginning of the project, however, it was necessary to identify potential hazards in order to ensure safety of the researchers.

7.1 Milestone - Qualitative Gas Analysis

To ensure safety of the researchers during the project, North Carolina State University's Environmental Health and Safety officials were asked to evaluate the operation of atmospheric plasma while stripping paint from test coupons. Test equipment was placed in locations typical of where the operator might be exposed to the hazard. Tests were conducted with plasma depainting operating in two modes - with the evacuation equipment activated and without, in order to create a worst case scenario. Due to the numerous safety interlocks on the plasma equipment, the use of digital flow meters, interlocks and limit switches on the ShopBot, and other measures, most hazards were mitigated. Data is presented in Table 20 which summarizes the safety review. Safety eye glasses are mandatory especially due to the use of compressed air and ejecta created during operation. Sound levels were negligible, although for extended operation ear protection is available and frequently utilized. Exhaust gases such as carbon monoxide, carbon dioxide, ozone, and NO_x which escaped confinement were well below acceptable limits. The greatest hazard detected was particulate matter. One known hazard with many types of paints which might be of special concern is crystalline silica particles below one micron in size. These can accumulate in the lungs and result in cancer. The TSI instrument used for the measurement is not capable of measuring particle size or chemistry but is a merely a total particle counter. Of interest to note was that measurement of the laboratory air away from the plasma equipment also gave particle counts at the saturation limit of the equipment. In other words, the laboratory was too contaminated to obtain accurate measurements. In response, additional experiments such as those in Task 7.2 were conducted. Nuisance dust masks are worn for extended operation.

Table 20: Quantitative measurements of gas and solid components which the operator would be exposed to during the operation of atmospheric plasma depainting.

Qualitative Gas Analysis (for researcher's safety)

NCSU Environmental
Health and Safety Review



Gas/Device	Non-vented	Vented
CO Draeger Tube	2 ppm	0 ppm
NO _x Draeger Tube	1.2 ppm	0.5 ppm
O ₃ Draeger Tube	None detected	None detected
O ₂ displacement Mini-Rae	None detected	None detected
VOC PID	10 ppm	1 ppm
Sound Extech	78 dB	85 dB
Particle count TSI	>50,000	>50,000

7.2 Lab-Scale Manual System

Waste Analysis of Solids

A 34 Liter aluminum cylindrical aluminum chamber with a closed bottom and sealing lid were cleaned thoroughly using isopropanol and acetone. Two holes were machined in the lid to allow an airtight pass-through of the plasma applicator and attachment of a vacuum hose. The inlet of the vacuum hose attached to the lid was covered with a copper filter mesh with 177 micron pore size. A sample mounting stage for 10.2 cm x 15.2 cm samples was placed inside the aluminum chamber and held in place using magnets. The 10.2 cm x 15.2 cm painted steel substrate was held in place atop the stage also using a magnet. The plasma applicator was affixed to the lid such that it was held a constant 4 mm away from the surface of the painted steel substrate. Figure 134 illustrates the collection setup in detail. All materials used inside the test chamber were cleaned and weighed before insertion into the test chamber. A set of 2.54 cm long adhesive carbon tape strips used to immobilize samples for Scanning Electron Microscopy (SEM) prior to application of plasma were also weighed. The paper towels that were used in collecting and cleaning the chamber after removal were individually weighed and marked with their pre-use weight.

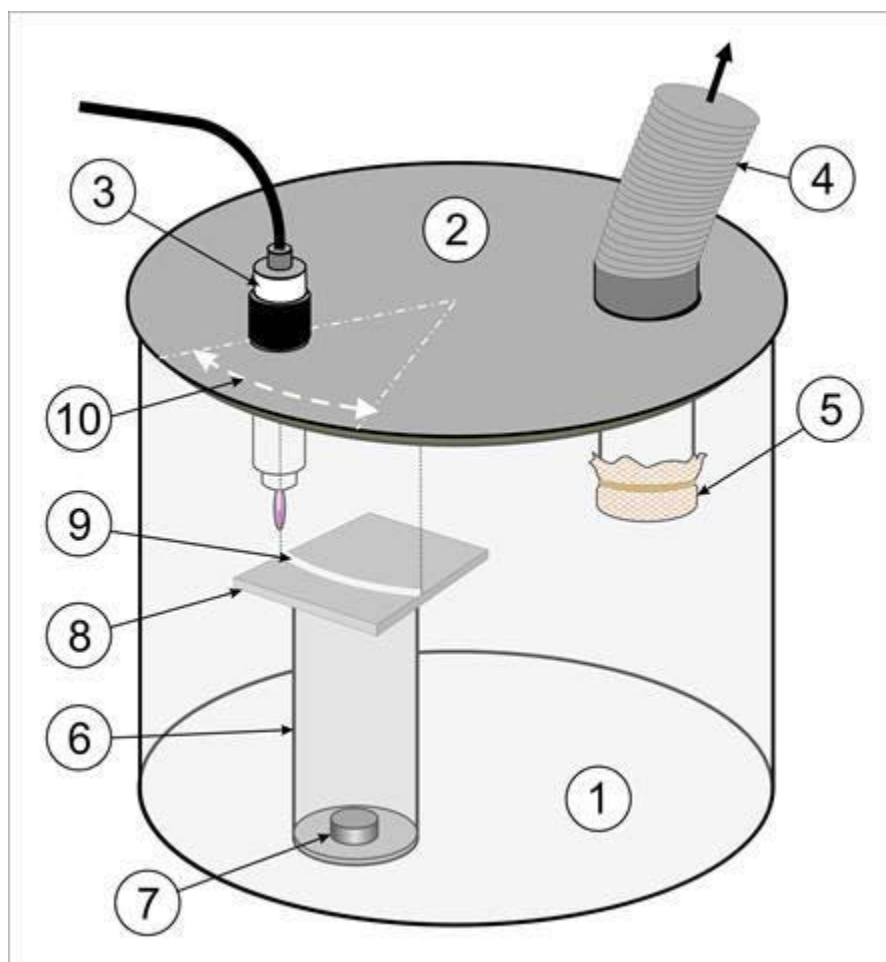


Figure 134: Schematic illustration of set up for ejecta collection during depainting.

The plasma was rastered across the painted steel substrate by rotating the lid. The pen was located 10.2 cm from the central axis of the lid, and the painted steel substrate was 10.2 cm wide. The arc length across which plasma pen was rotated was approximately 10.6 cm. Once a pass was completed, air flow into the chamber was stopped, the lid was opened and the sample was quickly shifted about 10 mm towards the center of the chamber to prepare for the next application. The lid was closed and airflow restored, then plasma was again applied in an arc across the painted steel substrate. Five application passes were completed on each painted steel substrate. The plasma conditions used for these removals were: four mm height above the painted steel substrate, applicator normal to the painted steel substrate, airflow of 115 slm, and an approximate speed of 100 mm/s. However, speed was found to be difficult to regulate, so removal was somewhat variable across each pass.

After plasma treatment, the sealed chamber was left undisturbed for several minutes to allow particulate matter to settle. The carbon tape was used to collect small samples from three locations: the painted steel substrate (approximately one inch away from the first removal stripe), the copper mesh filter, and the bottom of the chamber, where the largest particulate matter had collected. The tape strips were returned to their container and reweighed. The painted steel substrate and filter were removed from the chamber and reweighed as well.

The previously weighed paper towels were wetted with isopropyl alcohol and used to clean all particulate matter from the test chamber, lid, plasma pen, and stage. The isopropanol soaked towels were returned to their container and left to dry. The towels were reweighed repeatedly over several days until their weight had stabilized indicating complete evaporation of isopropanol solvent.

Conductive carbon tape strips were used to collect samples for SEM and Quantitative Energy Dispersive Spectroscopy (EDS) from three different areas within the test chamber as described above. The samples were delivered to EAG labs in Raleigh, NC for analysis to determine particle sizes and elemental composition of the solids.

Particle Size:

A rough idea of the particle size of the ablated paint residue was determined using SEM images and naked eye observations. An overview of the SEM images of both Freeboard and Antifouling residue showed a distribution from 100's of microns to less than one micron particles. Figure 135 and Figure 136 show typical Freeboard SEM images. Figure 137 shows an example SEM of Antifouling residue. Visual observation of the residues of both sample types with the unaided eye showed particle sizes ranging from five mm to less than 0.5 mm or 500 microns. It is assumed that a continuum of particles between 500 microns to 100 microns were also present although no data was specifically taken to prove this assumption. The methods used in this task to determine particle size do not give a useful particle size distribution, rather just an overview of the particle sizes present. Further investigation is required to produce a full particle size distribution indicating the percentage of particles present for each particle size range.

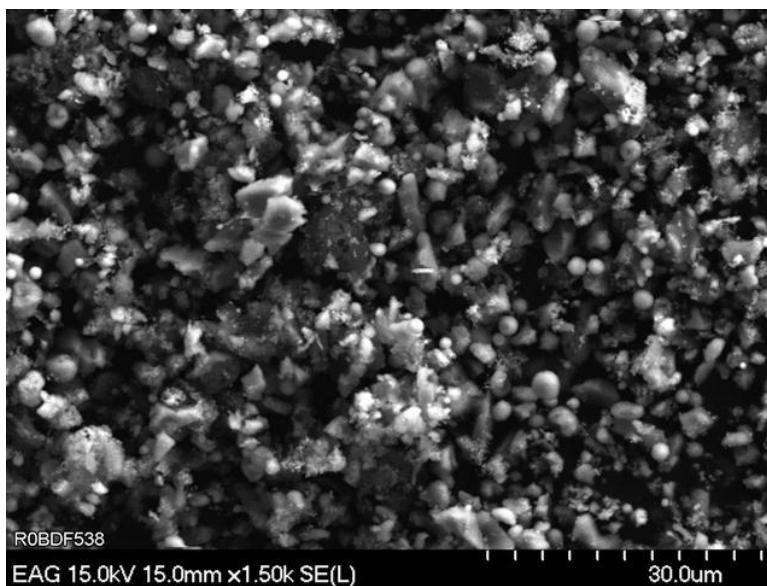


Figure 135: Example of SEM of smaller FB particles on Carbon tape.

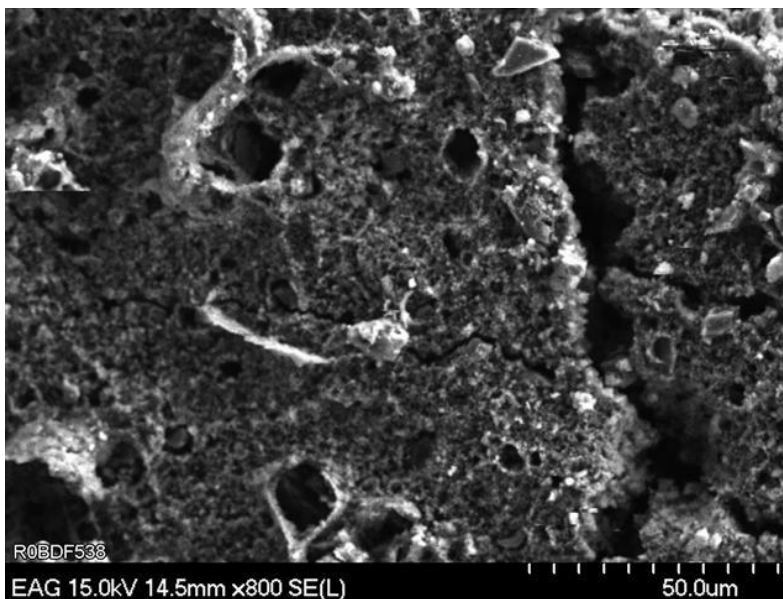


Figure 136: Example of SEM of larger FB particles on Carbon tape.

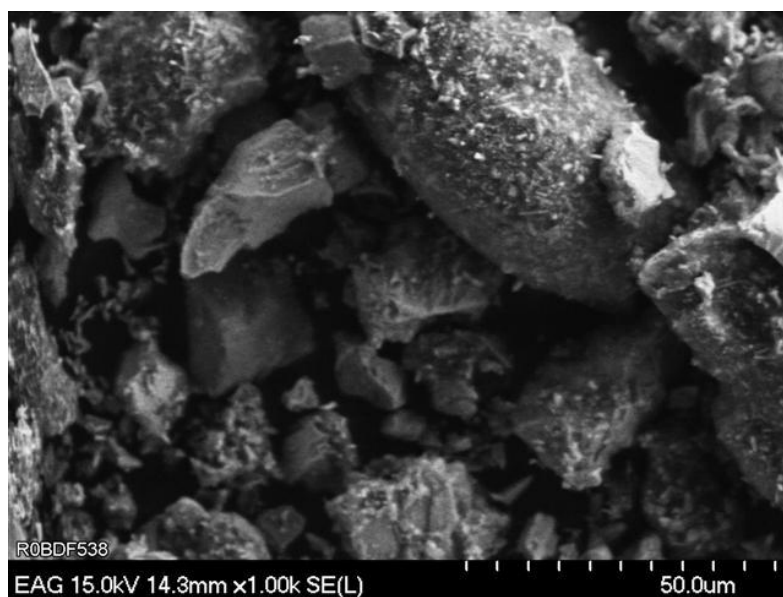


Figure 137: Example of SEM of AF particles on Carbon tape.

Elemental Composition:

Quantitative EDS can be used to determine the elemental components comprising a sample under observation. The EDS spectra emanate from a roughly spherical interaction volume of the electron beam into the sample. The interaction volume varies with accelerating voltage and average Z number of the sample but is typically between 0.25 and two microns from the surface. It is therefore important to note that it is possible to observe the substrate holder of the sample that is being investigated. In this experiment, carbon tape was used as the substrate holder. Therefore, there will likely be anomalously high levels of background carbon detected. The reader is therefore cautioned that the percentages of carbon in the samples are likely inaccurate.

Figure 138 and Table 21 show representative scans of the Freeboard residue collected during plasma removal runs. The intense calcium peak was a bit surprising but is likely due to partially decomposed calcium carbonate or possibly a calcium silicate. Calcium carbonate decomposes at a relatively low temperature into mainly calcium oxide. This rapid oxidation of calcium carbonate has been observed in other work that APS has investigated for a separate, unrelated project. Magnesium, aluminum and silicon were also present which may indicate a magnesium aluminum silicate material. The titanium was likely from some titanium dioxide in the pigment.

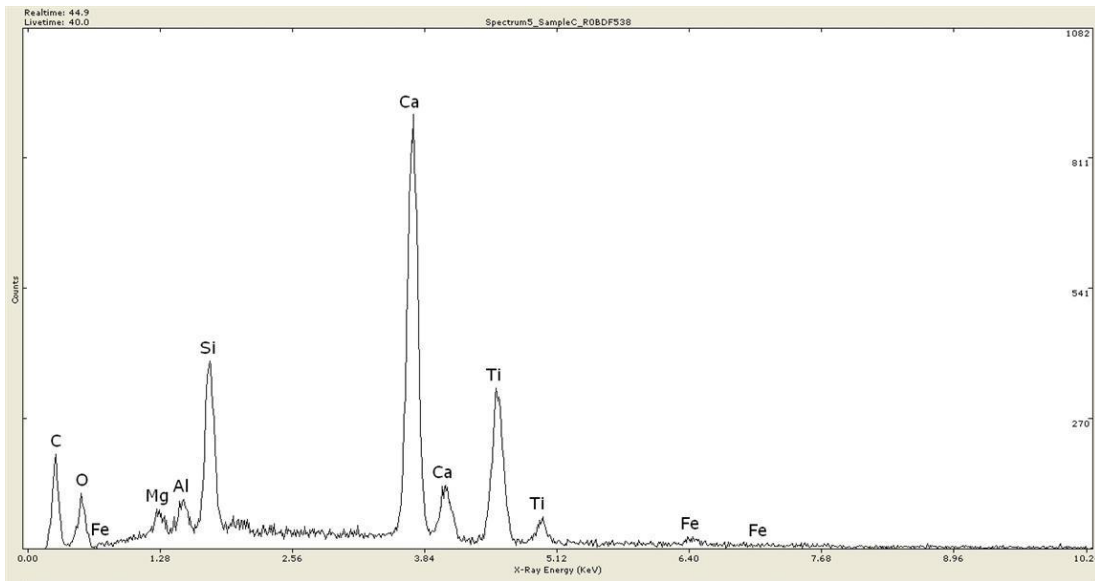


Figure 138: Area EDS scan showing elemental species present in the collected FB residue.

Table 21: Quantitative results from Area EDS scan of FB particulate residue.

Freeboard		
Element	Weight %	Atomic %
C	15%	32%
O	13%	21%
Mg	2%	2%
Al	2%	2%
Si	10%	9%
Ca	35%	22%
Ti	21%	11%
Fe	2%	1%

Figure 139 and Table 22 show representative scans of the Antifouling residue collected during plasma removal runs. The intense copper and zinc lines are expected due to the high solids content of the zinc anti-corrosion layer and the copper loaded Antifouling top layer.

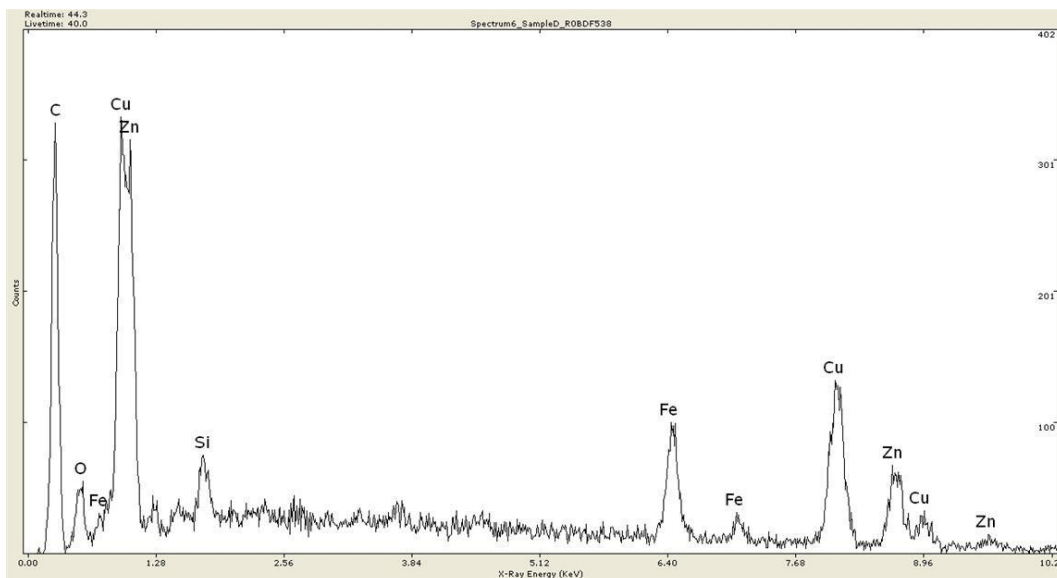


Figure 139: Area EDS scan showing atomic species present in the collected AF residue.

Table 22: Quantitative results from Area EDS scan of AF particulate residue.

Antifouling		
Element	Weight %	Atomic %
C	8%	32%
O	0%	0%
Si	2%	4%
Fe	12%	10%
Cu	50%	36%
Zn	28%	19%

All samples and materials used in the removal process were weighed before performing plasma removal. All surfaces inside the test chamber were wiped down with pre-weighed paper towels and isopropanol solvent. Table 23 shows the total mass unrecovered (or lost) per sample. After plasma removal was performed, a thorough cleaning of all inner surfaces of the chamber was performed until all internal chamber surfaces were clean. Based on the mass increase of the paper towels after drying, a total mass of recovered residue was determined. Freeboard samples showed a recovery of 54% of the solids, and Antifouling samples showed a recovery of 40% collected. Another, perhaps more useful, way to look at this percentage of unrecovered material would be to make the rough assumption that any solids not recovered are instead converted to gases by the plasma and are then vacuumed away. This could give a gas conversion estimate. This would indicate that as much as 46% by weight of the Freeboard paint and 60% by weight of the Antifouling is converted to gaseous by-products that are vacuumed away. This is an extremely important point to make to show that atmospheric plasma can actually reduce the overall waste stream by almost 50-60% depending on the paint being removed.

Sources of error include the possibility that the 177 micron filter may have let an unknown amount of solid particulates be vacuumed away and unaccounted for. Future experiments using

finer filters and a better vacuum system will provide better estimates. The current system was limited to using 177 micron filters because smaller filters proved to provide too much back pressure given the vacuum system available for this stage of the research.

Table 23: Total Mass Recovered and Unrecovered from FB and AF samples.

	Sample Weight (grams)			Residue Collected (grams)	Percent collected	Mass unrecovered (grams)	Percentage unrecovered
	Before	After	Mass Lost				
Freeboard	779.422	778.868	-0.554	0.300	54%	0.254	46%
Antifouling	784.984	783.176	-1.808	0.723	40%	1.085	60%

Waste Analysis of Gases

In order to identify the composition of waste gases produced during plasma depainting, a reaction chamber was fabricated and attached to the ShopBot as illustrated in the photo of Figure 140. The chamber was lined with aluminum having internal dimensions of 12 x 12 x 4 inches (30.5 x 30.5 x 10.2 cm). An acrylic lid was placed over the chamber and partially sealed with brush type weather stripping. The plasma system was rastered over a painted test coupon and measurements taken in real time. The reaction chamber was not evacuated during the experiments which allowed waste gases to accumulate. Any leakage from the chamber was subsequently collected using the standard dust collector outside of the chamber. It was assumed that this setup allowed for steady state to be reached during the time scale of the experiment. For gas analysis, a universal gas analyzer UGA300 from Stanford Research Systems² (SRS) was used equipped with a long thin capillary allowing only a very small amount of the gas into the unit. Atmospheric pressure is further reduced by differential pumping inside the SRS until the desired vacuum is achieved. A quadrupole mass spectrometer then analyzes the sample providing partial pressure vs mass data.

Figure 141 contains a mass spectrum acquired in analog mode during one of the depainting experiments. Operation in this mode is essentially like taking a snapshot at a specific moment during the depainting procedure. Inlet gas is ionized inside the mass spectrometer creating various fragments from each component along with their isotopes. The resulting spectrum is often complex and contains a summation of all fragments measured by the quadrupole as it scans the sample. Because spectra are often complex, algorithms have been developed for fitting data to fragment patterns of individual gases. Table 24 contains a summary of relative peak intensities and fragment patterns from the library of SRS of common gases related to plasma depainting. The SRS algorithm fit the acquired data and calculated relative percentage of each gas. Although not shown, the background spectrum from air alone is very similar to the spectrum from depainting. Major peaks are identified in the spectrum for reference which indicate that more than 99% of the sample analyzed was due to components from air such as nitrogen and oxygen, with traces of water and carbon dioxide. In this sample there was also a trace of nitric oxide (NO) detected. Notice that the pressure in Torr is presented on a log scale so even low concentrations of gas are detected. During other experiments, attempts were made to identify other reaction products such as CO, O₃, other NO_x species, alkanes or other carbon compounds, but none were detected.

² www.thinksrs.com

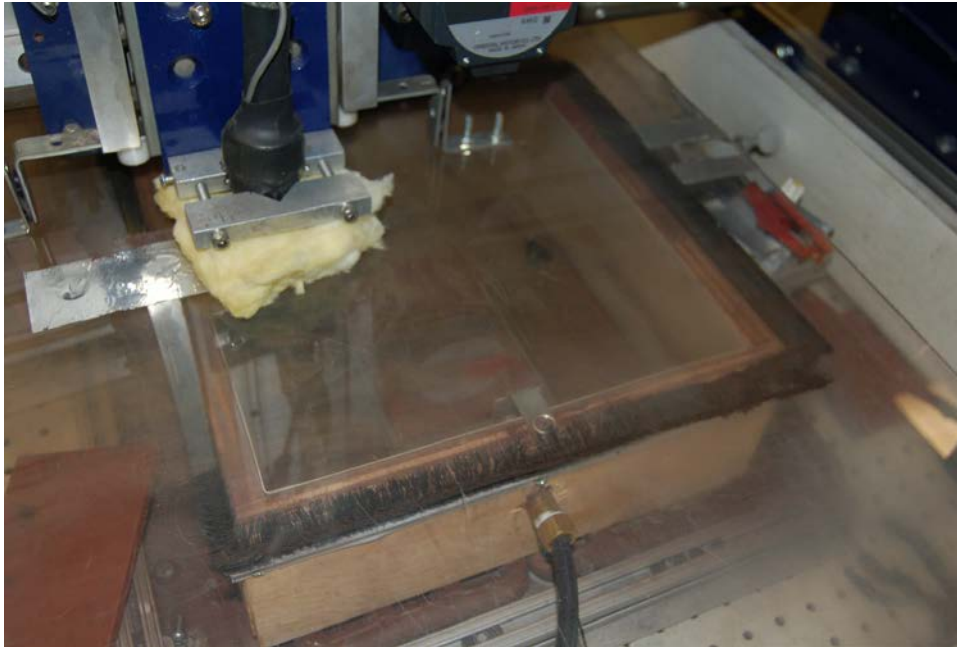


Figure 140: Reaction chamber for gas analysis connected to a UGA300 mass spectrometer via a capillary.

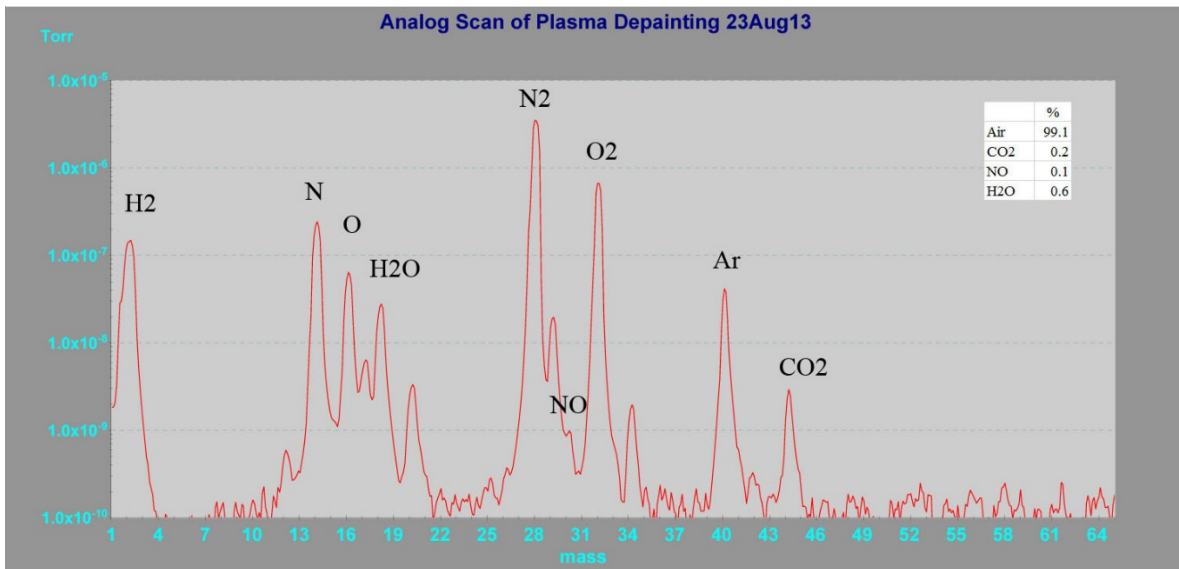


Figure 141: Mass spectrum obtained from plasma depainting of a test coupon.

Table 24: Mass spectra fragment patterns and relative peak intensity of gases from SRS UGA300 reference library.

Gas	Mass/charge																										
	1	2	11	12	13	14	15	16	17	18	19	20	21	28	29	30	31	32	33	34	35	40	41	44	45	46	
Air						4.4		2.2					73.0					19.7				0.7					
O2								10.2										89.4	0.1	0.4							
N2						6.7							92.6	0.7													
NO						7.1	2.2	1.8								88.4	0.4	0.2									
N2O						8.1	0.1	3.1						6.8	0.1	19.2	0.1							62.0	0.4	0.1	
NO2							5.9	13.0									59.0	0.2								21.8	
CO2				4.7					7.1							8.6									78.4	0.8	0.4
CO				4.6		0.9		1.8							91.6	0.9	0.2										
H2O								8.2	17.1	74.4	0.1	0.2															
H2	4.8	95.2																									

Since water vapor and carbon dioxide are naturally present in air, another type of experiment was conducted by running the mass spec in Pressure versus time mode. In this manner, concentration of gasses can be recorded as a function of time which aids in determining sources of gases and determining reaction products. Data obtained from one such experiment is shown in Figure 142. There is a lot of information on the plot of pressure (in Torr) versus time which for this experiment was five minutes total. Partial pressures were recorded for each of the gases as identified in the figure. At the start of the experiment, the compressed air was turned on in order to purge the chamber and warm up the mass spec setup. Notice a slow decrease in H₂O concentration which was expected and typical of a mass spec due to outgassing of adsorbed water. Although the instrument was equipped with a capillary heater and was used in some experiments, it was not necessary and therefore not used in this experiment. The original concern was that certain species might not travel the length of the capillary or survive the distance to the mass spec due to different sticking coefficients, but in general this was not the case.

At time 1:03 the plasma was turned ON but not moved and, therefore, only exposed to the air and not the painted sample. Based on previous work when Emission Spectroscopy was used to analyze the plasma plume, it was not surprising to observe an increase in NO concentration in the mass spec. Highly reactive atomic oxygen in the plume reacts with nitrogen in the air. There was also a slight increase in H₂O most likely due to continued outgassing because of the slight increase in temperature.

At time 1:59 the raster was started. There was an increase in several gases due to the depainting as expected, in particular H₂O and CO₂. For this experiment, the pressure of carbon (mass 12) showed a measureable increase during paint removal. In other experiments higher molecular weight hydrocarbons were expected but not detected in any of these experiments even with the spectrometer operating up to 300 amu. Carbon from CO₂ could be the source, but then increase in O concentration might be expected. However, since the pressure as measured on a log scale of CO₂ is 10⁻⁸, any increase in O would amount to about 1/100th or so of the total oxygen and therefore likely not noticeable.

There was a noticeable increase in H which is likely a combination from H₂O and hydrogen in the painted sample. In this case, since the base pressure of H was relatively low initially, the increase was measureable. Another interesting but not unanticipated result was the sawtooth or oscillation of pressures during the depainting process. The plasma is rastered over the test

coupon from zero to six inches. Since the sample is four inches in width, this means that 2/6 of the time the plasma was directed at air, and 4/6 of the time the plasma was removing paint. It is interesting to note, that the pressure oscillation of C somewhat follows the pressure oscillation of CO₂ providing some evidence for the origin of C. The presence even at very low pressure of NO₂ was only observed during the depainting cycle. It is known that NO will rapidly oxidize in the presence of O to form NO₂. At 3:02 the raster was stopped, but the plasma was still on. The pressure of gases which increased when rastering started, all decreased when rastering stopped. This is clear evidence that CO₂, H₂O, NO₂, and perhaps carbon were all products of plasma depainting. Finally, at 3:25 the plasma was stopped and the pressure of NO decreased.

The cursor at time 2:59 and the insert show the pressure of each gas at that time. Dalton's law states that in a mixture of non-reacting gases, the total pressure exerted is equal to the sum of the partial pressures of the individual gases. Further, the mole fraction of each gas is proportional to its partial pressure. In the SRS mass spec, the base pressure is approximately 10⁻⁴ or 10⁻⁵ Torr. So a comparison can be made regarding the concentration of each gas under those conditions. It will be left to the reader to compare and contrast each concentration. How each of these concentrations relate to actual concentrations at atmospheric pressure is speculation. However, just for a point of discussion, if each gas concentration scaled proportionally, the indication is that compared to the concentration of Oxygen and Nitrogen in the air, the volume of reactant gases is orders of magnitude lower in concentration. A significant result of this experiment is confirmation that the majority of paint is converted to CO₂ and H₂O.

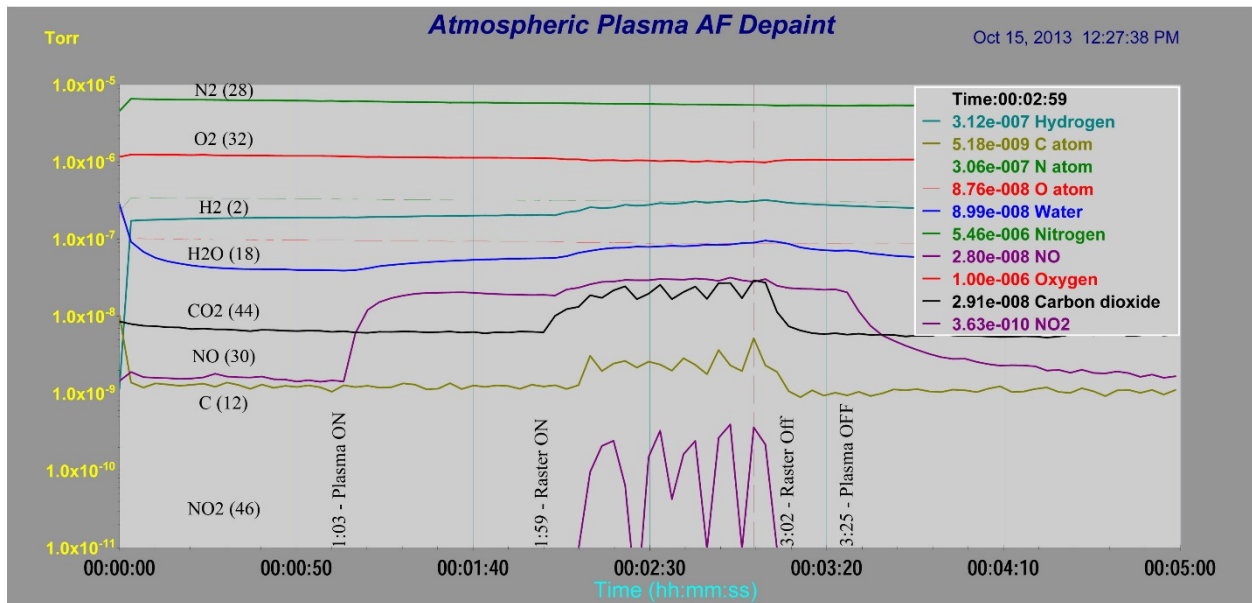


Figure 142: Graph in Pressure vs time mode of mass spectra obtained from plasma depainting of a test coupon.

It should be pointed out that these experiments were performed with a single-nozzle plasma operating without any type of waste collection system or shielding. With multiple nozzles in operation, some increment in overlap of the plasma plumes would be expected. Depending on the configuration and number of nozzles, the ratio of total plasma directly exposed to paint to the amount of plasma exterior exposed to air could be significantly increased. This would result in a number of beneficial improvements. It seems like common sense that towards the interior of the

plasma there is no air to react with, only paint. This would mean more paint removal and less “unused” plasma which might have reacted with air and become unavailable. Conversely, if more plasma is consumed by paint removal, less would react with air to create oxides with nitrogen. Although possible, additional experiments to only expose plasma to paint and not air were not conducted.

7.3 Large Area Automated System

A major advantage of SERDP projects is the value added by employing technology that alleviates environmental concerns while also maintaining operator safety. The goal of this Task was to quantify major aspects of plasma depainting which are or could be beneficial or detrimental to paint removal operations. This evaluation included identifying potential hazards such as sound intensity, UV/visible light emissions, RFI, or other electromagnetic radiation. It is recognized that some of this data had already been collected at least on one scale but needed repeating upon scale-up for the eight-nozzle system, while other aspects might need further identification or quantification beyond the scope of the current SERDP project. The safety testing and analysis has shown safe operation with regard to exposure to UV, audible noise levels, and Electromagnetic Interference, as well as identifying future work.

A distinct advantage of Atmospheric Plasma Coating Removal in comparison to alternative coating removal technologies is the reduction or elimination of some of the types of Personal Protective Equipment (PPE) and safety precautions required for operation. The lack of high velocity media used in grit blasting or water-jetting offers an obvious safety advantage. Other media free technologies, particularly laser coating removal, have other hazards including dangerous high-power optical radiation which requires specialized laser goggles for both operators and nearby workers. The purpose of this task is to analyze potential hazards that may be present with Atmospheric Plasma techniques when used in DOD coating removal operations.

Optical Safety (UV/Visible Light Emissions)

One potential safety hazard with any plasma system is emission of visible and ultraviolet (UV) light, which can exceed safe limits, requiring use of protective equipment. For instance, thermal atmospheric plasmas used in arc welders often produce levels of UV radiation capable of burning the skin and eyes. Previous testing of single-nozzle AP Solutions Atmospheric Coating Removal Systems have shown a much safer level of visible and UV radiation, but new testing was required with the newer scaled-up system used in this project in order to analyze potential safety requirements. The UV region of the spectra (200 to 500 nm) is shown, with the light below 400 nm considered to be the most dangerous to humans, requiring proper shielding. It was determined that it was necessary to characterize the light with wavelengths less than 400 nm and determine whether additional shielding would be required for the end users.

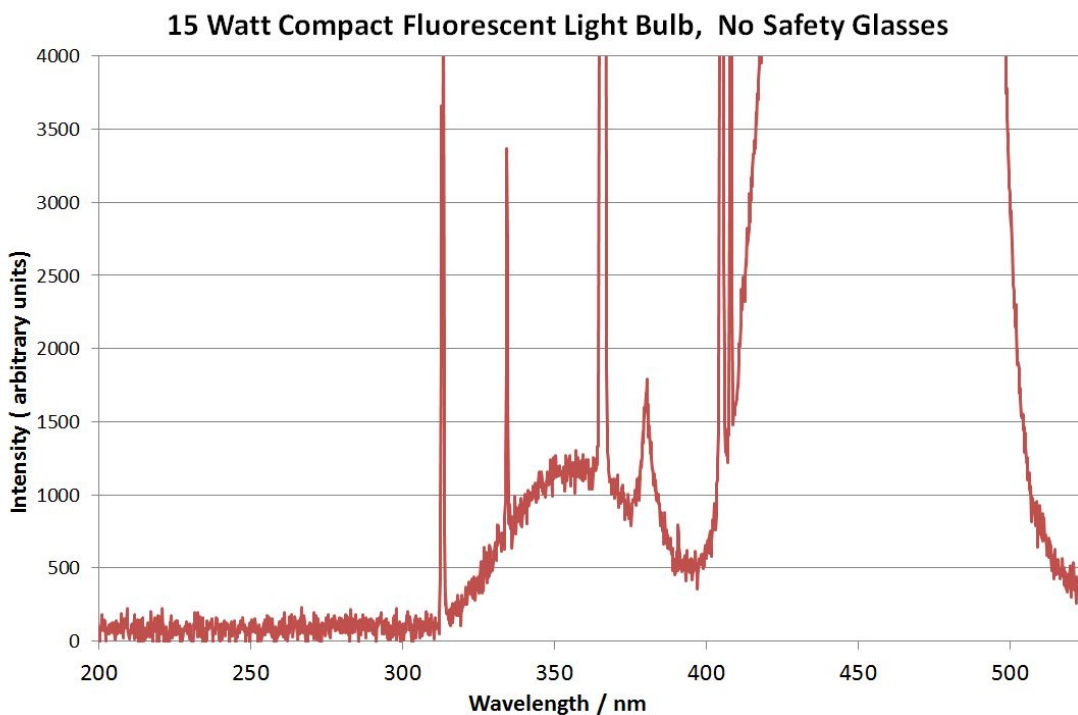


Figure 143: UV intensity of a bare 15 Watt Fluorescent Bulb.

An Ocean Optics UV/Vis spectrometer was used to record the optical output of the multi-pen plasma applicator. A 200 micron diameter quartz fiber was used to sample the spectra emanating from the plasma pen array. An integration time of 200 ms was used for all of the recorded spectra. For comparison, spectra were also obtained from a standard 15 watt compact fluorescent light bulb. A fluorescent light bulb was chosen because it is also a non-thermal plasma light source. Most people are also familiar with the relative brightness of such a bulb. For reference, 15 Watt compact fluorescent (CFL) bulbs are used to replace a standard 60 Watt incandescent light bulb. Two spectra of each light source were recorded for this experiment. One spectra was taken with no filter between the light source and the spectrometer. Figure 143 shows the spectra of the bare fluorescent bulb. Note the large grouping of spectral peaks below 400 nm. The second spectra was recorded with a pair of plastic safety glasses placed into the optical path of the spectrometer. Figure 144 shows the resulting spectra when a pair of safety glasses is inserted into the light path absorbing virtually all of the UV light below 400 nm.

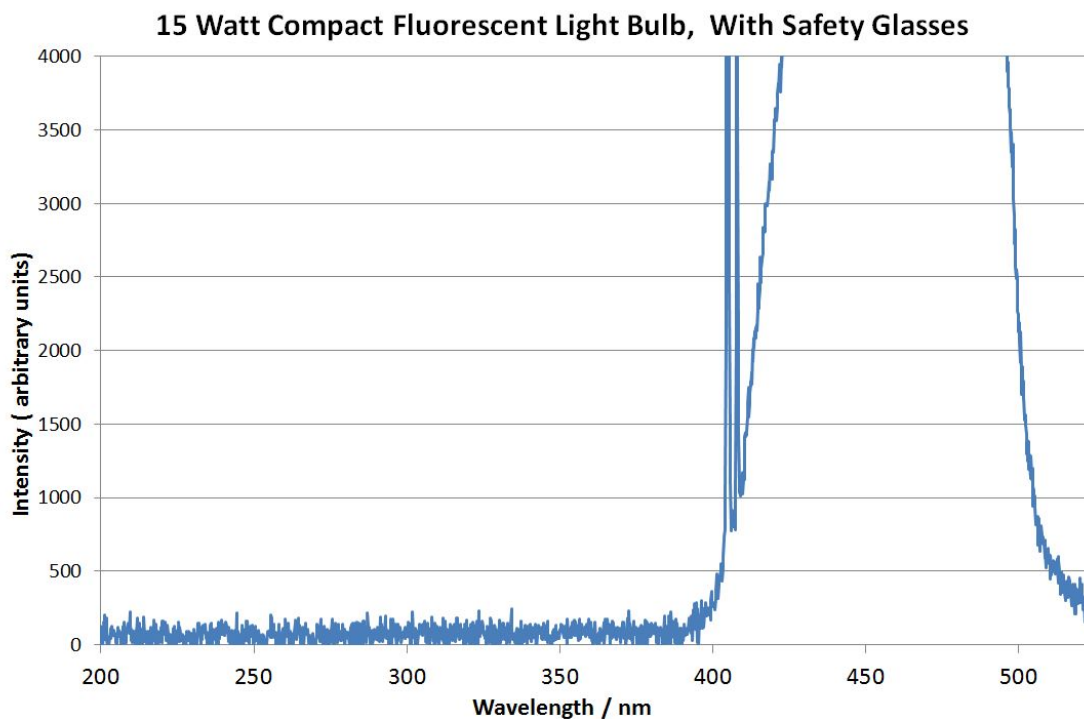


Figure 144: UV intensity of a 15 Watt Fluorescent Bulb through plastic Safety Glasses.

Figure 145 and Figure 146 show the spectra from the plasma pen array. Figure 145 shows the spectra taken of the multi-pen array without any filters between the plasma and the spectrometer. A number of peaks below 400 nm are visible with only a slight peak above 400 nm. Figure 146 shows a spectra of the multi-pen array with a pair of safety glasses inserted into the optical path between the spectrometer and the plasma. The plastic safety glasses attenuated virtually all of the UV light emanating from the plasma plumes. The small spectral peak above 40 nm was not

attenuated and is still visible in Figure 146.

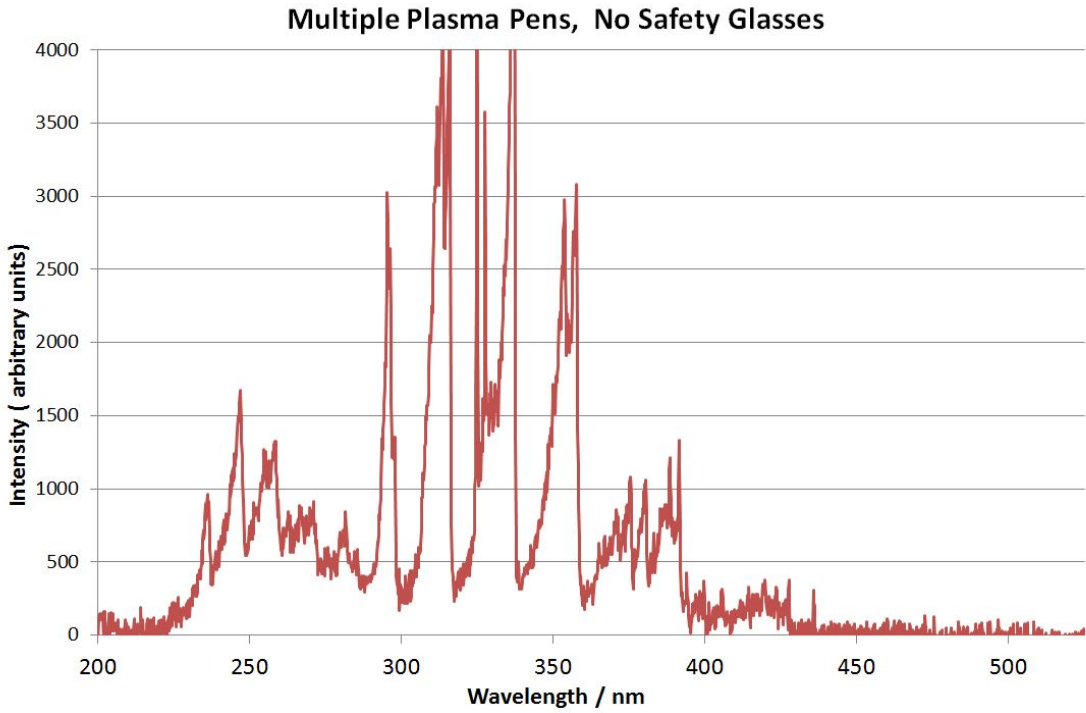


Figure 145: UV intensity of an unshielded plasma pen array (twelve inches from source).

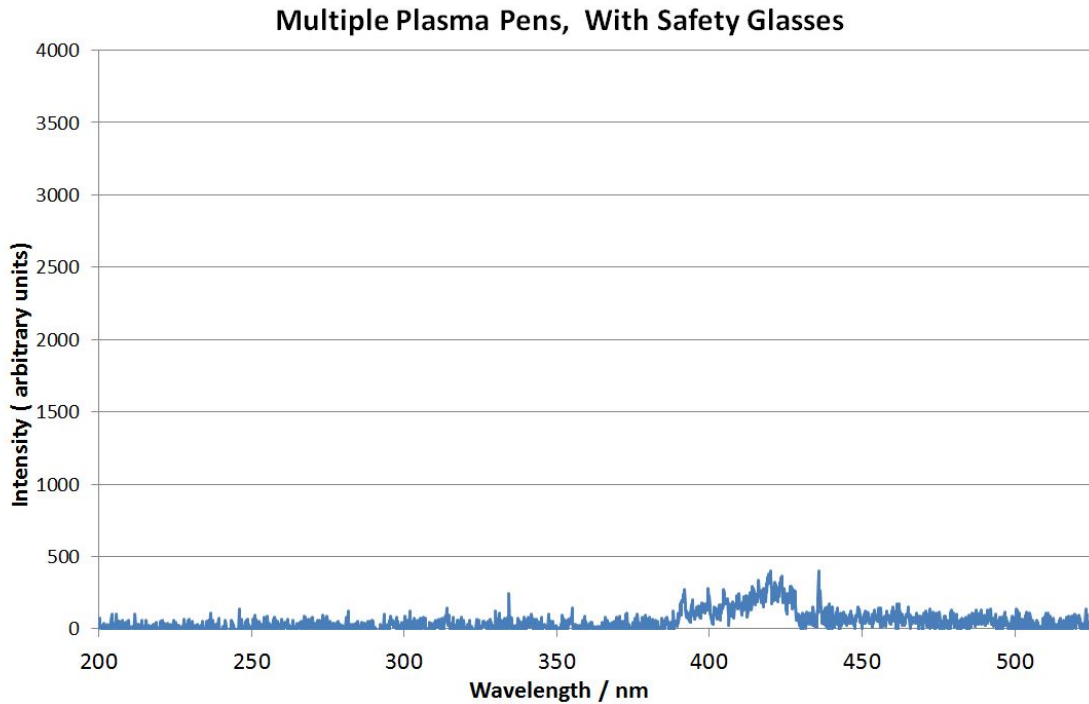


Figure 146: UV intensity of a plasma pen array through plastic safety glasses (twelve inches from source).

It should be noted that all spectra were taken with a 200 ms integration time so the light intensity (brightness) values are roughly similar between the 15 Watt fluorescent light bulb and the plasma

pen array. These results suggest that the use of inexpensive plastic safety glasses will render the plasma pen optically safe for humans wearing inexpensive plastic safety glasses at a distance of one foot or more from the operating plasma pen array.

Acoustic Safety (Sound Intensity)

Similar to media blasting, Atmospheric Plasma Coating Removal uses compressed air, albeit at much lower volumes than required for most grit blasting systems. Nonetheless, use of compressed air can lead to acoustic safety hazards if not properly managed. In this test, the sound intensity of the eight-nozzle applicator was measured while running plasma and waste collection system. An Exair Model 9104 sound level meter was used to sample the sound intensity, using the “A” Frequency weighting mode to represent the Human ear. It should be noted that the test setup for recording the sound intensity was inside a small room and thus likely represents higher sound levels than would be experienced outdoors without nearby walls to reflect sound back. Figure 147 shows the maximum sound intensity value recorded at two different distances, one and four feet from the plasma applicator.

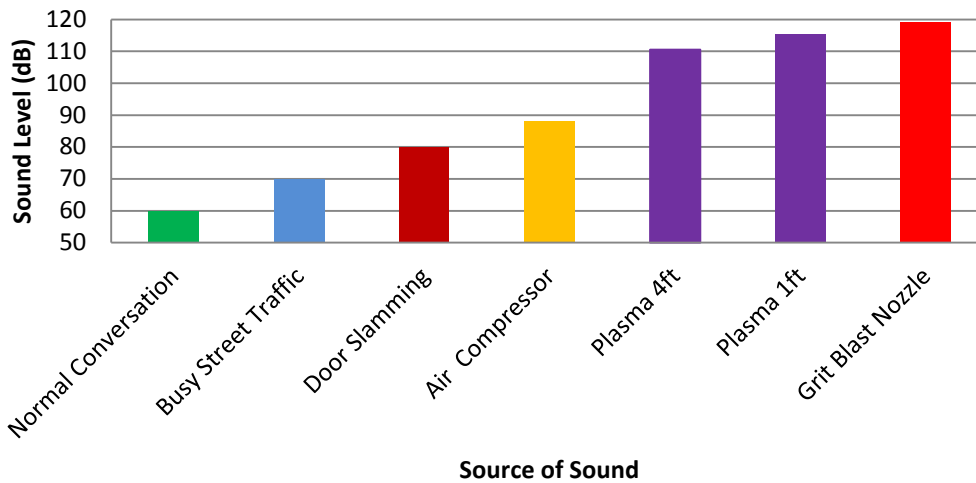


Figure 147: Common sound source intensities compared to an operating plasma applicator.

For comparison, common reference values are also plotted. Air compressor and grit blast nozzle noise levels are also shown, based on data from an OSHA safety guide for grit blasting. The scaled-up plasma system does produce considerable noise levels (115.5 dB at one ft), on the order of 10 dB higher than were typical for single nozzle systems. Nonetheless, the sound level is still >3 dB lower than the value for a grit blast nozzle (119 dB), meaning the sound intensity is actually less than half of grit blasting under the conditions tested (on a linear scale). OSHA guidelines indicate that long term exposure (eight hours) above 85 dB require safety measures to be taken. It is thus important for operators of this equipment to wear hearing protection while in the proximity of atmospheric plasma coating removal. Commonly available hearing protection (such as earplugs or ear muffs) provide attenuation levels of ~20 to ~33 dB, which would greatly reduce the risk of hearing damage for the operator and could bring the sound level into a safe operating range for long term use. The sound intensity of grit blasting, however, may be high enough to require multiple levels of hearing protection for safe operation.

Electromagnetic Field (EMF) Safety

As with any high-power device, the scaled-up Atmospheric Plasma Coating Removal System prototypes used in this work generate electromagnetic fields (EMF) as part of their normal operation. While regulations on acceptable EMF levels vary greatly depending on the application and environment, APS conducted a preliminary EMF safety audit on the eight-nozzle system. Data was collected using an Extech model 480836 EMF Meter, which measures EMF from low frequency up to 3.5 GHz. The meter was set to report the maximum value (in XYZ mode). Measurements were taken at one foot and four feet from the plasma applicator, as well as several other commonly encountered sources of EMF, which are plotted below for reference in Figure 148. A 3G cellphone streaming data at one foot yielded EMF levels over twice as high as the scaled-up plasma applicator while operating. A Wi-Fi wireless internet router at one foot had over three times the EMF level of the plasma applicator, while a standard consumer microwave oven (at one foot) was measured at over ten times that of the plasma applicator. It appears that no special precautions are required for potential EMF exposure to the operator; however, future work on transitioning and integrating this technology into a final product for DOD use will require further testing and development to ensure that EMF safety is maintained with large scale designs.

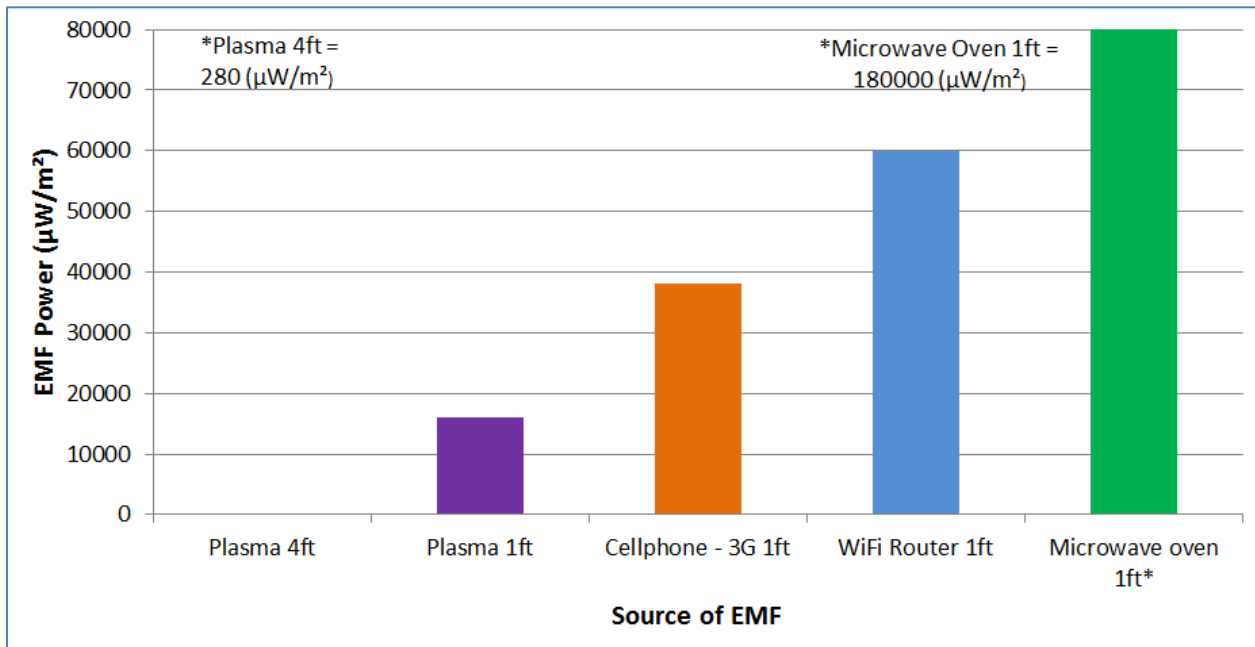


Figure 148: Electromagnetic Field Strength of Common Sources compared to plasma pen.

Other Potential Hazards

The above safety analyses represent the major concerns that have been identified at this stage in the project, but other possible hazards have been raised and investigated in the course of this project, in addition to other safety factors that will be addressed in future phases of this project. The following represent other possible hazards which may need to be studied in more depth.

Surface temperatures (of treated materials and the plasma applicator itself) during Atmospheric Plasma Coating Removal may exceed 60 °C (as investigated earlier in the project), and thus may represent a burn hazard, similar to many other military and industrial processes. Thus, operators

will be required to observe standard safety practices when working with and around hot surfaces. Along with the presence of hot surfaces, one potential hazard in a military environment is use in or near a flammable or explosive atmosphere. Such testing was beyond the scope of this project, but previous work with other plasma pen systems has shown a tendency to extinguish flammable materials (such as acetone) rather than ignite or support burning.

Because atmospheric plasma coating removal uses high-power electrical voltages and currents, there is also the potential for hazards, particularly in the event of damage to the cable or other parts of the equipment. While some safety devices have already been incorporated (shielding, some ruggedization of the power supply and other components), future integration work will need to account for the particular environmental risks to protect the system and operators from such occurrences.

Some work has been done analyzing the solid and gaseous by-products of the removal process, which may present respiratory or other hazards to operators in the field. This is an area that needs more focus in the future and Task 8.2.1 provides additional test data obtained while depainting with the application of a waste collection shroud.

7.4 Hybrid Modules (cancelled)

Task 8 Systems Integration and Transition

8.1 Lab-Scale Manual System and

8.2 Automated Systems

Up to this point in the program, waste collection had not been a major focus of the work. Some work had been completed on making waste collection systems to enable safe testing of the scaled-up coating removal systems, as well as investigations into commercially available waste collection technologies. APS has previously designed vacuum shrouds for this and other projects, and it was decided that demonstrating a vacuum shroud for the scaled-up system was an important component of the project moving forward. Such a demonstration serves several purposes simultaneously. In addition to gathering data on the performance requirements of successful waste collection and the effect of waste collection systems on coating removal, it is also important to provide a proof-of-concept as groundwork for future integration work.

In order to meet the goals of the project, this work demonstrates a proof-of-concept waste collection system using a four-nozzle multi-head plasma applicator module, rather than the eight-nozzle stacked configuration. The additional geometric complexities of physical setup (particularly alignment of nozzles to the surface) and analysis of the interactions of eight nozzles on the surface would have been prohibitive and yielded less usable data going forward. The concepts and data generated using this four-nozzle design will be directly applicable to larger-scale systems in the future.

Static Vacuum System Test

In order to get some preliminary data on waste collection and to investigate the effect on coating removal, a “static” test was conducted with the plasma applicator fixed over the painted sample

with a fixed vacuum hood near the site of removal. The goal of this experiment was to analyze how effective a static shroud might be at collecting particulate matter, as well as looking for qualitative changes to the removal pattern.

Setup

In order to maintain consistency with later testing, the applicator was set up with four nozzles firing plasma. Four additional nozzles were installed to the rear of the four active nozzles, and these were configured to flow air but no plasma. Thus, the plasma removal operation was bounded on one side by positive airflow and on the other by a static vacuum shroud, with the idea that this will assist in guiding the waste toward the vacuum shroud. This testing was conducted in the sealed 6' x 8' (0.18 m x 0.24 m) enclosure with two 6" (15 cm) ducts ~6" to either side of the sample stage. These ducts run to a 1550 cfm (4.4 x 104 slm) dust collector, which is always running while paint removal testing is conducted to maintain negative pressure inside the enclosure and prevent escape of airborne waste.

Figure 149 contains a photograph of the physical setup for the static vacuum testing. The static vacuum shroud itself was selected from several different styles of COTS vacuum attachments, with the 13.5" x 3" (34 cm x 7.6 cm) opening being well-suited to encompass one side of the 6" (15.2 cm) wide sample. This large opening did have the negative effect of spreading out the suction over a large cross-sectional area, and future static designs may benefit from a more focused design, but this will require more precise positioning to ensure that the static shroud is in the path of the ejected waste stream. The static vacuum shroud was connected to the C82906 Critical Filter Vacuum discussed later in order to provide the necessary suction.

Particulate Matter (PM) Measurement

In order to evaluate the effectiveness of waste collection systems, different methods of quantification were considered. Mass loss techniques were deemed to be too insensitive and prone to error when removing milligrams of paint from samples weighing several kilograms. While measuring mass accumulation on inline filters could be used, the surface area required for capturing small particles at the large airflows used in this study makes such a technique impractical. Other analytical techniques such as spectroscopic analysis or air sampling techniques were considered but would require a great deal of development work to obtain usable data, so commercial solutions were investigated.

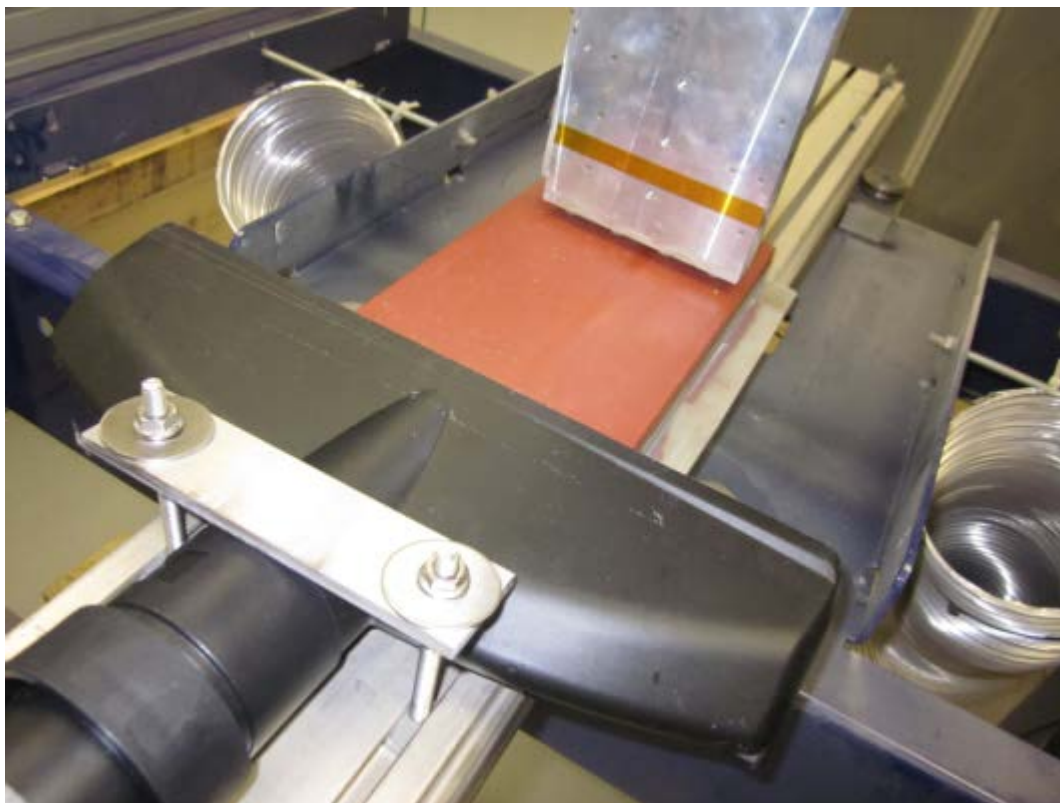


Figure 149: Static vacuum shroud test setup.

There are quite a few different technologies and products on the market that measure air quality through a range of techniques. Some techniques pull a sample of air through a filter or series of filters over a period of time and measure the accumulation of mass and are calibrated to give a reading of unit mass of particulates per unit volume of air. Other techniques count particles of different size ranges and give a read of particles of a particular size per unit volume. After reviewing the available options, a laser particle counter (Dylos Corporation DC1100 Pro) was selected. While this unit does not come with traceable calibration certificates, a number of third-party sources have shown the Dylos unit to have similar performance to precision-calibrated units. The DC1100 has the added benefit over many competing technologies that it can achieve a reading within seconds, while other techniques may take much longer to sample enough air for a reading. Though future work may require a higher precision calibrated air quality measurement system, the Dylos unit was determined to be appropriate for this stage in testing the efficacy of different vacuum shroud configurations at capturing particulate matter.

The DC1100 Pro uses a small fan to pull a sample of air through a chamber across the optical path of a laser beam and particle detector, which allows it to count the particles passing through the beam along with a basic particle size distribution. In the case of the DC1100 Pro, it provides a reading of the total number of particles greater than 0.5 micron, as well as the number of particles greater than 2.5 microns. The readings are factory-calibrated to give the number of particles per cubic foot. For reference, Dylos provides a chart of relative air quality for these readings, with <7,500 being Excellent, <105,000 being Fair, and >300,000 being Poor. Typical readings (without paint removal being conducted) ranged from 20,000 to 50,000 total particles, with 500 to 5,000 large particles (>2.5 micron). The DC1100 Pro laser particle counter was

installed at a distance of three feet (0.9 m) from the plasma applicator. It was set in continuous mode, where it reports the two readings approximately once per second, with a 10s averaging function built in. The initial value of the readings was recorded prior to starting each run, and then the maximum value was recorded after the run was completed.

Results

Static removal tests were conducted at standard conditions on Antifouling coating, with a height of 0.079" (2.0 mm), duration of one second, and no movement in the x or y axes during the removal run. Figure 150 shows the results of six such static four-nozzle runs, each separated by ~1.25" (31.8 mm) in the x-axis. The edge of the static vacuum shroud was located approximately at the bottom edge of the photograph, ~0.8" (~2.0 mm) away from the plasma pen at the bottom-most location. Each subsequent run was farther away from the static vacuum shroud. The top-most run (~6.8" or ~17 cm away from the shroud) was conducted with the vacuum turned off entirely to give a baseline reading.

Qualitatively, the removal pattern on the surface, as seen in Figure 149, does not seem to be significantly affected by the distance from the static vacuum shroud. Turning off the vacuum source also showed little effect in the appearance of the removal pattern. This early result gives some positive indication that the presence of a vacuum shroud may not impair coating removal. On the other hand, the vacuum shroud did have a major effect on measured PM levels, as measured by the Dylos particle counter. The maximum reading for the run closest to the activated static vacuum shroud was 1.52×10^6 total particles (with 2.8×10^5 greater than 2.5 micron). In comparison, the baseline run without the shroud activated registered 2.35×10^6 total particles (with 4.8×10^5 greater than 2.5 micron). This represents a 35% reduction in total particulate matter and over 40% reduction in larger particles.

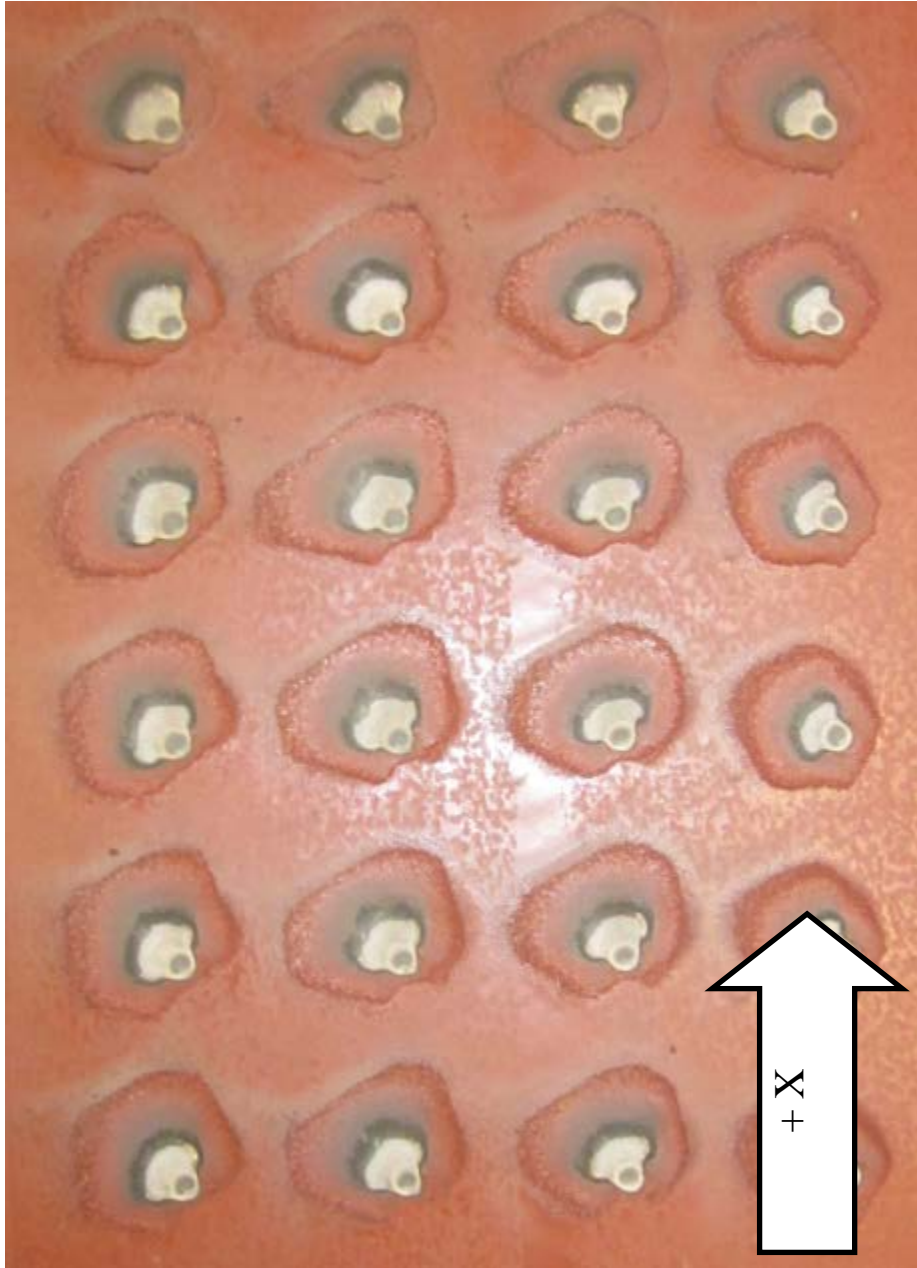


Figure 150: Removal pattern for static vacuum shroud testing (Antifouling sample). The vacuum shroud shown in Figure 149 was located at the bottom of the sample as oriented in this photograph (at $x \sim 0$).

Integrated Vacuum Shroud Design

The promising results with a static vacuum shroud provided a great deal of useful information. Further work with static vacuum shrouds may be useful in later demonstration/validation stages and will have to be designed in an application-specific way to provide the best performance. However, at this stage it was decided that a general use, fully-integrated vacuum shroud (totally encompassing the plasma nozzles) would be the most useful configuration for evaluation. In planning for this prototype, several technical requirements had to be addressed.

Technical Requirements

- Must provide high airflow (far exceeding plasma nozzles)
- High static pressure (maintain negative pressure through small constrictions)
- Should be as low-profile as possible to avoid adding weight and size
- Must withstand high temperatures near the plasma

Airflow

One of the primary criteria of the waste collection system is the total volumetric rate at which it can collect vapor and solid ejecta during coating removal. The airflow, measured in cfm, is one metric used to compare various models of vacuum systems, and is typically stated as the maximum flow one could achieve with minimal constrictions. This ideal maximum number is rarely achieved in practice due to the need to have some length of vacuum tubing and constrictions or fittings to redirect the flow, which decrease the overall flow. Table 25 shows the maximum airflow for three different types of vacuum systems tested during this Task.

Table 25: Comparison of performance of different vacuum sources.

	<i>Max airflow (cfm)</i>	<i>Static Pressure - datasheet (psi)</i>	<i>Static Pressure - measured (psi)</i>
Exair Line Vac (#130200)	110 [3100 slm]	0.52 [3.6 kPa]	~0.1 [~0.7 kPa]
Oskar Fume Collector (SPC-G3)	1200 [34000 slm]	0.09 [0.6 kPa]	~0.2 [~1.4 kPa]
Minuteman Critical Filter Vacuum (C82906)	95 [2700 slm]	3.07 [21.2 kPa]	~0.8 [~5.5 kPa]

In comparison to the four to five cfm flow coming out of each nozzle, all three of these vacuum systems provide several times the airflow of a four-nozzle applicator, which should give adequate margin to avoid loss of vacuum. However, due to the relatively compact nature of the scaled-up plasma system, large vacuum tubes several inches in diameter would not be practical, and so these maximum airflow numbers are likely higher than what can reasonably be achieved for a waste collection system for this task. In designing a waste collection system, an attempt was made to maximize the cross-sectional area of the airways at all locations, as much as practical, as described later in this report. An effort was also made to direct the airflow near the surface where particulate matter would be captured, in order to maximize efficiency of the system at collecting particulates.

Static Pressure

Based on airflow alone, the Oskar SPC-G3 appears to outperform the other two vacuum sources, but there is another critical factor for use in the type of waste collection system being designed in this task. The static pressure is a measure of how much pressure drop a vacuum can generate inside a closed volume with zero airflow. Even if a system has a high maximum airflow, when drawing vacuum on a system with restricted airflow (i.e., constrictions in cross-sectional area), if the static pressure is not high enough, the system may not be able to hold negative pressure to maintain suitable suction. The fact that the waste collection system for this task is required to

have constrictions in the cross-sectional area and must also capture high-velocity ejecta travelling away from the waste collection system necessitate that sufficient static pressure be present in the system.

Low Profile

Maintaining a small overall size and weight are important criteria so that scaled-up systems do not become unwieldy or impractical in the field. However, other aspects of performance, such as airflow and thermal performance may benefit from increased size or mass. In the face of these tradeoffs, any design will need to strike a balance between these competing factors to achieve an optimal result. The design also must not get in the way of other necessary parts of the system such as the handle/mounting rod, power cables, and air lines.

High Temperature Materials

With power levels exceeding 10 kW in scaled-up Atmospheric Plasma Coating Removal systems over a cross-sectional area of under 30 square inches (under 200 square cm), thermal design is going to be a crucial consideration for any waste collection system. While the actual temperature rise of a vacuum shroud design will depend on a number of factors (proximity to the plasma/surface, coating removal parameters, airflow, overall power level, thermodynamics of the particular coating removal process, etc.), only high temperature materials (aluminum, silicone, etc.) were considered for the initial prototype. One exception was the vacuum tubing and other downstream components which were far enough away from the coating removal operation to allow for short runs without degraded performance. For longer studies, higher temperature materials may be warranted.

Design Considerations

With the above criteria in mind, several features of the vacuum shroud design were selected. Other key considerations from the design process are summarized below. Figure 151 and Figure 152 contain photographs of the prototype and installation of the prototype vacuum shroud design for depainting, respectively.

Cross-Sectional Area

As discussed previously, the cross-sectional area of the airways must be as high as possible in order to maintain high airflow and reduce pressure losses in the system. This must be balanced against the need to keep the system relatively compact and to direct airflow close to the surface. For this prototype, the main vacuum port going into the vacuum shroud is 1.25" (3.18 cm) inner diameter, giving $\sim 1.23 \text{ in}^2$ (7.94 cm^2) of cross-sectional area. This opens into a rectangular chamber surrounding the pen body which has inner dimensions of 5.63" x 2.63" (14.3 cm x 6.68 cm). Three low profile supports were used to attach the pen body to the shroud, thus minimizing disruptions to the airflow and reductions in cross-sectional area. The area around the pen body has a cross-sectional area of approximately 9 in^2 (60 cm^2). A final critical area to analyze the cross-sectional area is the gap between the silicone "curtain" and the sample, discussed in the following section.

If future designs need increased airflow and reduced pressure drop, the inlet and connected vacuum tubing may need to be larger. Minimizing the length of vacuum tubing and using smooth walled tubing may also yield benefits, if needed, though this may reduce system

flexibility. However, based on the results of initial testing, the current setup appears to be adequate for this stage of testing.



Figure 151: Prototype integrated vacuum shroud installed on a four-pen applicator.

Curtain to Sample Gap Spacing

Also as discussed previously, the airflow of the vacuum system should well exceed the flow emanating from the plasma nozzles, which means that additional air must be supplied to the vacuum from outside the vacuum shroud through the gap. Because of the way the plasma plumes hit the sample surface, streams of gaseous and solid ejecta flow across the surface away from the nozzles at high velocity. Thus, a critical design parameter of the system is to have a gap that provides adequate cross-sectional area, such that it does not hinder the inward flow of outside air into the vacuum shroud (to counteract the outward flow from the nozzles). At the same time, if the gap is too large, the pressure differential at the surface may not be high enough and the inward flowing air may be “overpowered” by the outward flowing air. For these reasons, the design shown in Figure 151 allowed for adjustable spacing of the silicone curtains. Relatively hard/rigid silicone rubber was chosen to prevent “flapping” of the curtain with the rapid flow of gas. The front curtain was also made from translucent material to allow some visibility of the plasma process.

The final spacing of the curtain was chosen to give a total cross-sectional area of the gap slightly less than that of the vacuum port inlet. The curtains thus extended about 0.015” (0.4 mm) below the bottom of the plasma nozzles, leaving about 0.064” (1.6 mm) of gap above a flat surface. The performance at this spacing was first analyzed by holding a string next to the gap on the surface and observing whether it was drawn into or pushed away from the vacuum shroud. The

string was drawn in very forcefully all around the vacuum shroud, indicating that this spacing would be effective.

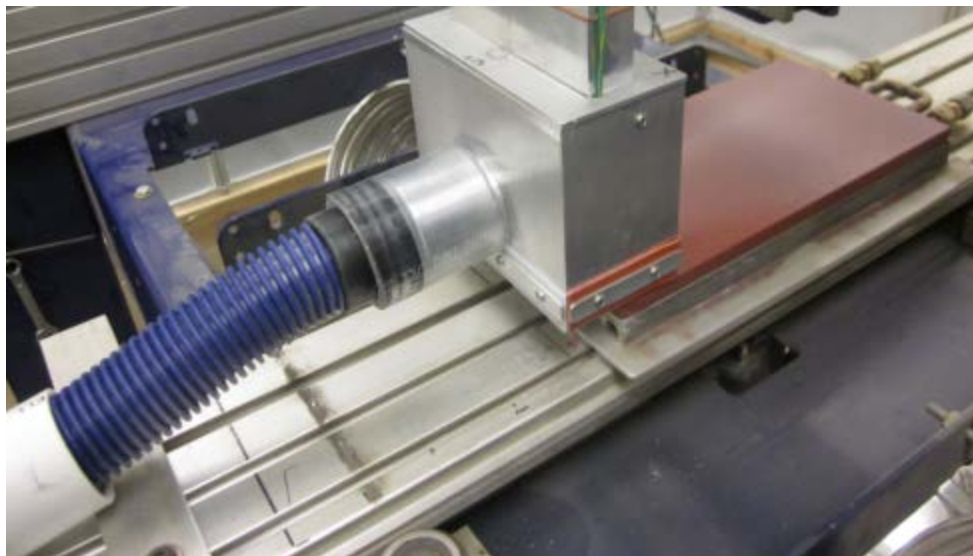


Figure 152: Prototype vacuum shroud as installed for testing.

Static Pressure Assessment

In order to select which vacuum source to use for testing, a method was devised to characterize the actual static pressure each vacuum source could maintain under realistic conditions. Once the prototype vacuum shroud was constructed, it was connected to the different vacuum sources listed in Table 25. A series of flat plates of different weights were laid down on a mat and the vacuum shroud lowered onto each until a seal was achieved (yielding almost no airflow). The shroud was then lifted straight up in order to determine if the vacuum could provide enough force under static conditions to lift each plate. The static pressure was found by dividing the weight successfully lifted (in pounds) by the cross-sectional area under vacuum (in square inches) to yield psi as shown in the table. By using the same setup that would be used in actual testing, this method provided a quick estimate of the relative static pressure for each vacuum source under realistic conditions. These tests confirmed that the Minuteman vacuum far exceeded the others in static pressure, and for this reason it was chosen for this testing.

Results

After initial setup, analysis, and testing the vacuum shroud was installed onto a four-nozzle applicator to begin paint removal testing. Flat 6" x 12" (15.2 cm x 30.5 cm) Antifouling samples were used, with the four plasma nozzles oriented to align with the shorter side of the sample. The sample was set up to translate in the x-direction, such that the four nozzles would have minimal interaction with each other. For this stage of testing, it was determined that minimizing interactions between nozzles would simplify analysis of the removal pattern and allow for easier interpretation of the effect of the vacuum shroud. For this same reason, single pass runs were conducted rather than multi-pass runs. Samples were run at the standard nozzle height of 0.079" (2.0mm) and a speed of approximately 5 in/s (13 cm/s) in the x direction. Runs were conducted with the vacuum shroud installed and operating as described above, as well as without the vacuum operating (and silicone curtains removed) to provide a baseline. The standard dust

collector was operating within the enclosure as described in the Static Vacuum System Test – Setup section.

Initial results indicate that the vacuum shroud did not significantly change the coating removal performance, although further testing would be needed to more carefully analyze effects of the vacuum shroud. Mass loss values for runs with and without the shroud were similar, as was the appearance of the removal pattern. Larger area runs would be required to obtain more high-resolution data on the effect on mass loss and surface temperature. With these short runs, no thermal damage to the vacuum shroud materials was observed, although some buildup of solid ejecta did occur inside the shroud. The most important result and the focus of this testing, however, was the effect of the vacuum shroud on the particulate levels in the vicinity of the coating removal operation.

The testing showed a major decrease in PM levels with the vacuum shroud active. In single pass testing, total particle levels measured at a maximum of 1.38×10^6 total particles (0.5 micron and larger) per cubic foot with the shroud versus 6.38×10^6 without the shroud activated, representing a reduction of over 75% in total count. The large particle (>2.5 micron) count showed even better reduction at 0.39×10^6 with the vacuum shroud and 3.48×10^6 without, showing a greater than 85% reduction. This is an extremely promising result, particularly for an early prototype. While capturing 100% of the ejected material is considered an unrealistic goal, these results provide a proof-of-concept that high levels of waste capture are possible with such a design.

Recommendations for Future Work

Based on the extremely promising results of the initial testing, more work with this prototype is recommended. Several potential optimizations have been identified, including fine tuning the curtain gap spacing, increasing the cross-sectional area of the vacuum hose, and/or identifying higher-power vacuum sources to increase performance. Because many of the potential optimizations involve engineering tradeoffs, multiple configurations or designs may need to be tested to achieve maximum performance of the waste collection without negatively impacting coating removal. Testing should also be extended to multi-pass treatments and larger samples, which will require further work on the sample stage and sample setup to enable testing. Longer runs would be needed to understand the thermodynamics of the system and determine if the design and high temperature materials are appropriate for long term use. Other analytical techniques may also be explored, including analysis of the vapor-phase waste to see how effectively a vacuum shroud captures the exhaust.

Once sufficient data has been gathered on the four-nozzle system, work could be extended to a system for eight-nozzles or larger. This larger system will likely require a significant upgrade to the vacuum system and supporting hardware used in the lab. Such a system, however, would be similar to industrial systems already in use for large scale paint-removal operations. Mechanical standoffs or hold-downs may also need to be incorporated in future designs, as the prototype vacuum shroud did not have enough suction to lift the sample off of the stage. An alternative line of investigation would be to conduct more tests with static vacuum shrouds and directed airflow to try to optimize their performance.

Task 9 Conferences and Meetings

9.1 NAVSEA Coordination meeting

The original proposal called for a coordination meeting to be conducted in the Carderock vicinity in order to kick off the project and review significant program details. Due to weekly telecommunications meetings and rapid progress, the team decided it would be more valuable and productive to visit shipyards to obtain valuable information onsite. The plasma team made short field visits to BAE and Metro Machine Corporation shipyards in Virginia on 12/1/11. Some of the highlights of the trip are summarized in Table 26. Not all problems are the same at every shipyard, but there are many circumstances that apply universally. These particular shipyards had floating dry docks, wherein the ship moves into the dock, is supported below the water line, then the dock is raised above water. After operations are complete, the entire dock including the ship is lowered back into the water.

A major issue with grit blasting is the inside of tanks (ballast, fuel, etc.) as there are numerous nooks and crannies, confined spaces, limited visibility, and limited exhausting capabilities. Hoses and evacuation equipment must traverse from the dock, to the interior job location. It was described as a worker going into a tank and blasting for a shift with near zero visibility and another shift coming in to remove the waste and then this process was repeated until the tank was clean. One size of the tank access hatch visited was small enough (18"x 24" guess) to restrict several members of our tour group from entering and as well place restrictions on the workers. Although this was a special situation, it demonstrated that there are areas on ships which will always require special handling. At this stage in the project, it was noted, but determined that due to budget, timing, and stage of the research, the main focus of the SERDP project should continue to address removal of paint from large relatively flat exterior exposed hull surfaces. Photography was prohibited during the visit, but an example photo obtained from the web is shown in Figure 153. Many of the difficulties of depainting ships are well known and include: limited access from the deck, need to conduct various operations simultaneously, waste containment and collection, minimization of hazards, cost effectiveness.

Table 26: Shipyard visit highlights.

1.	Contractors operation is turnkey, all equipment is brought onto the job site
2.	Wind is huge factor, blows debris, alters containment (night time blasting reduces wind, no other work ongoing, clouds visibility)
3.	Energy: On site electrical, compressed air, vacuum collection is available for plasma
4.	Approximately 10% of debris is collected, the rest scooped up at end of shift (coal slag is not recycled)
5.	Removal rates can be fast on large flat areas to slow on geometric or sensitive areas (sonar domes, ports,)
6.	Specific sites on the hull area used for dry dock support are not painted until next cycle.
7.	Maneuverability is limited due to supports and other equipment
8.	Many areas have confined access.
9.	Internal blasting (ballast tanks) are also part of service

10.	The depainting contractor also typically performs the RE-painting.
-----	--



Photo from Web

Figure 153: Photographic example from the web of a ship's hull supported in dry dock for renovation (from [www](#)).

Another interesting observation was that most grit blast is performed at night for several reasons. The most significant is that wind is drastically reduced at night. Large sheaths which cost hundreds of thousands of dollars are used around the ship to help with containment and can get damaged by high winds. Debris generated from the removal is also easier to manage. There are two types of vacuum collection. The first is used for general area cleanup in an attempt to keep dust to a minimum. This setup only collects part of the debris mostly in the form of light particles. Figure 154 shows an example of one such setup. A second type of vacuum is used primarily in confined spaces to draw waste away from the operator who would be wearing a protective hood. The operator is continuously fed a fresh supply of air to minimize exposure to the waste. Numbers provided regarding cost included \$2.6 million for grit blasting the USS Stout (which was in the dry dock) and \$2.8 million for grit blasting the USS Barry. At the time of the visit \$280,000 had already been spent on wind curtains used on the USS Stout which apparently was having some serious wind issues. The curtains can be damaged by strong winds and eventually would be discarded.



Figure 154: Example collection setup for general area vacuum containment (From www).

It was noted that only 21 days from start to finish is allocated for a ship this size to complete renovation of any and all activity. Stripping and repainting the ship is only one task to complete and must be performed while all other renovations are conducted.

Dry dock services range from \$6,800-\$24,000 per day depending on the size of the dock, the former for the destroyer class size and the latter for the larger docks capable of handling the carriers. This does not include any work or other considerations; it only covers essential services such as electricity, water, and basic services. Ship security is maintained by ship personnel, while dock security is different.

There were six modules available for grit blasting at the USS Stout. Each hopper can hold 28 tons of grit, and the operator mentioned it has problems with valve blowouts. Each blast hose has 850 cfm delivered with a capability of eight hoses operating simultaneously with 110 psi at the nozzle, and the hose has a pressure drop of four psi/50'. The compressors have an output up to 1600 cfm per unit. When stripped to bare metal, the workers have six-eight hours before the surface has to be repainted, otherwise the surface needs recertification or resurfacing. The largest cost is associated with the waste and hazmat. Inexpensive type grits such as black beauty (coal slag) are typically only used once. Much of the debris simply drops to the dock, where front loaders scoop up the piles for disposal. Fire watchers are generally not needed for grit blasting since it is not considered hot work; however, safety watchers are required if the work is confined or elevated. Removal rates for grit blasting tanks quoted were approximately 250 sq ft/8 hr shift/person and for grit blasting hulls as approximately 1,600-2,200 sq ft/8 hr shift/person. True area removal rates vary significantly depending on the operation and are closely guarded by contractors as proprietary since they are part of the job cost quotes.

When the ship first comes into the dock, it is typically given low pressure 3,500 psi water pretreatment to wash off barnacles and marine growth. The ship rests on a series of blocks set in place by divers while the dock is flooded. The blocks are not repositioned during the time in dry dock resulting in some areas of the hull not receiving a new coating for two times in the dry dock, although on subsequent returns to the dry dock the blocks are positioned in different locations so those areas can be treated and to avoid any detrimental effects to the metal from

having rested on the same locations. It was noted that 15% of the surface area of the underwater hull can be exposed and still be compensated by the anodes to avoid corrosion; the main issue would then be fouling. The sonar domes located at the bow are protected by custom built rubber coverings with extreme care being paid to protect the rubber and avoid any overspray while grit blasting. One of the grit blasting workers described the work as brutal on the body and demonstrated a starting position that entailed leaning into the nozzle at a 45 degree angle to compensate the opposing force of the nozzle in operation. Towards the end of the visit, the team realized how important alternate methods are needed to remove paint.

9.2 External Conferences

1. ASETSdefense 2011 Sustainable Surface Engineering for Aerospace and Defense, February 8-10, 2011, New Orleans, LA
2. IEEE 38th International Conference on Plasma Science and 24th Symposium on Fusion Engineering, Chicago, Illinois, June 26-30, 2011
3. 64th Gaseous Electronics Conference, November 17th, 2011, Salt Lake City, UT
4. IEEE 39th International Conference on Plasma Science, July 8-12, 2012, Edinburgh, UK

9.3 SERDP/ESTCP Washington Annual Symposium

1. Partners in Environmental Technology Symposium & Workshop, Nov 29-Dec 2, 2010
2. Partners in Environmental Technology Symposium & Workshop, Nov 29-Dec 1, 2011

9.4 In Progress Review Meetings

1. Feb 23, 2011
2. April 17, 2012
3. April 23, 2013

Task 10 Reports

1. Monthly financial and quarterly technical reports
2. 11Apr11 White Paper Response to 24Feb11 Request
3. 25May2012 White Paper Response to 8May2012 Request
4. Interim Report: W912HQ-10-C-0026 SERDP WP1762 "Atmospheric Plasma Depainting", December 2012, pp.119
5. Final Report: W912HQ-10-C-0026 SERDP WP1762 "Atmospheric Plasma Depainting", August 2014

Conclusions and Implications for Future Research/Implementation

Atmospheric plasma was investigated as an innovative media-free coating removal system for use on Department of Defense ship and vehicle platforms. The research focused on two main types of paint used on Navy ships - Freeboard haze gray used above the waterline, and Antifouling used below the waterline. It was found that atmospheric plasma removed these coating systems to bare metal without significantly altering the profile of the DH36 steel surface. Depainted surfaces examined using x-ray photoelectron spectroscopy indicated that plasma was able to remove all traces of paint, while grit blasting tended to have residue from incomplete removal. While grit blasted surfaces contained air grown oxides, the surface oxide produced using plasma was primarily Fe_3O_4 (magnetite) and Fe_2O_3 (hematite) as determined using glazing angle x-ray diffraction and x-ray photoelectron spectroscopy. Test panels depainted using plasma along with grit blasting panels for comparison, were subsequently coated with new paint, then subject to performance tests including adhesion pull-off, B117 salt fog, cathodic disbondment, and alternate immersion in sea water. Some panels were repainted immediately, but one set was aged two weeks after plasma depainting before they were recoated for performance testing. There were no statistically significant differences in coating adhesion performance in any of the sample sets. These results demonstrated the suitability of using atmospheric plasma for removing coatings with no additional steps needed prior to repainting in order to achieve satisfactory performance. This information could be used in the development of a military specification sheet which would be a logical next step for this process.

The use of a low pressure compressed air source (90 psi) and electricity produces a special form of atmospheric pressure plasma. The PlasmaFlux™ system created a highly chemically activated plasma which attacks (oxidizes) the organic components of paints and other coatings. Optical emission spectroscopy was used to identify the presence and distribution of chemically active atomic and molecular species of oxygen and nitrogen in the complex makeup of the plasma. Organic components of paint were broken down into small molecular weight components, primarily carbon dioxide and water, as determined by mass spectroscopy. Inorganic fillers used in the paint were the primary components of solid waste as determined using optical and electron microscopy and energy dispersive x-ray analysis. Depending on the operational conditions, especially when using aggressive removal conditions upon scale-up of the plasma system, some smaller not completely broken down fragments of the coating system were also part of the waste stream. Theoretical calculations were performed to determine the mass of gaseous and solid products which would be expected if all initial paint was converted to mineral constituents including carbon dioxide and water. As an example, removing paint from one aircraft carrier would produce carbon dioxide in an amount similar to that produced by five average automobiles per year. In terms of solid waste, using plasma to remove paint, approximately 40 to 54% of the original coating mass is collected, primarily due to the inorganic fillers, the remainder of which is converted to gas. These numbers were confirmed experimentally by measuring mass before and after a confined depainting experiment. When operated with free exhaust to the air, NO, a nuisance gas, was detected. Through design and ensuring that plasma is in contact with paint for removal, generation of nuisance gas should be minimized. These results demonstrate numerous benefits for operational and environmental performance by eliminating the use of media and the significant reduction in waste generated.

Mass or area removal rates measured using a single plasma applicator indicated that approximately eight to fourteen nozzles would be needed to achieve comparable commercial rates on the order of 50 ft²/hour minimum. Scale-up in design, manufacture, and testing was performed in increments up to an eight-nozzle plasma system including the power supply in order to meet that objective. Removal rates were calculated in many experiments and found suitable for scale-up potential. In order to transition this technology for field use, the ultimate system size needed would require several steps in order to move the system further towards commercial use. A small area system is ready for demonstration with minor configuration adjustments as needed, depending on the intended end use. A cost benefit analysis is recommended in order provide details on how large the system would need to be in order to balance operational and environmental benefits compared to grit blasting. Further system development would be required in a demonstration phase to identify pros and cons of a manually operated full size system, versus full or partial automation. This would include additional investigation of the waste management system which was integrated with the plasma system in this research and found suitable for preliminary operation and experimentation.

The technology investigated was found to be portable, could be operated by manual or automatic means, was scaled to a desired size, presented no undue hazards to the tool operators, and created no significant waste beyond the breakdown products of the original coating materials. Although no significant occupational or environmental hazards were created such as sound, EMF, or UV/visible light, upon further scale-up additional requirements might need to be considered for field transition. For example, once the size of the system is determined and a decision is made on manual or automated operation, there will be size and weight considerations. Integration with the waste collection system onto the plasma applicator for manual operation might be cumbersome for an operator, but robotic operation would be more able to handle the forces. Compared to the forces created during grit blasting, it is anticipated that the air flow of the plasma would be at least partially offset by the suction of the vacuum collection system.

Further consideration will be needed to ensure operational efficiency. During most of this research, repainting was performed using a robotic stage. For field use, mechanisms would need to be developed to allow operation over various surface geometries. An example would be rollers or wheels equipped with appropriate standoff mechanisms such as springs with stops and feedback controls to ensure complete paint removal for efficient operation over rivets or uneven surface areas. Additional safety devices would be needed to ensure the plasma is triggered only when actively involved in the paint removal process and attached to a surface. Other improvements could ensure operational safety such as lights or indicators which an operator could monitor during the process real time. Integration with computer systems would allow metrics of removal operations to be monitored such as power consumed and area stripped in a given period of time or shift. Although various components of the system were designed for rugged field use, only operation over a long period of time under a variety of different field conditions will prove performance of the technology as a whole. There is much known about waste collection systems, but integration, scale of size, and field performance are needed to identify any potential weaknesses during extended operation.

In response to a request from SERDP, implications of Title V Clean Air Act ((CAA § 501-507; USC § 7661-7661f), which has to do with permits, were evaluated. Title V of the Clean Air Act

as amended in 1990 requires all major sources and some minor sources of air pollution to obtain an operating permit. The permit includes all air pollution requirements that apply to the source, including emissions limits and monitoring, record keeping, reporting requirements, and other requirements. These requirements are rather complex and vary by locality.

Title V requires operating permits in several cases:

1. The EPA has identified 187 chemicals or chemical compounds as hazardous air pollutants and has defined a major source of those pollutants as a stationary source (building, facility, or installation) which emits or has the potential to emit 10 tons per year or more of any hazardous air pollutant or 25 tons per year or more of any combination of hazardous air pollutants
2. Sources emitting sulfur oxides, sulfur dioxide, nitrogen oxides, and nitrogen dioxide as well as particulate matter with a diameter less than or equal to a nominal 10 microns are required to have a permit.

Requirement 1 is not relevant to atmospheric plasma depainting, since none of the identified pollutants are produced. Requirement 2 may be relevant depending on many details which will not be described here. However if existing operations utilizing grit blasting are currently NOT required to have a permit based on being a source of particulate matter (PM), then a permit would likely not be required for atmospheric plasma paint stripping operations. If, on the other hand, they ARE required based upon current emissions, the permit might not be needed by converting to plasma paint removal. Since no media is used, there could be an immediate 100% reduction in emissions based on grit, depending on the situation, and a dramatic decrease in the amount of “paint waste” produced.

The only other potential concern is with the “new” potential emission of nitrogen oxides which are primarily produced only when the plasma is in free flow mode and not removing paint. By incorporating devices to ensure plasma is active only when removing paint, and having sufficient waste collection systems, any nitrogen oxides produced could be contained. In the worst case scenario, catalysts which are already commercially available, could be employed to eliminate any potential emissions. In summary, there should be no significant negative impact when implementing atmospheric plasma for paint removal relative to Title V, but there might be a huge opportunity for savings if current permits were no longer needed. The answers to these questions can be obtained through a demonstration validation program.

Literature Cited

- [1] J. Claar, J. J. Cuomo, D. Diehl, C. Oldham, R. Sanwald, T. Wilt and P. Yancey, "Methods for Removal of Polymeric Coating Layers from Coated Substrates". US Patent 2006/0000488 A1, 5 January 2006.
- [2] A. L. Bimman and A. A. Bimman, "Dual Torch Plasma De-painting of Aluminum Substrates," *SAE*, vol. 983118, pp. 107-111, 1998.
- [3] R. A. Weber, J. Boy, R. Zatorski and A. Kumar, "Demonstration and Validation of Thermal Spray Vitrification of Lead-Containing Paint on Steel Structures," US Army Construction Engineering RL, Champaign, IL, Dec 1998.
- [4] A. Kumar and J. P. Petreanu, "Removal of Lead Based Coatings by Vitrification". US Patent 5292375, 8 March 1994.
- [5] P. Kaste, R. Daniel, R. Pesce-Rodriguez, M. Schroeder and J. Escarsega, "Hydrogen Plasma Removal of Military Paints: Chemical Characterization of Samples," Army Research Laboratory ARL-TR-1825, October 1998.
- [6] K. Kunaver, M. Mozetic and M. Klansjek-Gunde, "Selective Plasma Etching of Powder Coatings," *Thin Solid Films*, vol. 459, pp. 115-117, 2004.
- [7] M. Araya, T. Yuji, T. Watanabe, J. Kashihara and Y. Sumida, "Application to Cleaning of Waste Plastic Surfaces Using Atmospheric Non-Thermal Plasma Jets," *Thin Solid Films*, vol. 515, pp. 4301-4307, 2007.
- [8] "<https://sems.serdp-estcp.org>," [Online].
- [9] "www.shopbottools.com," [Online].
- [10] "www.sas.com," [Online].
- [11] T. H. Arnold, J. Meister and G. Bohm, "Atmospheric Plasma Jet Machining: Simulation of Spatiotemporal Substrate Surface Temperature Distributions," *OSA FiO, OF&T*, 2008.
- [12] A. Neira, "Thermal Modeling Simulation of Electron Beam Melting for Rapid Prototyping on Ti6Al4V Alloys," North Carolina State University, Materials Science & Engineering, Ph.D. Thesis, Raleigh, NC 27695, 2012 in press.
- [13] "“Review of Acceptable Flash Rusting for Ship Coatings”, Final Report," Advanced Technology Institute by Atlantic Marine Florida and Elzly Technology Corp. , August 2009.
- [14] "www.wikipedia.org," [Online].
- [15] L. d. Campo, R. B. Perez-Sae and M. J. Tello, "Iron Oxidation Kinetics Study by using Infrared Spectral Emissivity Measurements below 570 C," *Corrosion Science*, vol. 50, pp. 194-199, 2008.
- [16] Corpro Companies, "Evaluatin of high-solids/high-performance coatings applied over flash-rusted surfaces," NAVSEA, Feb 2004.
- [17] Atlantic Marine Florida and Elzly Technology Corp, "Review of acceptable flash rusting for ship coatings, Final Report," 2009.
- [18] J. Sheffield, *Plasma Scattering of Electromagnetic Radiation*, NY: Academic Press, 1975.
- [19] I. Hutchinson, *Principles of Plasma Diagnostics*, Cambridge, UK: Cambridge University Press, 1987.
- [20] PLASUS, Trathstraße 5 B, D-86438 Kissing, Germany, [Online]. Available:

www.plasus.de.

- [21] I. Ocean Optics, 830 Douglas Avenue, Dunedin, FL 34698, [Online]. Available: www.oceanoptics.com.
- [22] Y. Ralchnko, A. E. Kramida and J. Reader, "physics.nist.gov/asd," National Institute of Standards and Technology,, 2011. [Online].
- [23] Z. Navrátil, "www.physics.muni.cz/~zdenek/span/index.php .," Department of Physical Electronics, Masaryk University,, 2011. [Online].
- [24] R. A. Gottscho and T. A. Miller, *Pure and Appl. Chem.*, vol. 56, no. 2, pp. 1898-208, 1984.
- [25] T. J. Cotler, *J. Appl. Phys.*, vol. 69, no. 1, pp. 2885-2889, 1991.
- [26] K. Saski, Y. Okumura and R. Asaoka, "Article ID 627571," *International Journal of Spectroscopy*,, 2010.
- [27] <http://etd.ohiolink.edu/send-pdf.cgi/Choi%20Inchul.pdf?osu1299098588> .. [Performance]. Department of Mechanical Engineering, Ohio State University, 2011.
- [28] J. Torres, *J. Phys. D: Appl. Phys.*, vol. 36, pp. 55-59, 2003.
- [29] T. Wujec, H. W. Janus and W. Jelenski, *J. Phys. D: Appl. Phys.*, vol. 36, pp. 868-877, 2003.
- [30] C. O. Laux, *Journal of Quantitative Spectroscopy & Radiative Transfer*,, vol. 68, pp. 473-482, 2001.
- [31] S. Y. Moon and W. Choe, *Spectrochimica Acta, Part B*, vol. 58, pp. 249-257, 2003.
- [32] J. RuizCamacho and R. Castell, *Phys. Scr.*, Vols. T131, 014016,, 2008.
- [33] MiWiTron, "miwitron.com/index.html .," [Online].
- [34] A. Berchtikou, J. Lavoie, V. Poenariu, B. Saoudi and Raman, "Thermometry in Noble Gas Dielectric Barrier Discharges at Atmospheric Pressure using Optical Emission Spectroscopy," *IEEE Transactions on Dielectrics and Electrical Insulations*, vol. 18, no. 1, pp. 24-33, 2011.
- [35] L. Yu, C. O. Laux, D. M. Packan and C. Kruger, "Direct-current glow discharges in atmospheric pressure air plasmas," *Journal of Applied Physics*, vol. 91, no. 5, pp. 2678-2686, 2002.
- [36] C. O. Laux, T. G. Spence, C. H. Kruger and R. N. Zare, "Optical diagnostics of atmospheric pressure air plasmas," *Plasma Sources Sci. Technol.*, vol. 12, pp. 125-138, 2003.
- [37] Y. Ralchenko, A. E. Kramida and J. Reader, 29 May 2012. [Online]. Available: <http://physics.nist.gov/asd>.
- [38] A. Descouedres, C. Hollenstein, R. Demellayer and G. Walder, "Optical emission spectroscopy of electrical discharge machining plasma," *Journal of Materials Processing Technology*, vol. 149, pp. 184-190, 2004.
- [39] L. X. Mao, M. A. Shannon and A. J. Fernandez, "Temperature and Emission Spatial Profiles of Laser-Induced Plasmas during Ablation Using Time-Integrated Emission Spectroscopy," *Applied Spectroscopy*, vol. 49, no. 7, pp. 1054-1062, 1995.
- [40] C. O. Laux, *Optical diagnostics and radiative emission of air plasmas*, Department of Mechanical Engineering at Stanford University, 1993.
- [41] F. Kaufman, "The Air Afterglow and Its Use in the Study of Some Reactions of Atomic Oxygen," *Proc. R. Soc. Lond. A*, vol. 247, pp. 123-139, 1958.

- [42] W. Roodebush, "The Reaction Between Nitric Oxide and Atomic Oxygen," *Chem. Rev.*, vol. 17, no. 3, pp. 409-412, 1935.
- [43] V. V. Zhdanok and S. A. Naumov, "Afterglows in Nonequilibrium Reactive Plasma Flows Near Atmospheric Pressure," *Physica Scripta*, vol. T63, pp. 295-296, 1996.
- [44] C. O. Laux, "Optical diagnostics and radiative emission of air plasmas," *Dissertations s.l.*, 1993.
- [45] M. e. Chung, in *Proceedings of the IEEE International Power Modulators and High Voltage Conference*, May 2008.
- [46] J. P. Boris, A. M. Landsberg, E. S. Oran and J. H. Gardner, "A Flux-Corrected Transport Algorithm for Solving Generalized Continuity Equations," NRL, April 1993.
- [47] S. P. Kuo, E. Koretzky and R. J. Vidmar, "Temperature Measurement of an Atmospheric Pressure Plasma Torch," *Review of Scientific Instruments*, vol. 70, no. 7, pp. 3032-3034, 1999.
- [48] A. Schute, J. Y. Yeong and S. E. Babayan, "The Atmospheric-Pressure Plasma Jet: A Review and Comparison to Other Plasma Sources," *IEEE Transactions on Plasma Science*, vol. 26, no. 6, pp. 1685-1694, 1998.
- [49] N. Bourdet, M. Laroussi and A. Karakas, "Experimental Investigations of Plasma Bullets," *J. Phys. D.*, vol. 42, 2009.
- [50] A. Chirokov, A. Gutsol and A. Fridman, "Atmospheric Pressure Plasma of Dielectric Barrier Discharges," *Pure Applied Chemistry*, vol. 77, no. 2, pp. 487-495, 2005.
- [51] J. R. Roth, J. Rahel, X. Dai and D. M. Sherman, "The Physics and Phenomenology of the One Atmosphere Uniform Flow Discharge Plasma (OAUGDP) Reactors for Surface Treatment Applications," *J. Phys. D: Appl. Phys. Vol. 38*, 2005.
- [52] A. I. AlShamma, S. R. Wylie and J. Lucas, "Design and Construction of a 2.45 GHz Waveguide-based Microwave Plasma Jet at Atmospheric Pressure for Material Processing," *J. Phys. D*, vol. 34, no. 18, pp. 2734-2741, 2001.
- [53] J. Park, I. Henins, H. W. Herrmann and G. S. Selwyn, "Neutral Bremsstrahlung Measurement in an Atmospheric-Pressure Radio Frequency Discharge," *Physics of Plasmas*, vol. 7, no. 8, pp. 3141-3144, 2000.
- [54] M. M. Kekez, M. R. Barrault and J. D. Graggs, "Spark Channel Formation," *J. Phys. D: Appl. Phys.*, vol. 3, p. 1886, 2000.
- [55] D. Graves, "Plasma Interaction with Biological Systems," *To appear in PSST*, 2012.
- [56] S. Starikovskaia, "Plasma Assisted Ignition and Combustion," *J. Phys. D: Appl. Phys.*, vol. 39 R265, 2006.
- [57] X. P. Lu and M. Laroussi, "Dynamics of an Atmospheric Pressure Plasma Plume Generated by Sub Microsecond Voltage Pulses," *J. Appl. Phys.*, vol. 100, no. 063302, 2006.
- [58] D. Staak, B. Farouk and A. Gutsol, "Stabilization of the ionization Overheating Thermal Instability in Atmospheric Pressure Microplasmas," *J. Appl. Phys.*, vol. 106, no. 013303, 2009.
- [59] M. Heintze, R. Zeditz and G. H. Baure, "Analysis of High-rate a-Si:H Deposition in a VHF Plasma," *J. Phys. D: MI Phys.* 26, pp. 1781-1786, 1993.
- [60] X. Wang, R. Huang and J. Song, "Microstructure and Initial Growth Characteristics of

- Nanocrystalline Silicon Films Fabricated by Very High Frequency Plasma Enhanced Chemical Vapor Deposition with Highly H₂ Dilution of SiH₄," *J. Appl. Phys.* 107, 124313, 2010.
- [61] V. A. Godyak, "Soviet Radio Frequency Discharge Research," Delphic Associates Inc., Falls Church, VA, 1986.
- [62] K. McKay, F. Iza and M. G. Kong, "Excitation Frequency Effects on Atmospheric-pressure Helium RF Microplasmas: Plasma density, Electron energy and Plasma impedance," *Eur. Phys. J. D* 60, pp. 497-503, 2010.
- [63] M. A. Lieberman and A. J. Lichtenberg, Principles of Plasma Discharges and Materials Processing, 2nd Edition, Hoboken, NJ: Wiley Interscience, 2005.
- [64] S. Zhang and X. W. Hu, "New Microwave Diagnostic Theory for Measurement of Electron Density in Atmospheric Plasmas," *Chin. Phys. Lett.*, vol. 22, no. 1, p. 168, 2005.
- [65] A. A. Garamoon and D. M. El-Zeer, "Atmospheric Pressure Glow Discharge Plasma in Air at Frequency 50Hz," *Plasma Sources Sci. Technol.*, vol. 18, 2009.
- [66] J. Park, I. Henins, H. W. Herrmann and G. S. Selwyn, "Discharge Phenomena of an Atmospheric Pressure Radio-Frequency Capacitive Plasma Source," *J. Appl. Phys.*, vol. 89, no. 1, 2001.
- [67] April 2012. [Online]. Available: http://en.wikipedia.org/wiki/Iron_oxide.
- [68] T. W. Egar and N. S. Tsai, "Temperature fields produced by traveling distributed heat sources," *Welding Research Supplement*, p. 346s, 1983.
- [69] N. S. Tsai and T. W. Eaga, "Distribution of heat and current fluxes in gas tungsten arcs," *Metallurgical Transactions 16B.*, p. 841, 1985.

Appendices

A. Glossary of Terms for Multiple Nozzles

The additional dimension of complexity added by using multiple nozzles concurrently necessitates that certain terms be clearly defined. The following definitions were used for experiments utilizing multiple nozzles.

Multi-nozzle : generic term for an applicator capable of supporting multiple active plasma nozzles concurrently

y-direction : The fast axis in which the plasma applicator is moved across the plane of the sample surface in a single pass; typically this is defined as the short axis of the sample's surface

x-direction : The slow axis in which the plasma applicator is moved between subsequent passes during a multi-pass treatment

z-direction : Height above the sample in the z-direction, normal to the surface (for flat samples); defined as the distance between the sample surface and the closest point of the nozzle

s : Surface speed of a pass in the y-direction

Subpass : For two-dimensional arrays of nozzles, if smaller-spaced passes are conducted in the area between adjacent rows of nozzles before indexing to a new location, these are considered subpasses (see Figure 2 for illustration)

Swath : A contiguous area of treated coating on a sample resulting from single or multiple passes of single or multiple nozzles over one or more sweeps

Sweep : A sequential grouping of passes conducted over a fixed area of a sample is a single sweep; a multisweep treatment adds further treatment within the same area, although an offset is generally added to prevent treatment of the exact same location by passes from subsequent sweeps

Pass : Any single movement of the plasma applicator to treat a surface without changing direction; typically the pass is conducted at a constant speed, s

Stripe : In rare cases, the exact same x-location may be treated over multiple sequential passes before moving to the next location, in which case the swath is said to consist of multi-pass stripes

Treatment rate: Area treated by the plasma per unit time, calculated based on scan speed, s , effective interpass spacing Δx , and number of repeat sweeps, n , using the following formula, which factors in only time spent directly over the sample.

$$\text{Treatment Rate} = s * \Delta x / n$$

Multi-pass : A treatment consisting of multiple sequential passes in the y-axis separated by an interpass spacing, Δx

Multisweep : A treatment consisting of multiple sweeps

Internozzle spacing : Center-to-center distance between two adjacent nozzles on the plasma applicator, not affected by the movement or angle of the applicator. The current multi-nozzle applicator design has a fixed internozzle spacing of 1.25"

Δx : **Interpass spacing** : For simple, single-nozzle treatment patterns, this is the distance that the applicator is physically translated between subsequent passes in the x-direction; typically a positive non-zero number; with more complex multi-nozzle sweep patterns, the effective interpass spacing is calculated as the average distance between adjacent treatment stripes

Δx_n : **Interpass spacing between nozzles** or **nozzle-interpass spacing**: The distance between the centerlines of two adjacent swaths created by two adjacent nozzles scanned at an

array angle of α ; this is not affected by the physical translation of the applicator between passes (Δx)

Δx_o : *Interpass spacing offset*: The distance added to the initial pass of subsequent sweeps of a multisweep treatment in order to prevent treating the exact same locations on the sample on multiple sweeps (see sweep)

θ : *nozzle angle* : The angle between the z axis of the applicator (through the center of the nozzle outlet) and the z-axis of the sample (normal to the surface); may be defined as being in the yz, xz, or other plane as well as positive or negative depending on the application

α : *array angle* : The angle between the alignment axis of a multi-nozzle applicator and the direction of motion of the applicator (y) over the sample surface; typically held between 0° (total overlap) and $+90^\circ$ (minimum overlap)

B. List of Scientific/Technical Publications

1. In Progress Review, WP1762 NCSU, AP Depainting, April 23, 2013, Washington, DC
2. MCWILLIAMS, ANTHONY JOSEPH (2012). "Characterization of Atmospheric Pressure Plasma Torch and the Surface Interaction for Material Removal". (Doctoral dissertation). North Carolina State University, pp218, <http://www.lib.ncsu.edu/resolver/1840.16/8030>
3. A. J. McWilliams, S. J. Hudak, S. C. Shannon, and J. J. Cuomo, "Characterization of a hybrid atmospheric pressure air plasma torch using optical emission spectroscopy", Plasma Sources Science & Technology, submitted for publication
4. NEIRA ARCE, ALDESON (2012). "Thermal Modeling and Simulation of Electron Beam Melting for Rapid Prototyping on Ti6Al4V Alloys." (Doctoral Dissertation) North Carolina State University, 2012, pp.228, <http://www.lib.ncsu.edu/resolver/1840.16/8202>
5. S.J. Hudak, In partnership with NCSU, AP Solutions, NSWCCD, NAVAIR, AFRL, Interim Report: W912HQ-10-C-0026 SERDP WP1762 "Atmospheric Plasma Depainting", December 2012, pp.119
6. A. J. McWilliams, S. J. Hudak, S. C. Shannon, J. J. Cuomo, "Analysis of Atmospheric Pressure Plasma Torch and the Effects of Multiple Gas Compositions on Plasma Chemistry and Its Interaction with High Density Polyethylene", 39th IEEE International Conference on Plasma Science, Edinburgh, Scotland, UK July 8-12, 2012, session 2C-8
7. B. R. Byrns, A. Lindsay, S. Shannon, "Vhf Ballasting for High Density Atmospheric Glow Discharges", 39th IEEE International Conference on Plasma Science, Edinburgh, Scotland, UK , Edinburgh, Scotland, July 8-12, 2012 Session 2P-169
8. S.J. Hudak, S.C. Shannon, "Atmospheric Plasma Depainting", 25May2012 White Paper Response to 8May2012 Request, Jerry Cuomo, PI, White Paper submitted to SERDP
9. 17April 2012 In Progress Review, WP1762 NCSU, AP Depainting, Arlington VA
10. S.J. Hudak, J.J. Cuomo, A. McWilliams, "Atmospheric Plasma for surface modification", ASETS Defense 2011: Sustainable Surface Engineering for Aerospace and Defense, Feb 8-10, 2011 New Orleans, LA
11. 23Feb2011 In Progress Review WP1762 NCSU AP Depainting, Arlington VA.
12. 11Apr11 White Paper Response to 24Feb11 In Progress Review
13. A.J. McWilliams, S.C. Shannon, S.J. Hudak, J.J. Cuomo, "Optical Emission Spectroscopy Characterization of Atmospheric Pressure Plasma Removal of High Density

Polyethylene”; Proceedings of the 64th Annual Gaseous Electronics Conference, Salt Lake City, UT, November 11-14, 2011

14. A.J. McWilliams, S. J. Hudak, S. C. Shannon, J.J. Cuomo, “Optical characterization of a plasma torch for HDPE removal”; submitted to J. Vac. Sci. Technol. A., October 2011

15. S.J. Hudak and A. McWilliams, “Atmospheric Plasma Depainting”, Poster for SERDP Partners in Environmental Technology Symposium and Workshop, Nov 27-29, 2012
Washington, DC

16. B.R. Byrns, D. Wooten, S.C. Shannon, “Design and characterization of a novel coaxial VHF plasma source for air plasma formation”; Proceedings of the 64th Annual Gaseous Electronics Conference, Salt Lake City, UT, November 11-14, 2011

17. B.R. Byrns, D. Wooten, S.C. Shannon “A VHF driven coaxial atmospheric air plasma: electrical and optical characterization”; J. Phys. D., July 2011

18. A.J. McWilliams, S. J. Hudak, S.C. Shannon, J.J. Cuomo, “Analysis of Atmospheric Pressure Plasma Torch and the Effects of Multiple Gas Compositions on Plasma Chemistry and Its Interaction with High Density Polyethylene”, 39th IEEE International Conference on Plasma Science, Edinburgh, UK, July 8-12th 2012. 17:30 2C-8

19. A. McWilliams, S.C. Shannon, S.J. Hudak, J.J. Cuomo, “Optical Emission Spectroscopy Characterization of Atmospheric Pressure Plasma Removal of High Density Polyethylene”, Presentation at 53rd Gaseous Electronics Conference, Salt Lake City, Utah, November 14-18th 2011.

20. A.J. McWilliams, S.C. Shannon, S.J. Hudak, J.J. Cuomo, “Optical Characterization of Atmospheric Torch Operating Modes”, 38th IEEE ICOPS, Chicago, IL, June 26-30, 2011.